BRUSHLESS DC MULTIPHASE RELUCTANCE MACHINES AND DRIVES

Teză destinată obţinerii
titlului ştiinţific de doctor inginer
la
Universitatea Politehnica Timişoara
în domeniul INGINERIE ELECTRICĂ
de către

Ing. Dragoș Ursu

Conducător ştiinţific: prof.univ.dr.ing. Ion Boldea
Referenţi ştiinţifici: prof.univ.dr.ing. Mircea Rădulescu
                           prof.univ.dr.ing. Iulian Birou
                           conf.univ.dr.ing. Lucian Nicolae Tutelea

Ziua susţinerii tezei: 29.09.2014

Acknowledgements

I would like to express my sincere gratitude to my supervisor Prof. Ion Boldea for his encouragement and support during the course of this study. I would like to thank also Prof. Babak Fahimi from the University of Texas at Dallas for his support during my research period at UTD.

Professor Lucian-Nicolae Tutelea is gratefully thanked for his assistance and valuable technical and scientifically discussions during my work. Also I thank prof. Cristian Lascu for fruitful discussion on control strategies of electrical machines.

My deepest appreciation goes to all those professors from the Faculty of Electrical Engineering who contributed to my engineering education.

My colleagues Mircea Baba, Sorin Agarliţă, Ana Popa-Moldovan and Emil Guran, are thanked for all they have done, both directly and indirectly in helping me.

I feel grateful to my friends Luci and Carina for their encouragement during these years.

Finally, and most of all, I want to thank all family members who supported me during challenging times.

Timişoara, September 2014

Dragoş Ursu

**To my father Doru and
my brothers Alexandru and Ana-Maria**

Abstract,
　　In an yet another effort to produce better PM-less, rotor-winding-less, brushless electric motor drives, this thesis reports on design, optimization, numerical analysis and control of a multiphase, high saliency rotor, dual-flat-top alternative current control BLDC reluctance machine drives. The aim is to produce high torque density, low loss / torque in a PM-less, rotor winding-less machine by full usage of machine windings and core and of inverter kVA.
　　A new derivation of the principle of operation, essential rotary and linear machine topologies and a 2D FEM analysis for torque density and torque pulsations on the designed prototypes are made available and show promising results. Advanced iron loss computation by FEA indicates moderate core loss, although high air-gap magnetic flux density and current harmonics occurs as a natural behavior of a BLDC machine. Experimental flux-decay and run-out tests results are presented, which, together with standstill torque measurements, validate the FE design.
　　An optimal design code for an automotive application was developed based on particle swarm optimization and magnetic equivalent circuit for performance evaluation.
　　Electrical and mechanical parameter identification is followed by BLDC-MRM mathematical model and control strategy development. Running experiments (motoring and generating) with speed reversal and field weakening modes (thus 4-quadrant operation) is also shown on two different test-rigs, one for the 5 phase BLDC-MRM (supplied by a full bridge inverter) and one for the 6 phase BLDC-MRM (working with a reduced number of switches).

Table of Contents

Motivation

The motivation behind this work relates to cost reduction, design simplification, fault-tolerant operation, better inverter kVA utilization and improved performances of the existent electrical machines.

Eliminating the high energy product PMs (or replacing them by low cost ferrite PMs), but maintaining good performance in electric machine drives, has become lately a main way to deal with rare earth PMs rather high price.

The high saliency rotor (with multiple flux-barriers (FB), or axially laminated anisotropic (ALA) rotor) reluctance synchronous machine (RSM) – without or with ferrite PMs assistance (in q-axis) – and 3-phase inverter field oriented or direct torque sinusoidal current control seems the obvious way to good performance without high energy product PMs. However, the reluctance 3-phase synchronous machine with sinusoidal current control does not make full use of inverter kVA (as known from the comparison with BLDC PMs motors working with rectangular current control).

The 3 (4 , 5) phase 400 Nm switched reluctance machine (SRM) drives, recently proved to produce 45 Nm/L and 95% efficiency at 5000 rpm, with special magnetic core, still suffer from rather low utilization of inverter voltage and limited torque production typical to variable reluctance machines.

In the hunt for higher torque density, without PMs, BLDC multiphase reluctance machine (BLDC – MRM) principle was investigated decades ago with promising preliminary results. However the spectacular advance of PMSMs had led to their practical abandoning for twenty years. The 90° interaction angle between "field" phases and "torque" phases magnetic fields and the recent dramatic progress in multiphase inverter make the revival of BLDC-MRM timely.

This thesis represents a revival attempt of a twenty years old idea presenting advanced numerical simulation models, optimization algorithms and dynamic experimental results.

Thesis objectives

The major objectives of the thesis are as follows:

➢ to develop an analytical electromagnetic design procedure;

➢ to develop MatLab embedded, script based, 2D-FEA models using free or commercial software and to compute key parameters and performances, including iron losses;

➢ to develop a fast numerical model for the optimal design code performance evaluation based on magnetic circuits theory;

➢ to analyze state of the art optimization algorithms, put them to test and choose one for the optimal design of the BLDC-MRM;

➢ to reduce the cost of the machine by an optimal design program;

➢ to measure the electrical and mechanical parameters and use them to validate the simulation models;

➢ to develop a dynamic model of the machine and drive based on the computed parameters;

➢ to control a 5 phase BLDC-MRM using a full bridge inverter and to test its steady-state performances in a 4:1 speed ratio;

➢ to propose a new control strategy for the BLDC-MRM with reduced number of switches;

➢ to control a 6 phase BLDC-MRM using a reduced number of switches by a proper phase connection to a null point and adopting the new developed strategy;

➢ to test four-quadrant machine operation with field weakening operation;

➢ to perform experimental validation of the dynamic model and 2D-FEA model;

Thesis outline

The thesis is organized in 7 chapters following the above objectives.

➢ Chapter one starts this work by presenting the state of PM-less and less PMs drives. The principle of operation of the Brushless DC Multiphase Reluctance Machines (BLDC-MRM) is also presented.

➢ Chapter two deals with preliminary design of a BLDC-MRM generator used in a micro-grid system and finite element analysis of the 5/6 phase BLDC-MRM including state of the art iron loss computation.

➢ Chapter three starts by investigating a few stochastic optimization algorithms. In the light of performance evaluation on test functions the best one is selected. A numerical non-linear model based on magnetic equivalent circuits and node potential theorem is developed for BLDC-MRM performance computation in the optimization algorithm routine. The optimization mechanism of the BLDC-MRM takes the prior design prototype and searches the best machine in terms of total cost objective function.

➢ Chapter four analyzes the development of the circuit dynamic model for transient study. Electrical and mechanical parameter identification methods are covered, since they represent the heart of a good drive simulation model.

➢ Chapter five presents the control of the five/six phase BLDC-MRM with full bridge inverter phase connection and with reduced number of switches inverter operation.

➢ Chapter six describes the two test platforms of the BLDC-MRM, from the hardware and software point of view, designed and developed at two universities (UTD and UPT).

➢ The last chapter of the thesis, chapter seven, draws the conclusion, presents the original contributions and proposes future line of work.

1. PM-less and less PM electrical machines for renewable energy and transportation: A review

Abstract

This chapter offers an overview of the PM-less and less PM electrical machines for renewable energy and transportation. In the search of a cost effective, fault tolerant, high torque density electrical machine, advantages and drawback of various types of variable reluctance electrical machines are presented. Deduction of the BLDC-MRM principle of operation from a DC machine point of view is given at the end of this introduction chapter.

1.1 Introduction

Electromechanical energy conversion devices are part of everyday life, from home appliances to large wind/hydro generators. The vast number of electrical machines available in all industries in the mW to GW power range has an increasing trend and serves as the heart and muscle of our society. In the past century electrical engineers have designed various configurations of electrical machines (linear/ rotating) with fixed or traveling magnetic fields, each with its own advantages and drawbacks. Numerous types of windings (distributed/ concentrated) in a multiphase structure have been used in order to create a radial/axial magnetic flux distribution. Salient (flux barrier, axially laminated anisotropic, or segmented pole) versus non-salient rotors with or without PM's, are manufactured for diverse applications. A cost effective, fault tolerant and reliable machine implies simplicity in mechanical structure combined with a copper-less, PM-less rotor and a multiphase stator winding. The advantages are obvious: reduced price (compared to PM machines), better cooling (stator can be cooled more efficient), no rotor copper losses and low rotor iron loss (ideal none). Also, the required power per phase rating of the inverter is lowered, and torque production is increased if a multiphase winding is employed [1.1]. Possible applications that exploit these topologies are: electric aircraft, railway traction, ship propulsion and off-shore wind energy harnessing [1.2-1.5]. This study focuses on a PM-less, high saliency synchronous machine, whose benefits lies both in the financial part and in long run drive exploitation.

Nowadays, Reluctance Synchronous Machines (RSM), especially those with an Axially Laminated Anisotropic (ALA) [1.6-1.8] or with multiple flux barriers (FB) rotor, are becoming more and more attractive for electric power generation from wind/ hydro energy. This is due to lack of PMs and rotor windings; so in theory, at synchronous operation (and sinusoidal traveling air-gap magnetic flux), all the losses should be in the stator from which heat can easily can be extracted. Compared to Switched Reluctance Machines (SRM), RSM makes use of all the air-gap volume for energy conversion, works at lower level of saturation and has lower torque pulsations. Induction Machines (IM) are also a good candidate for the job, but they work in asynchronism, and rotor winding losses must be accounted for.

Most of PM machines are unattractive at this point, because of the too higher cost of high energy PMs, and due to low rotor temperature limitations related to PM demagnetization.

1.2 PM-less and less PMs Reluctance Machines

The common ground of reluctance machines is the salient structure of the rotor and/or the stator, which in the end dictates the machine performances, torque production and power factor. Besides that, the winding arrangement is a crucial factor in effectiveness of power conversion.

1.2.1 Reluctance Synchronous Machines

The Reluctance Synchronous Machine is a singly salient machine whose rotor is built up so as to employ the principle of reluctance torque to produce electromechanical energy conversion. The torque is produced by the tendency of its movable part to advance to a position where the inductance of the excited winding is maximized. The rotor is made of conventional lamination sheets or axial laminations and due to its structure high rotational speed is achievable. Rotor cage winding could be present for line-starting and stable transient operation. Although RSM doesn't need field winding or PM's on the rotor, their existence certainly improves the machine performances, at a higher initial machine cost. The stator of a RSM has no major differences compared to the IM stator geometry. The machine has uniformly distributed slots with concentrated or distributed multiphase singly or doubly layer windings. A comprehensive unitary study of this subject can be found in [1.9].

A high saliency ratio is needed for the RSM to increase the torque production and the power factor. Rotor anisotropy is mainly produced by three different structures: flux barriers, axially laminated or segmental rotor (Fig. 1.1). A flux barrier rotor is also a viable option for the rotor of RSM and it could even be competitive with the IM if q-axis low cost ferrites PMs are present [1.10, 1.11]. Although segmented rotor is the next in line, being much cheaper than the mentioned two rotor solutions, it should in general be avoided due to well-known lower performance.
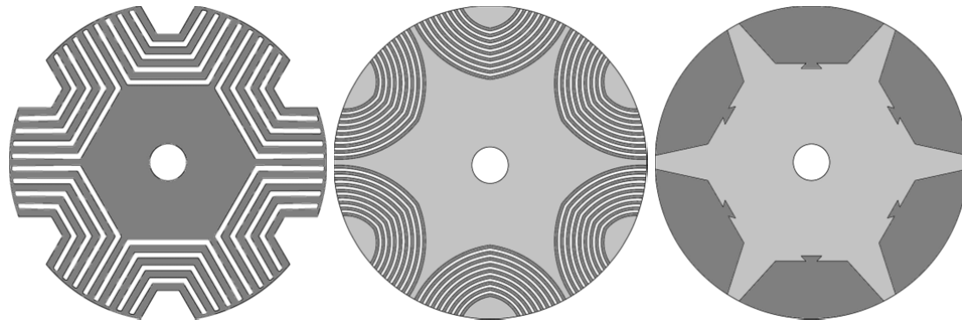
Fig.1.1. RSM rotors: flux barrier rotor (left), axially laminated rotor (middle), segmental rotor (right)

A more expensive solution such as ALA rotor with high number of lamination/insulation packets is needed for high saliency ratios which provide high torque density and good power factor, making the machine competitive. In an ALA machine the armature reaction is controlled through interleaving layers of material with high reluctance between iron lamination, thus increasing the reluctance of the armature field path, and creating a reduced armature reaction machine. The armature reaction increases the air-gap flux density at the leading edge of the pole. High flux densities at the pole edge give rise to an enlarged slot width and enlarged leakage inductance that deteriorates the commutation properties. A low pole number design gives a higher inductance ratio due to less slot leakage and higher pole pitch to air-gap height ratio. Authors from [1.8] reports a 0.91 power factor, and a 90% efficiency for a 1.1 kW ALA rotor, 2 pole, 3 phase RSM. This was accomplished by adopting a 0.3 mm air-gap, a 0.5 mm lamination thickness and 0.3 mm insulation thickness layers, which led to an unusually high saliency ratio equal to Ld/Lq = 21, unsaturated, and 16 at rated load.

Polyphase reluctance machines were studied since the early 1960s [1.12]. For the same machine volume an increase of the number of phases will make the torque per ampere ratio larger. Because of special converters and high number of switches a multiphase machine is likely to be limited to specialized applications [1.2-1.5].

In an effort to design an automotive starter-alternator with superior performances compared to the classical Claw Pole Alternator, the authors from [1.13] presents a concept based on a four pole RSM with a flux barrier, ferrite PM assisted rotor and a rotor field winding (Fig.1.2) called Biaxial Excitation Generator for Automobiles (BEGA). The machine achieved 80% efficiency at 3000 rpm, and 70% at 6000 rpm, which is better than the obtained performances of the classical Lundell machine but inferior compared to a modified Interior Permanent Magnet CPA [1.14]. Dynamic results under vector control at unity power factor as a starter-alternator were shown in [1.15]. Although is a viable solution and a strong competitive of the Lundell machine BEGA was not yet enacted by the industry.
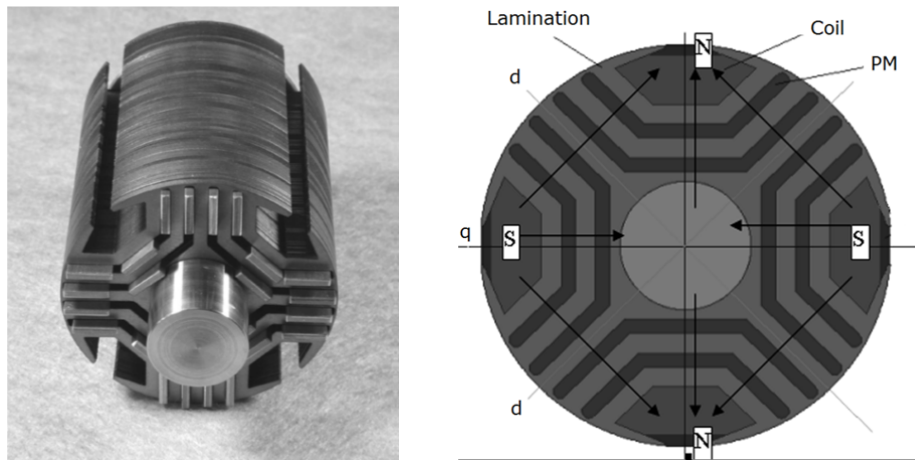
Fig.1.2. BEGA rotor without field winding (left) and cross-sectional view of the FB rotor and PM magnetization [1.13]

1.2.2 Switched Reluctance Machines

The switched reluctance machine (SRM) is a double salient machine with a passive rotor, which produces torque by the tendency of its rotor to reach a position of maximum inductance [1.16]. Usually each stator pole has its own coil connected in series with the adjacent coil on the opposite pole. The phases are independent and the excitation represents a sequence of voltage pulses applied to each phase at a time. In contrast to IM the SRM has concentrated coils and all the torque developed is reluctance torque. The salient pole rotor is somehow similar to that of RSM, without any windings, cages or PMs. There are a vast number of possible combinations for the number of phases and stator and rotor poles. The SRM easily achieves an 8÷10 saliency with 6/8 poles.

Although the name SRM was introduced in the late 1960's [1.17]; this type of machine is much older. The first one seems to have been used to propel a locomotive in Great Britain in 1838. In 1840 a primitive structure of SRM was patented by Taylor while in 1920s Walker patented the stepper motor which is the closest relative of the SRM [1.16]. The converter-fed SRM was developed in the '70s, and since then lots of improvement have made both to machine and to the power electronics, the drive becoming a strong contestant when fault tolerance operation was needed, but it seems that in the last few years most of its limits have been reached.

The SRM is not in the true sense an AC machine nor a DC machine. It does not have a referential frame for constant voltage, current and flux as in RSM or IM. In SRM the field current cannot be separated from armature current by vector control, like in the IM or RSM, tough is has same effect as in IM : it produces both the field and the torque, so about the same copper weight is expected.

The SRM has a simple construction, low rotor inertia, high-speed performance and low-cost. A disadvantage related to SRM is that only one phase conducts at a time. For a 5 phase SRM, only a fifth of the air-gap periphery contributes to torque production which leads to poor iron utilization. The doubly salient structure makes SRM to operate at high magnetic saturation levels in order to be competitive with IM, which make the iron losses higher.

SRM needs to work in a saturated mode for two main reasons: to increase the ratio of kW/kVA (without decreasing the torque too much) and to make the phase current commutation easier. Working in generator mode the situation is trickier because one would have to install the current on the high level of the inductance. Even within a saturated SRM the kW/kVA ratio which is something similar to power factor remains below 0.65-0.7, so a big converter is needed. The equivalent power factor is 10% smaller than in an IM at the same efficiency. The sequential current switching together with sever magnetic saturation make the torque ripple larger than in IM or IPMSM, although techniques that improve the torque ripple and the noise have been presented in the last years. The torque ripple is reduced by employing more phases; theoretically an infinite number of phases are needed for a zero torque pulsation in a SRM.

Because the SRM is already working saturated in normal conditions, at rated torque, the peak transient torque is in general 80% above the rated torque, while in the IM with rotor field oriented control the transient torque can rise to 12 times the rated toque at low speeds.

The use of SRM as a starter-alternator system on an aircraft was reported in [1.18, 1.19], with experimental results on a 1500 hp, 48000 rpm model. The machine was tested in motoring mode in the constant torque region to a speed of 26000 rpm after which it was run as a generator delivering constant power over a 2:1 engine operating speed.

A variant of the SRM has been recently proposed for vehicle transportation [1.21, 1.22]. Double Stator Switched Reluctance Machine DSSRM has higher torque density than the conventional SRM by a design than maximize the tangential force, while reducing the radial force thus reducing the vibrations and acoustical noise. 300% more torque is obtained by the 8/6/8 DSSRM (Fig.1.3 right) compared to the 8/6 SRM (Fig.1.3 left). The mechanical complexity and the need to extract the heat from the inner stator also, make the machine less reliable compared to SRM and IM. The classical version of a high-speed SRM has been used in aeronautic industry passing tight restrictions and regulations. Work form [1.22] reports on 80% more torque generation compared to PMSM with the same material cost.

For now, no full-scale competitive prototypes for SRM or DSSRM have been fully demonstrated to be a practical solution for automotive applications.
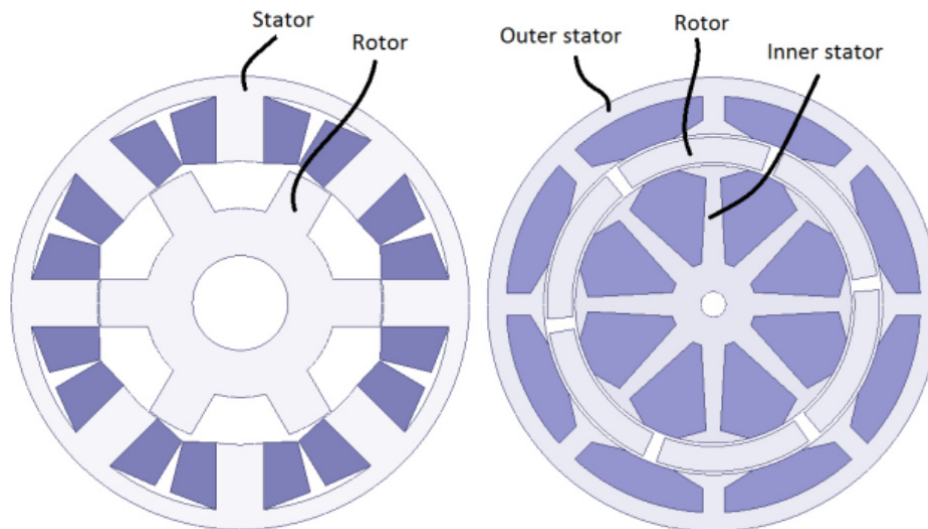
Fig.1.3. Cross-sectional view of a classical SRM (left) and DSSRM (right) [1.23]

1.2.3 Claw Pole Machines

Claw-pole machine is a special type of electrical machine with a simple construction that uses only one DC excitation winding for all poles. The rotor consists of forged pole pieces (claw poles) secured around a circular field coil (Fig. 1.4). Regulating the field current controls the alternator system diode (rectified) output voltage. Changes in field current occur with a L/R field winding time constant that is typically on the order of 0.1 s or more. To minimize cost, single layer stator windings, with q=1 (one slot per phase per pole) are used.

The main advantage of claw-pole machines lies in their ability to yield higher torque density values than is obtainable from a conventional machine, because the number of poles can be increased without decreasing the conductor volume. This is to be compared with a conventional machine where the electric and magnetic parts compete for the same space, and a higher number of poles only give less flux per pole and thus no change in torque. According to [1.24], the transverse flux machine and the claw-pole machine can be included in the family of torque magnification (TM) machines. In [1.25], is calculated a possible torque density of 28 kNm/m^3 (compared to 5,75 kNm/m^3 for an equivalent size induction motor). However, the high torque density has its price: leakage flux is often high, resulting in low power factor and efficiency. They also found that the leakage between claws was 30-50% of the main flux. According to [1.26], the excessive eddy currents limit the claw-pole designs to small sizes and/or low speeds resulting a low efficiency. Skin effect at high frequency decreases the efficiency, because the transversal component of the magnetic flux density doesn't penetrate the laminated sheets of the stator, also the same phenomena increase the stator winding resistance making the copper losses to increase with frequency.

The main drawbacks of this type of generator are: high saturation, high magnetic leakage between claws (about 30-40% of the main flux), low efficiency, relatively large field time constant and high armature leakage reaction [1.26]. The availability of reasonably priced power diodes in the 1960s paved the way for the automotive industry to start the series production of the claw-pole alternator (Lundell machine) for on-board energy production.

The studies performed by Perreault, Caliskan and Whaley have investigated means of extracting more electrical power from the Lundell alternator using the switched-mode rectifier (SMR) [1.27-1.29]. The MIT electrical engineering team proposed an increase in voltage and replacement of the classical diode rectifier with a controllable rectifier along with a special load matching control technique that allows higher level of output power and efficiency [1.27]. Introducing a SMR increases the power at 14 Vdc by a factor of 2 at 42 Vdc, while the efficiency increases from 40% to 60% at 6000 rpm [1.27], but the SMR additional cost has to be considered.

Placing the PM between poles gives better performance on the whole speed range. Inserting PMs in the inter-polar regions will provide magnetic flux that will reduce flux leakage between two successive rotor poles [1.14]. A modified Bosch alternator is analyzed (using magnetic equivalent circuit (MEC) and 3D-FEM), in [1.14] showing that a short-time braking power of 8 kW can be recovered if the voltage is increased three times (form 14 Vdc to 42 Vdc) and inter-polar magnets (IPM) are used. Experimental results on a retrofitted Bosch 3.2 kW, 42 Vdc IPM-CPA show 80 % efficiency at 3000 rpm, 78% at 6000 rpm and 60% at 18000 rpm.
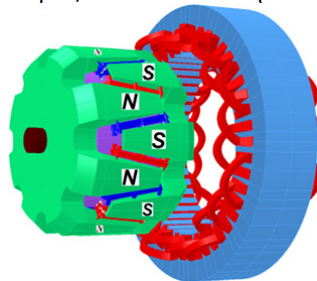

Fig.1.4. The geometry of the Interior Permanent Magnet CPA

1.3 Multiphase Drives

A multiphase drive requires less power per phase rating of the inverter; which is a key feature in high-power (railway traction, ship propulsion) and high current (EV and HEV) applications [1.30-1.31]. Another advantage is the additional degree of freedoms available in control that can be used to increase the torque production (by high order stator current signal injection) or to make the drive fault tolerant.

Conventional three-phase machines exhibits as a rule a virtually sinusoidal distribution of exciter field and armature current loadings. The attainable mean thrust density is therefore at most half as large as the maximum value which can be derived from the amplitudes. The mean thrust density can be easily enlarged if both the currents and the field have square wave characteristics.

Previous studies [1.32] have shown that sinusoidal flux distribution in a multiphase machine with concentrated windings is often an undesirable feature of a multiphase machine since the stator iron is poorly used, i.e. just one stator tooth (the one under the maximum value of flux) being saturated. This leads to a trapezoidal current waveform (just like in a BLDC), for each current harmonic to interact with correspondent flux harmonic and produce torque. By using a rectangular air-gap magnetic flux density waveform larger yoke is needed to manage the same flux, compared to the sinusoidal case, if the maximum value is kept

The authors of [1.33] have found out that by using a rectangular current profile in a 6 phase multiphase induction machine, with a concentrated winding, at the same volume and copper losses, the torque density of the machine was 15% higher compared to sinusoidal current profile.

The separately excited DC-brush machine principle has been successfully applied for a decoupled field and torque control in a high phase order IM, without the use of coordinate transformation and flux linkage estimators and simplifying the control algorithm [1.34-1.35]. The authors from this work use two equivalent windings supplied essentially by two trapezoidal currents (field and torque), thus making full use of machine iron, through an evenly distributed saturation.

1.4 BLDC-MRM principle of operation

The birthplace of the presented concept was in München, in 1986, where authors from [1.36] proposed the application of inverted-fed multiphase synchronous machine, based on DC machine operation, with electronically commutated phases. Instead of the usually employed sinusoidal shape of current a rectangular field wave of the *mmf* was introduced. The machine presented in [1.39] had a null point connection of phases because the existent phase shift between two adjacent phases was $m \cdot 2\pi/p$, which ensures that the sum of currents (for ideal commutation) is at all times zero. Stable operation is possible only if information on the pole position is available. Their study did not give any drive performance data. Work from [1.38] presents experimental results (static torque and inductance determination) of a 28 kW machine design working at 500 rpm. A four quadrant DC transistor chopper was used to supply each motor phase in [1.38].

The idea behind the operation of this type of electrical machine is to replace what it is done mechanically in a DC machine by a commutator (that ensures a fixed orientation of the armature current to the exciter field) with an electronically commutator, through a voltage inverter and current regulators. This concept was already applied on AC drives (on induction machine and synchronous machine) under the name of field oriented control FOC. One should keep in mind that vector control is based on coordinate transformation and flux/torque observers, while the BLDC-MRM machine achieves the decoupling of the field and the torque current "by nature", through stator/rotor geometry and winding configuration.

This type of machine has been "baptized" in the past with various names (Field Regulated Reluctance Machine FRRM [1.38], Series-Connected Switched Reluctance Motor SSRM [1.40]) but probably the most suitable term encoding the principle of operation and design was introduced in [1.41]. The proposed machine configuration is the closest to a true brushless DC machine (as we shall see next), due to its trapezoidal current waveform and a strong resemblance with a classical DC machine in terms of operation. The realization of this technique is best achieved with a multiphase winding layout and a reluctance rotor. Putting all these head to head the term Brushless DC Multiphase Reluctance Machine BLDC-MRM came naturally.

The BLDC-MRM principle will be explained in parallel for the 5-phase and 6-phase machine through the equivalence with the DC machine as shown in Figs. 1.5, 1.6. Let us consider a two pole, 5/6 coil-rotor, exciter-less DC brush machine, with brushes moved away from neutral axis (q-axis) to the corners of the rotor poles and with enlarged magnetic saliency in the stator. In both cases two coils (D, E for the 5-coil and E, F for the 6 coil rotor) placed in the q-axis, were selected to produce the field flux (ψ_f) along *d*-axis. The field coils (always changing as the rotor spins) take the role of the stator excitation winding from the classical DC machine. The remaining 3/4 coils (A,B,C and A,B,C,D) under the pole shoe, work as armature coils, producing torque. A lower number for field coils is not acceptable because the commutation process will introduce large torque ripple, while a higher number of is unnecessary since they act on the minimum reluctance path of the magnetic circuit. In this case the average torque will decrease as a result of fewer available coils for torque production. The stator flux barriers increase the saliency of the machine and reduce the armature reaction controlled also trough air-gap length.
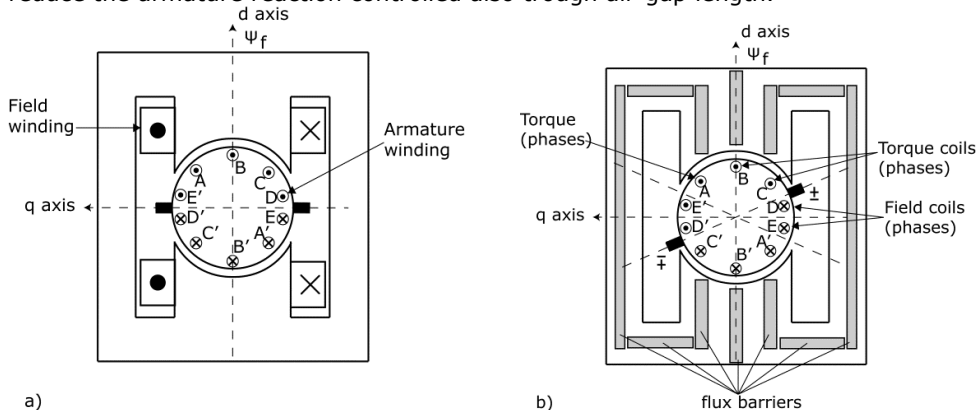
Fig.1.5. Cross-sectional view of the a) conventional DC machine and b) Equivalent 5-phase exciter-less DC machine
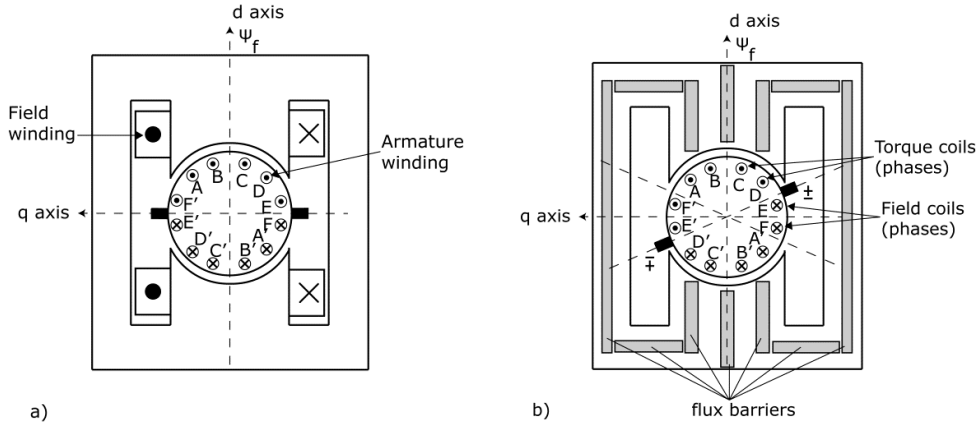
Fig.1.6. Cross-sectional view of the a) conventional DC machine and b) Equivalent 6-phase exciter-less DC machine
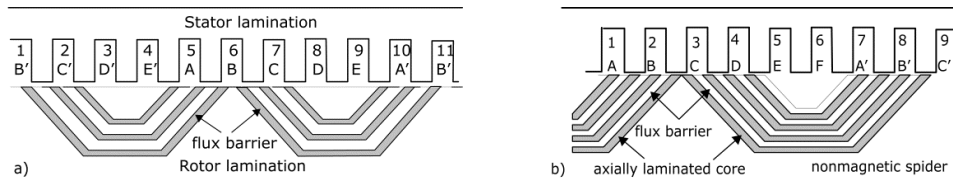
Fig.1.7. a) 5-phase linear (rotary) FB-rotor BLDC-MRM simplified geometry, b) 6-phase linear (rotary) ALA-rotor BLDC-MRM simplified geometry

Now we can easily imagine how the electronically commutated phases of machine from Fig. 1.7 work. Basically it is the same machine inside out except that the mechanical inverter is replaced by a voltage source inverter. Each phase current has a "field current" time interval and a "torque current" time interval and is bipolar. Now it is evident that phases D,E (Fig.1.7.a) and E,F (Fig.1.7.b) play the role of field phase while the rest of the winding acts as the armature and produce torque. As the rotor spins, each phase assumes both roles (field and torque producing phase) depending on the rotor position. Because a non-sinusoidal air-gap *mmf* is required, q=1. However the stator slots are deeper than in the IM and thus the stator teeth core losses are higher and the stator external diameter and core weight are higher. Better cooling than in the IM case is obtainable because all the copper losses occur in the stator. The rotor saliency (FB as in Fig. 1.7.a or ALA design as in Fig.1.7.b) is mandatory for a reduced armature reaction, and not for torque production as in a Reluctance Synchronous Machine. In order to avoid saturation effect it should be assumed that the sum of the lamination thickness at least correspond to that of tooth widths. The force generation resembles that in a conventional DC machine, Lorentz force being generated by the interaction between the field flux and the torque (armature) current, resulting in an overall developed average torque exerted on the rotor. This configuration and control ensures a 90 electrical degrees angle between field flux and torque producing coils currents. The interaction between field and torque phase fields (*mmfs*) takes place close (within ± 15 degree) around 90° (not between 60° and 120° as in standard 3 phase BLDC PM motors).

If the torque phases are in series with the field phases the machine behaves like a DC series machine, and the same equations could be written if the saturation is neglected. While in sinusoidal RSM is not advantageous to increase the ratio of pole pitch to polar step beyond 2/3 because the saliency starts decreasing here the width of the pole depends solely on the torque-producing phase number. In both cases the saliency increases with the ratio of the pole pitch to air-gap length. In the BLDC-MRM case a too large saliency will increase the armature reaction and will make the current commutation more difficult, just as in the DC machine case.

A BLDC-MRM can be also viewed as a synchronous machine in which the field windings are located on the stator. Significantly lower conduction losses compared to the IM are found to be in the BLDC-MRM for the same amount of active materials and considering the same force density [1.38].

A higher force generation and better overall performance can be obtained by a square wave input. Typical flat-top bipolar level current waveform is presented in Fig. 1.8. The "field" and "torque" currents time intervals t_f and t_t are related to field and torque number of phases m_f and m_t divided by total number of phases m (eq.1.1).

$$t_f = \pi \cdot \frac{m_f}{m}; \quad t_t = \pi \cdot \frac{m_t}{m} \tag{1.1}$$

The downside of this system of currents is the created asymmetry due to the π/m phase shift between two adjacent phases. The problem is that you will always end up with a non-zero current through the null connection, so the machine star connection of phases must be carefully handled. When getting under or out of the pole shoe, only one phase commutates from field to armature role. The commutation process should last less than the time period required for the rotor to rotate with the angle corresponding to one slot pitch. In this time interval the commutating phase experiences a small motion induced voltage by the other torque producing phases which tends to slow down the commutation process. Up to base speed the field current level is equal to the level of torque current level. Above base speed a field weakening strategy is employed to extend the constant power speed range, which will lead to smaller copper losses.
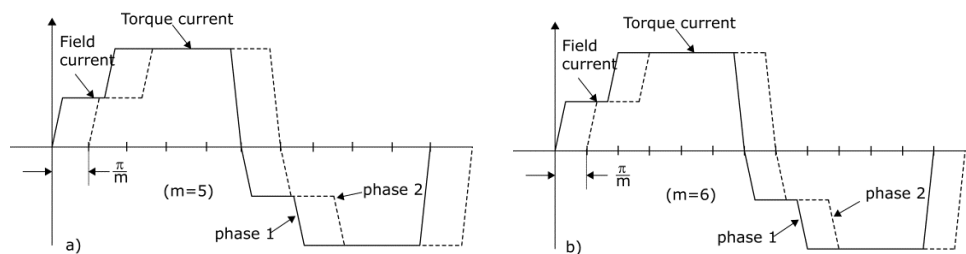
Fig.1.8. Typical flat-top bipolar level current waveform for the: a) 5-phase BLDC-MRM and b) 6-phase BLDC-MRM

A speed control as flexible as in a separately excited DC machine is obtained by the independent control of field and armature current, the two decoupled 90° windings (field/excitation winding and torque/armature winding) ensuring a fast torque response.

High harmonics are expected from this class of machines due geometry stator slotting, rotor slotting and the current waveform. The harmonics present in the radial component of magnetic flux density translate into torque pulsations, additional eddy current losses, vibration and noise. Throughout this work torque pulsations, speed ripple and eddy current losses are analyzed. The vibration and noise could represent future work, if testing equipment and special FEA software modules are acquired. Based on author personal experience with two tested drives the acoustic noise and mechanical vibrations in on the existent platforms were in acceptable parameters, meaning that a normal conversion between two people is possible next to the drive at full load operation.

The control of bipolar two-level current mode is very similar to field oriented control in the sense that the reference current waveforms in the m-phase may be generated based on encoder output as the current vector rotator does for sinusoidal mode (Fig.1.9). Field weakening can easily be implemented by monitoring the reference speed value. Negative torque may be obtained by a change of sign of the torque current. An independent control of field current and armature current gives a speed control flexibility known in the DC machines, can be derived. A linear version of the BLDC-MRM can be controlled by the proposed scheme of Fig. 10.
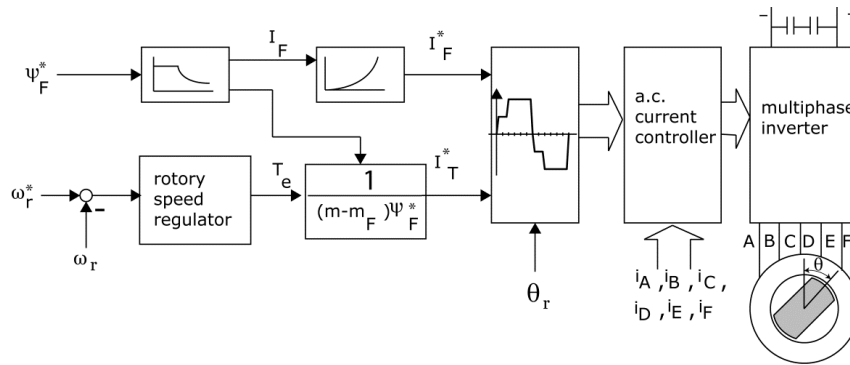
Fig.1.9. Rotary machine control
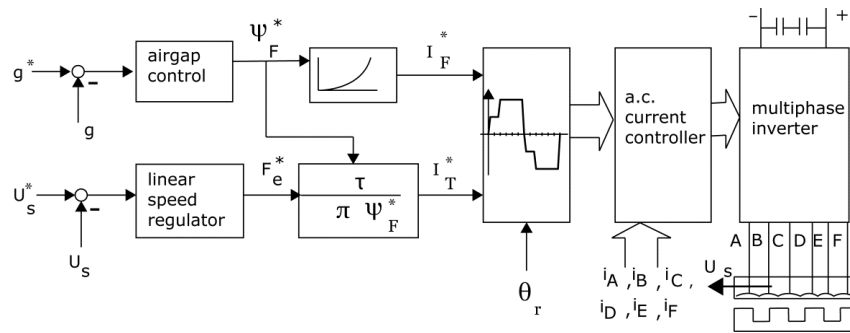
Fig.1.10. MAGLEV control (g-air-gap length, Us – synchronous speed)

Conclusion

The BLDC-MRM goes back and mimics the DC machine, but we took out the stator excitation and move the brushes to the neutral axis. The price for this will be paid in the inverter; because we need rotor position triggered electronic commutation of phases, one after the other. The field current control is not fully independent of armature (q-axis) reaction field, but not far from that, as the field phase's field-axis stays close to the d-axis. The machine takes advantage of space and time harmonics introduced by geometry and current waveform to produce more torque.

Also the idea is to use a simpler control without using coordinate transformation, a control that mimics the behavior of the DC brush Machine. Vector control, based on the so-called dq-reference frame has been invented precisely for this scope, to make the AC machine easier to control with better dynamics through a decoupling of the field and torque producing current in the machine. The BLDC-MRM principle of operation does this decoupling naturally, but, of course other aspect has to be considered and studied thoroughly.

The subject seems worth reviving with new design and control methodologies to exploit the full potential of the inverter-fed BLDC-MRM, characterized by full utilization of copper and iron core, and interaction at around 90 degrees between field phases and torque phases, with a good inverter kVA utilization and good fault tolerance.

References

[1.1]   E. Levi, M. Jones, A. Iqbal, S.N Vukosavic and H.A. Toliyat, "*Induction Machine / Synchronous – Reluctance Two – Motor Five – Phase Series-Connected Drive*", IEEE Trans. On Energy Conversion, Vol. EC-22, No. 2, pp. -281-289, 2007

[1.2]   C. Sanabria-Walter, H. Polinder and J.A. Ferreira, " *High torque desnity high efficiency Flux-Switching PM Machine for Aerospace Applications,* " IEEE Journal of Emerging and Selected Topics in Power Electronics, Vol. 1, No. 4, 2013, pp. 327-336

[1.3]   M.D. Hennen, M. Niesse, C. Heyers and H.J. Brauer, "*Development and Control of an integrated and distributed inverter for a fault tolerant Five-phase switched reluctance traction drive*", IEEE Trans. on Power Electronics, Vol. 27, No.2, 2012, pp. 547-554

[1.4]   A.M. El-Refaie, "*Motors/generators for traction/propulsion applications: A review*", IEEE Vehicular Technology Magazine, Vol. 8, No.1, 2013, pp. 90-99

[1.5]   S. Muller, M. Deicke and R.W. de Donker, "*Doubly Fed induction Generator systems for wind turbines*", IEEE Industry Applications Magazine, Vol. 8, No. 3, 2002, pp. 26-33

[1.6]   A.J.O. Cruickshank, R.W. Menzies and A.F. Anderson, "*Axially Laminated Anisotropic* Rotors *for Reluctance Motors*", Proc. IEE, Vol. 113, No. 12, 1966, pp. 2058-2060

[1.7]   A.J.O. Cruickshank, A.F. Andersona and R.W. Menzies, "*Theory and performance of reluctance Motors with axially laminated anisotropic rotors*", Proc. IEE, Vol. 118, No. 7, 1971, pp. 887-893

[1.8]   I. Boldea, Z.X. Fu and S.A. Nasar "*Performance evaluation of axially-laminated anisotropic (ALA) rotor reluctance synchronous motors",* Conf. Rec. of IAS, 1992, vol.1, pp. 212-218

[1.9]   I. Boldea, "*Reluctance Synchronous Machines and Drives*", Clarendon Press, Oxford, 1996

[1.10] L.N. Tutelea, A. Moldovan and I. Boldea, "*50/100 kW, 1350-7000 rpm (600 Nm peak torque, 40 kg) PM assisted Reluctance synchronous machine : optimal design with FEM validation and vector control*", IEEE, International Conference on Optimization of Electrical and Electronic Equipment, OPTIM-2014, pp. 276-283

[1.11] Vagati, A.; Boazzo, B.; Guglielmi, P.; Pellegrino, G., "*Ferrite Assisted Synchronous Reluctance Machines: a General approach*", ICEM 2012, pp: 1315- 1321

[1.12] P.J. Lawrenson and L.A. Agu, "*Theory and performance of polyphase reluctance machines*", Proc. Of IEE, Vol. 111, no. 8, 1964, pp. 1435-1445

[1.13] S. Scridon, I. Boldea, L.N. Tutelea, F. Blaabjerg and A.E. Ritchie, " *BEGA – A biaxial Excitation Generator for Automobiles: Comprehensive Characterization and Test Results*", IEEE Trans. On Industry Applications, Vol. IA-41, No.4, 2005, pp. 935-945

[1.14] L.N. Tutelea, D. Ursu, I. Boldea and Sorin Agarlita: „*IPM Claw Pole Alternator System for more vehicle braking energy recuperation*", Journal of electrical engineering, www.jee.ro, Vol. 12, No. 3, 2012

[1.15] I. Boldea, V. Coroban_Schramel, G.D. Andreescu, F. Blaabjerg and S. Scridon, "*BEGA Starter/Alternator – Vector Control Implementation and Performance for Wide Speed Range at unity power factor operation*", IEEE Trans. On Industry Applications, Vol. IA-46, No.1, 2010, pp. 150-159

[1.16] TJ Miller, "*Switched reluctance motors and their control*", Clarendon Press. Oxford, 1993

[1.17] S.A. Nasar, "*DC Switched reluctance motor*", Proc. Of IEE, Vol. 116, No.6, 1969, pp. 1048

[1.18] S.K. MacMinn and W.D. Jones, "*A Very High Speed Switched-Reluctance Starter Generator for Aircraft Engine Applications,*" Proceedings of NAECON '89, Dayton, Ohio, May 22-26, 1989, pp. 1758-1764.

[1.19] S.R. MacMinn and J.W. Sember "*Control of a Switched-Reluctance Aircraft Engine Starter/Generator Over a Very Wide Speed Range,*" Proceedings of IECEC, August 6-1 1,1989, pp. 631-638

[1.20] A. Chiba, M. Takeno, N. Hoshi, M. Takemoto and S. Ogasawara, "*Consideration of number of turns in Switched-Reluctance Traction Motor Competitive to HEV IPMSM*", IEEE Trans. On Industry Applications, Vol. IA-48, No.6, 2012, pp. 2333-2340

[1.21] M. Abbasian, M. Moallem and B. Fahimi, "*Double-Stator Switched Reluctance Machines (DSSRM): Fundamentals and Magnetic Force Analysis*", IEEE Trans. On Energy Conversion, Vol. EC-25, No.3, 2010, pp. 589-598

[1.22] W. Wang, C. Lin and B. Fahimi, "*Comparative analysis of Double stator switched reluctance machine and permanent magnet synchronous machine*", International Symposium on Industrial Electronics, ISIE-2012, pp. 617-622

[1.23] A.H. Isfahani and B. Fahimi, "*Multi-physics analysis of a double stator switched reluctance machines*" Energy Conversion Congress and Exposition (ECCE), 2013 IEEE, pp. 2827 – 2833

[1.24] D. Qin, Q. Ronghai, "*A novel electric machine employing torque magnification and flux concentration effects*", Industry Applications Conference, Thirty-Fourth IAS Annual Meeting, Conference Record of the 1999 IEEE, Vol. 1, pp. 132-139,1999.

[1.25] M. R. Harris, and B. C. Mecrow , "*Variable reluctance permanent magnet motors for high specific output*" Electrical Machines and Drives, Sixth International Conference on (Conf. Publ. No. 376): 437-442, 1993.

[1.26] Y. G. Guo, J. G. Zhu, "*Design and analysis of a three-phase three-stack claw pole permanent magnet motor with SMC stator*" Paper 85, Proceedings of Australasian Universities Power Engineering Conference (AUPEC 2003).

[1.27] D.J. Perreault, T. A. Keim, J. H. Lang and L.M. Lorrila," *Applications of power electronics in automotive power generation*", Automotive power electronics conference Paris, 21-22 June, 2006

[1.28] S. Chung, T. A. Keim and D.J. Perreault, "*Thermal modeling of Lundell Alternators"*, IEEE Trans On Energy Conversion, Vol. EC-20, No.1, 2005, pp. 25-36

[1.29] D. Krahenbruhl, C. Zwyssig, J.K. Kolar, "*Half-Controlled Boost Rectifier for Low_Power High-Speed Permanent-Magnet Generators*", IEEE Trans on Industrial Electronics, Vol. 58, No.11, 2011, pp. 5066-5075

[1.30] E. Levi, "*Multiphase Electric Machines for variable-speed applications"*, IEEE Trans. Industrial Electronics, Vol. IE-55, No.5, 2008, pp. 1893-1909

[1.31] E. Levi , R. Bojoi, F. Profumo, H.A. Tolyat and S. Williamson " *Multiphase Induction motor drives- a technology status review"*, IET Elec. Power Appl., Vol. 1, No.4, 2007, pp. 489-516

[1.32] H.A. Toliyat, Xu Longya and T.A. Lipo," *A Five-Phase Reluctance Motor with High Specific Torque"*, IEEE Trans on, Vol.IA-23, No 3, 1992, pp.659-677

[1.33] T.A Lipo and Feng X. Wang, "*Design and Performance of a Converter Optimized AC machine"*, IEEE Trans on Industry Applications, Vol. IA-20, No 4, 1984, pp. -834-844,

[1.34] Yong-Le Ai, M.J. Kamper, A.d.Le Roux, " *Novel direct flux and direct toprque control of six-phase induction machine with nearly square air-gap glux density"* IEEE Trans on Industry Applications, Vol. IA-43. No. 6, 2007, pp. 1534-1544

[1.35] N. Gule and M.J. Kamper, "*Multiphase Cage-Rotor inductuion_machine Drive with direct Implementation of Brush DC Operation*", IEEE Trans on Industry Applications, Vol. IA-48, no. 6, 2012, pp 2012-2020

[1.36] R. Mayer, H. Mosebach, U. Schroder, H. Weh, "*Inverter-fed multiphase reluctance machine with reduced armature reaction and improved power density*", in Proc. Of ICEM-1986, Munchen, Part.3, pp. 1138-1141

[1.37] Weh, Poschadel, Schroder, "*GTO inverter for the supply of multiphase synchrpnous machine*s", ICEM 1986

[1.38] J. D. Law, A. Chertok and T.A. Lipo,*"Design and performance of field regulated reluctance machine"*, IEEE Trans. On Industry Applications, Vol. IA-30, No.5, 1994, pp. 1185-1192

[1.39] H. Mosebach, H. Weh, "*Design concepts and force generation in inverter fed synchronous machines with PM excitation*," IEEE Trans. On Magnetics, Vol. MAG-20, No. 5, pp. 1756-1760, 1984

[1.40] I. Boldea, G. Papusoiu, S.A. Nasar and Z. Fu, "*A novel series connected switched reluctance motor"*,in Proc. of ICEM-1990, Part 3, pp 1212-1217.

[1.41] I. Boldea, L.N. Tutelea and D. Ursu,*"BLDC Multiphase Reluctance Machines for Wide Range Applications: a revival attempt"*, Power Electronics and Motion control Conference, EPE/PEMC-2012, IEEE, pp. LS1b.1-1 - LS1b.1-6

2. BLDC-MRM preliminary design and FEA characterization

Abstract

The present chapter offers a preliminary design routine for a 3 kW, 200 rpm, 12 poles, FB rotor BLDC-MRM working as a wind generator. The design was built and assembled as part of a micro-grid system project.

A description of the finite element method and two studied computer software's based on finite elements method are briefly presented. The finite element analysis was applied to three prototypes studied across this work: a 5 phase, 6 pole, FB rotor BLDC-MRM (designed, built and tested at University Texas of Dallas), a 6 phase, 6 pole, ALA rotor BLDC-MRM (designed, built and tested at University Politehnica of Timisoara) and a 6 phase, 12 poles, FB rotor small power wind generator (also designed and built at U.P.T). The first two were designed as a low speed, high torque machines for traction applications.

Magnetic flux density variation in different parts of the machine shows that conventional iron loss computation methods are unacceptable, especially if non-sinusoidal driving source and concentrated coils (q=1) are used. Based on this observation an advanced iron loss computation method was developed and implemented to a commercial FEA software for all three tested machines, using a scripting program.

2.1 Preliminary Design of a BLDC-MRM wind generator

General design rules for this machine were already described in works presented by authors from [2.1] and [2.2], both of them completing with an ALA rotor based BLDC-MRM prototype of different powers and phase numbers. Although these designs targeted a low armature reaction machine, the economical constraints impose, in today's industry and market, a more practical solution based on a flux barrier rotor, capable of comparable results.

This section is focused on the analytical design of a BLDC-MRM wind generator whose data are presented in Table 2.1. The phase voltage (300 V) corresponds to a null point connection of phases (as explained in section 5.3) linked to a 600 V, DC network. The machine power and rated speed were chosen in the micro-grid project.

The stator design follows similar rules as the ones for induction and synchronous machine (very well described in [2.3-2.4]) but keeping in mind the rectangular magnetic flux density waveform. In order to reduce the overall project cost the design started from an existent stator core (Appendix 12), frame, shaft and bearings from an induction machine provided by a local company. Given the stator lamination sheet data (Table 2.2), some constraints become obvious, if one would like to use this geometry as a starting point for designing a BLDC-MRM based on principles presented in Chapter 1.

The 72 slots stator core imposes a 6 phase design (in order to keep the inverter price as low as possible) and a 12 pole rotor, for one slot per pole per phase configuration. The disadvantage of using the existent lamination sheet is that it was design for a 6 pole machine (not 12). This mean that the yoke is twice as thick as needed, so the machine is heavier and the torque/weight ratio is smaller. Also the uneven saturation of different stator parts could produce vibration and consequently noise. From the existent 6 phases a minimum of two are required to produce the machine excitation field while the rest 4 phase are expect to produce the torque.

The minimum imposed average under the pole shoe air-gap magnetic flux density is selected to be 0.55 T, and the rated slot current density (under normal cooling conditions) is j_S =5.5 A/mm^2. The number of rotor slots per pole is chosen to be 9 in order to avoid rotor-stator interaction and because of the limitations related to cutting cost and torque pulsations.

Table 2.1. General input data

No.	Variable	Value
1	Rated power **Pb** [W]	3000
2	Phase voltage **Vph** [V]	300
3	Rated speed **nb** [rpm]	200
4	Number of poles **poles**	12
5	Total phase number **m_p**	6
6	Torque phase number **m_t**	4
7	Airgap magnetic flux density **B_{agsp}** [T]	0.55
8	Rated efficiency **etan**	0.77
9	Rated slot current density **j_s** [A/mm^2]	5.5
10	Slot fill factor **ksfill**	0.5
11	Paralell paths **a**	1
12	Number of layers **layers**	2
13	Slot per pole per phase **q**	1
14	Airgap height **hag** [mm]	0.4
15	Rotor tooth bridge **brt**[mm]	0.8
16	Rotor slot inner radius **rR**[mm]	0.5
17	Number of rotor slots per pole **Nr**	9
18	Rotor tooth width to rotor slot pitch ratio	0.55

Table 2.2. Stator lamination sheet dimensions

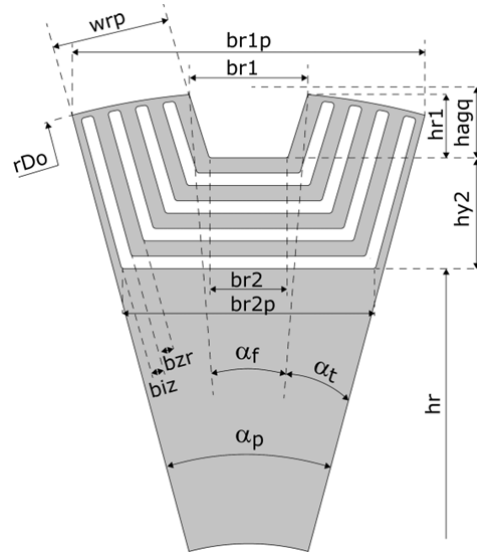| No.	Variable	Value
1	Number of stator slots **Ns**	72
2	**sh4** [mm]	1
3	**sh3** [mm]	1
4	**sh2** [mm]	0
5	**sh1** [mm]	27
6	**sW1** [mm]	6.9
7	**sRad**	1
8	**sW2** [mm]	4.6
9	**sW3** [mm]	4.6
10	**sMs** [mm]	3
11	**sDi** [mm]	208
12	**sDo** [mm]	305.2

Fig.2.1. Flux barrier rotor pole geometry

If the design starts from scratch the first step is usually stator inner diameter computation based on Esson equation [2.4] which is based on the expected tangential force (force of rotation, per unit area of the air-gap), after which the stator slot shape is chosen and designed.

The flux barrier rotor pole geometry is presented in Fig. 2.1. Three important angles defining (in radians) the span of the pole α_p , of the field α_f and of the torque α_t phases are defined in eqs. 2.1-2.3.

$$\alpha_p = \frac{2 \cdot \pi}{poles} = 0.5236; \tag{2.1}$$

$$\alpha_t = \alpha_p \cdot \frac{m_t}{m_p} = 0.3491; \tag{2.2}$$

$$\alpha_f = \alpha_p \cdot \frac{m_f}{m_p} = 0.1745; \tag{2.3}$$

The width of rotor half pole *wrp* is:

$$wrp = \frac{rDo}{2} \cdot \left(\sin\left(\frac{\alpha_t}{2} + \alpha_0 \right) - \sin(\alpha_0) \right) = 18 \quad mm; \tag{2.4}$$

were α_0 adjusts the tilt of the rotor slot base respect to the machine radius. In our case this angle is 0, so all rotor slots walls are parallel to the radius that crosses through the middle of respective pole. This was preferred because a rectangular air-gap magnetic field is needed. For a sinusoidal magnetic field, such as those existent in a 3 phase RSM, it's desirable that the widths of the rotor teeth to decrease from the pole center to pole extremities, to follow the sinusoidal field pattern.

The number of stator teeth corresponding to half a pole nzs is:

$$nzs = \frac{Ns}{poles} \cdot \frac{m_t}{m_p} \cdot \frac{1}{2} = 2;$$ (2.5)

A ratio of 0.55 between rotor tooth width and rotor slot pitch (*bzrPtaur*) will give a rotor slot pitch τ_r equal to:

$$\tau_r = \frac{wrp}{n_{pack} \cdot (1 - bzrPtaur) + (n_{pack} + 0.5) \cdot bzrPtaur} = 4.2082 \quad mm;$$ (2.6)

were n_{pack} represent the number of rotor slots per half pole, 4 in our case.

The pole pitch τ_p is:

$$\tau_p = \frac{\pi \cdot sDi}{poles} = \frac{\pi \cdot 208 \text{ mm}}{12} = 54.45 \quad mm;$$ (2.7)

The width of rotor tooth *bzr* and of the flux barrier can be found using eqs. 2.8-2.9.

$$bzr = \frac{round(bzrPtaur \cdot \tau_r \cdot 100)}{100} = 2.31 \quad mm;$$ (2.8)

$$biz = \frac{round((\tau_r - bzr) \cdot 100)}{100} = 1.9 \quad mm;$$ (2.9)

The width of the *q*-axis opening *br1* and the width corresponding to one pole opening *br1p* are a linear function of rotor outer diameter *rDo* (eq.2.10-2.11).

$$br1 = rDo \cdot \sin\left(\frac{\alpha_f}{2}\right) = 207.2 \cdot \sin\left(\frac{\alpha_f}{2}\right) = 18.058 \quad mm;$$ (2.10)

$$br1p = rDo \cdot \sin\left(\frac{\alpha_p}{2} - \alpha_0\right) = 44.669 \quad mm;$$ (2.11)

Rotor active yoke height *hy2* is:

$$hy2 = n_{pack} \cdot (bzr + biz) = 16.84 \quad mm;$$ (2.12)

Other important dimensions (as defined in Fig.2.1) are *hr, hr1, br2* and *br2p.*

$$hr = \frac{rDo}{2} - hy2 - hagq = 76.76 \quad mm;$$ (2.13)

were *hagq* is a an input variable defining the q-axis air-gap height (10 mm).

$$hr1 = \frac{rDo}{2} \cdot \cos\left(\frac{\alpha_f}{2}\right) - hr - hy2 = 9.605 \quad mm; \tag{2.14}$$

$$br2 = br1 - 2 \cdot hr1 \cdot \tan\left(\frac{\alpha_p}{2} + \alpha_0\right) = 11.982 \quad mm; \tag{2.15}$$

$$br2p = br1p - 2 \cdot hr1 \cdot \tan\left(\frac{\alpha_p}{2} + \alpha_0\right) = 38.593 \quad mm; \tag{2.16}$$

Some of rotor dimensions such as the rotor bridge thickness (0.8 mm) and the rotor slot curvature (0.5 mm radius) at each change of direction of the cutting tool are a priori information related to the mechanical rigidity and technological cutting process. All the rotor main dimensions are presented in Fig. 2.2. The complete data following this design are given in the technical drawings of Appendix 12.
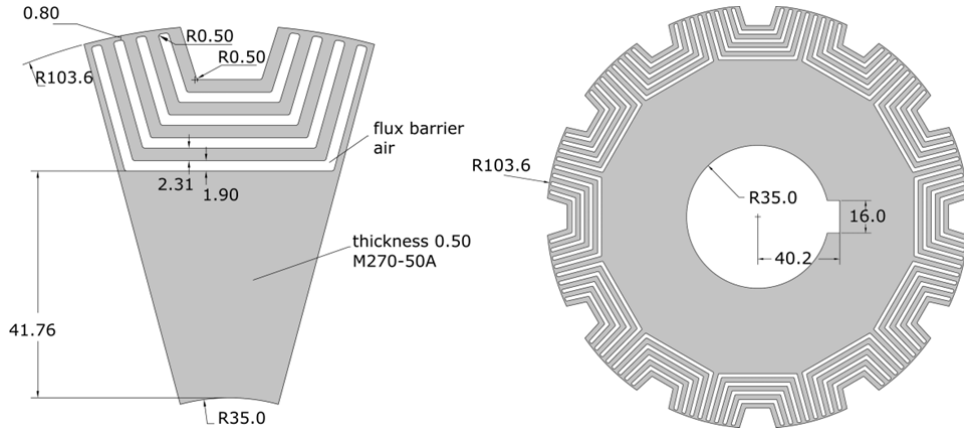
Fig.2.2. BLDC-MRM flux barrier rotor main dimensions (in mm)

The machine length has an upper limit imposed by the existent frame related to the stator lamination sheet. By choosing a shape factor value λ$_c$ (usually between 1 and 4) and knowing the stator inner diameter value the machine length could be found by eq.2.17.

$$lc = \lambda_c \cdot sDi; \tag{2.17}$$

A preliminary finite element analysis showed that in order to produce 190 Nm of average torque (3 kW at 200 rpm) the core length should be at least 180 mm at rated (5.5 A/mm^2) slot current density. By going with a 190 mm core length (which is the upper limit for the existing frame and shaft) a reserve in the produced torque is obtained. For this length the shape factor will be 0.913, which is a good trade-off between cooling, rotor inertia, machine volume and end winding losses.

Knowing the phase voltage Vph (Table 2.1), the rotor angular speed Ω_{bmec} (2.18) and main stator dimensions (Table 2.2) the number of turns per phase can be computed by 2.19:

$$\Omega_{bmec} = \frac{2 \cdot \pi \cdot nb}{60} = 20.94 \quad \text{rad/s;} \tag{2.18}$$

$$Nt = \frac{Vph}{B_{agsp} \cdot sDi \cdot lc \cdot 10^{-6} \cdot \Omega_{bmec}} = 169 \quad \text{turns;} \tag{2.19}$$

The number of turns per coil sb is defined as in eq.2.20 while the number of conductors per slot CpS is calculated in 2.21.

$$sb = round\left(\frac{2 \cdot m_p \cdot Nt \cdot a}{Ns \cdot layers}\right) = 55 \quad \text{turns;} \tag{2.20}$$

$$CpS = sb \cdot layers = 110 \quad \text{turns;} \tag{2.21}$$

The copper area A_{copper} in one slot is:

$$Acopper = Aslot \cdot ksfill = 160\,mm^2 \cdot 0.5 = 80 \quad mm^2 \tag{2.22}$$

The conductor area A_{cond} is:

$$A_{cond} = A_{copper} / CpS = 0.7273 \quad mm^2; \tag{2.23}$$

The diameter of one conductor is computed by:

$$d_{cond} = 2 \cdot \sqrt{\frac{A_{cond}}{\pi}} = 0.9623 \quad mm; \tag{2.24}$$

A standard conductor with a diameter of 0.95 mm was selected, the new copper being 77 mm^2, which corresponds to a filling factor of 0.48. Now the torque current value is:

$$It = \frac{A_{copper} \cdot js}{CpS} = 3.9 \quad A \tag{2.25}$$

Authors from [2.1] proposed an analytical way to compute the BLDC-MRM torque (eq.2.30) based on two current factors (eq.2.26-2.27), the machine volume (eq. 2.28) and electrical loading (eq.2.29). The analytical computed torque (223.7 Nm) by this method is remarkably close to the maximum torque value computed the FEA as shown in Fig.2.1 (221.5 Nm), but 15 % bigger than the average value (189 Nm).

$$crt_{K1} = \frac{mt}{mp} = 0.6(6); \tag{2.26}$$

$$crt_{K2} = \sqrt{\frac{m_p}{m_t + m_f}} = 1; \tag{2.27}$$

$$A = \frac{It \cdot Ns \cdot CpS}{\pi \cdot sDi \cdot 10^{-3}} = 47251 \quad A/m \tag{2.28}$$

$$V = 2 \cdot \pi \cdot \left(\frac{sDi}{2}\right)^2 \cdot lc \cdot 10^{-9} = 0.0129 \quad m^3 \tag{2.29}$$

$$Te = crt_{K1} \cdot crt_{K2} \cdot B_{agsp} \cdot A \cdot V = 223.7 \quad Nm \tag{2.30}$$

2.2 Finite Element Analysis

Approximate flux path calculations such as those used in the magnetic equivalent circuit are indispensable for rapid, reasonably accurate calculations for electrical machine design and analysis. Since the permeances of each cell are related to geometrical constants of the machine a good understanding of the relationship between the machine dimensions and their effect on the motor electrical parameters is obtained. However, more advanced methods are needed to asses more accurately the final characteristics of the design. Another method of analysis which takes full advantage of computing power of existing processors is the method of finite elements. This is used to obtain solutions to partial or integral equations that are non-linear and can't be solved by analytical methods.

The emergence of FEM took place in the early 1960's and since then its use has spread to virtually all field of engineering. The first applications in electrical machine problems were presented in the early 1970's. In the 1980's the research on numerical field computation methods expanded rapidly. The method offers almost unlimited flexibility in geometrical shape, material properties and applied boundary conditions in different regions of the machine. The solution of the problem defined by the finite element method is the flux distribution for given current or magnetic sources. Still, it remains the task of the analyst to interpret the data and to relate the field solution with the machine parameters. Most of today's FEA software's use advanced and friendly graphical user interface and scripting languages for fast problem definition and data analysis.

2.2.1 Finite Element Method

The details of finite element method are a demanding subject which is well described in [2.5-2.6]. The basis of this method will be presented next.

In electromagnetics finite element method solves for Maxwell equations which are described by eq. 2.31 written in differential form.

$$\nabla \times H = J$$
$$\nabla \bullet B = 0$$
$$\nabla \times E = -\frac{dB}{dt} \tag{2.31}$$
$$\nabla \bullet D = \rho_V$$

were H is the field intensity vector A·turns/m, B is the magnetic flux density vector in T, j represents the current density A/m^2, E is the electric field intensity vector V/m and ρ_V is the volume density of electric charge.

In most electrical machines applications the problem domain may be subdivided in three main sub-regions (air, iron, and conductor), for which different field equations apply. In each sub-region the material properties states that:

$$B = \mu_0 \cdot \mu_r \cdot H \tag{2.32}$$

where μ_0 is the permeability of free space and μ_r is the relative permeability.

These equations can be coded in a graphical form called Tonti's arrow system [2.7]. Vertical arrows were used for differential operators $\nabla, \nabla\cdot, \nabla\times$ while horizontal arrows were employed for material operators μ, ε and perpendicular to material and geometry arrows we can find the time derivative $\partial / \partial t$ operator.
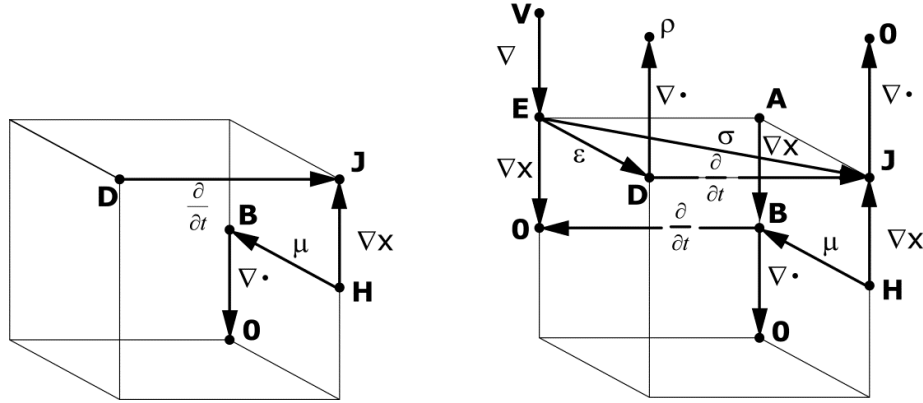

Fig.2.3. Tonti's diagram for the magnetic field (left) and electro-magnetic field considering Ohm's law (right)

From Gauss law (second equation of 2.31) we can observe that B can be derived from a variable called magnetic vector potential since the divergence operation applied to a curl operation will always give zero as a result.

$$\nabla \bullet B = 0 \quad \wedge \quad \nabla \bullet (\nabla \times A) = 0 \quad \rightarrow \quad B = \nabla \times A \tag{2.33}$$

For a two-dimensional problem, the vector potential concept is a powerful one, which reduces the number of unknowns from two (B_x and B_y) to one (A_z). If A is defined as a linear function then B will be constant in each element of the mesh, but if A is described by a second order function then B will be represented by a first degree function of space in each element. The relations between A and B components in two-dimensional space and cartesian coordinates are:

$$B_x = \frac{\partial A_z}{\partial y} \quad \wedge \quad B_y = \frac{\partial A_z}{\partial x} \tag{2.34}$$

In a magneto-static problem the variation of the electric field function of time is zero, so the Ampere equation (the first equation from 2.31) can be re-written considering the vector potential:

$$\frac{\partial D}{\partial t} = 0 \quad \wedge \quad \nabla \times A = B \quad \rightarrow \quad \nabla \times \left(\frac{1}{\mu_0} \cdot \nabla A \right) = J \tag{2.35}$$

In the various regions the following field equations uniquely define the magnetic field. In a source or current region were the permeability is that of free space the Poisson equation can be applied directly, but only if the materials are homogenous and the permeability is constant.

$$\nabla^2 A = -\mu_0 J \; ; \text{ or in Cartesian coordinates } \frac{\partial^2 A_z}{\partial x^2} + \frac{\partial^2 A_z}{\partial y^2} = -\mu_0 J_z \qquad (2.36)$$

If j=0 the above equation is transformed into Laplace equation, applied to current free air region.

$$\nabla^2 A = 0 \; ; \text{ or in Cartesian coordinates } \frac{1}{\mu_0}\frac{\partial^2 A_z}{\partial x^2} + \frac{1}{\mu_0}\frac{\partial^2 A_z}{\partial y^2} = 0 \qquad (2.37)$$

In the case of current free iron-regions the so-called quasi-Laplace equation is applied:

$$\frac{\partial}{\partial x}\left(\frac{1}{\mu_0\mu_r}\frac{\partial A_z}{\partial x}\right) + \frac{\partial}{\partial y}\left(\frac{1}{\mu_0\mu_r}\frac{\partial A_z}{\partial y}\right) = 0 \qquad (2.38)$$

These are a rather simple formulation of the field problem but they are difficult to solve, especially in electrical machines. This is due to complicated geometry, the time dependency of the magnetic field and the non-linearity's due to magnetic saturation of the iron. Furthermore, the equations of the magnetic field are coupled with the electric circuit equations of the windings and the motion of the rotor.

The method of the finite element is a numerical method approach by which the general differential equations (describing a certain physical phenomenon in a structure) can be solved in an approximate manner. These equations are assumed to hold over a certain region structure, which can be one-, two-, or three d-dimensional. In fact, the region is divided into smaller parts, so-called finite elements, and the approximation is then carried out over each element. The advantage of breaking a structure into a large number of simple elements is that a small but difficult to solve problem transforms into a big but relatively easy to solve problem. The approximation, usually a polynomial, is actually some kind of interpolation over the element, and it is assumed that the variable is known at a certain points within the element, called nodal points. The precise manner in which the variable changes between its values at the nodal points is expressed by the specific approximation, which may be linear, quadratic, cubic, etc. The coefficients of the polynomials are chosen in such a way that the variational principle is approximately satisfied. Having determinate the behavior of all elements, they are then patched together, using some specific rules, to form the entire region. The collection of all elements is called a finite element mesh. The mesh is programed to contain structural and material properties which define how the structure will react at certain loading conditions. The mesh density along the structure depends on the applied stress level in a given region. A finite element cannot contain discontinuities; it has to be a homogenous medium. The mesh is created in different ways by each software, but usually the ratio of largest and smallest angle should tend to unity and the ratio of maximum to minimum side length of a triangle should also tend to unity. The discretization process creates a linear algebra problem with the number of unknowns equal to the number of nodes.

The variable that is solved in the electromagnetic FEM is the magnetic vector potential at the nodes. The solution algorithm is often based on the minimization of a mathematical function that is related to the stored potential energy in the field. Although numerous methods can be used to solve the quasi-Poisson equation (numerical relaxation, integral equation solution method and direct discretization of the differential operator by the finite difference method) the variational approach can be successfully related to the finite element discretization scheme. It is based on construction of a set of approximate functions which minimize the energy stored in the system. The variational method is mathematically rigorous which lead to a convergent, unique solution. This can be explained by the fact that the stored energy of the system is the prime quantity and any set of approximating functions or linear combinations of functions which minimize the stored energy will naturally lead to a unique solution. The energy term does not necessarily have the meaning of a physical energy, although sometimes has. The energy function can be expressed in terms of the functions representing the vector potential and the current density [2.6]. Hence, the energy representation is termed a functional, which is clearly a scalar. Solving a FEA problem could be viewed as an optimization problem since a minimum of the energy functional has to be found (Rayleight-Ritz method method). The method is well described in [2.8].

From the node potentials, the parameters of the machine are obtained using various formulations. In all electromagnetic field examples it is essential that the potential is defined at one point in the domain at least, otherwise an infinite number of solutions could be generated by adding an arbitrary constant to the solution.

The magnetic flux can be computed based on eq. 2.39. The inductance calculation is straightforward when the flux and current are known.

$$\Phi = \int_S \nabla \times A \cdot \bar{n} \cdot ds \qquad (2.39)$$

The most difficult quantity to calculate is the electromagnetic torque, and better formulations are still being developed. The torque presents significant information about the electrical machine, which needs to be known as accurately as possible, often also as a function of the rotor position. All the methods used for torque calculation are based on the solution of the magnetic field by finite element method using the triangular discretization element. Consequently, the accuracy of torque calculations depends on the accuracy of the FEM, and the accuracy of the FEM depends on the size and shape of discretization elements. As the number of element is limited, their size cannot be infinitely reduced. Also due the complicated shape of machine parts and the deformation of elements in the air-gap, it is impossible to assure an equilateral triangular shape of discretization element. This indicates that FEM error is always present [2.5]. The basic limitation of the finite element solutions is that the accuracy of the solution is related to the size of the discrete elements.

The virtual work method is normally approximated evaluating the rate of change of the magnetic co-energy between two positions with respect to the step angle. The magnetic co-energy $W_m^{'}$ is defined as [2.6]:

$$W_m^{'} = \int_0^i \psi \cdot di \qquad (2.40)$$

At a constant current the electromagnetic torque is produced by the tendency of the machine to increase its entire magnetic co-energy as the rotor position changes (eq. 2.41).

$$Te = \left.\frac{\partial W_m'}{\partial \theta}\right|_{i=cst} \tag{2.41}$$

$$Te = \frac{l_{core} \cdot R_{air-gap}}{\mu_0} \oint_l B_n \cdot B_t \cdot dl \tag{2.42}$$

A more common and faster method is based on the Maxwell stress tensor (eq.2.42). It allows calculating the force acting on all parts within a volume (the rotor) by evaluating a curve (integral) around an enclosed surface (in the 2D space). The Maxwell stress method is based on the distribution of the magnetic field on the closed surface in the air-gap around the rotor. The volume should be totally enclosed by the surface and the surface itself should be completely in non-ferromagnetic region (in the middle of the air-gap) [2.6-2.8].

2.2.2 FEA Software's

Two different FEA computer software's (FEMM 4.2 and Opera 2D v.13) were analyzed and tested before choosing the best for our purpose. Both of them offer easy to use GUI, scripting possibility and the most important thing they can communicate with MatLab, which makes both of them suitable for an embedded FEM optimal design MatLab written program. The analysis modules and the solvers set them apart in terms of program size, solution accuracy and the price (FEMM being a freeware).

2.2.2.1 FEMM 4.2

 FEMM represents one of the best free or charge suite of programs for solving low frequency electromagnetic problems on two-dimensional regions. A low frequency problem is one in which the displacement currents can be ignored, because they are typically relevant to magnetics problems studied at radio frequencies [2.9], not at existent frequencies in electrical machines.

The software offers the user the possibility to build and analyze different geometries and evaluate the post-processing results through the integrated Lua scripting language, simplifying the analysis process. The software can handle linear/nonlinear magneto-static problems, linear/nonlinear time-harmonic magnetic problems, linear electrostatic problems and steady-state heat flow problems. FEMM is based on three main parts: Interactive shell (femm.exe), triangle.exe which handles domain discretization and solvers (fkern.exe) whose job is to take a set of data files describing the problem and to solve the system of equations. The program offers a material library also, from which PM, soft-magnetic materials or non-magnetic conductors can be selected and imported in the model.

FEMM can be connected to MatLab through a set of functions via OctaveFEMM toolbox. The syntax of the OctaveFEMM toolbox functions are similar to the one used by Lua scripting language embedded in version 4.2 with very small differences. Probably the biggest one between Lua and OctaveFEMM is the matrix-oriented nature of the last, which simplify the pre- and post-processing stages.

2.2.2.2 Vector Fields Opera 2D

Opera 2D from Cobham Vector Fields is a commercial software [2.10]. The software offers electromagnetic, stress and thermal analysis programs within its environment. The electromagnetic fields are computed by state of the art algorithms and advanced numerical analysis procedures. The basis of the methods used in the analysis programs is the finite element discretization. The program offers the local error (in flux density units) and the RMS error over the whole problem.

Opera 2D has the following upper limits on a 32-bit operating system: 5000 regions, 0.75 million elements and 1.68 million nodes; while on a 64-bit operating system they are: 5000 regions, 5 million elements and 11 million nodes. The maximum number of nodes is always 2.25 times the maximum number of elements.

The software provides the following analysis modules: Steady-State AC Analysis (AC), Demagnetization Transient Analysis (DM), Linear Motion (LM), Rotating Machines (RM), Stress Analysis (SA), Space Charge Beam Analysis (SP), Static Field Analysis (ST), Transient Analysis (TR), Thermal Analysis (TH) and Velocity Analysis (VL), each of them very well described by the manufacturer [2.10]. This work uses only the ST and RM modules.

The Static Field Analysis program solves for time invariant magnetic fields. The model can include nonlinear permeability of the material. The program solves for the vector potential defined by a nonlinear Poisson equation, because the scalar potential solution cannot include current as a field source.

The Rotating Machine program is a transient eddy current solver, extended in such a way to include the motion effects. The module provides access to external circuits and the possibility of coupling a mechanical equation to the model. Opera-2D/RM models may be constructed with either linear or quadratic elements. The driving fields are provided by the source currents, non-zero potential boundary conditions and permanent magnet coercitive forces. This work uses prescribed shape of current waveform function of time through the transient time table option in the RM program as shown in chapter 5. The table consists of files containing up to 1000 pairs of numbers, one pair per line. The first number of each line specifies the time, while the second gives the function value.

2.3 FEA Models and results

If the designer wants to use only first order elements and magneto-static analysis, then it is easier and faster for a novice to use the FEMM 4.2 software, such as torque computation in a few key position or inductance calculation at a few saturation levels, in an optimal design routine. In this situation small differences were observed compared to Opera 2D results (ST solver and first degree elements). For example the same model took 9.8 s (pre- and post-processing stages combined) in FEMM 4.2 (23000 elements and 11500 nodes) and 11.42 s in Opera 2D (10630 nodes and 7520 elements). The computed torque was 0.4 % larger in the first case compared to Opera result. If the same model was studied in Opera 2D using quadratic elements (28000 nodes and 7500 elements) the time for analysis increased to 21.6 s and the computed torque was 1.4% bigger than the linear elements case. These are results for magneto-static analysis, which does not justify the price of this package of the commercial software. In conclusion FEMM 4.2 is good enough for static analysis, fast and easy code implementation which is suitable for optimal design implementation, still this work use Opera 2D with quadratic

elements for advanced FEA computations such as steady-state operation and iron loss computation.

The FE models of the BLDC-MRM were implemented in Opera 2D using a scripting routine. The code was written in a parametrical way. The machine analysis was performed using the Static Field Analysis module (ST) for the standstill simulations and the Rotating Machines module (RM) for the steady-state operation. For a good field approximation, with a minimum error, the air-gap was constructed out of three layers of mesh in all cases. Nonlinear BH curves, corresponding to used materials were assigned to each model. The models have quadratic elements, convergence is achieved using Newton algorithm (within 20 iterations), adaptive time-step is adopted and a 0.001 tolerance value was set.

For a fast analysis the presented FEA models take advantage of the rotational symmetry, only one pole being studied. In this case is not possible to identify surfaces were the field is normal or tangential, so pairs of matching surfaces are searched and identified, where the potentials have the reverse sign but equal magnitude, the so-called negative symmetry. A two pole analysis will have a positive symmetry: the same sign and magnitude on the chosen planes. A zero potential was assigned to the outer stator surface (near the frame) and to the inner rotor surface (near the shaft).

2.3.1 Five-phase, 6 poles, FB-rotor BLDC-MRM

The five-phase BLDC-MRM data are presented in section 6.1, and running experiments are presented in section 5.2. Here we focus on stand-still analysis: flux distribution, expected machine performances and parameter computation.

The Opera 2D-FEA model of the 5-phase, 6 poles, FB rotor, BLDC-MRM with mesh and flux lines distribution at nominal load can be viewed in Fig.2.4, while the iron saturation and current density distribution at rated load can be observed in Fig.2.5.

The average value of air-gap magnetic flux density, over one pole pitch, in no load conditions (I_F = 4 A and I_T = 0 A) is 0.65 T while at rated load conditions (I_F = 4 A and I_T = 4 A) is 0.61 T (Fig.2.6).   In the motoring mode the armature reaction make the saturation to occur at the leading tip of the pole, due to an increase in the magnetic flux density at the leading pole. The net result is that the average flux density under the pole face is reduced, yielding a lower output torque. A large force density is usually associated with large flux density levels and high armature current so it is important to observe the armature field under the poles. We need a small armature field, small armature reaction so the core won't saturate too much under the pole edge.

The radial component of the air-gap magnetic flux density (Bn) is potted in Fig. 2.7 for the tested speeds from section 5.1, from base speed up to 4 times base speed, in a field weakening situation. The FEA torque pulsations and the supplied currents are also presented in Chapter 5. The average values of Bn are: 0.48 T at 250 rpm, 0.52 T at 500 rpm, 0.36 T at 750 rpm and 0.3 T at 1000 rpm. We can observe that the results of Bn taken at steady state operation in RM-module (Fig.2.7) are quite different from the results taken from ST-module (Fig.2.6), and a smaller average value of Bn appears.

With a proper cooling the machine is capable of producing 160 Nm of electromagnetic torque at 12 A/mm^2 torque and field phase current densities (Fig.2.8), which correspond to a tangential force of 3.5 N/cm^2 (Fig.2.9) and 6 Nm/kg (Fig.2.10).

The machine inductances (Fig.2.11) were computed from FEA results by keeping one phase current at a constant value and reading the fluxes in all phases. Dividing them by the constant current one will find out self and mutual inductances of that phase. In order to have some sense of reality we measured with an LC meter the d-axis, and q-axis phase A inductances: $Lad = 0.4$ H and $Laq = 0.185$ H. Since the winding and the machine are symmetric only one phase has to be analyzed. A curve fitting, Fourier analysis based (as explained in section 4.2), is applied on phase inductances (continuous line) in order to express the waveform as a cosine function (dashed line) as shown in Fig. 2.11. From this figure it is obvious that one term (the fundamental component) is enough for the inductances reconstruction.
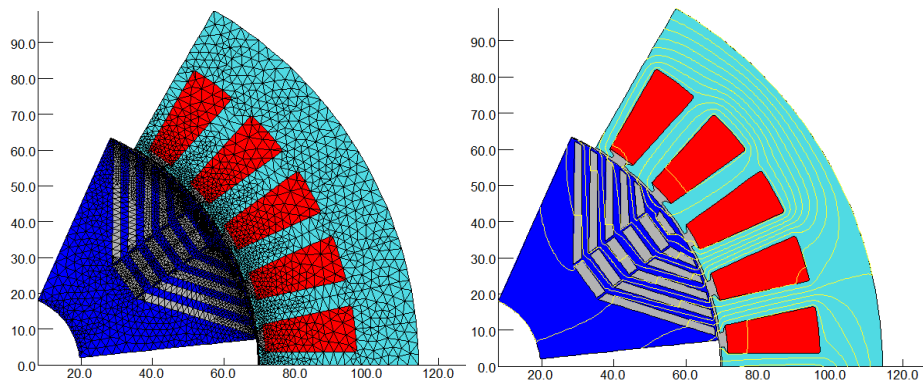

Fig.2.4. Five phase, 6 poles BLDC-MRM 2D FEM model, mesh (left) and flux lines at rated load (right)
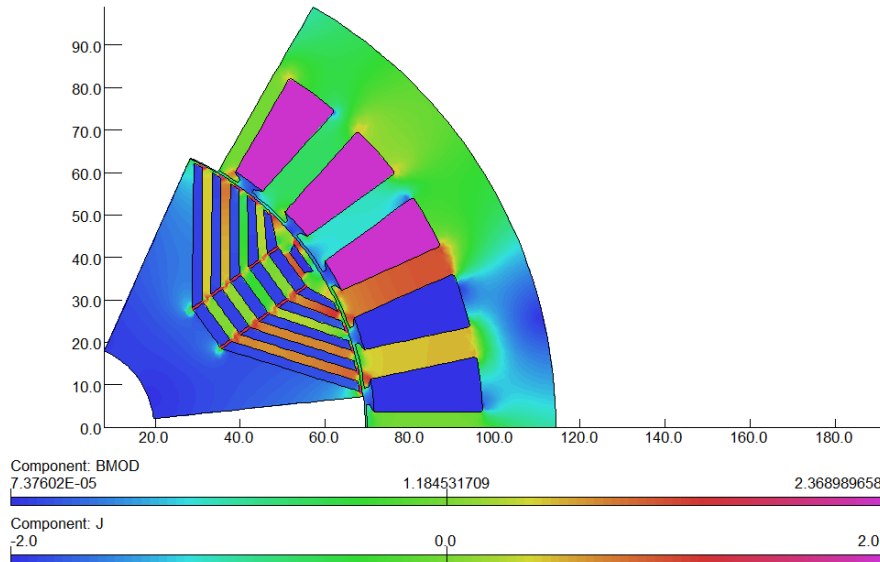

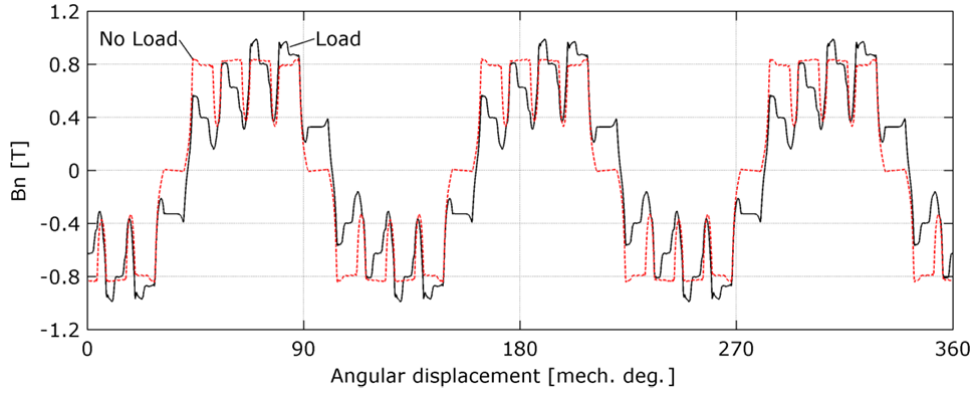Fig.2.5. Five phase, 6 poles BLDC-MRM saturation level at rated load conditions ($I_F = I_T = 4A$, Te = 33 Nm)

Fig.2.6. Radial component of air-gap magnetic flux density (Bn) at no load (I_F = 4A, I_T = 0A) and rated load conditions (I_F = I_T = 4A, Te = 33 Nm)
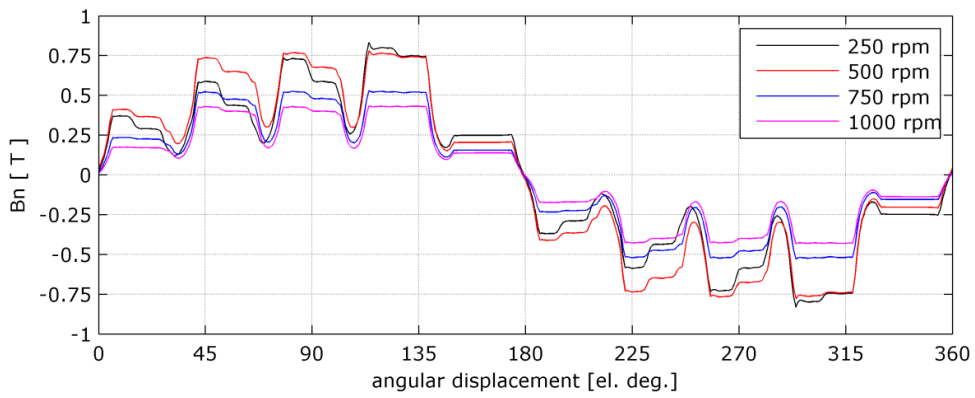

Fig.2.7. Radial component of air-gap magnetic flux density (Bn) over two pole pitches at four different speeds
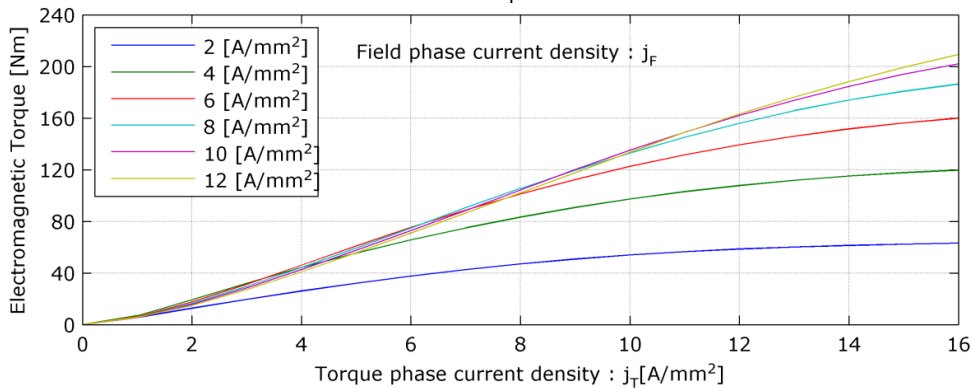

Fig.2.8. Electromagnetic torque vs. torque phase current density at various field current density
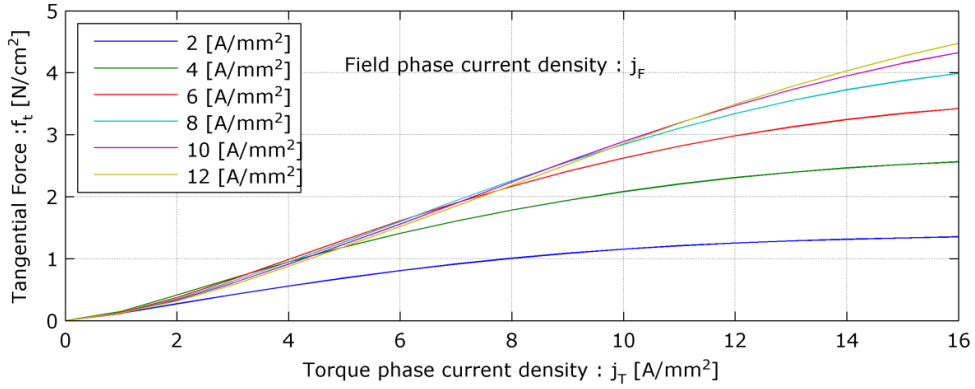
Fig.2.9. Tangential force vs. torque phase current density at various field current density
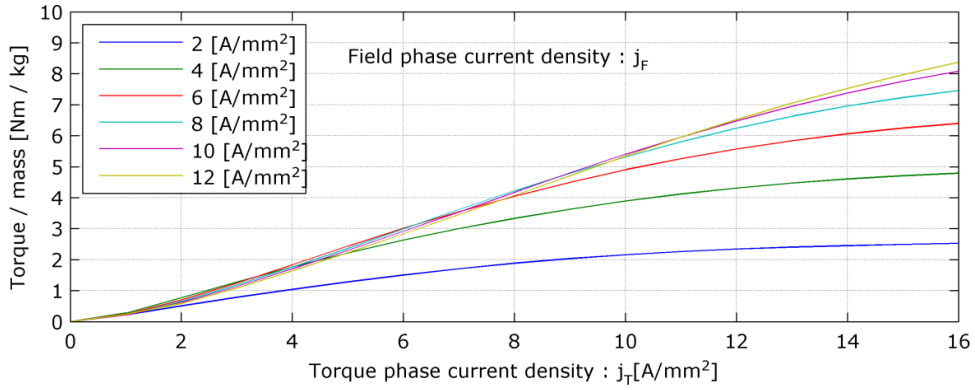

Fig.2.10. Torque / weight vs. torque phase current density at various field current density
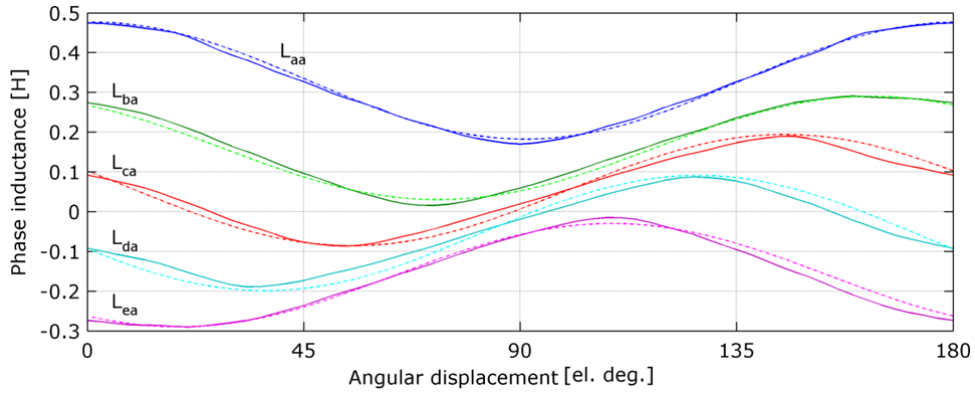

Fig.2.11. FEM (continuous line) and curved fitted (dashed line), self (Laa) and mutual (Lba...Lea) inductances of the BLDC-MRM at rated current

2.3.2 Six-phase, 6 poles, ALA-rotor BLDC-MRM

A 6 phase, 6 poles (36 slots) stator with ALA rotor BLDC-MRM was investigated and built for experimental purpose (Fig.2.12). The machine has been analyzed by employing symmetry conditions (just as in the previous case) in the Opera 2D ST-module. The saturation levels at rated slot current density are presented in Fig.2.13.

The average, under the pole, value of the air-gap magnetic flux density at zero torque current (i.e. no-load condition) is 0.57 T while at rated/equal field and torque current values it drops at 0.56 T (Fig.2.14). As expected, due to the ALA rotor a smaller influence of the armature reaction is observed compared to previous (FB rotor) design.

Extensive simulations with various excitation ($I_F \cdot W_1$) and torque ($I_T \cdot W_1$) coil *mmf* values have been run to expose the torque capability of this prototype, for a wide range of currents. For a more general analysis of the machine, total current density in field/torque phases is given as a parameter. The rotor is "fixed" in a maximum torque position and the current densities are varied. Field current density j_F would give rise to a field phase current equivalent to *d* –axis current, and torque current density j_T to a *q* – axis current, responsible for torque production.

Studying Figs. 2.15-2.18 we can deduce that at $j_F =12$ A/mm^2 (flat top) and $j_T = 24$ A/mm^2 (flat top) an almost 120 N·m torque (average value) is obtained at 6.7 N·m/kg (36.5 N·m/L) of active materials, which is quite competitive.

The machine inductances for one phase, so important for the dynamic model, are computed and plotted in Fig. 2.19.
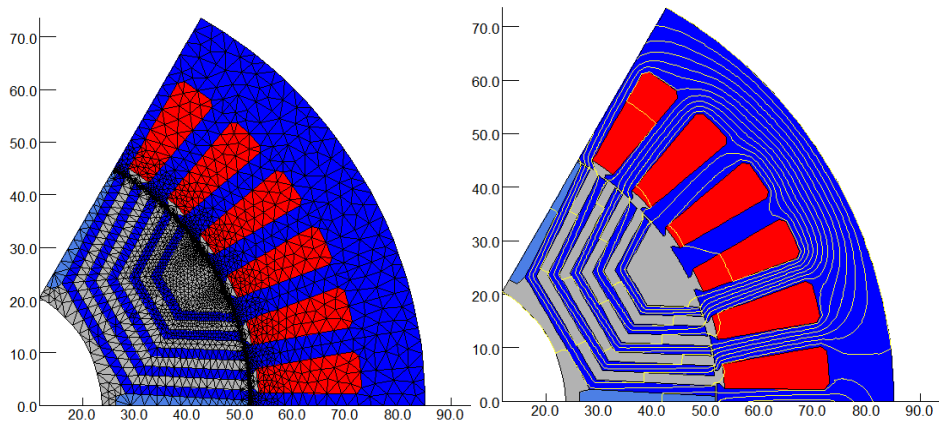

Fig.2.12. Six phase, 6 poles BLDC-MRM 2D FEM model, mesh (left) and flux lines at rated load (right)
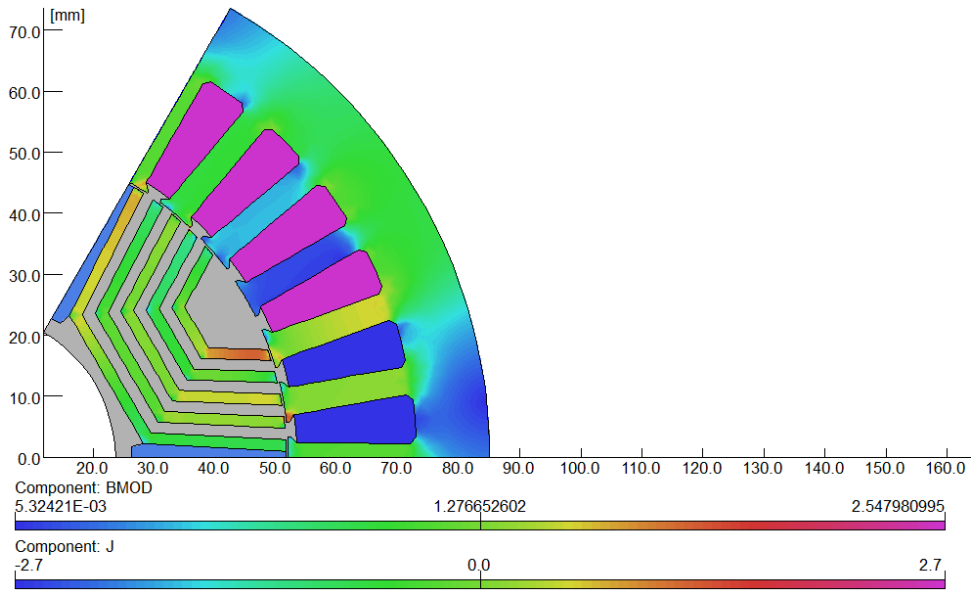
Fig.2.13. Six phase, 6 poles BLDC-MRM saturation level at rated load conditions ($I_F = I_T = 12$ A, Te = 35 Nm)
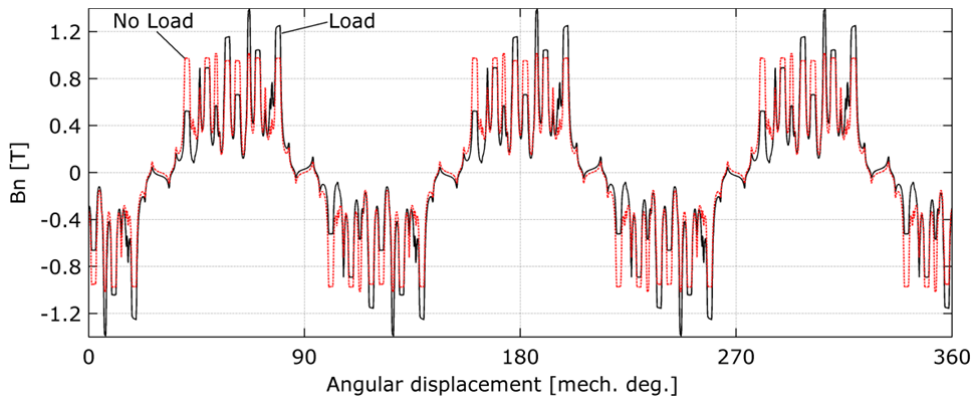
Fig.2.14. Radial component of air-gap magnetic flux density (Bn) at no load($I_F = 12A$, $I_T = 0A$), and rated load conditions ($I_F = I_T = 12A$, Te = 35 Nm)
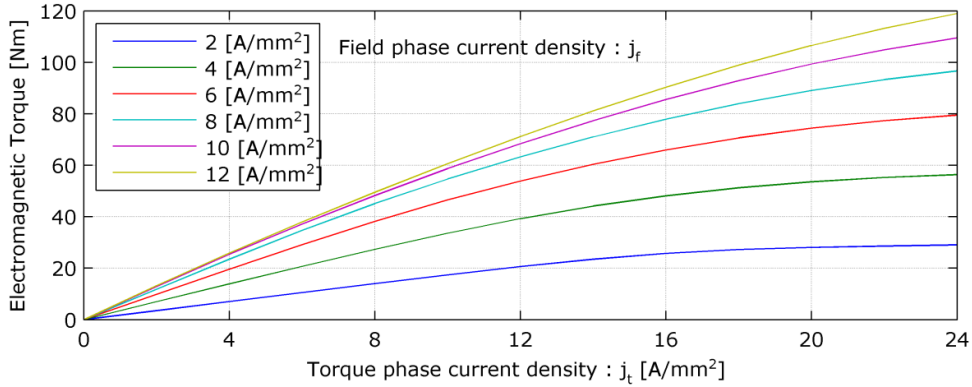
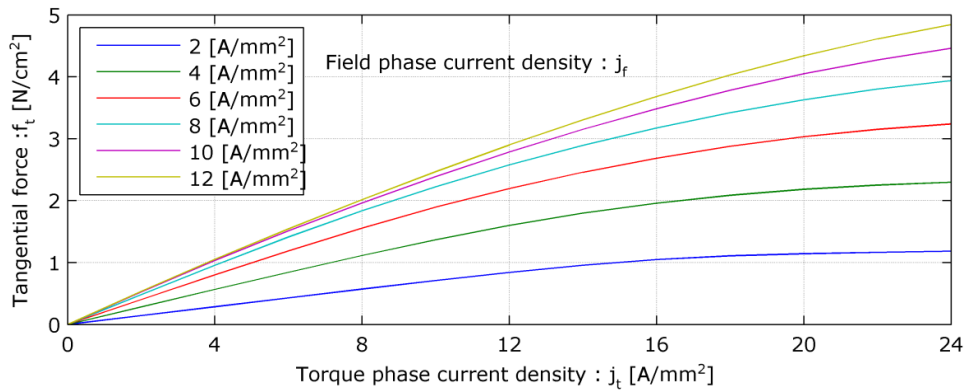Fig.2.15. Electromagnetic torque vs. torque phase current density at various field current densities

Fig.2.16. Tangential force vs. torque phase current density at various field current densities
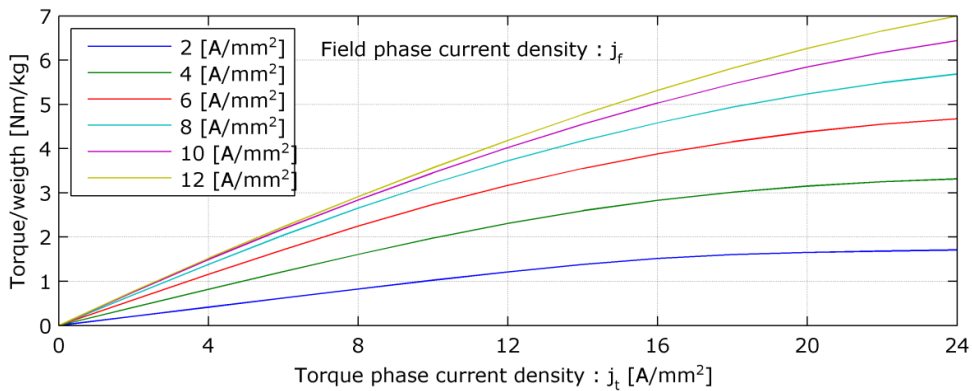

Fig.2.17. Torque / weight vs. torque phase current density at various field current densities
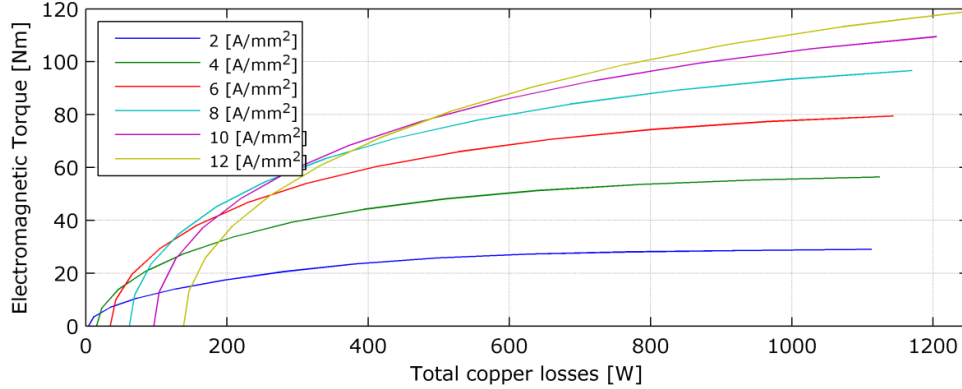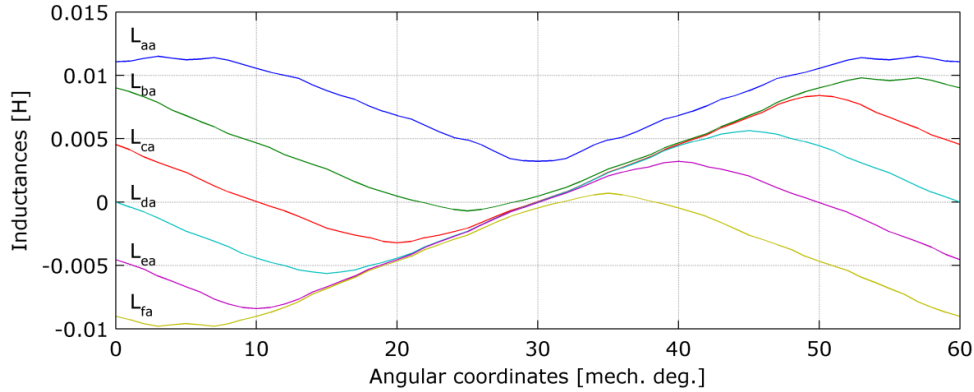
Fig.2.18. Electromagnetic torque vs. total copper losses at various field current densities

Fig.2.19. FEM self (Laa) and mutual (Lba…Lea) inductances of the BLDC-MRM at rated current

A certain degree of confidence needs to be established in the model before dynamic FE analysis is performed later in this work. For that standstill 2D-FEA results are compared with measured data for the studied 6 phase BLDC-MRM.

By connecting two adjacent phases in series and the remaining four also in series, a two phase, decoupled machine is obtained, something similar to a *dq*-winding machine, were *d*-winding is the field winding (the coils in the *q*-axis) and the *q*-winding is the armature winding (the coils under the pole shoe). Using a load cell (as shown and explained in section 6.2.2.1) the static torque was measured for various pairs of field and torque current values from 0 up to the rated current (12 A). The results were compared to simulated FEM results in Fig. 2.20 and show acceptable agreement between them.

Experimental torque was compared to simulated FEM torque for a series connection of phases at various phase currents (Fig. 2.21-2.22). The geometrical imperfection, mechanical coupling and encoder errors made the results inconclusive in some analyzed positions.

The torque was also tested for a 3 phase connection of phases as sketched in Fig.2.23. Like in the case of the series phase connection a "missing" point in experimental torque can be observed, due to a geometrical fault.
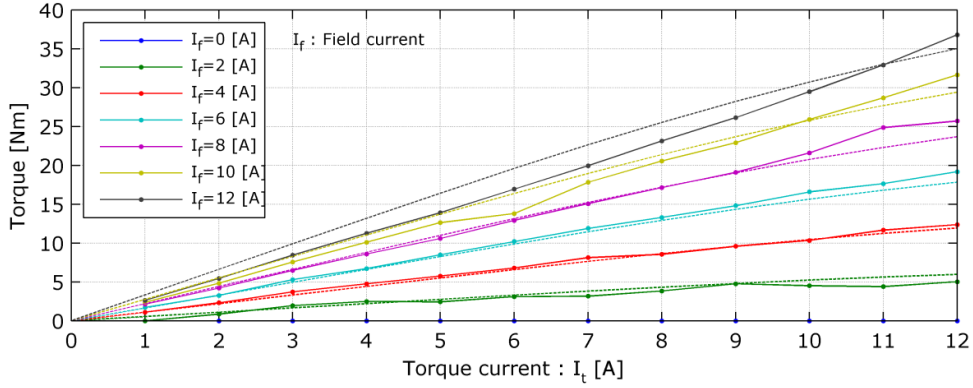
Fig.2.20. BLDC-MRM torque vs. torque current at different field current values
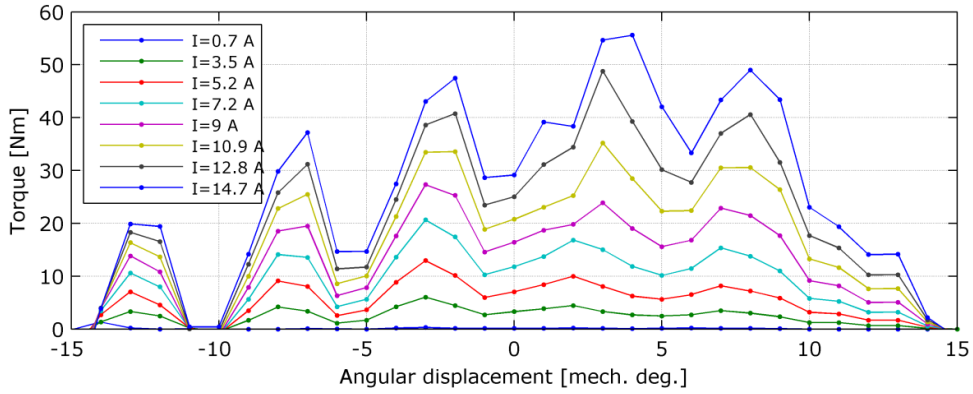
Fig.2.21. Experimental torque of the BLDC-MRM with a series connection of all phases vs. rotor position
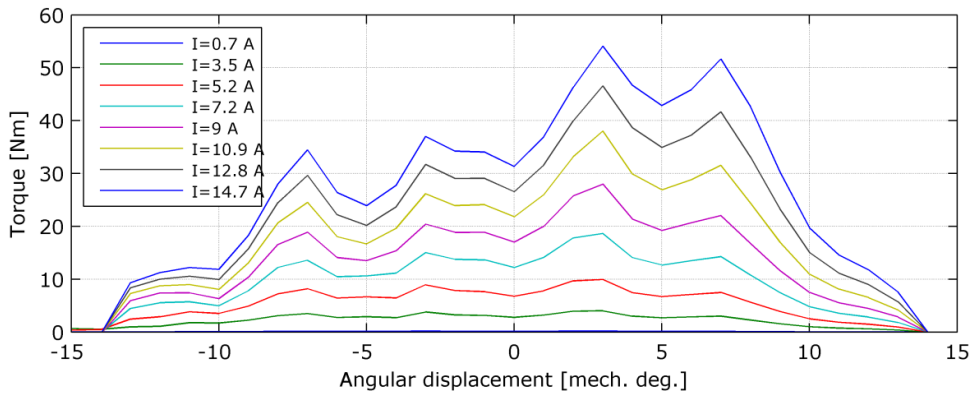
Fig.2.22. FEM torque of the BLDC-MRM with a series connection of all phases vs. rotor position
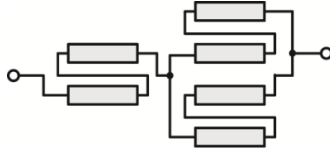
Fig.2.23. Electrical wiring of the 3 phase RSM (q=2)
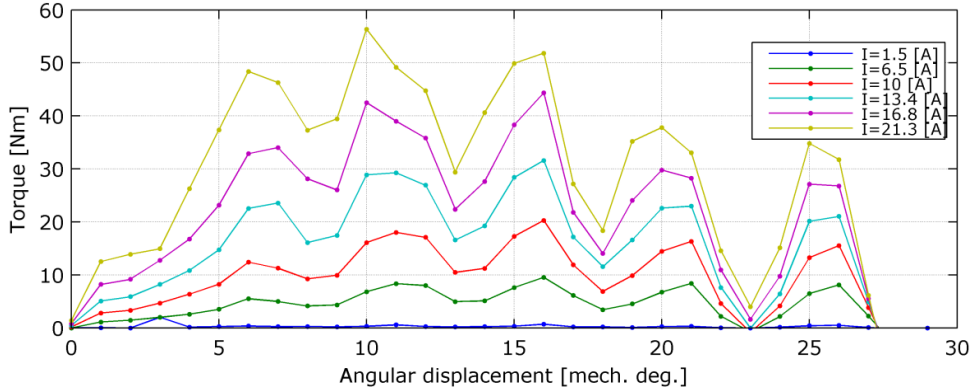
Fig.2.24. Experimental Torque of the BLDC-MRM with a 3phase RSM connection
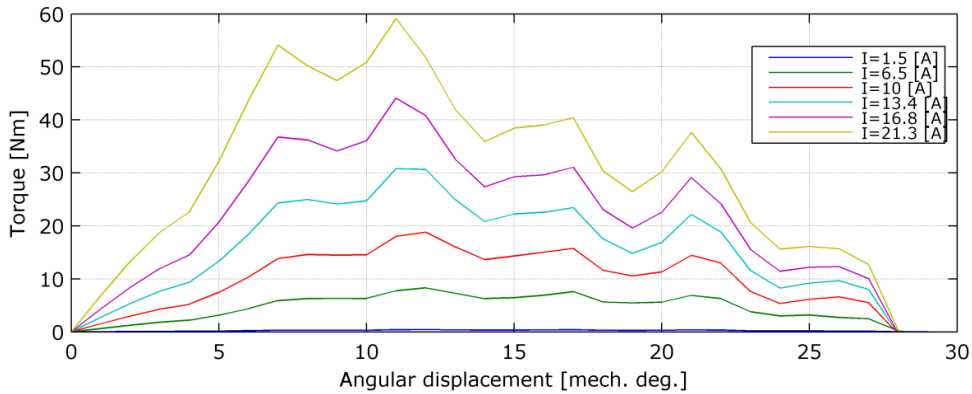
Fig.2.25. FEM Torque of the BLDC-MRM with a 3phase RSM connection

The torque pulsations for rated current density $j_{co} = j_F = j_T = 5$ A/mm^2 can be reduced by 50% if half of the rotor is shifted with half a slot pitch, while maintaining the 35 N·m average torque value, while for $j_{co} = 20$ A/mm^2 the torque ripple decreased by 40% and the average torque increased with 10% (Fig. 2.26).

Ferrite PMs were added in the bottom of rotor flux barriers (in the q-axis), thus destroying the armature reaction and bringing 10% more torque to the motor (Fig. 2.27). Adding the same volume of NdFeB magnets (as for ferrites) will actually make the situation worse since too much flux is produced in q-axis, which leads to deeper local magnetic saturation; more than is needed to cancel the q-axis armature reaction, resulting in a decrease of average torque by 15% (in our case) and increase of torque pulsations by 75% (Fig. 2.27).
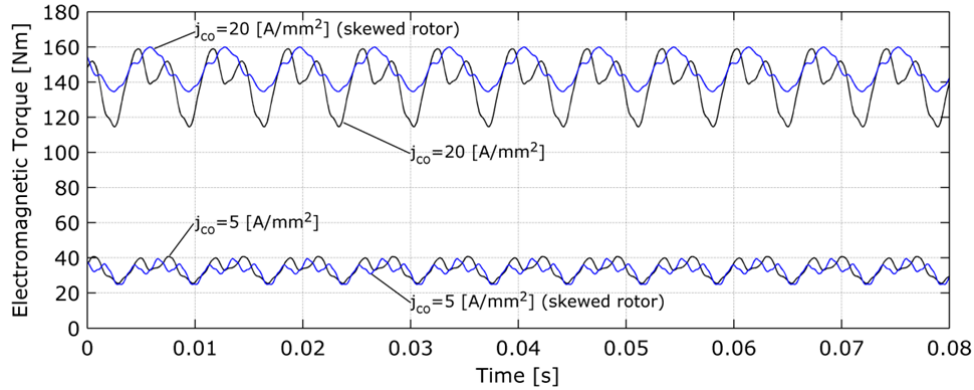
Fig.2.26. Torque pulsations of the BLDC-MRM ar rated ($j_F=j_T=5$ A/mm^2) and peak conditions ($j_F=j_T=20$ A/mm^2)
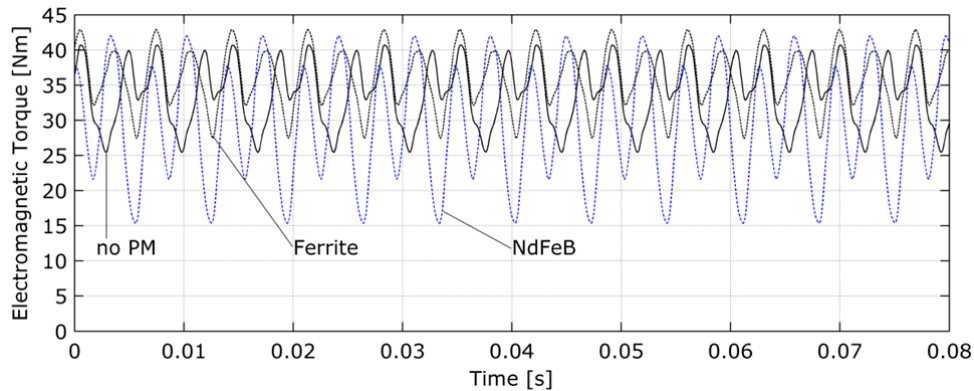
Fig.2.27. Torque pulsations at rated conditions ($j_F=j_T=5$ A/mm^2) for normal rotor (no q-axis PMs) and modified rotor (q-axis Ferrite/NdFeB PM)

2.3.3 Six-phase, 12 poles, FB-rotor BLDC-MRM

The same analysis was performed on the 6-phase, 12 poles, FB-rotor BLDC-MRM generator designed in section 2.1. More details about this machine can be found also in section 6.3.

Now that the 2D-FEM model of the machine has been validated in the previous section extensive 2D-FEM simulations with various excitation and torque coil *mmf* values have been run to expose the torque capability.

In a no-load operation the average air-gap magnetic flux density radial component has a value of 0.9 T while in a rated load conditions it decreases to 0.84 T (Fig.2.30).
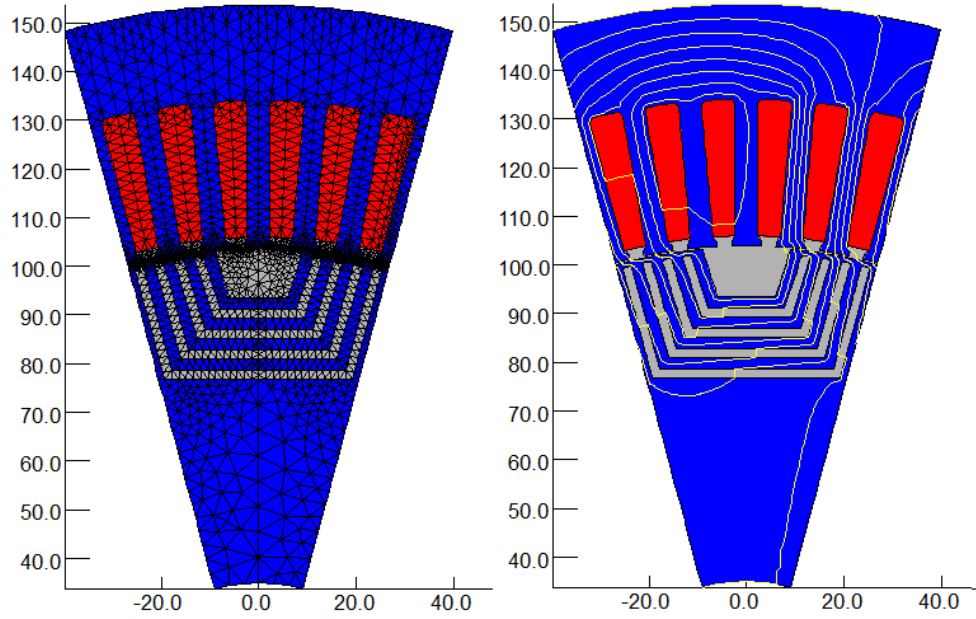
Fig.2.28. Six phase, 12 poles BLDC-MRM 2D FEM model, mesh (left) and flux lines at rated load (right)
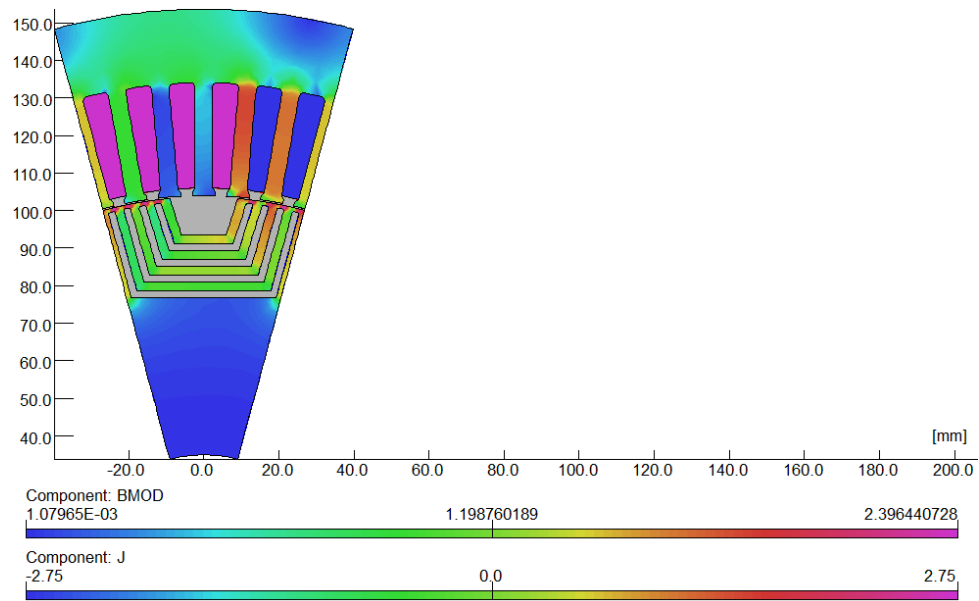
Fig.2.29. Six phase, 12 poles BLDC-MRM saturation level at rated load conditions

The results from Fig. 2.31-2.33 show that the generator can double its rated torque of 190 Nm by doubling the rated current density, 400 Nm of torque being obtained at 10 A/mm^2 field and torque current density, which corresponds to 3.5 N/cm^2 at 7 Nm/kg.

A plot of phase "a" inductances function of rotor position is given in Fig. 2.34. These have to be confirmed by the measured ones using the flux decay test.

The torque pulsations (Fig. 2.35) were obtained employing a phase *mmf* with equal levels of torque and field corresponding to the rated values as presented in Fig. 2.36.
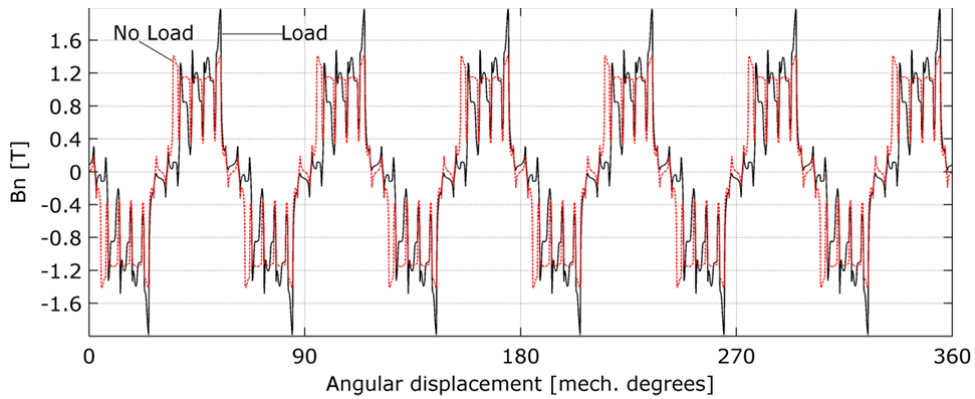
Fig.2.30. Radial component of air-gap magnetic flux density (Bn) at no load, and rated load conditions
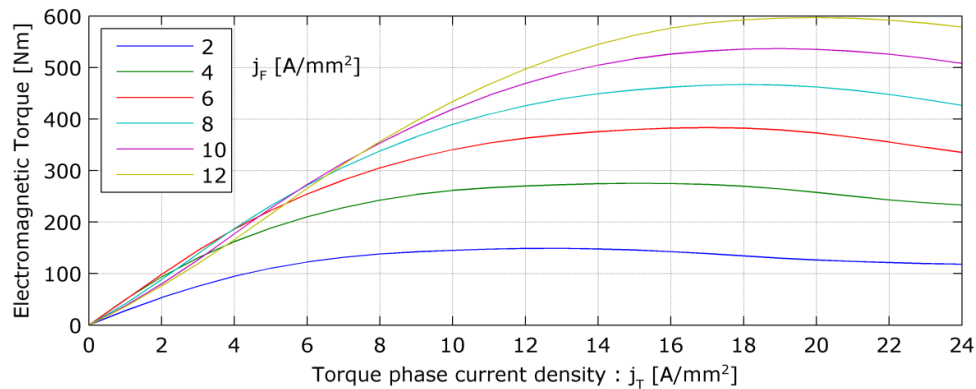
Fig.2.31. Electromagnetic torque vs. torque phase current density at various field current density
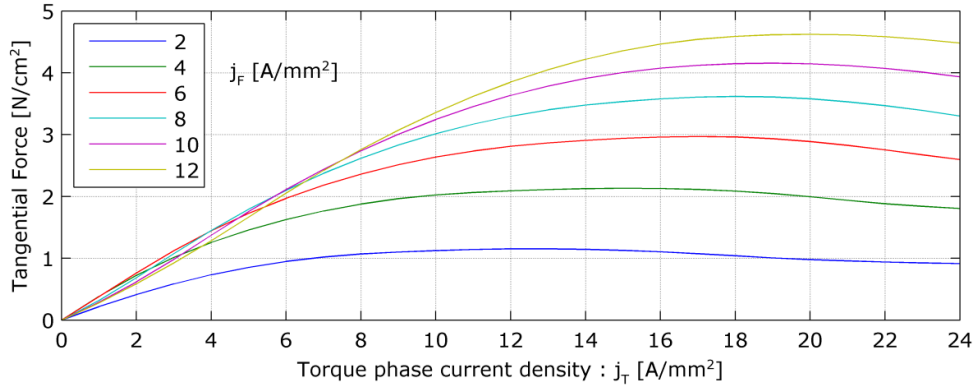
Fig.2.32. Tangential force vs. torque phase current density at various field current density
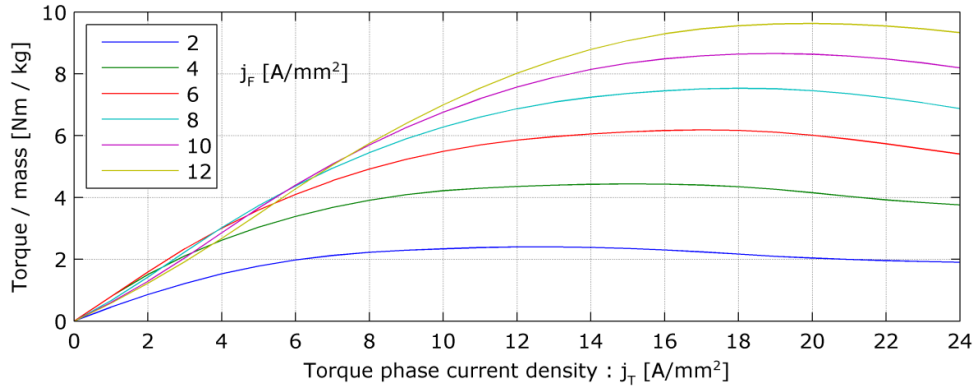
Fig.2.33. Torque per weight vs. torque phase current density at various field current density
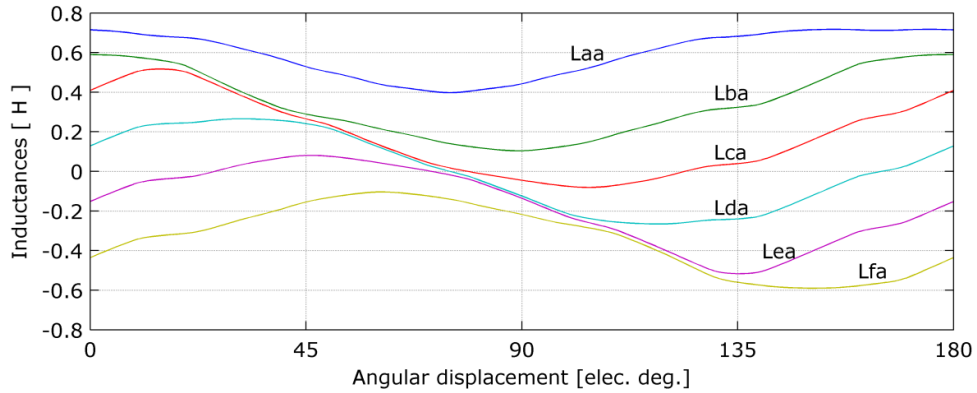
Fig.2.34. FEM self (Laa) and mutual (Lba…Lea) inductances of the BLDC-MRM at rated current
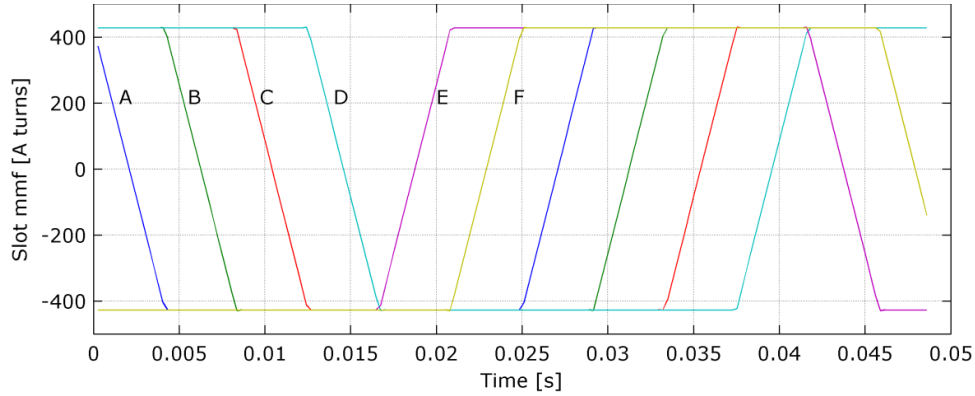
Fig.2.35. Phase mmf variation with time at 200 rpm
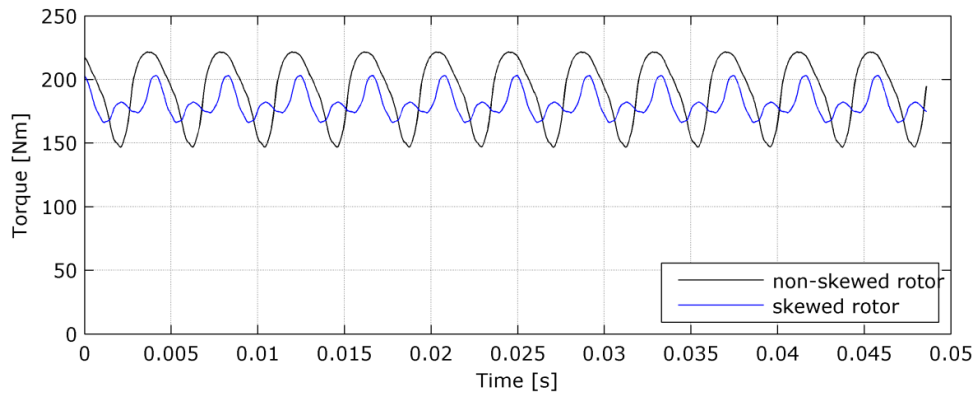
Fig.2.36. BLDC-MRM torque pulsations at synchronous speed (200 rpm) at rated current density j = 5.5 A/mm^2

2.4 Advanced iron loss computation

Ideally, at steady-state operation, a synchronous machine with a sinusoidal air-gap flux will encounter zero rotor iron losses. When the machine design implies utilization of an ALA rotor, or even a FB rotor, but a non-sinusoidal air-gap *mmf*, the designer has to compute the expected iron losses, which at high speeds could be equal to copper losses. This would eventually lead to a lower efficiency, but the first real problem that has to be considered is the temperature rise in the machine due to additional losses, which could damage the winding insulation before the efficiency becomes of any importance.

2.4.1 Introduction to iron losses

Nowadays it's usual for an engineer to compute iron losses based on eq. [2.11]. This three terms equation started from Steinmetz [2.12], followed 30 years later by a contribution of Jordan who defined the two components: static (hysteresis) and dynamic (eddy current) losses. Bertotti introduced the third term excess-anomalous losses [2.13]. The coefficients k_h (hysteresis iron loss coefficient) and k_a (anomalous iron loss coefficient) cannot be estimated analytically, both of them having a strong dependence on magnetic flux density B (amplitude and frequency) and material properties.

$$P_{fe} = k_h \cdot f \cdot B^\alpha + k_e \cdot f^2 \cdot B^2 + k_a \cdot f^{1.5} \cdot B^{1.5} \quad \text{W/m}^3; \tag{2.43}$$

The lamination sheet thickness can drastically reduce the eddy current loss as we can see from the definition of the term k_e (eddy current iron loss coefficient) resulted from Maxwell equations:

$$k_e = \frac{\pi^2 \cdot \sigma \cdot d^2}{6}. \tag{2.44}$$

where: σ is the material electric conductivity and d is the lamination thickness .
  Boglietti studied 8 different materials at frequencies between 10 Hz and 150 Hz for magnetic flux densities in the range 0.6 T – 1.7 T [2.11]. His results show that the excess losses coefficient (k_a) is zero, if the experimental data from an Epstein frame are interpolated using the third term Steinmetz-Jordan-Bertotti equation, concluding that the individual contribution of eddy current losses and excess losses cannot be separated by measurements on an Epstein test bed. The two terms Steinmetz formula (eq.2.45) is used in this paper for iron loss estimation in the BLDC-MRM.

$$P_{fe} = k_h \cdot f \cdot B^\alpha + k_e \cdot f^2 \cdot B^2. \tag{2.45}$$

It should be kept in mind that separation of iron losses in different terms is an empirical approach, in the sense of trying to separate the influence due to frequency and magnetic flux density, rather than explaining the physical phenomena directly. Steinmetz based equations are best suited for fast and rough iron loss determination and can be easily integrated in Finite Element simulation. A script was written in Opera 2D (Appendix 1) in order to compute the iron losses for each harmonic (from 1 to 30) of the magnetic field density components (radial and tangential) for every element of the mesh [2.10].
  Since we didn't have an Epstein test bed, but knew the lamination material, we used the data for M19 material from [2.11]. The computations are based on the following data: k_h = 139.95 W/m³, α =1.92; k_e computed by (eq.2.45) is 0.589 W/m³ (d = 0.35 mm, ρ = 7650 kg/m³, σ = 2 .17·10⁶ S/m).
  All the computations are a roughly estimation since the magnetic material is not perfect and the cutting process can increase the iron losses (especially in the tooth region), where they can be doubled [2.14]. Still this analysis can't be bypass especially for new designs.

The 2D-FE analysis of the iron losses and magnetic flux density variation at steady state operation was done on two of the previous presented machines: the five phase machine and the six phase machine. Samples of radial (Br) and tangential (Bt) magnetic flux density components versus time were plotted for three selected points (at bottom of the tooth P1, at middle of the tooth P2 and at middle of the yoke P3) as shown in Fig. 2.37. The high harmonic nature of the magnetic flux density is obvious in all cases. Studying the variation of these components as functions of time and of each other it is clear that at steady state operation a Fourier harmonic analysis (under the assumption that the contribution of the fundamental frequency is largely dominant) is mandatory, because the Steinmetz formula only holds up for a sinusoidal waveform of *B*. So, (2.45) is applied for each of the studied harmonics (in our case 30 terms), the total core losses being obtained by summing up the core losses for each element according to the variation of *B* in that element [2.15-2.16].
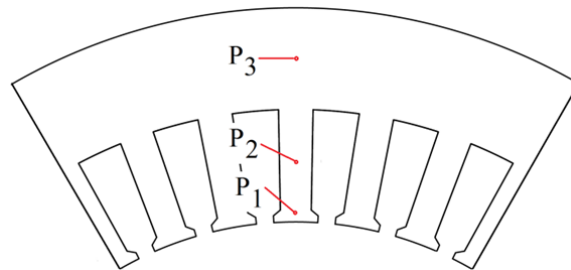
Fig.2.37. Selected points for magnetic flux density analysis

2.4.2 Five-phase BLDC-MRM

The variation of radial and tangential magnetic flux density component function of time, in the above presented three stator selected points, are shown next at base speed: 250 rpm (Fig. 2.1.a, c, e). The radial component is larger than the tangential one in the stator tooth while in the yoke the tangential component amplitude exceeds the radial component value. The dependency of the two magnetic flux density components at 4 speeds in a steady state operation is presented in Fig.2.1 b, d, f. The 4:1 speed ratio is achieved by a field weakening operation as explained and presented in section 5.2. The current waveforms presented there (in a load operation) were also used for this analysis, in fact the same 2D-FEA results were used to compute the torque pulsations and the iron losses. The only difference was the post-processing scripts applied on the "Rotating Module" file result.

The computed total iron losses at the studied four speeds for each magnetic flux density harmonic are presented in Fig. 2.38. At 500 rpm they seem to have the highest value while at 750 and 1000 rpm they are relatively close to each other due to the field weakening effect (decrease of field current level). Also they do not represent a problem in this FB rotor BLDC-MRM and as we shall see later in this work their influence on the efficiency is small.
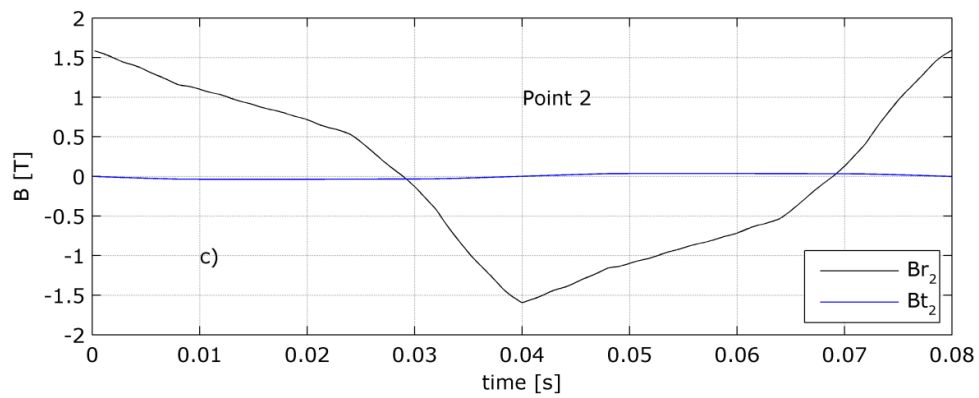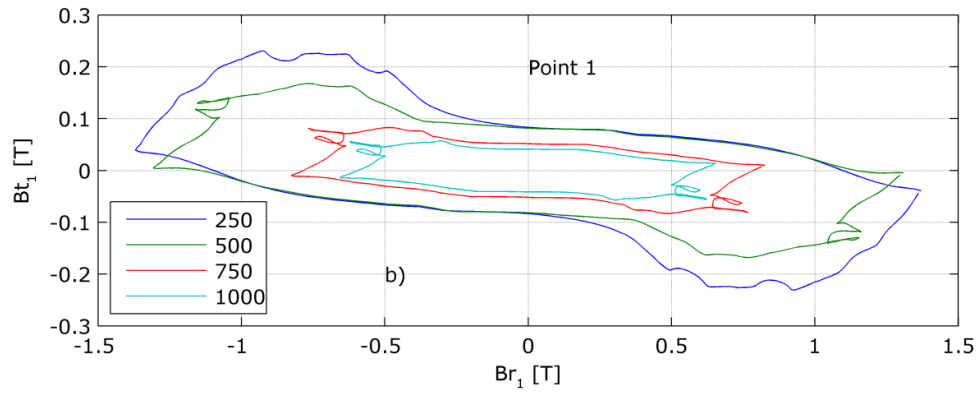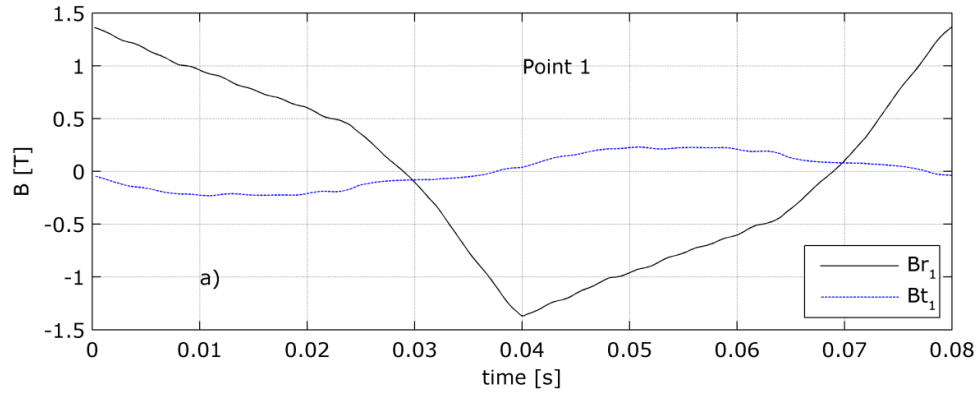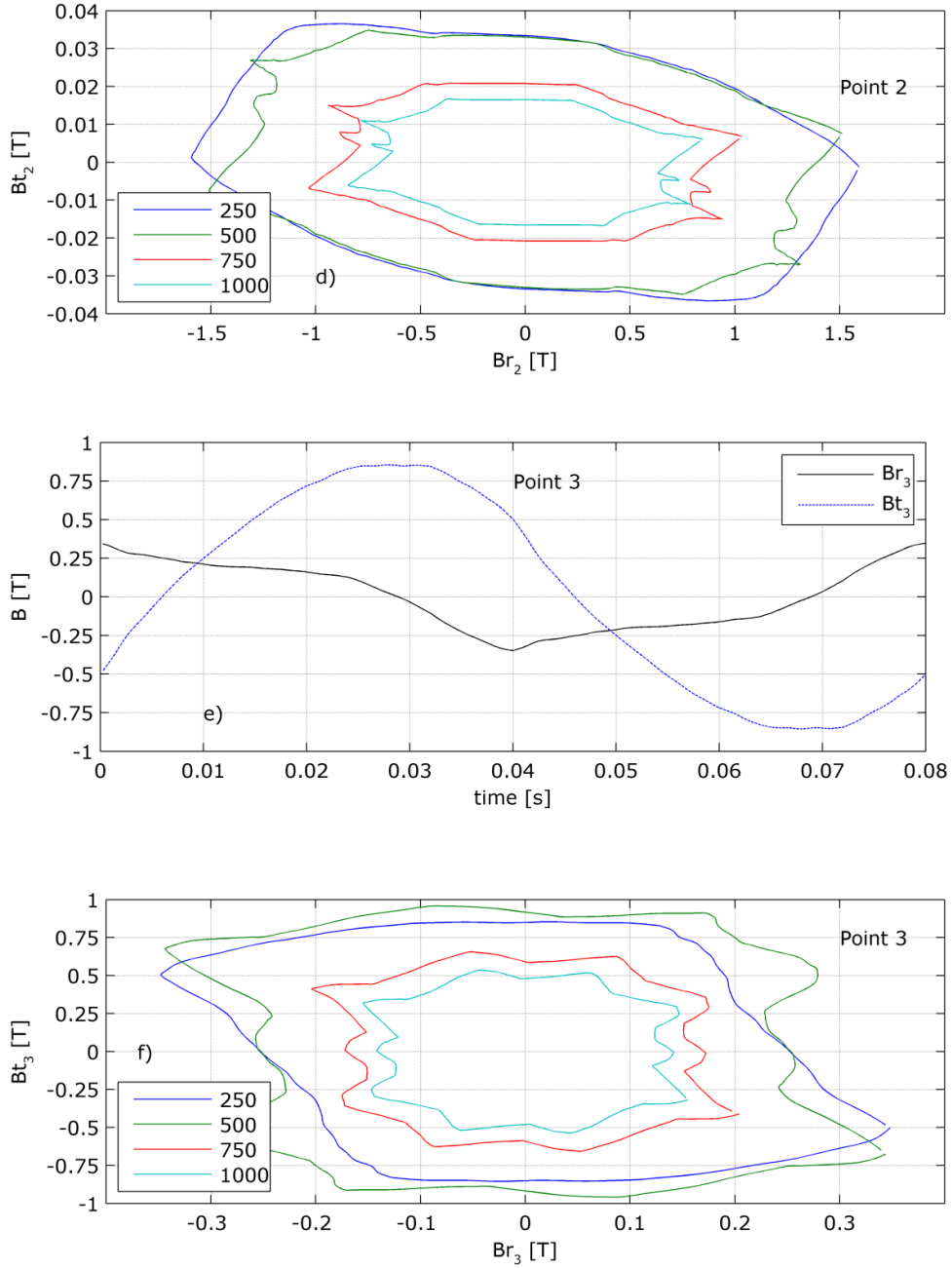
Fig.2.38. Variation of magnetic flux density function of time and of each other in the selected 3 key stator points
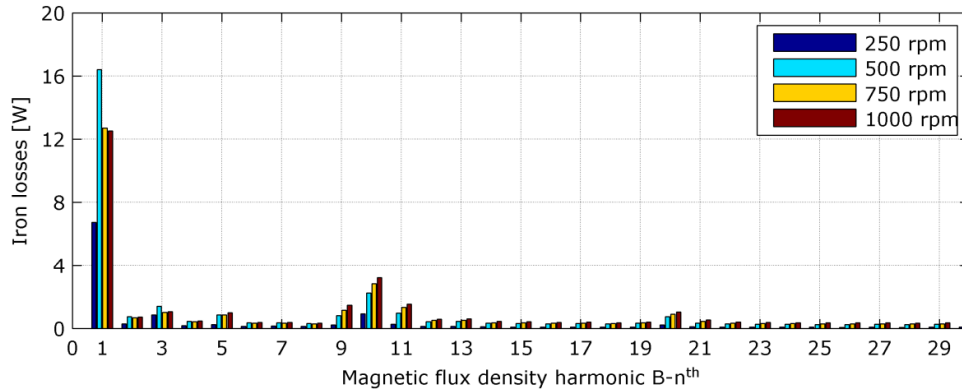
Fig.2.39. Total iron losses at 4 different speed for each magnetic flux density harmonic

2.4.3 Six-phase BLDC-MRM

The same analysis as for the five phase BLDC-MRM were done also for the 6 phase ALA rotor BLDC-MRM but only at the base speed and rated load steady-state operation. While we can find some resemblance in the pattern of Point 2 and 3 magnetic flux variation between the 5 and the 6 phase BLDC-MRM, the ALA rotor influence on the stator iron is more obvious next to the air-gap, in Point 1 (Fig. 2.40).

Total iron losses (11 W), stator iron losses and rotor iron losses, for the first 30's harmonics of B, are shown in Fig. 2.41. These results were somehow expected, since the machine was designed for a low speed operation (250 rpm, e.g. 12.5 Hz), with the possibility of being used as a small wind generator. Although the total rotor iron laminations volume is 35% of the stator volume, 50% of the total iron losses (5.4 W out of 11 W) occur in the rotor due to high number of magnetic flux harmonics, as expected due to *mmf* waveform. First, third, fifth and seventh harmonic are responsible for stator iron losses, while all the other harmonics produce rotor iron losses.
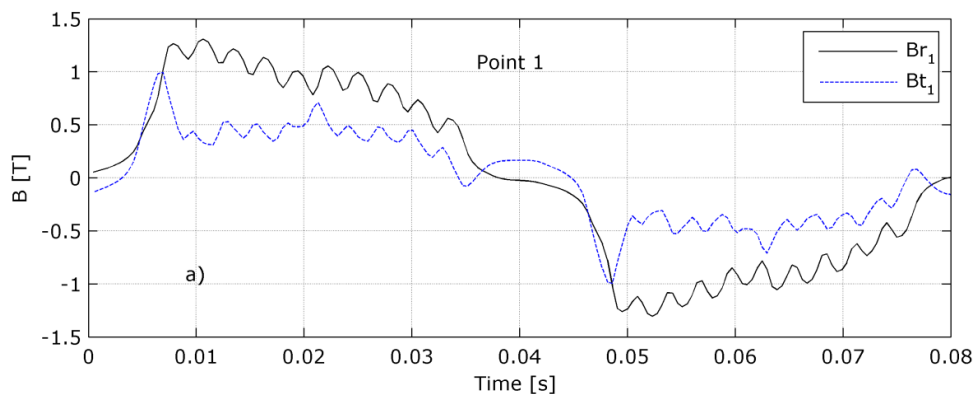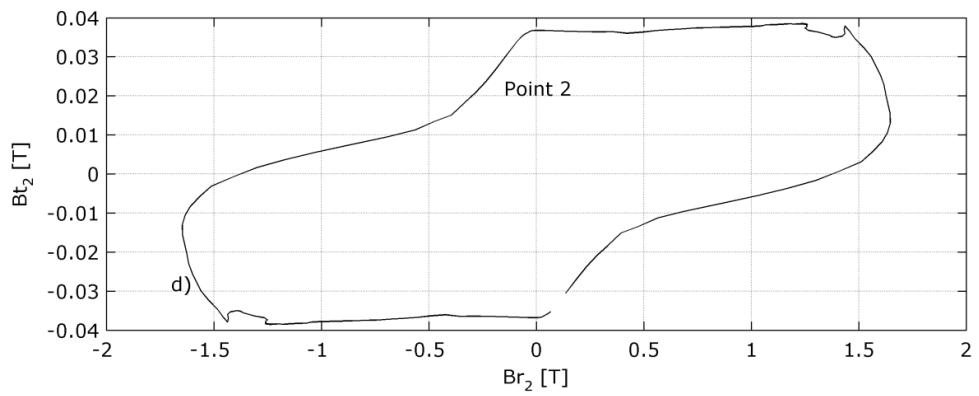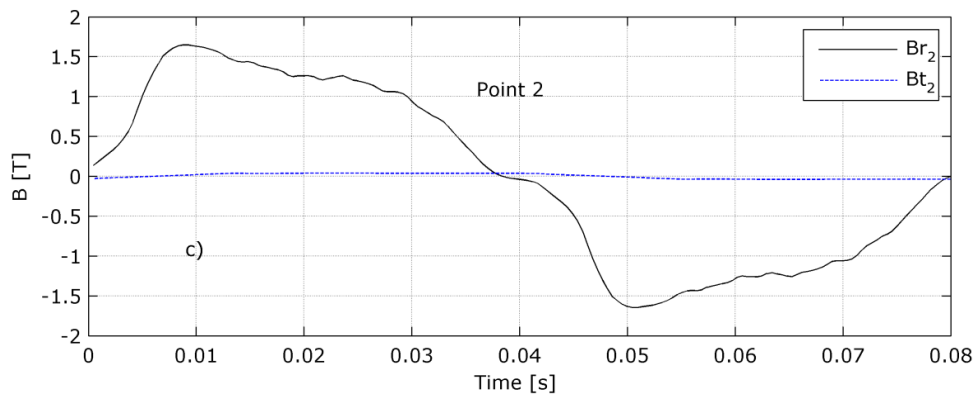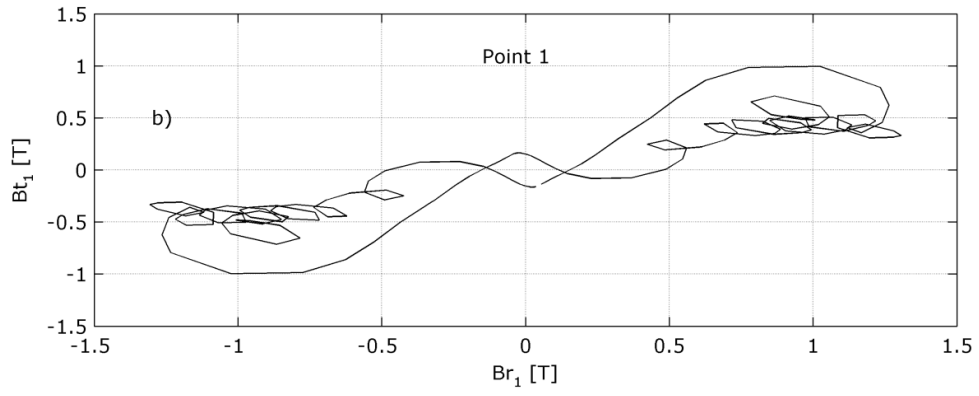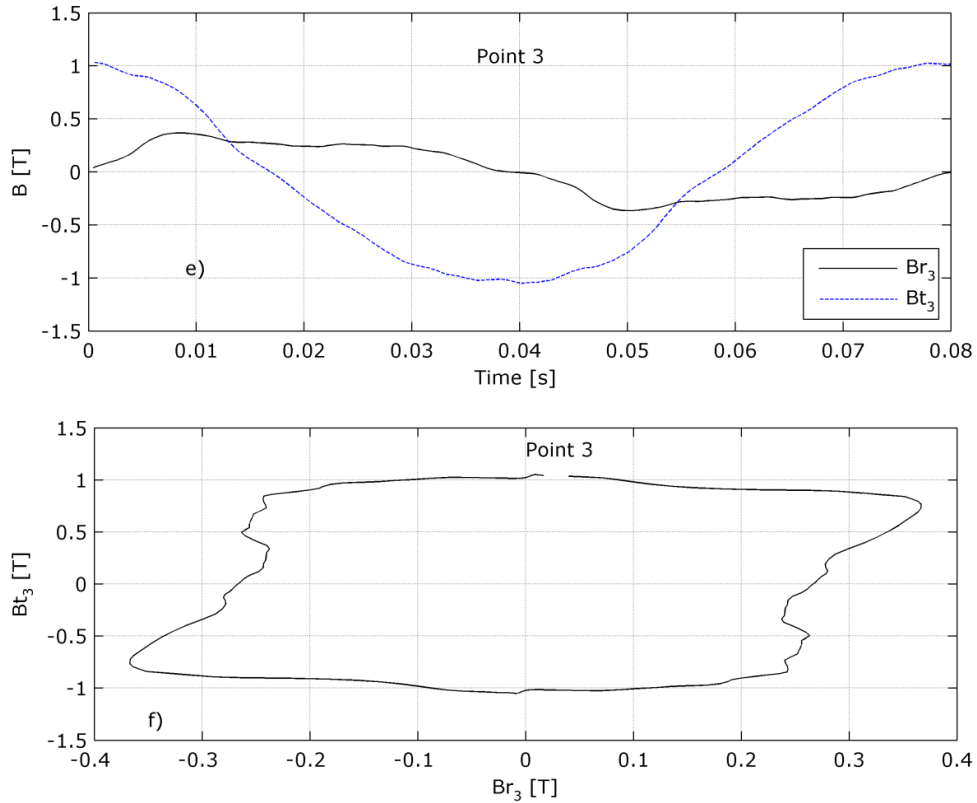
Fig.2.40. Variation of magnetic flux density function of time and of each other in the selected 3 key stator points
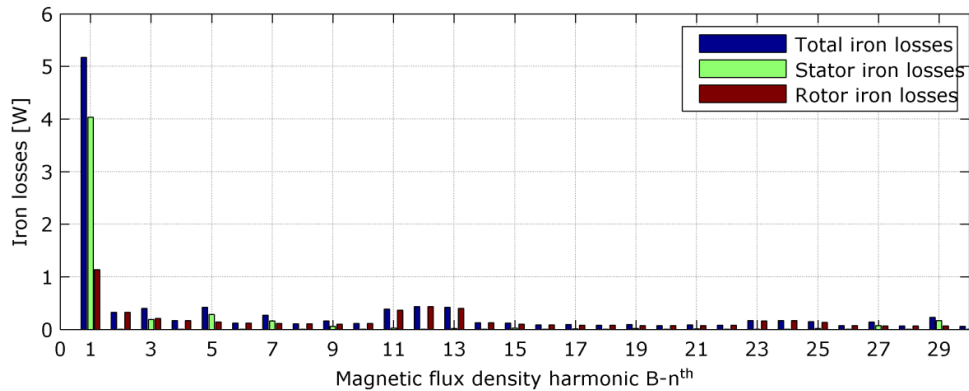
Fig.2.41. Iron losses at base speed for each magnetic flux density harmonic

Iron losses were also computed for the 6-phase FB rotor BLDC-MRM generator at rated load (Fig.2.42).
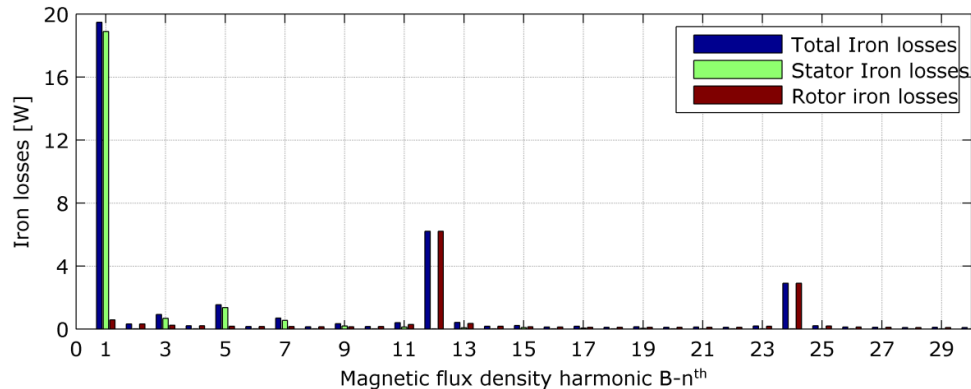
Fig.2.42. Iron losses at base speed for each magnetic flux density harmonic

Conclusion

A preliminary design code of a FB rotor BLDC-MRM was presented. This will be the basis of the optimal design code program developed in the next chapter, by adding also the stator lamination design.

Today, numerical methods are used more often for computation of the electromagnetic fields. Finite element method is an advanced numerical method valuable in the final stage design verification, where is used to verify the saturation level and magnetic air-gap magnetic flux density waveform. There are a variety of commercial computer programs based on FEM used for this purpose. This method offers higher accuracy compared to MEC. While some performances of the initial design can be checked using a magneto-static module, a transient program such as the RM module present in Opera 2D is mandatory (though more time consuming) for the correct analysis of various running regimes. In all cases some experiments are mandatory to gain some trust level in the developed numerical model.

Losses are an important issue in the operation of any machine, and among them iron loss computation rises problems due to their complexity. They could prove more important than the copper losses in high speed, non-sinusoidal air-gap magnetic flux density, so they are important to asses correctly. In a low speed machine, as in our case they are checked because of the employed current waveform, winding distribution and rotor geometry, still they are found to be negligible in all tested cases.

References

[2.1]   J. D. Law, A. Chertok and T.A. Lipo,*"Design and performance of field regulated reluctance machine"*, IEEE Trans. On Industry Applications, Vol. IA-30, No.5, 1994, pp. 1185-1192

[2.2]   L.N. Tutelea, "*Reactive series motor with static commutation* ", License Thesis, Politehnic Institut "Traian Vuia" of Timisoara, 1989

[2.3]   I. Boldea and S.A. Nasar, "*The Induction Machine design handbook – 2nd edition*", CRC Press, Taylor and Francis Group, New York, 2010

[2.4]   A.K. Sawney, "*A course in Electrical Machine Design*", Published by J.C. Kapoor, B.A. for Dhanpat Rai and Sons, 1974

[2.5]   N. Bianchi, *"Electrical machine analysis using finite elements*", book, CRC Press, Taylor and Francis Group, Boca Raton, 2005.

[2.6]   S.J. Salon, "*Finite Element Analysis of Electrical Machines*", book, Kluwer Academic Publisher, Third Priting, 2002.

[2.7]   K. Hameyer and R. Belmans, "*Numerical modeling and design of electrical machines and drives*", MIT Press, 1999, UK

[2.8]   P.S. Silvester, "*Finite elements for electrical engineers*", book, Cambridge University Press, 3rd edition, 1996

[2.9]   D. C. Meeker, Finite Element Method Magnetics, Version 4.2 (15Nov2013 Build), http://www.femm.info

[2.10] Cobham Technical Services, Vector Fields Software, Opera v.13.

[2.11] A. Boglietti, A.Cavagnino, M. Lazzari, M. Pastorelli, "*Predicting Iron Losses in Soft Magnetic Materials With Arbitrary Voltage Supply: An Engineering Approach*," IEEE , Trans.On Magnetics, vol.Mag-39, no.2., pp. 981-989, 2003.

[2.12] C.P. Steinmetz, "*On the Law of Hysteresis*," Trans. AIEE, vol. IX, no.1, pp. 1-64, 1892.

[2.13] G. Bertotti, A. Boglietti, M. Chiampi, D. Chiarabaglio, F. Fiorillo, M. Lazari, "*An Improvement Estimation of Iron losses in Rotating Electrical Machine*," IEEE Trans. On Magnetics, vol. Mag-27, no.6, pp. 5007-5009, 1991

[2.14] A. Kedous-Lebouc, B. Cornut, J.C. Perrier, P.F. Manfe, Th. Chevalier, "*Punching influence on magnetic properties of the stator teeth of an induction motor*," Journal of Magnetism and Magnetic Materials, pp. 124-126, 2003.

[2.15] D. Ursu, L.N Tutelea, I. Boldea, "*Proposal with 2D FEM analysis of a six phase, 12 poles, 3kW, 200 rpm BLDC Multiphase Reluctance Machine wind generator*", Power Electronics and Applications European Conference (EPE), 2013 IEEE , pp. 1-9

[2.16] Agarlita, S.; Ursu, D.; Tutelea, L.; Boldea, I.; Fahimi, B. "*BLDC multiphase reluctance machines: A revival attempt with 2D FEM investigation and standstill tests*", Energy Conversion Congress and Exposition (ECCE), 2013 IEEE, pp. 1850 – 1857

3. BLDC-MRM optimal design methodology and code

3.1 Introduction

Optimization represents the act of finding the best possible solution for a certain problem, under given circumstances. According to [3.1] even intelligence can be viewed as an optimization process, since intelligent behavior can be successfully defined as a force that acts to maximize future freedom of action. In other words intelligence doesn't like to get trapped. This idea has been implemented in: robotics, finance and even game play [3.1]. Computers started to win chess games against grandmasters starting with 1997 (Deep Blue vs. Gary Kasparov), but despite the raw computation power and advanced algorithms the game of GO, for example, remained a challenge for calculus machines because of the related high branching factor. This barrier starts to crack and nowadays computers surpass human players at GO, using techniques that mimics the above definition of intelligence. It seems that the best approach for computer playing GO is the one that tries to maximize future options during gameplay. Although promising results have been shown, human intelligence is much more complex, and a true artificial intelligence is unlikely to be "born" without a quantum computer or another powerful parallel computing device that can emulate neurons and synapses [3.2].

This chapter will present BLDC-MRM optimal design using nature inspired heuristic algorithms. They are population based algorithms that search the solution in a parallel fashion, and use stochastic variables that make unlikely the entrapment in a local minimum. Deterministic (gradient-based) algorithms have been applied in the past for electrical machine optimal design [3.3], with higher computation time compared to evolutionary algorithm and also at a higher probability to get stuck in a local optimum, even if the search starts from a few randomly distributed points. We should keep in mind that humans have been copying nature for many years, since it offers powerful and elegant solution for different problems.

A numerical model that takes into account iron saturation is needed for machine performances evaluation. The easiest and accurate way is to use an embedded 2D-FEA routine in the optimization algorithm [3.3], but the downside is represented by high computation time compared to MEC when thousands of machines are being analyzed during optimization, regardless of the FEA software [3.4]. Although MEC request more programming knowledge and more attention in the model design stage, it pays out when implemented in the optimization routine due to short computation time. An initial test (on the BLDC-MRM nonlinear numerical analysis model) has shown a computation time reduction of almost three orders of magnitude if MEC is used instead 2D-FEA. Considering this, a nonlinear MEC routine that simulates steady state behavior is used in the optimization code, while FEA is adequate in the final stages of design and machine performance evaluation (such as torque pulsations and advanced iron loss computation). Although [3.5, 3.6] present numerical analysis of the BLDC-MRM via MEC, the model is solved through flux loops, not by node potential equation, which is faster and more suitable for computer code implementation (known from FEA solvers).

3.2 Magnetic Equivalent Circuit analysis

The basis of the whole MEC method is the flux tubes (Fig.3.1). They represent space regions in which all field lines are perpendicular to their bases and no lines of flux cut their sides. A flux tube has two equipotential planes with magnetic scalar potentials u_1 and u_2. The magnetic scalar potential has no physical meaning, because there is no quantity in magnetic fields that is analogous to the change in electrostatic field. The tube reluctance - R_m can be expressed function of geometrical properties and material permeability (eq. 3.1) or as the ratio of potential difference - θ divided by flux through tube surface - Φ (eq. 3.2).

$$R_m = \int_0^x \frac{dx}{\mu(x) \cdot A(x)}; \quad \rightarrow \quad \begin{cases} \mu(x) = cst. \\ A(x) = cst. \end{cases} \Rightarrow R_m = \frac{L}{\mu \cdot A} = \frac{1}{G_m} \tag{3.1}$$

$$R_m = \frac{u_2 - u_1}{\Phi} = \frac{\theta}{\Phi} \quad \text{where}: \quad \theta = \int_0^x \overline{H} \cdot \overline{dx}; \quad \Phi = \iint \overline{B} \cdot \overline{dA}; \tag{3.2}$$
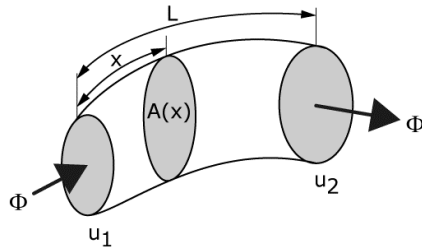
Fig.3.1. Magnetic flux tube
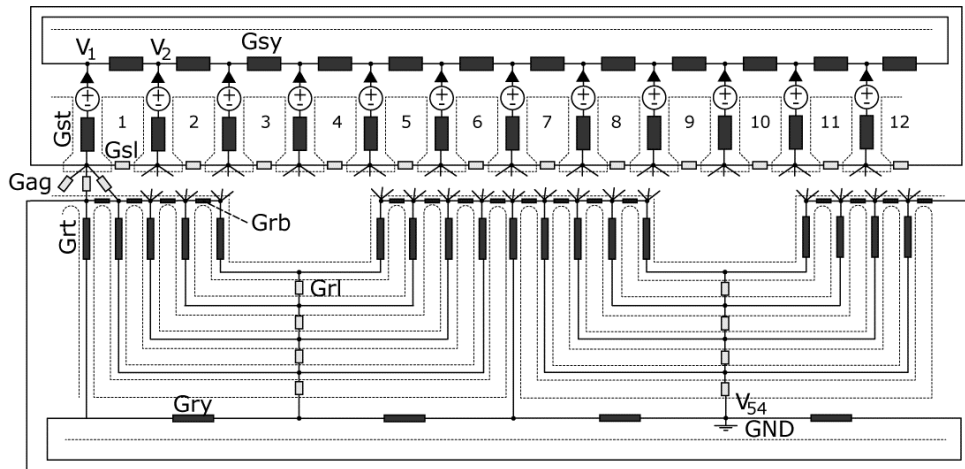
Fig.3.2. BLDC-MRM Magnetic equivalent circuit

Magnetic equivalent circuit (MEC) technique transforms the complex magnetic circuit of an electrical machine into "resistive" (permeance) electrical network (Fig.3.2), which is solved using electric circuit theory [3.7]. According to [3.7] elements that appear in MEC can be separated in two groups: active (sources) and passive (permeances). Each region is replaced by a permeance whose flux direction is restricted to two directions (known before the method is applied). Stator and rotor yoke permeances (Gsy, Gry) accounts only for the tangential component of flux, while stator and rotor tooth permeances (Gst, Grt) accounts only for radial component of flux. Total numbers of elements (and nodes) are chosen in the first design stage and represent a trade-off between computation cost and achieved accuracy.

The permeances can be divided in: constant, parametrically nonlinear and inherently nonlinear. Constant permeances are used in those places were a constant flux tube geometry and permeability exist. Usually they will model the machine leakage paths: stator slot leakage permeance (Gsl) and rotor flux barrier leakage permeance (Grl).

Flux tubes with variable dimensions (but a constant permeability) have a parametrically nonlinear permeance. This situation occurs in machine air-gap, since the rotor position changes respect with stator. Because electromechanical energy conversion takes place in this region, this is the most important part of a machine, so great care must be taken when it's modelled. Permeance between i-th stator tooth and j-th rotor tooth ($G_{i,j}$) is defined as an analytical function of the rotor mechanical angle γ as described in eq. 3.3 (Fig.3.3-3.4).

$$G_{i,j} = \begin{cases} G_{max} & 0 \le \gamma \le \gamma_t' \ \vee \ 0 \le \gamma \le \gamma_t' \\[3mm] G_{max} \cdot \dfrac{1 + \cos\left(\pi \dfrac{\gamma - \gamma_t'}{\gamma_t - \gamma_t'}\right)}{2}; & \gamma_t' \le \gamma \le \gamma_t \\[3mm] G_{max} \cdot \dfrac{1 + \cos\left(\pi \dfrac{\gamma - 2\pi + \gamma_t'}{\gamma_t - \gamma_t'}\right)}{2}; & 2\pi - \gamma_t' \le \gamma \le 2\pi \\[3mm] 0 & \gamma_t' \le \gamma \le \gamma_t \end{cases} \qquad (3.3)$$

were:

$$G_{max} = \mu_0 \frac{l_c \cdot w_t}{g}; \quad w_t = \min(w_{st}, w_{rt})$$

$l_c -$ machine length

$w_{st} -$ width of stator tooth (at the air-gap)

$w_{rt} -$ width of rotor tooth (at the air-gap)

$g -$ air-gap length

$$\gamma_t' = 2 \cdot \frac{|w_{st} - w_{rt}|}{sDi - g}$$

$$\gamma_t = 2 \cdot \frac{w_{st} + w_{rt} + sMs + rMs}{sDi - g}$$

$sDi -$ stator inner diameter

$sMs \ / \ rMs -$ stator/rotor mouth slot
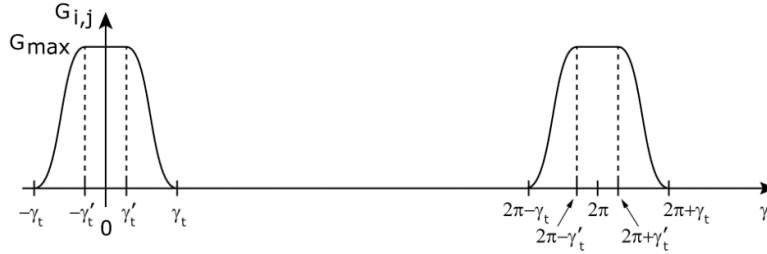
Fig.3.3. Air gap permeance variation vs. rotor position
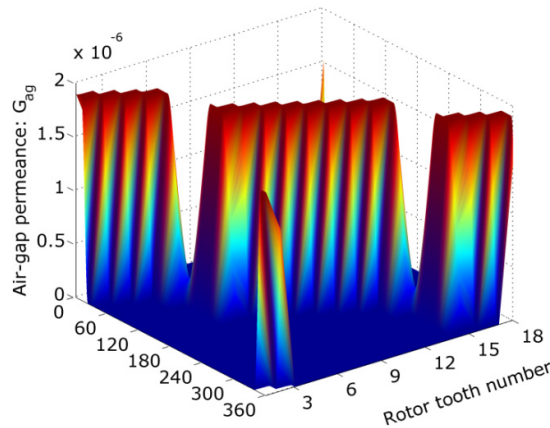
Fig.3.4. Air gap permeance variation vs. rotor position between one stator tooth and all rotor teeth

Since the potential between one stator tooth and another rotor tooth usually is different from zero, only an imposed 0 value permeance ($G_{i,j}$=0) between them will make the flux also 0, when they don't "see" each other anymore, as it is in reality.

The fringing effect makes all air-gap permeances slightly higher. This effect is accounted by multiplying the permeance by c_f [3.7].

$$c_f = \frac{\dfrac{sMs}{w_{st}}}{\ln\left(1+\dfrac{sMs}{w_{st}}\right)} \tag{3.4}$$

The air gap permeance matrix is continuously changing at each new rotor position and new connections form between each stator teeth and each rotor ones.

Inherently nonlinear permeances are employed in a static geometry and saturable materials. Permeance value depends on the amount of flux that passes through it. MEC code use magnetization curve from Fig.3.5 and a linear interpolation routine. The saturation influence on the permeance can be seen in Fig.3.6. Above last known measured point where μ_r is 15, we assume linear (paramagnetic) slope of BH curve (Fig. 3.7) were μ_r =1, regarding of the flux through it.
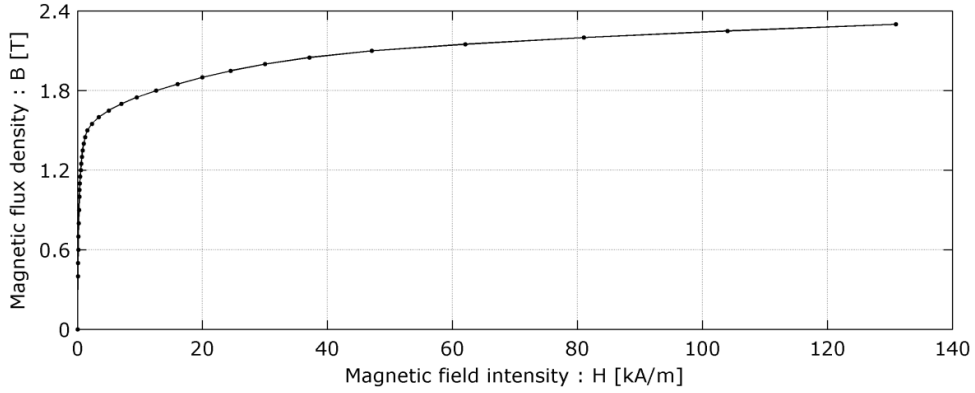
Fig.3.5. B-H curve used for MEC analysis and 2D-FEA analysis (material type: M45)
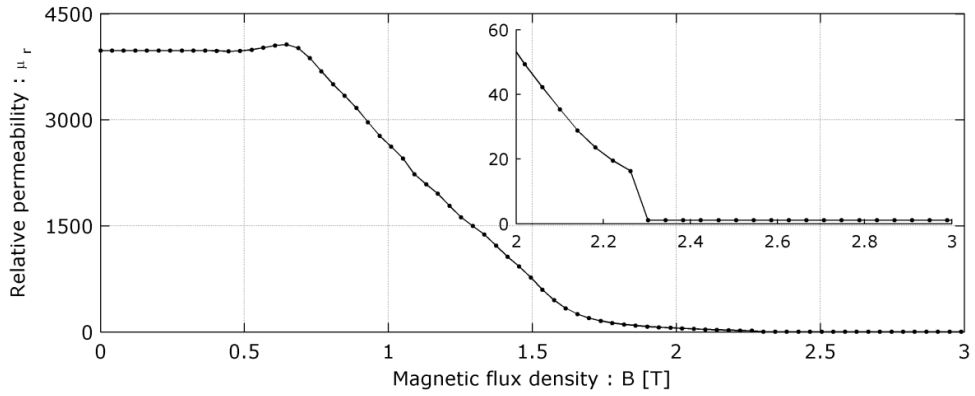
Fig.3.6. Variation of relative permeability vs. magnetic flux density
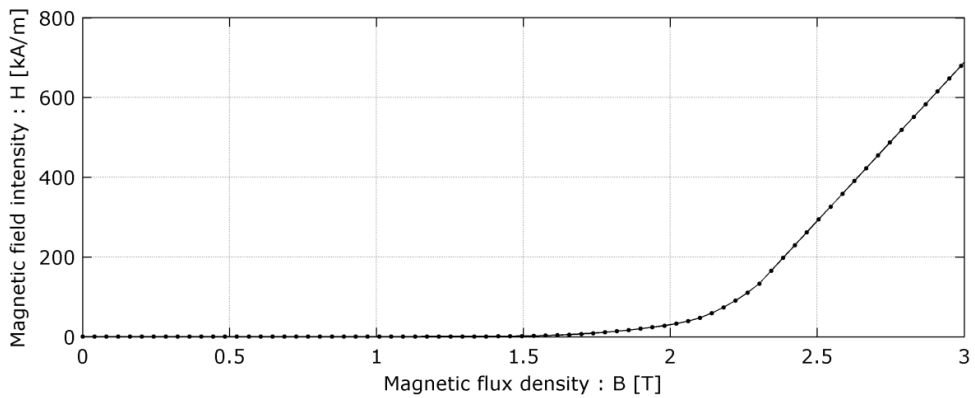
Fig.3.7. Magnetic field intensity function of magnetic flux density
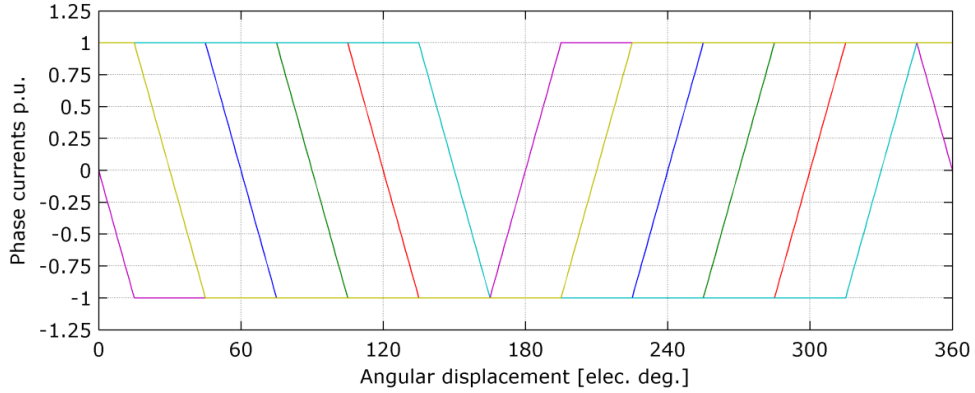
Fig.3.8. Per-unit phase currents ($I_F = I_T$) in a steady state operation function of rotor angular displacement
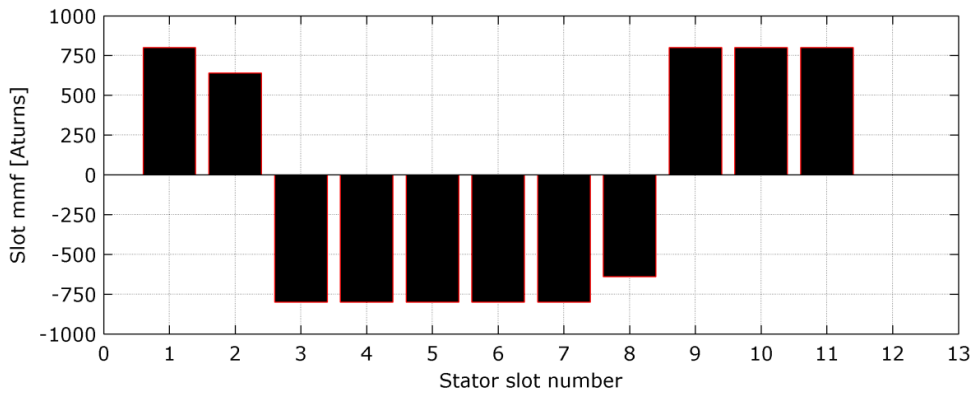
Fig.3.9. Applied slot *mmf* value for steady state operation of the BLDC-MRM
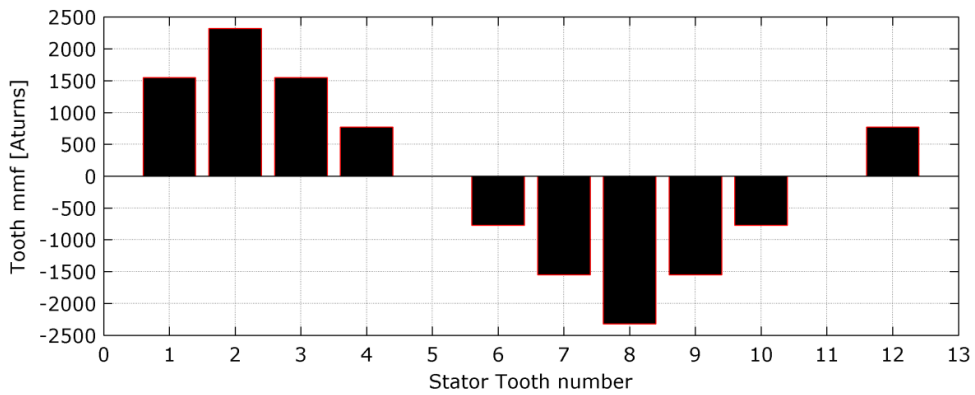
Fig.3.10. Computed tooth *mmf* value for steady state operation for a given rotor position

Sources are represented by tooth *mmf* value (Fig.3.10) computed from slot *mmf* values (Fig.3.9) which are based on phase currents values (Fig.3.8) as described in [3.7].

A few assumptions have been made when the MEC model (Fig.3.2) was built:

- number of phases = 6 (2 field phases and 4 torque phases);
- q = 1;
- rotor tooth per pole = 9 (not dividable by 4). A lower number increase torque pulsations, while a higher one increase cutting cost.

The above points states that the number of rotor tooth and of phases are given as a priori information and cannot be optimization variables, because the global matrix [*G*] would have a completely different structure (due to new elements and nodes), and the order of equation system changes.

As already stated the nonlinear system of equations is solved iteratively by node potential method. In the absence of hysteresis, for given initial conditions one unique solution will exist [3.8]. BLDC-MRM MEC model has 54 nodes, but since node 54 is put to ground ($V_{54}=0$), the system order is reduced to 53. MEC is completely described by a set of algebraic equations, where fluxes and permeance matrix are known and magnetic scalar potentials are unknown (eq. 3.5).

$$\left[G\right]\cdot\left[V\right]=\left[\phi_t\right] \tag{3.5}$$

were the definition and matrix size are:

$\left[G\right]-$ global permeance matrix $\rightarrow 53\times53$

$\left[V\right]-$ node potentials $\rightarrow 53\times1$

$\left[\phi_t\right]-$ tooth fluxes $\rightarrow 53\times1$

As in FEA, MEC model also takes advantage of machine symmetry, and through an intelligent connection of nodes (Fig.3.2) only 2 poles of the machine needs to be studied, corresponding to positive boundary conditions.

MEC is used for iron loss and electromagnetic torque computation. Iron loss were calculated based on an adapted procedure presented in [3.9] for FEA. Information about computed magnetic flux density (in all inherently nonlinear permeances), mass, and operation frequency are used for iron loss computation. Equation (3.6) is applied for each region, the final result being a sum of all computed losses. A more complex and accurate approximation have been used in 2D-FEA [3.10], based on Steinmetz formula applied for all magnetic flux harmonics (from 1 to 30) in each mesh element as shown in section 2.4.

$$P_{fe}=p_{10}\cdot\left(B^2\cdot k_e\cdot\left(\frac{f_b}{50}\right)^2+B^2\cdot k_h\cdot\left(\frac{f_b}{50}\right)^2\right)\cdot m;\quad B=\max\left(abs\left(B_r\left(t\right)\right)\right); \tag{3.6}$$

were:

$B_r\left(t\right)-$ region magnetic flux density time variation

$p_{10}=3$ W/kg (at 1T and 50Hz);

m $-$ region mass [kg]

Eddy current and hysteresis coefficients are computed bellow based on lamination thickness - d, material electrical conductivity - σ and lamination iron density ρ_{fe}.

$$k_e = \frac{\pi \cdot d^2 \cdot \sigma}{6 \cdot \rho_{fe}} = \frac{\pi \cdot \left(0.35 \cdot 10^{-3}\right)^2 \cdot 2.17 \cdot 10^6}{6 \cdot 7.650 \cdot 10^3} = 1.8194 \cdot 10^{-5} \quad \frac{m^4 S}{kg} \tag{3.7}$$

$$k_h = \frac{140}{\rho_{fe}} = 0.0183 \tag{3.8}$$

$$f_b = \frac{n_b \cdot poles}{120} = \frac{3000 \cdot 6}{120} = 150 \quad Hz \; \left(\text{base frequency}\right) \tag{3.9}$$

Electromechanical energy conversion takes place in the air-gap only, so it depends on the air-gap conditions. Electromagnetic torque is calculated as a sum of products between the square of the *mmf* values between the teeth and variation of corresponding permeance respect to rotor position (eq. 3.10) as proved in [3.7].

$$T_e = \frac{poles}{2} \cdot \sum_{i=1}^{N_S} \sum_{j=1}^{N_R} \left(V_i - V_j\right)^2 \frac{dG_{i,j}}{d\gamma} \tag{3.10}$$

were:

N_S – Number of stator tooth = 12

N_R – Number of rotor tooth = 18

$V_{i,j}$ – Node potentials

For a given set of sources (*mmf*) the program solves for node potentials. The created nonlinear system of equation can't be solved analytically, only numerically, by an iterative procedure. Usually the nonlinear system converges in less than 15 iterations. Sub-relaxation factors (k_a) between 0.1 and 0.9 have been tested and the best convergence was obtained for k_a =0.44. The algorithm is presented next.

compute B based on $B_{air\text{-}gap}$
compute μ_r
compute all permeances
for *θ_{er} = 0 : 360*
    compute $G_{air\text{-}gap}$ matrix based on new θ_{er}
    compute tooth mmf based on new currents
            while *(Berror > 10^{-3}) && (Loop < 30)*
                    $\mu_{r\_o} = \mu_r$
                    $\mu_r = \mu_r + k_a \cdot (\mu_{r\_o} - \mu_r)$
                    compute inherently nonlinear permeances
                    global matrix assembly
                    compute flux vector ϕ_t
                    solve the equations
                    compute new fluxes
                    compute Berror

$B = B + min(k_a·abs(Berror),k_a)·sign(Berror)$
compute new μ_r

end

save all nonlinear permeance B
compute and save torque

end

compute iron losses

      The computed tooth magnetic flux density is shown in Fig.3.11 for one position. The steady state operation is obvious in Fig. 3.12 (tooth magnetic flux density versus rotor electrical angular displacement).   The MatLab routine can be studied in Appendix 2.
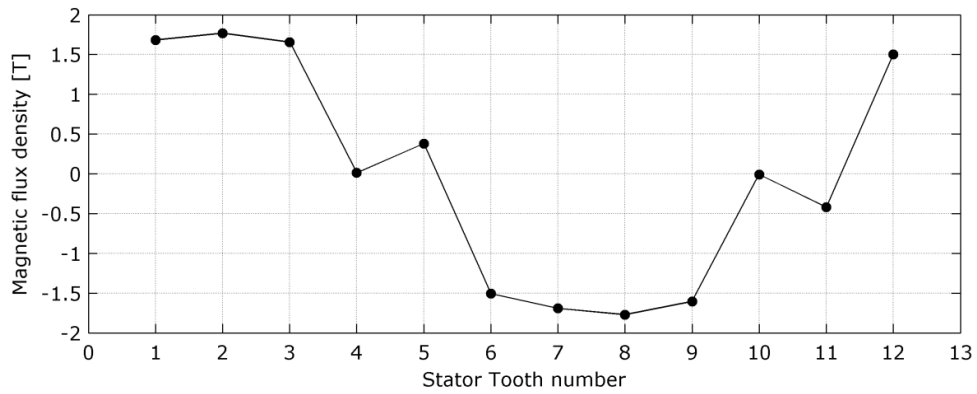
Fig.3.11. Tooth magnetic flux density after solving the non-linear system of node potential equations
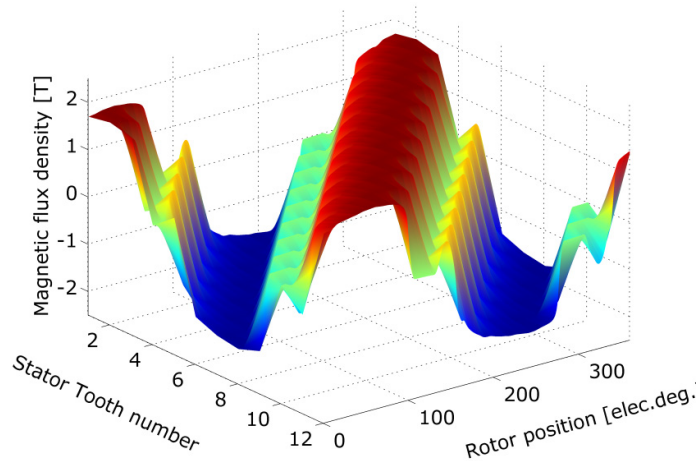
Fig.3.12. Tooth magnetic flux density vs. rotor position

A comparison between computed MEC torque and 2D-FEA torque of the same machine working in similar conditions are plotted and compared in Fig. 3.13. The 2D-FEA results show a realistic torque pulsations and average torque because they are computed from a 3 layer air-gap mesh using Maxwell stress tensor , compared with one layer elements and discrete evaluation of energies at two positions using spatial derivatives of G_{ag} as in MEC. Obvious torque pulsations can't be an objective of the optimization process, but average torque can be used since the maximum MEC torque value varies (for different machines) between average and minimum FEA torque pulsation. **In the optimization the maximum values of torque (computed by MEC) were used for the average values of developed BLDC-MRM torque (as confirmed by FEA results)**. The computation time between the two methods for graphs from Fig 3.13 (with one electrical degree time step) is pretty high: 4 seconds for MEC compared to 3700 seconds for 2D-FEA. Even if you increase the time step to 1 mechanical degree and reduces the simulation to one stator slot pitch you will still need 130 seconds. If required, FEA should be used after optimization stage for accurate iron loss computation and torque pulsations.
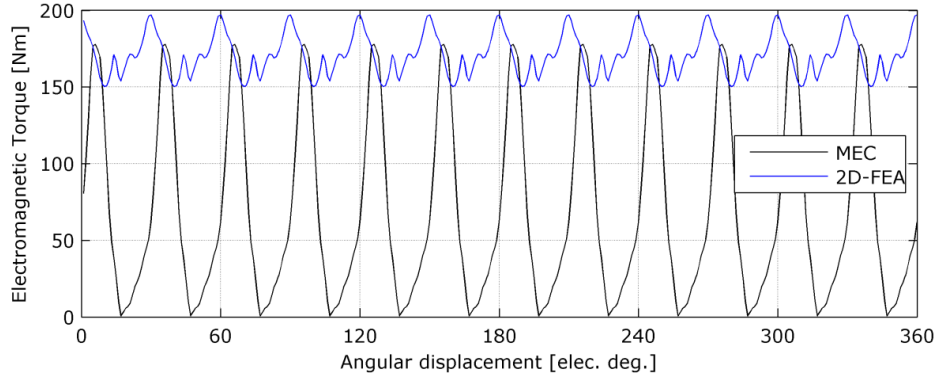
Fig.3.13. Comparison between MEC and 2D-FEA computed electromagnetic torque

3.3 Optimization algorithms
3.3.1 Introduction

The optimization algorithm has to find out a set of parameters coded in a vector $\overline{X}$, which minimizes (or maximizes) an objective function $F_{ob}(\overline{X})$. Usually the term objective function is replaced by fitness function when evolutionary algorithms are employed. Nature is able to find an optimum solution for various problems through elegant and powerful processes, thus in the last few years it became a trend, and later a good practice, to solve engineering problems copying nature behavior. For example Japanese engineers have solved an important aerodynamic problem of high speed trains by studying and copying the seagull beak. Replacement of deterministic algorithms with heuristic one becomes a must as the number of search-space dimensions increase, though no specific stochastic algorithm has been proven to take advantage in electrical machine design.

Astrophysics, classical gravity theory and birds behavior represent the main fields from which three state of the art algorithms are created and used for a fair comparison in terms of computation time and search for optimum. All the presented algorithms are written as MatLab functions (Appendices 3-6).

3.3.2 Meta-heuristic optimization algorithms

Heuristic algorithms use stochastic random search of hyper-space (without using derivative information) with good computation power and without excessive computation time. A meta-heuristic algorithm is a problem independent technique that search for solution in a parallel manner using multiple initial points, by guiding a subordinate heuristic. Stochastic behavior (random variation and selection) is present in these algorithms, which increases drastically the probability of finding a position close enough to global optimum without getting trap in a local one.

Nature inspired meta-heuristic algorithms such as: Genetic Algorithms [3.10], Simulated Annealing [3.11], Ant Colony Optimization [3.12], Intelligent Water Drops [13], Harmony Search Optimization Algorithm [3.14], Big Bang-Big Crunch Optimization [3.15] and many other had been used in many fields from economy to engineering. All these are population based algorithms and have in common two aspects: space exploration (ability to expand search space) and space exploitation (finding the optimum around a good solution). In the first part of the search, exploration must prevail while in the last part the computation effort must be concentrated on space exploitation.

The following study analyzes four state of the art stochastic algorithms: Black Hole Based Optimization (BHBO) [3.16], Particle Swarm Optimization (PSO) [3.17], Gravitational Search Algorithm (GSA) [3.18] and a hybrid version between PSO and GSA [3.19]. Since each one of them has been "praised" by their creator, a fair comparison between them must be made in order to find who has the greatest potential. Only one of them will be implemented in BLDC-MRM optimal design code, based on computed performances on four benchmark test functions: two unimodal (DeJong and Rosenbrock) and two multimodal (Ackley and Rastring).

An algorithm that has the ability to learn from past experiences and adapts his behavior according to environment can be seen as artificial intelligence, which according to [3.20] should follow five principles:

- *Proximity principle* : simple space and time computation made by population members;
- *Quality principle* : the population should be able to carry simple space and time computation;
- *Diverse response principle* : the population should not allocate all search resources in excessively narrow spaces;
- *Stability principle* : the population behavior should not change significantly at every environmental change;
- *Adaptability principle*: the population must be able to change behavior when computation price is worth it.

All four presented algorithm respect at least one of the above, but one of them (PSO) tracks all five principles.

3.3.3 Black Hole Based Optimization

Although the idea of the Black Hole was first announced by prof. John Michell in 1783 at Cambridge (based on Newton theories), the term Black Hole (BH) as we know it today was introduced two centuries later, in 1967 by Dr. John Wheeler (Princeton), who understood well enough the Einstein's general theory of relativity consequence on behavior of mass and gravity in a space-time frame.

BH describes a region of space (singularity) with such a strong gravitational field that not even light can't escape from. This occurs when a strong mass

compression takes place in an extremely small volume. For example a BH as big as an atom has approximately the mass of Mount Everest.

Schwarzschild radius was introduced in order to describe the radius of the sphere-shape boundary (the so-called event horizon) and is proportional to the product between BH mass and the gravitational constant G divided by the square value of the speed of light in vacuum [3.21]. Anything that crosses this limit will permanently disappear from our observable universe. Arguable no information can be obtained from the BH. Quantum mechanics states that a field can't be exactly zero, because then, one would have a precise value for position and speed (equal to 0) which violates the uncertainty principle (stated by Heisenberg in 1927) [3.22]. Based on this S. Hawking has proven that the BH has a measurable temperature, due to quantum fluctuation of void energy [3.23]. So in the end the BH it's not that black, it emits radiation but usually the temperature is much smaller ($\sim 10^{-6}$ °K) than the background temperature of the universe (~ 2.7 °K), so is undetectable.
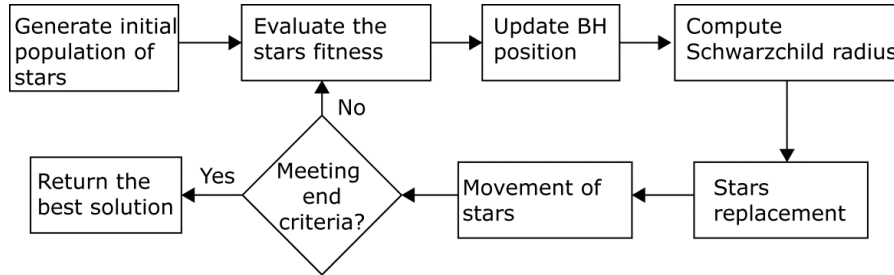
Fig.3.14. BHBO flowchart

BHBO algorithm (Appendix 3) is based on BH phenomena and it works according to flow-chart from Fig.3.14. An initial population of stars is randomly generated in D-dimensional space. The position of ith agent in the multidimensional space (used for all presented algorithms) is:

$$x_i = \left(x_i^1, x_i^2 ... x_i^D \right). \quad D - \text{number of dimensions}$$

The fitness value of all stars is computed, and the best candidate is selected to be the BH (at each iteration), toward whom all the other stars goes to. Each star makes a variable (random) step toward BH position according to (3.11):

$$x_i(t+1) = x_i(t) + rand(0,1) \cdot \left(x_{BH} - x_i(t) \right), i = 1 ... P \tag{3.11}$$

where: P - number of stars, t – iteration step, x_{BH} - BH position, $x_i(t)$- i^{th} star position at iteration t. The position of the BH remains unchanged until another star finds a better position. If the distance between the star and the BH R_i (eq.3.12) is smaller than Schwarzschild radius R_S (eq.3.13), it will be absorbed by the BH and replaced by another star in a random manner.

$$R_i(t) = \sqrt{\sum_{d=1}^{D} \left(x_{BH}^d - x_i^d \right)^2} ; \tag{3.12}$$

$$R_S = \frac{f_{BH}}{\displaystyle\sum_{i=1}^{N} f_i} \rightarrow \begin{cases} f_{BH} - \text{BH fitness value} \quad f_i - \text{i}^{\text{th}} \text{ star fitness value} \\ \quad x_i^d - \text{i}^{\text{th}} \text{ star position in dimension d} \end{cases} \qquad (3.13)$$

The advantage of this method is represented by its simple structure with no parameter tuning.

3.3.4 Particle Swarm Optimization

Particle swarm optimization is tied to artificial life, emulating the behavior of bird flocking or fish schooling [3.17]. The foundation of this algorithm lies in the idea that social sharing of information among group members offers an evolutionary advantage compared to non-cooperative populations. Individuals profit from discoveries and previous experience of all group members during search for food. When the food resources have an unpredictably space distribution, the advantage of cooperation among individuals outweighs the disadvantage of competition for food items.

Compared to BHBO, each particle (besides a unique position - x_i) also has a velocity - v_i. The PSO behavior and algorithm flowchart (Appendix 4) can be studied in Fig.3.15. After the random initialization of particles and evaluation of fitting values, the best position in space (g_{best}) and best position for each particle (p_{best}) are memorized. Based on this data the new velocity at time ($t+1$) is computed (eq. 3.14). P_{best} resembles autobiographical memory, and the velocity adjustment with this term is called "*simple nostalgia*", making the individual to want to return to the place where the food supply was best. On the other hand g_{best} is similar to publicized knowledge.
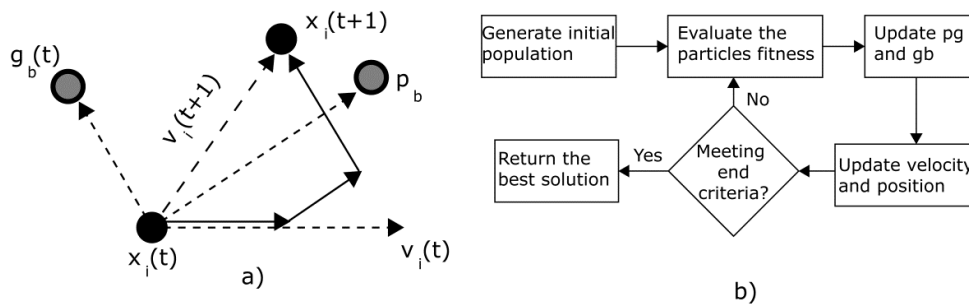
Fig.3.15. a) Particle space movement, b) PSO flowchart

$$v(t+1) = w(t) \cdot v(t) + c_1 \cdot rand(0,1) \cdot (p_{best} - x(t)) + c_2 \cdot rand(0,1) \cdot (g_{best} - x(t));$$
$$x(t+1) = x(t) + v(t+1). \qquad 3.14$$

were:

c_1 - self confidence factor : $c_1 < 2$

c_2 - swarm confidence factor : $c_2 < 2$

w - weight factor (ussualy decreases from 0.9 to 0.4)

Compared with BHBO, PSO need two "random kiks" in order to avoid entrapment. Position and velocities are updated at each time step. When a particle finds a position better that it has found previously it stores it. The difference between (p_{best}) and the individual current position is stochastically added to current velocity together with the difference between (g_{best}) and current position, thus making the algorithm to search the solution around these two points. Inertia weight factor – w is usually decreased linearly from 0.9 to 0.4 as time goes by to improve the convergence by a better space exploration at the beginning and better space exploitation at the end.

Although the above presented (classical) version of PSO was initially used, it was observed that the algorithm has a rather slow convergence rate in hyper-space, so a modified version that uses a constriction factor - k (eq. 3.15) as explained by Clerc in [3.24] has been used.

$$v(t+1) = k \cdot \left(v(t) + c_1 \cdot rand(0,1) \cdot \left(p_{best} - x(t) \right) + c_2 \cdot rand(0,1) \cdot \left(g_{best} - x(t) \right) \right). \quad (3.15)$$

$$k = \frac{2}{\left| 2 - \varphi - \sqrt{\varphi^2 - 4\varphi} \right|}, \quad \text{where } \varphi = c_1 + c_2, \quad \varphi > 4$$

φ was set to 4.1, which resulted in $k = 0.729$, while the acceleration factors were $c_1 = c_1 = 2.05$. This is equivalent to using (eq. 3.14) with $w = 0.729$ and $c_1=c_2=1.49445$, which respect the original constraints c_1 & $c_2 < 2$. Same steps: velocity update, position update and fitness calculation are done until and end criteria is met. Drastically improvements are observed using this modified version as shown in 3.2.5.

PSO can be compared to human social behavior since additional to behavior adjusting according to cognitive variables; humans tend to adjust their beliefs to conform to those of their social peers. Because PSO uses primitive mathematical operations is expected to be fast, though not that fast as BHBO (needs computation of speed also). Also compared to BHBO has parameters that need to be tuned and it uses more memory for position tracking of all particles.

3.3.5 Gravitational Search Algorithm

The gravity is one of the four fundamental forces in nature next to electromagnetic force, weak force and the strong nuclear force, and represents the tendency of masses to accelerate toward each other, according to Newton's second law of motion. The gravitational force between two objects is directly proportional to the product of their masses and gravitational constant and inversely proportional to the square of the distance between them. The actual value of gravitational constant has a decreasing effect, depending on the age of universe (eq. 3.16).

$$G(t) = G(t_0) \times \left(\frac{t_0}{t} \right)^\beta \quad \frac{m^3}{kg \cdot s^2}; \quad \beta < 1 \quad\quad\quad (3.16)$$

were:

$G(t_0)$ - value of the gravitational constant at the first quantum interval t_0

The GSA operates in an isolated system of masses, an artificial universe that obey Newton laws, and it is based on the law of gravity and mass interactions. The agents are a collection of masses which interact based on Newtonian law of gravity: "Every particle in the universe attracts every other particle with a force that is directly proportional to the product of their masses and inversely proportional to the

square of the distance between them" and the laws of motion. The mass of an agent represents their performance. A kind of cooperation between agents is achieved through gravitational field. The resultant force upon a mass is computed by vector summation of all forces exerted by rest of planets and is towards the heaviest masses (Fig.3.16.a). The heavier the mass the slower the agent moves so an exploitation of space around good solution is guaranteed. Since each mass represents a solution, the algorithm navigates by adjusting the gravitational and masses.
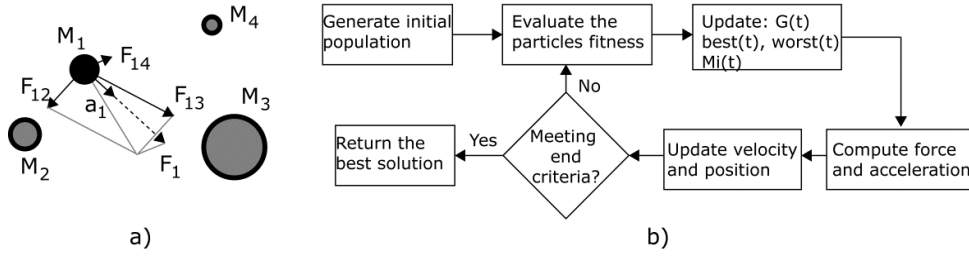
Fig.3.16. a) Force computation, b) GSA flowchart

GSA flowchart is shown in Fig.3.16.b while the code can be studied in Appendix 5. The first part is common to previous algorithms. After computing the current generation fitness value the mass of each agent $M_i(t)$(eq.3.18) is calculated.

$$m_i(t) = \frac{fit_i(t) - worst(t)}{best(t) - worst(t)} \tag{3.17}$$

were:

$$best(t) = \min_{j \in \{1,...,N\}} \left(fit_j(t) \right) - \text{for a minimization problem}$$

$$worst(t) = \max_{j \in \{1,...,N\}} \left(fit_j(t) \right) - \text{for a minimization problem}$$

$$M_i(t) = \frac{m_i(t)}{\sum_{j=1}^{P} m_j(t)} \tag{3.18}$$

The total force that acts on agent i in a dimension $d - F_i^d$ is the randomly weighted sum of the d components of the forces from the rest of the agents, giving a stochastic behavior of the algorithm. In order to compute the agent acceleration a_i (eq.3.22) the overall forces are computed first from eq.3.19.

$$F_i^d(t) = \sum_{j \in kbest, j \neq i} rand_j \cdot G(t) \cdot \frac{M_j(t) \cdot M_i(t)}{R_{ij}(t) + \varepsilon} \cdot \left(x_j^d(t) - x_i^d(t) \right); \tag{3.19}$$

$$G(t) = G_0 \cdot e^{-20\frac{iter}{iter_{Max}}} \tag{3.20}$$

$$R_{ij}(t) = \sqrt{\sum_{d=1}^{D} \left(x_i^d - x_j^d \right)^2} \tag{3.21}$$

were $G(t)$ (eq. 3.20) is the gravitational constant at time t, and R_{ij} (eq. 3.21) is the Euclidian distance between the agent i and j.

From the second law of motion results:

$$a_i^d(t) = \frac{F_i^d(t)}{M_i(t)} = \sum_{j \in kbest, j \neq i} rand_j \cdot G(t) \cdot \frac{M_j(t)}{R_{ij}(t) + \varepsilon}\left(x_j^d(t) - x_i^d(t)\right) \tag{3.22}$$

Agent masses are proportional to their fitness value. A heavier particle has bigger gravitational force and moves slowly through space, which is good since they are more probably to lie near the global minimum.

The new velocities $v_i^d(t+1)$ are computed as a fraction of old velocity $v_i^d(t)$ added to the acceleration $a_i^d(t)$.

$$v_i^d(t+1) = rand_i \times v_i^d(t) + a_i^d(t) \tag{3.23}$$

Finally the new position $x_i^d(t+1)$ is:

$$x_i^d(t+1) = x_i^d(t) + v_i^d(t+1) \tag{3.24}$$

GSA doesn't need to store information as PSO but it needs more computations.

3.3.6 Particle Swarm Optimization Gravitational Search Algorithm

PSO simulates the social behavior of birds while GSA is inspired by a physical phenomenon. The idea is to use the advantages of both algorithms, mainly the exploitation ability of PSO and exploration capability of GSA. Since this hybridization uses both of them simultaneously, in parallel, is called co-evolutionary algorithm and it combines the social thinking with the local search capability [19].
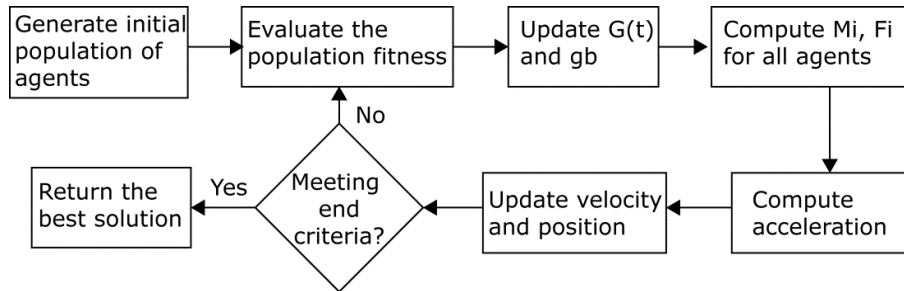
Fig.3.17. PSOGSA flowchart

The PSOGSA flowchart is shown in Fig.3.18. The MatLab code is presented in Appendix 6. The speed is computed after acceleration a_i is computed (through gravitational forces gravitational constant a priori calculation).

$$v_i(t+1) = w \cdot v_i(t) + c_1 \cdot rand(0,1) \cdot a_i(t) + c_2 \cdot rand(0,1) \cdot \left(g_{best} - x_i(t)\right);$$
$$x_i(t+1) = x_i(t) + v_i(t+1). \tag{3.24}$$
$$c_1 = 0.5; \quad c_2 = 1.5;$$

3.3.7 Optimization Algorithms performance evaluation

The performances of the above-presented algorithms are tested using well-defined benchmark functions (eq. 3.25-3.28) drawn for 2 variables in Fig.3.18. DeJong and Rosenbrock are unimodal (one optimum) while Ackley and Rastring are multimodal functions (many local optimum and one global optimum). All of them are usually restricted to hypercube under given limits, and they can be easily implemented for any dimension size through a few lines of code (Appendix 7).

$$f_{dejong} = \sum_{i=1}^{D} x_i^2; \quad -5.12 < x_i < 5.12 \tag{3.25}$$

$$f_{rosen} = \sum_{i=1}^{D} \left(100\left(x_{i+1} - x_i^2\right)^2 + \left(1 - x_i\right)^2\right); \quad -2.048 < x_i < 2.048 \tag{3.26}$$

$$f_{ackley} = -20\exp\left(-0.2\sqrt{\frac{1}{D}\sum_{i=1}^{D} x_i^2}\right) - \exp\left(\frac{1}{D}\sum_{i=1}^{D}\cos\left(2\pi x_i\right)\right) + 20 + e;$$
$$-32.768 < x_i < 32.768 \tag{3.27}$$

$$f_{rastring} = \sum_{i=1}^{D} \left(x_i^2 - 10\cos\left(2\pi x_i\right) + 10\right); \quad -5.12 < x_i < 5.12 \tag{3.28}$$
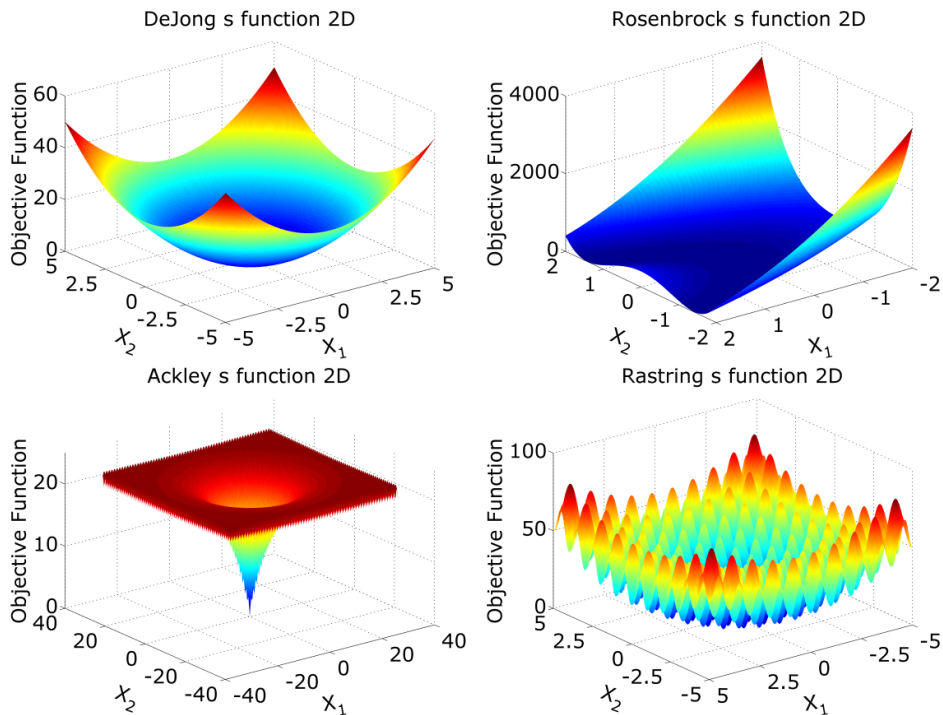
Fig.3.18. 2-variables benchmark test functions

The behavior analysis is done on a population of 100 particles ($P = 100$) that have 1000 iterations ($iter_{max} = 1000$) to find the best solution ($F(x) = 0$) in a 30-dimensional ($D = 30$) hyperspace. Since all algorithms are subject to stochastic behavior the results are averaged over 30 trials, so the computation time (Table 3.1) refers to 30.000 iterations.

Figures 3.19 – 3.22 presents the convergence behavior of the best averaged solution at each iteration -left part and of the population (average of the sum of all members' fitness values) –right part for each test function. PSO_O acronym stands for the original version of the PSO and has the slowest convergence rate from all candidates. Using the modified version of the PSO (PSO_M) with the above presented constriction factor not only that it brings a strong improvement in convergence, but it manage to finish the job in an acceptable time period (Table 3.1). Studying the population we see strong oscillations for BHBO, because of randomly generated stars at each time step. Also the lack of a "cooperation" process between individuals makes the group diverge from the optimal solution. The hybrid version PSOGSA seems to have the best group behavior.
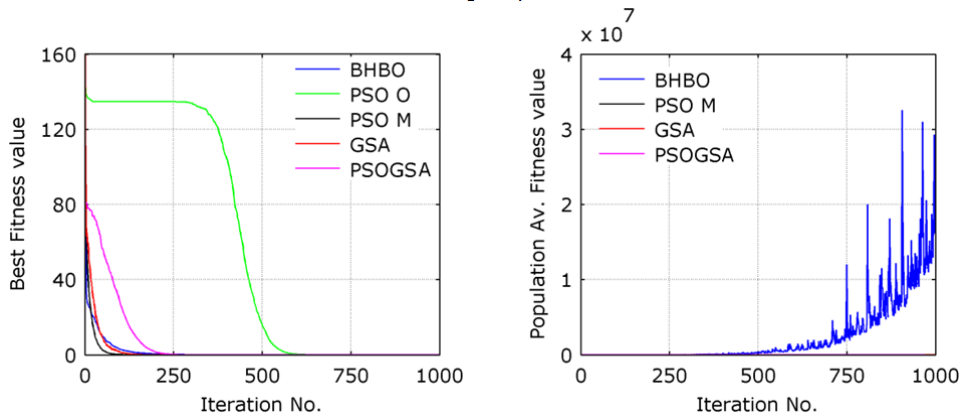
Fig.3.19. DeJong test results
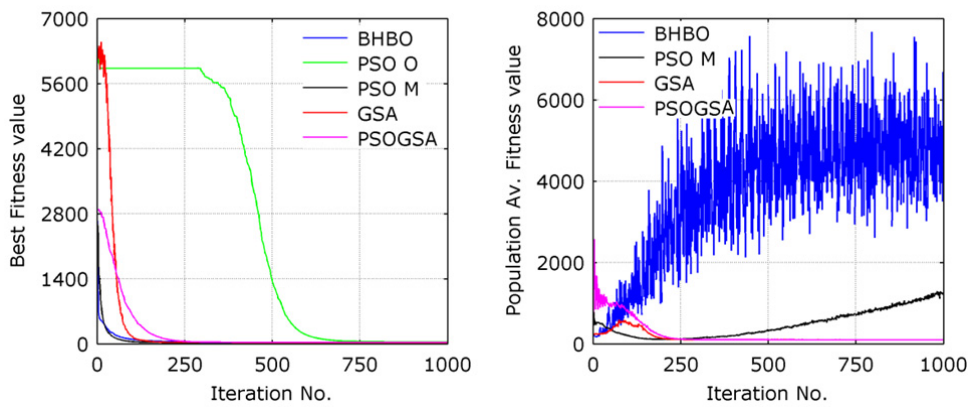
Fig.3.20. Rosenbrock test results
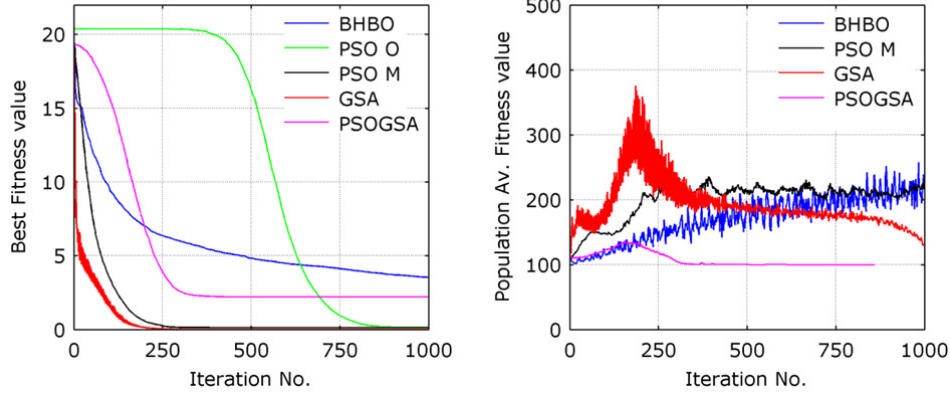
Fig.3.21. Ackley test results
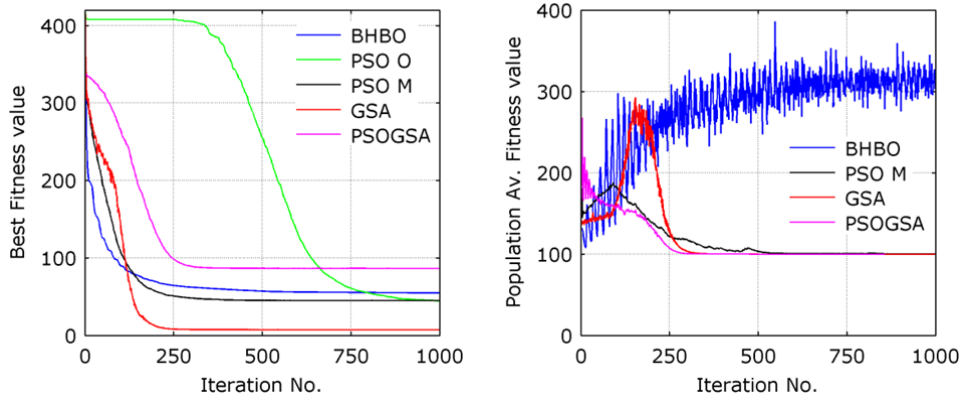
Fig.3.22. Rastring test results

Table.3.1. Performance evaluation

		DeJong	Rosenbrock	Ackley	Rastring
BHBO	Time [s]	19.4	41.5	25.5	25.2
	Best Fitting Val.	$9.5 \cdot 10^{-6}$	26.2	1.65	28.87
PSO_O	Time [s]	21.8	43.1	25.9	25.1
	Best Fitting Val.	$6.3 \cdot 10^{-16}$	12.4	$9.3 \cdot 10^{-7}$	24.9
PSO_M	Time [s]	25.5	45.1	27.51	28.8
	Best Fitting Val.	$2.5 \cdot 10^{-27}$	12.5	$9.5 \cdot 10^{-13}$	19.8
GSA	Time [s]	897.2	953.4	902.9	899.2
	Best Fitting Val.	$1.5 \cdot 10^{-18}$	25.7	$1.1 \cdot 10^{-9}$	3.97
PSOGSA	Time [s]	926.8	933	948	927.7
	Best Fitting Val.	$4.8 \cdot 10^{-8}$	15.4	0.037	41

      The results are summarized in Table 3.1. GSA and PSOGSA are abandoned due to high computation time compared to BHBO and PSO (O and M). BHBO is also rejected due to population instability. Even if we neglect all these it is obvious that

the best value for all test cases is obtained by PSO_M at reasonable computation time cost (slightly slower that BHBO or PSO_O).

Based on all these the modified version of the PSO was used for BLDC-MRM optimization. This is consistent with Occam's razor (the simplest algorithm has the highest probability to obtain the best results).

3.4 BLDC–MRM optimization

3.4.1 Optimization variables, constraints and objective function

First step consist of optimization variables selection, based on which all machine candidates are evaluated. The variables are grouped in vector $\overline{X}$, which is fed to optimization algorithm. These variables have the greatest impact on the final design. Various ratios for magnetic flux paths (such as $bzP\tau_S$) were used as optimization variables and the values of magnetic flux density in those regions were computed based on air-gap magnetic flux density value.

$$\overline{X} = \left[f_{\tan}, \ B_{ag}, \ j_S, \ \lambda, \ bzP\tau_S, \ sMs, \ shyP\tau_P, \ bzrP\tau_R, \ hag_q, \ hag, \ rhyP\tau_P \right]$$

f_{tan} – tangential force [N/cm^2], B_{ag} – air-gap magnetic flux density [T], j_S – slot current density [A/mm^2], λ - form factor (machine length/polar step), $bzP\tau_S$ - tooth width per slot pitch ratio, sMs – stator slot width, $shyP\tau_P$ - stator yoke height per polar step, $bzrP\tau_R$ - rotor tooth width per rotor slot pitch, hag_q – q axis air-gap length, hag – air-gap length, $rhyP\tau_P$ - rotor yoke height per polar pitch.

The optimal machine is searched by a population of 100 particles through a time period of 50 iterations in a hypercube whose boundaries are imposed by the machine designer ($\overline{X}_{\min} < \overline{X} < \overline{X}_{\max}$):

$$\overline{X}_{\min} = \left[0.5, \ 0.4, \ 2, \ 0.6, \ 0.3, \ 1, \ 0.25, \ 0.35, \ 5, \ 0.35, \ 0.3 \right].$$

$$\overline{X}_{\max} = \left[3, \ 1, \ 10, \ 2.4, \ 0.7, \ 3, \ 0.7, \ 0.65, \ 20, \ 1.2, \ 0.7 \right].$$

After speed computation and position update of each particle the new position is rounded according to $\overline{X}_r$, imposed by the designer, according to technological constraints and realistic variation.

$$\overline{X}_r = \left[0.05, \ 0.01, \ 0.1, \ 0.1, \ 0.05, \ 0.1, \ 0.1, \ 0.05, \ 1, \ 0.05, \ 0.1 \right].$$

Second step consist of setting the population size (P = 100) and the maximum number of steps ($Iter_{max}$ = 50). All the initial particles positions are stochastically initialized and memorized by $\overline{X}_i$.

$$for \quad i = 1 : P$$
$$\overline{X}_i = round \left(\overline{X}_{\min} + rand(0,1) \cdot \left(\overline{X}_{\max} - \overline{X}_{\min} \right), \overline{X}_r \right). \tag{3.29}$$
$$end$$

For a better convergence the first computed analytically design (outside of the optimization routine) is added to this vector, through the initial values $\overline{X}_{init}$.

$$\overline{X}_{init} = [1.9, \ 0.65, \ 5.5, \ 1, \ 0.6, \ 2, \ 0.33, \ 0.55, \ 10, \ 0.4, \ 0.7]; .$$

The algorithm flowchart is the one presented in 3.3.4. Since this optimal design is for automotive propulsion (50kW at a base speed equal to 3000 rpm), the challenge is a reduced mass and volume, with high efficiency. The goal of this design is to find a cheap and highly efficient electric motor. Although they seem opposite, an optimum between them exist in the search space.

The objective function is represented by the total cost (t_{cost}) (eq.3.30) which is a sum of active material cost (m_{cost}), energy cost (e_{cost}) and penalty costs (Pen_{cost}). A penalty is used for every criterion that is not fulfilled. If the penalties coefficients are carefully chosen, the requirements will be achieved in the end.

$$t_{\text{cost}} = m_{\text{cost}} + e_{\text{cost}} + Pen_{\text{cost}} \tag{3.30}$$

Active material cost m_{cost} depends on copper, lamination and shaft mass plus the cost of passive materials which depends on the machine total mass (eq.3.31).

$$m_{\text{cost}} = Copper_{\text{cost}} + Lam_{\text{cost}} + Shaft_{\text{cost}} + PasM_{\text{cost}} \tag{3.31}$$

Energy cost is computed based on developed power. This is important since a low efficiency motor will have high losses that will be paid by the final customer. If the computed efficiency is smaller than the minimum one the final cost of the machine increases (eq. 3.31).

if $\eta_N < \eta_{\min}$

$$e_{\text{cost}} = e_{price} \cdot P_N \cdot \left(\frac{1}{\eta_N} - \frac{1}{\eta_{\min}} \right) \cdot hpy \cdot ny; \tag{3.32}$$

else

$$e_{\text{cost}} = e_{price} \cdot P_N \cdot \left(\frac{1}{\eta_N} - 1 \right) \cdot hpy \cdot ny; \tag{3.33}$$

end

In the above equations e_{price} is the energy price (0.5 \$/kW), *hpy* means hours per year 720h (2 h/day) and *ny* represents the number of years (15).

Penalties cost is a sum of over temperature cost ($Temp_{cost}$) and power cost (Pow_{cost}).

$$Pen_{\text{cost}} = Temp_{\text{cost}} + Pow_{\text{cost}} \tag{3.34}$$

Thermal verification is probably the most important step, since every 10°C increase of winding temperature, decreases the live of the machine by half , thus it's mandatory to integrate this part in penalty function. In order to compute temperature cost we first calculate winding temperature T_w using electrical losses (p_{co} and p_{fe}), ambient temperature T_a, machine cooling area A_c and thermal coefficient a_1.

$$T_w = \frac{p_{cop} + p_{fe}}{a_1 \cdot A_c} + T_a;$$

(3.35)

were:

$$a_1 = 50 \frac{W}{m^2 \cdot °C}; \quad 15 < a_1 < 100 \quad \text{and } T_a = 40 \text{ }°C;$$

Finally the temperature cost is computed.

$$Temp_{cost} = \max\left(0,(T_w - T_m)\cdot m_{cost}\right)$$

(3.36)

At base speed the machine must provide the minimum power of 50 kW. If it can't provide the requested torque an additional cost is added according to eq. 3.37.

$$if \quad P_N < P_{min}$$
$$Pow_{cost} = 2 \cdot (P_{min} - P_N) \cdot m_{cost};$$

(3.37)

end

By using a more complex numerical model (dynamic MEC or static FEA if the time permits), more objectives can be imposed.

3.4.2 Optimization results

The results taken from the best particle of the swarm are plotted in Fig. 3.23-3.30. The optimization process was written using MatLab programming tool and took about 20000 s to check the 5000 machines (50 iterations x 100 particles) on a 2.2 GHz, Intel i5 processor.

The objective function has an exponential decreasing tendency from initial cost of 680 $ to the optimal one 250 $ (Fig. 3.23).Evolution of the tangential force and air-gap magnetic flux density is presented in (Fig.3.24). In Fig. 3.25 we can observe how the machine is searching for best ratios, while in Fig. 3.26 slot opening and air-gap are shown for each iteration. The slot current density and the air-gap height in the *q*-axis for the best solution at each iteration is plotted is Fig. 3. 27. The PSO algorithm searches the best efficiency (Fig. 3.28) through the modification of electrical losses (Fig. 3.29). Finally the active material mass drops from 40 kg to half after 50 steps (Fig.3.30).
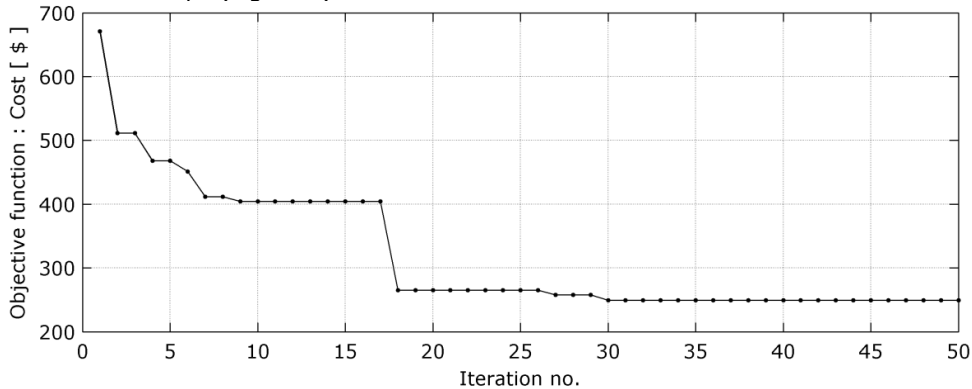
Fig.3.23. Fitting function evolution
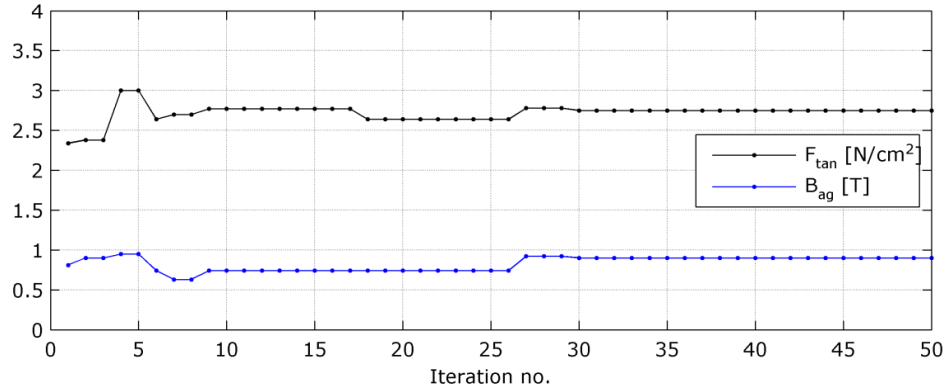
Fig.3.24. Tangential force and air-gap magnetic flux density evolution
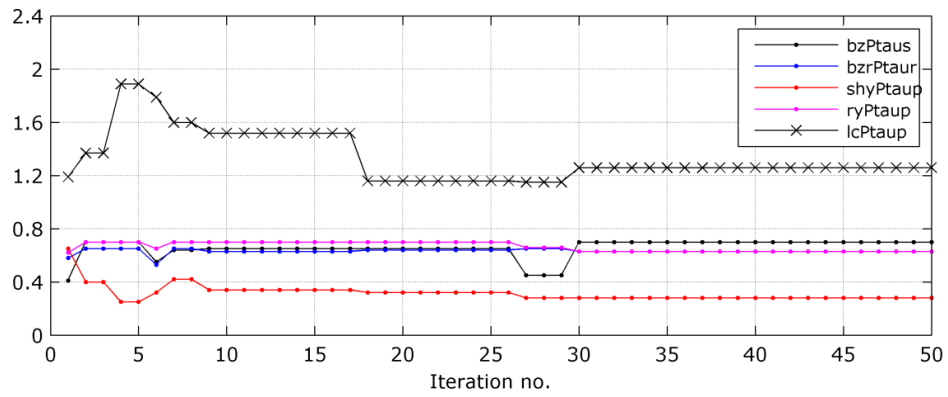
Fig.3.25. Main machine ratios evolution
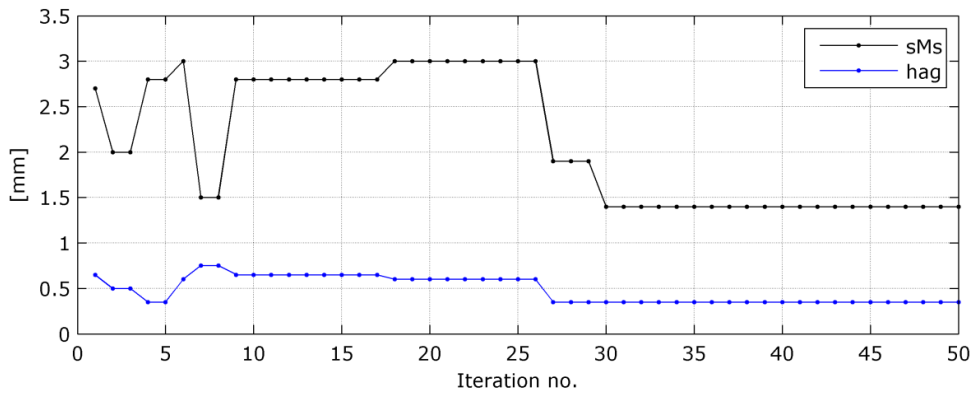
Fig.3.26. Slot opening and air-gap length evolution
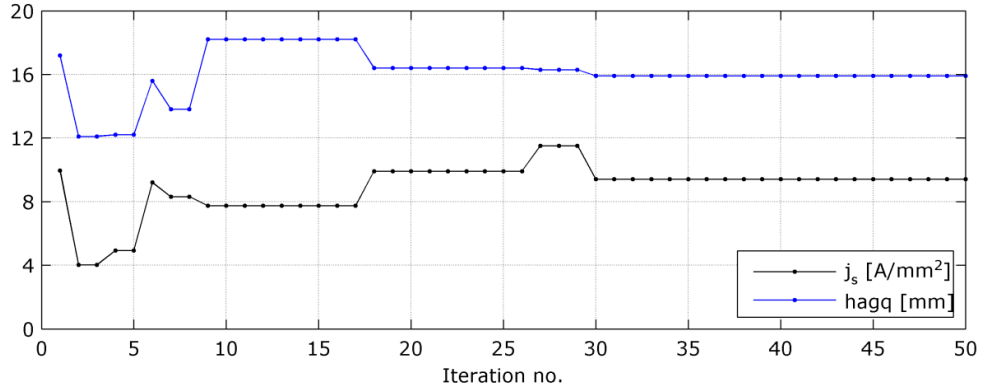
Fig.3.27. Slot current density and q-axis depth evolution
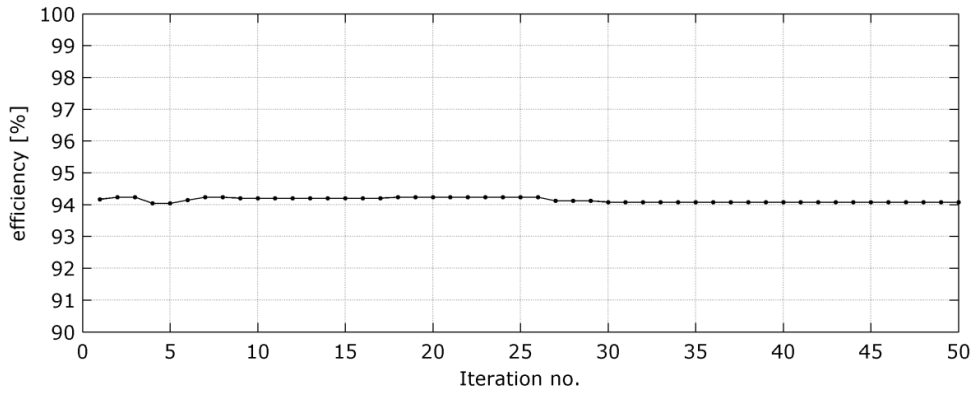
Fig.3.28. Efficiency evolution
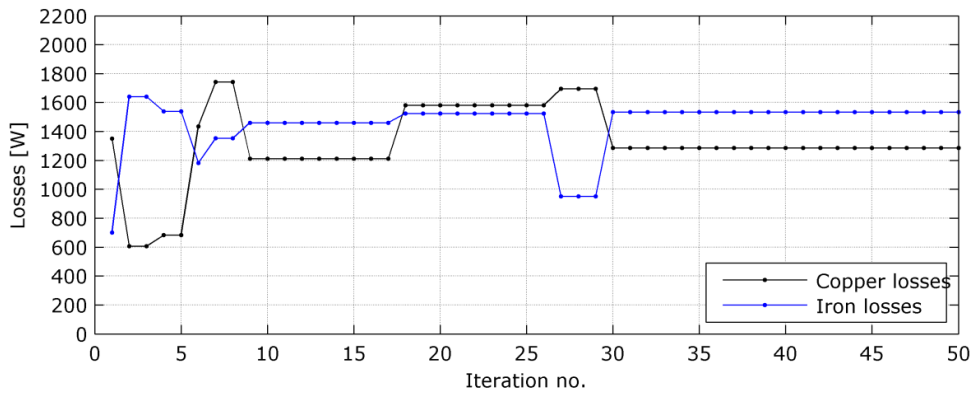
Fig.3.29. Copper and iron losses evolution
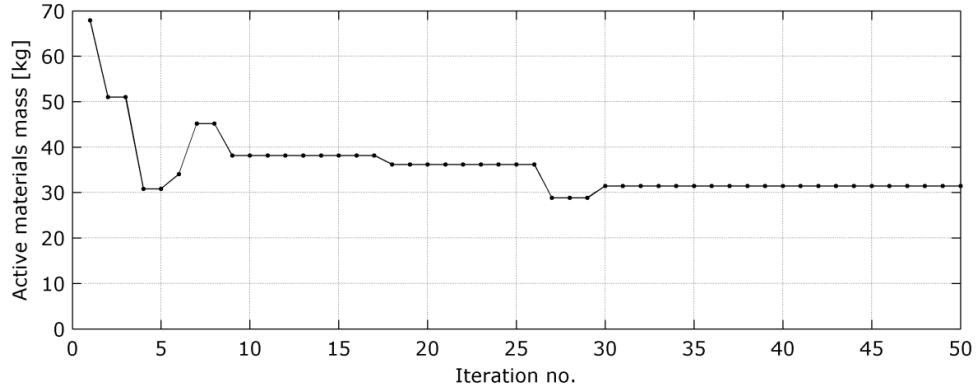
Fig.3.30. Active materials cost evolution
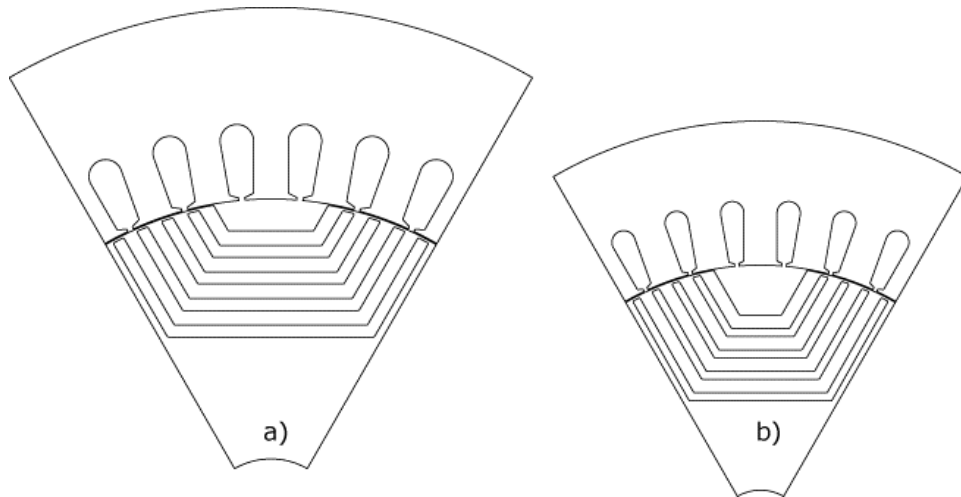
Fig.3.31. Initial BLDC-MRM and optimal

A comparison between first motor prototype (Fig.3.31.a) and optimal motor (Fig. 3.31.b) found by the algorithm is presented in Table 3.2. The objective is achieved by increasing tangential force, air-gap magnetic flux density and slot current density. A 94 % efficiency is achieved (within the constraints limits), while the active material mass is decreased by 35 % (with a 36 % reduction of motor volume).

Table.3.2. Performance evaluation

Variable name	Variable [unit]	Initial	Optimal
Tangential force	f_{tan} [N/cm²]	1.9	2.75
Air-gap magnetic flux density	B_{ag} [T]	0.65	0.9
Slot current density	j_s [A/mm²]	5.5	9.4
Form factor	λ	1	1.26
Stator tooth ratio	bzPtaus	0.6	0.7
Stator slot opening	sMs	2	1.4
Stator yoke ratio	shyPtaup	0.33	0.28
Rotor tooth ratio	bzrPtaur	0.55	0.63
q-axis air-gap depth	hagq	10	15.9
d-axis air-gap depth	hag	0.4	0.35
Rotor yoke ratio	rhyPtaup	0.7	0.63
Computed performances			
Active material mass	m [kg]	47.69	31.45
Efficiency	η [%]	94.6	94.1
Average Torque	Te [Nm]	168	163
Secondary dimensions			
Stator inner diameter	sDi [mm]	217	177
Stator outer diameter	sDo [mm]	342	271
Core length	Lc [mm]	120	123.1
Rotor inner diameter	rDi [mm]	47	30
Rotor outer diameter	rDo [mm]	216.2	176.3
Stator tooth width	bz [mm]	11.3	10.8
Rotor tooth width	bzr [mm]	4.8	4.4
Slot height	shOA[mm]	24.8	21.17
Turns per coil	sb	31	27

Conclusion

The present Chapter was focused on machine performances computation through a non-linear numerical model based on magnetic equivalent circuits and node potential equations.

Choosing a suitable optimization stochastic algorithm, based on benchmark test results was the second step. After the algorithm selection, the optimal design code was written and the search of a machine that respected the imposed constraints under a minimum cost was search. Although the efficiency didn't improve substantially the active material mass was decreased to twice its initial value.

Future work is needed to investigate the possibility to improve the MEC model, in order to be able to compute also the torque pulsations, keeping the same amount of reasonable computation time, which could become another constraint in the final optimization code if the application requires it.

References

[3.1] A.D. Wissner-Gross and C.E. Freer, "*Causal Entropic Forces*", Pysical Review Letters, PRL-110, 2013

[3.2] S. Furber, *"To build a brain",* IEEE Spectrum, vol. 49, no.8, 2012, pp. 44-49

[3.3] V. Gradinaru, L.N. Tutelea and I. Boldea, *"Hybrid Analytical/FEM Optimization Design for SPMSM for Refrigerator Compressor Loads",* Proceeding of ACEMP, 2011 IEEE, pp. 657-662

[3.4] V. Ostovic, "*A Novel Method for Evaluation of Transient States in Saturated Electric Machines*", IEEE Trans. On Industry Applications, Vol. IA-25, No. 1, 1989, pp.96-101

[3.5] J.D. Law, T.J. Buch and T.A. Lipo, *"Magnetic Circuit Modeling of the Field Regulated Reluctance Machine Part 1: Model Development",* IEEE Trans. Energy Conversion, Vol. EC-11, No.1, 1996, pp. 49-55

[3.6] T.J. Buch, J.D. Law and T.A. Lipo, *"Magnetic Circuit Modeling of the Field Regulated Reluctance Machine Part 2: Saturation Modeling and Results",* IEEE, Trans. On Energy Conversion, Vol EC-11, no. 1, 1996, pp. 56-62

[3.7] V. Ostovic, " *Dynamics of saturated machines",* Springer-Verlag, New York, 1989

[3.8] V. Ostovic, " *A Simplified Approach to Magnetic Equivalent-Circuit Modeling of Induction Machines ",* IEEE Trans. On Industry Applications, Vol. IA-24, No.2, 1988, pp.308-317

[3.9] I. Boldea and L.N. Tutelea, *"Electric Machines – Steady state, Transients and Design with Matlab",* CRC Press, Taylor&Francis Group, 2010

[3.10] S. Agarlita, D. Ursu, L.N. Tutelea, I. Boldea and B. Fahimi *"BLDC Multiphase Reluctance Machines: a Revival Attempt with 2D FEM Investigation and Standstill Tests",* Energy Conversion Congress and Exposition (ECCE), 2013 IEEE, pp. 1850 – 1857

[3.11] R.L. Haupt and S.E. Haupt, *"Practical Genetic Algorithms",* second ed., John Wiley & Sons, 2004.

[3.12] D.S. Johnson, C.R. Aragon, L.A. McGeoch, C. Schevon, *"Optimization by Simulated Annealing. An experimental evaluation. Part I. Graph partitioning,"* Operations Research 37 (1989) 865–892.

[3.13] H. Shah_Hosseini, *"Problem solving by intelligent water drops",* IEEE Congress on Evolutionary Computation, CEC 2007, pp. 3226–3231.

[3.14] X.Z. Gao, X. Wang, K. Zenger, Xiaofeng Wang and J. Zhang, *"Harmony Search method-based multi-modal optimal design of a wind generator"* Industrial Electronics Society, IECON 2013 - 39th Annual Conference of the IEEE, pp. 2887-2892

[3.15] O.K. Erol and I. Eksin, "*A new optimization method: Big Bang-Big Crunch",* Elsevier, Advances in Engineering Software no. 37, 2006, pp. 106-111

[3.16] A. Hatamlou, *"Black hole, a new heuristic optimization approach for data clustering"* Inf. Sci., vol. 222, pp. 175–184, 2013.

[3.17] J. Kennedy and RC. Eberhart*, "Particle swarm optimization",* Proceedings of IEEE international conference on neural networks, vol. 4, 1995, pp. 1942–1948.

[3.18] E. Rashedi, S. Nezamabadi, and S. Saryazdi, *"GSA: A Gravitational Search Algorithm"*, Information Sciences, vol. 179, no. 13, pp. 2232-2248, 2009

[3.19] A. Hatamlou, S. Abdullah and Z. Othman*,"Gravitational Search Algorithm with Heuristic Search for Clustering Problems"*, 3rd Conference on Data Mining and Optimization (DMO), 2011 IEEE, pp 190-193

[3.20] M.M. Millonas, *"Swarm, Phase Transitions, and Collective Intelligene, Artificial life III"*, Addison Wesley, Reading, MA 1994

[3.21] R.P. Feynman, "*Lectures on Physics",* Addison Wesley Longman, 1970

[3.22] W. Heisenberg, "*Über den anschaulichen Inhalt der quantentheoretischen Kinematik und Mechanik*", Zeitschrift für Physik, 43 1927, pp. 172-198. English translation: J. A. Wheeler and H. Zurek, Quantum Theory and Measurement Princeton Univ. Press, 1983, pp. 62-84.

[3.23] S. W. Hawking, *"Particle creation by black holes"*, Communications in mathematical physics, Vol. 43, no. 3, 1975, pp. 199-220

[3.24] M. Clerc and J. Kennedy, *"The particle swarm - explosion, stability, and convergence in a multidimemional complex space,"* IEEE Trans. Evolutionary Computation, vol. 6, issue 1, 2002, pp. 58-73.

4. BLDC-MRM circuit modeling for transients and control

"A simulation model should be as simple as possible, but no simpler is the key to a successful simulation."

Abstract

This chapter focuses on developing of a dynamic model for the BLDC-MRM. Experimental identification of electrical and mechanical parameters is done on the 6 phase, 6 poles (35 Nm of torque, ALA rotor) BLDC-MRM, for an accurate modeling of machine behavior in MatLab/Simulink environment.

The speed control scheme is developed and implemented based on machine phase coordinates model and stator reference frame current regulators.

4.1 Introduction

Electric drive complexity requires accurate determination of all machine parameters (electrical, thermal and mechanical), who eventually dictates the machine behavior in all regimes. The most important parameters, from a transient state point of view, are the machine inductances and the moment of inertia. They are also the trickiest to find. Two methods are presented and employed: flux decay test [4.1] and run-out test [4.2].

Flux-decay test is used in order to find the machine inductances variation with rotor position by voltage and current recording when the phase power source is cut-off. An accurate data acquisition system is needed as well as precise measurement of phase resistance and initial conduction current.

The run-out test implies acceleration of the drive to the rated speed. The drive power is switched-off and the plant will be decelerated by loss torque while the speed is saved as a function of time $n(t)$. Based on $n(t)$ first derivative value, the moment of inertia can be computed from Newton second law of motion.

The machine model (based on Kirchoff's laws) and the control strategy are built based on machine parameters [4.3]. Due to a non-sinusoidal flux distribution, the phase coordinate mathematical model is more suitable than the dq model [4.4, 4.5] for simulation purpose.

Besides the machine circuit model, the multiphase inverter and controllers must also be built. The inverter could be full bridge (as we will use for the 5 phase machine testing) or with reduced number of switches (used by us for 6 phase machine testing). This way a wider view on the BLDC-MRM, from a drive point of view, is gained. This chapter presents only the second type inverter mode, with PI current controllers and a slightly more complicated control strategy compared to the first one. For the full bridge inverter the model is much simpler, since each phase has its own full bridge inverter, which can be modeled by two levels, hysteresis (bang-bang) current controllers.

4.2 Flux decay test

4.2.1 Introduction

To study the transient behavior of the machine it is necessary to solve the complete set of voltage equations taking into account the variations of the inductances and mutual inductances with time and space. The inductances are found by the flux decay analysis.

Flux decay test involves reading the decaying current and voltage in a circuit whose DC source has been interrupted. One inverter leg (upper switch and the lower fly-back diode) were used for this purpose. By summing up the area of the decaying current multiplied by the circuit resistance (R) and the diode voltage area, and dividing the result to the initial conduction current (I_{cond}), one could find out the total inductance of the circuit - L (eq. 4.1). The integral is done from the moment the transistor is blocked until the voltage and the current become 2% of their initial values.

$$L = \frac{R \cdot \int_{t_{off}}^{t,i=0} i(t)dt + \int_{t_{off}}^{t,Vd=0} V_D(t)dt}{I_{cond}} \qquad (4.1)$$

where: R is the circuit resistance (computed at the beginning of every test, due to resistance variation with temperature), $i(t)$ represents the instantaneous value of current and $V_D(t)$ the instantaneous value of the diode voltage.

4.2.2 Inductances identification

Figure 4.1 presents the electrical diagram for one phase current decay test (R and L represent the parameters of one phase). This will yield to self-inductance L_{aa} and (by reading the induced *emfs* in the remaining 5 phases) mutual inductances L_{ba}, L_{ca}, L_{da}, L_{ea}, L_{fa} versus rotor position from Fig.4.2, which shows acceptable agreement with 2D-FEA results. This result validates again the 2D-FEA model of the BLDC-MRM. By using proper magnetization curves for steel materials and knowing accurate enough machine dimensions the flux decay test can be successfully replaced by FEA in early stages of design and dynamic control strategies simulations.
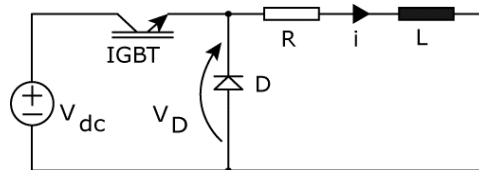
Fig.4.1. Electrical diagram for self and mutual inductances identification
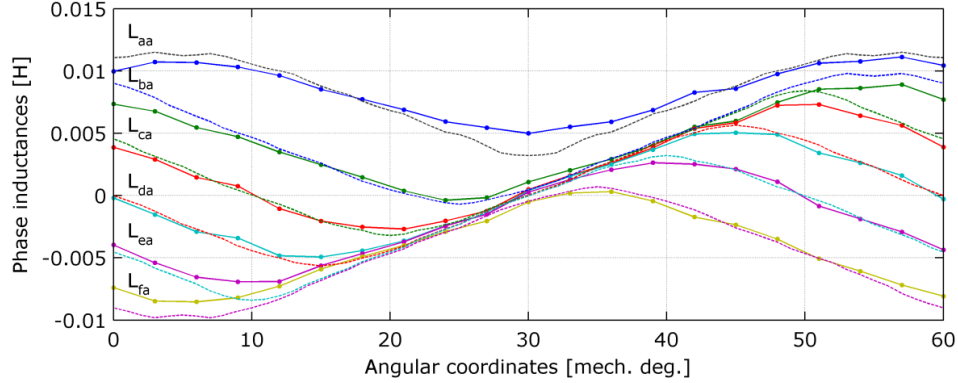
Fig.4.2. Self and mutual inductances of the BLDC-MRM phase *a*, at rated current (I = 12 A):
continuous line – experiment, dotted line - 2D-FEA

Taking advantage of the machine symmetry, only phase *a* inductances must be curve fitted using a Fast Fourier Transform (F.F.T.) routine (MatLab implemented) and cosine functions (eq. 4.2). The other phases are reconstructed from the first one, since the winding is symmetrical, as we can observe from phase *b* inductance reconstruction (eq. 4.3). The other phases (*c*, *d*, *e* and *f*) follow a similar pattern.

The curve fitting process was employed on experimental results data, but it can also be applied on FEA results with the advantage that the total time starting with machine design (based on given data), phase inductances computation (from FEA results), (F.F.T. based) curve fitting and inductance matrix assembly for dynamic control simulation is reduced to a matter of minutes (on a modern CPU), since all these are part of a MatLab script connected to the FEA software.

F.F.T. analysis is used to give for each (self and mutual) phase inductance the average (L_{xx_0}) and amplitude value (L_{xx_2}) for the first harmonic of the inductance waveform (function of twice the electrical rotor angular displacement - $2 \cdot \theta_{er}$). They were found to be: L_{aa_0}=0.0077 H , L_{ba_0}=0.0041 H , L_{ca_0}=0.0021 H , L_{da_0}=0 H , L_{ea_0}=-0.0021 H , L_{fa_0}=-0.0041 H , L_{aa_2}=0.025 H , L_{ba_2}= 0.035 H, L_{ca_2}= 0.045 H , L_{da_2}=0.039 H , L_{ea_2}=0.039 H , L_{fa_2}= 0.039 H.

A comparison between 2D-FEA and reconstructed inductances (Fig. 4.3) make us conclude that using just the second harmonic term in cosine function ($2 \cdot \theta_{er}$) is enough for an accurate inductance estimation of the BLDC-MRM.

The global matrix of inductances [$L(\theta_{er})$] (eq. 4.4) is used in the dynamic model for flux computation while a derivative version is used for electromagnetic torque computation.

$$L_{aa} = L_{aa\_0} + L_{aa\_2} \cdot \cos(2 \cdot \theta_{er});$$
$$L_{ba} = L_{ba\_0} + L_{ba\_2} \cdot \cos(2 \cdot \theta_{er} - \pi/6);$$
$$L_{ca} = L_{ca\_0} + L_{ca\_2} \cdot \cos(2 \cdot \theta_{er} - 2 \cdot \pi/6);$$
$$L_{da} = L_{da\_0} + L_{da\_2} \cdot \cos(2 \cdot \theta_{er} - 3 \cdot \pi/6);$$
$$L_{ea} = L_{ea\_0} + L_{ea\_2} \cdot \cos(2 \cdot \theta_{er} - 4 \cdot \pi/6);$$
$$L_{fa} = L_{fa\_0} + L_{fa\_2} \cdot \cos(2 \cdot \theta_{er} - 5 \cdot \pi/6);$$

(4.2)

$$L_{bb} = L_{bb\_0} + L_{bb\_2} \cdot \cos(2 \cdot \theta_{er} - \pi / 6); \qquad L_{bb\_0,(2)} = L_{aa\_0,(2)};$$

$$L_{cb} = L_{cb\_0} + L_{cb\_2} \cdot \cos(2 \cdot \theta_{er} - \pi / 6 - 2 \cdot \pi / 6); \qquad L_{cb\_0,(2)} = L_{ba\_0,(2)};$$

$$L_{db} = L_{db\_0} + L_{db\_2} \cdot \cos(2 \cdot \theta_{er} - 2 \cdot \pi / 6 - 2 \cdot \pi / 6); \qquad L_{db\_0,(2)} = L_{ca\_0,(2)}; \qquad (4.3)$$

$$L_{eb} = L_{eb\_0} + L_{eb\_2} \cdot \cos(2 \cdot \theta_{er} - 3 \cdot \pi / 6 - 2 \cdot \pi / 6); \qquad L_{eb\_0,(2)} = L_{da\_0,(2)};$$

$$L_{fb} = L_{fb\_0} + L_{fb\_2} \cdot \cos(2 \cdot \theta_{er} - 4 \cdot \pi / 6 - 2 \cdot \pi / 6); \qquad L_{fb\_0,(2)} = L_{ea\_0,(2)};$$

$$L_{ab} = L_{ba};$$

$$\left[L(\theta_{er}) \right] = \begin{bmatrix} L_{aa} & L_{ab} & L_{ac} & L_{ad} & L_{ae} & L_{af} \\ L_{ba} & L_{bb} & L_{bc} & L_{bd} & L_{be} & L_{bf} \\ L_{ca} & L_{cb} & L_{cc} & L_{cd} & L_{ce} & L_{cf} \\ L_{da} & L_{db} & L_{dc} & L_{dd} & L_{de} & L_{df} \\ L_{ea} & L_{eb} & L_{ec} & L_{ed} & L_{ee} & L_{ef} \\ L_{fa} & L_{fb} & L_{fc} & L_{fd} & L_{fe} & L_{ff} \end{bmatrix}; \qquad (4.4)$$
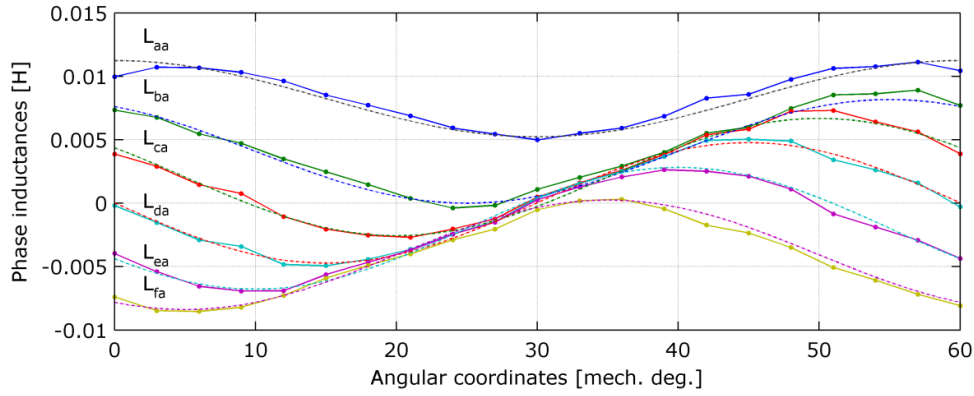
Fig.4.3. Self and mutual inductances of the BLDC-MRM phase *a*: continuous line – 2D-FEA, dotted line - curved fitted

4.2.3 Extended flux decay test

By connecting 4 adjacent phases in series, and the remaining two also in series, we obtain an equivalent 2 quadrature windings, an equivalent *dq* – winding configuration. One of the winding is producing the field (through field current I_f) and the other one is responsible for torque production (through torque current I_t).

The machine control is based on the idea that the speed controller provides the reference torque current value, while the field current value decreases linearly above the base speed, imposing a field weakening operation.

Since one of the initial statements of the BLDC-MRM principle of operation was an inherently decoupled control of field and torque current, this is tested next using the electrical diagram from Fig. 4.4. The coupling between the two magnetic axes is tested in a maximum torque position. For clarity in representation the experimental results and finite element results are plotted on separate graphs for all cases.

Studying Fig. 4.5-4.6 we can see negligible saturation is present at rated current; also a good agreement between experiment and numerical analysis is obvious. A slight coupling exists between the two magnetic axes, due to iron local saturation. The large value of q-axis air-gap makes the q-axis flux variation respect to q-axis current, linear (Fig. 4.7-4.8).
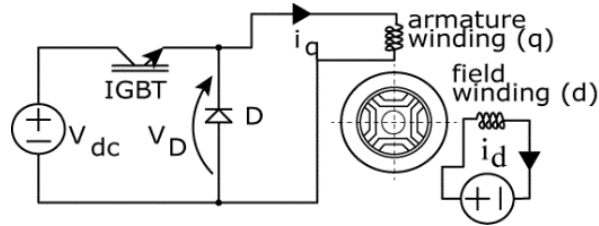
Fig.4.4. Electrical diagram for the equivalent two phase machine
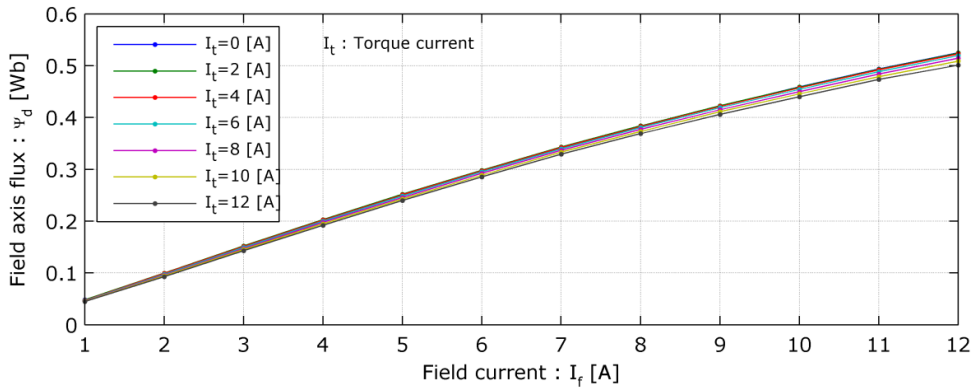
Fig.4.5. Experimental d-axis flux vs. d-axis current at different values of torque current
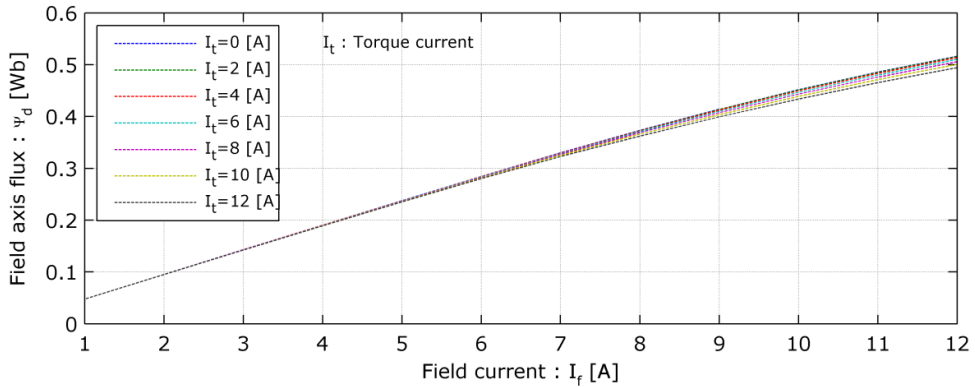
Fig.4.6. 2D-FEA d-axis flux vs. d-axis current at different values of torque current
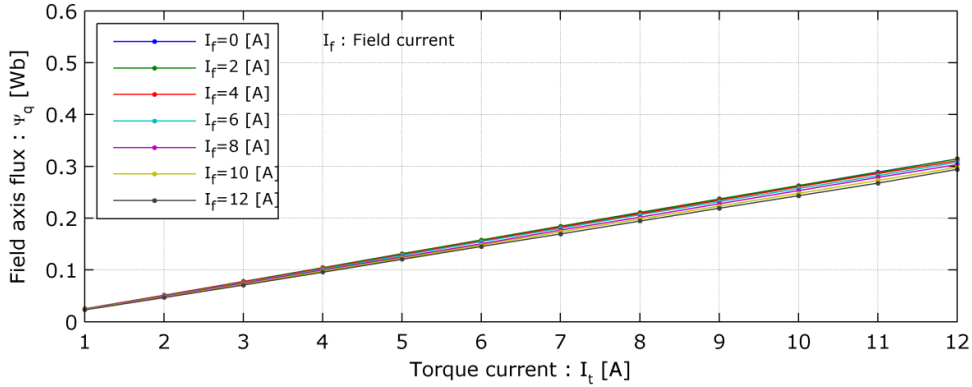
Fig.4.7. Experimental q-axis flux vs. q-axis (torque) current at different values of field current
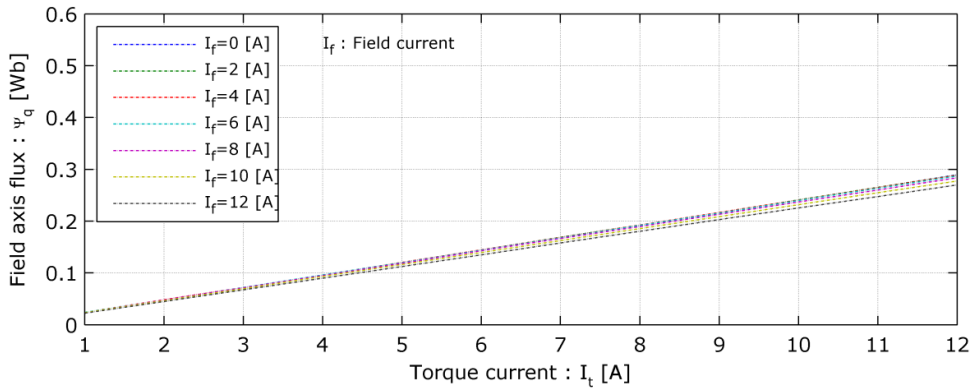
Fig.4.8. 2D-FEA q-axis flux vs. q-axis (torque) current at different values of field current
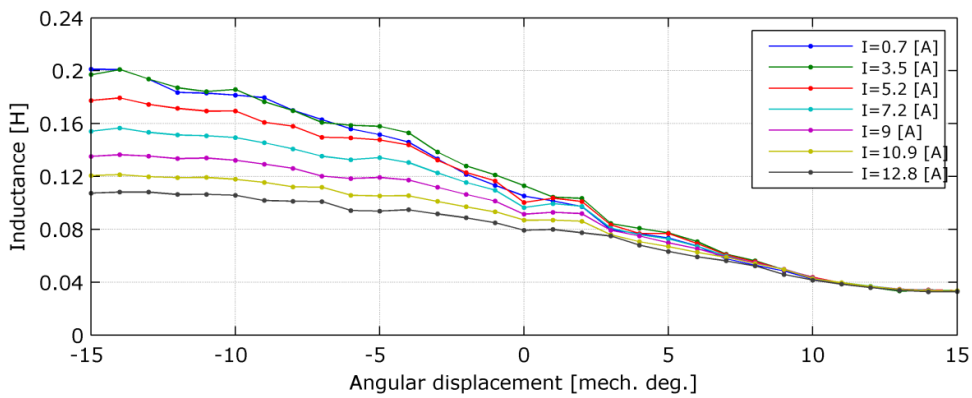
Fig.4.9. Experimental inductance for a series connection of all phases
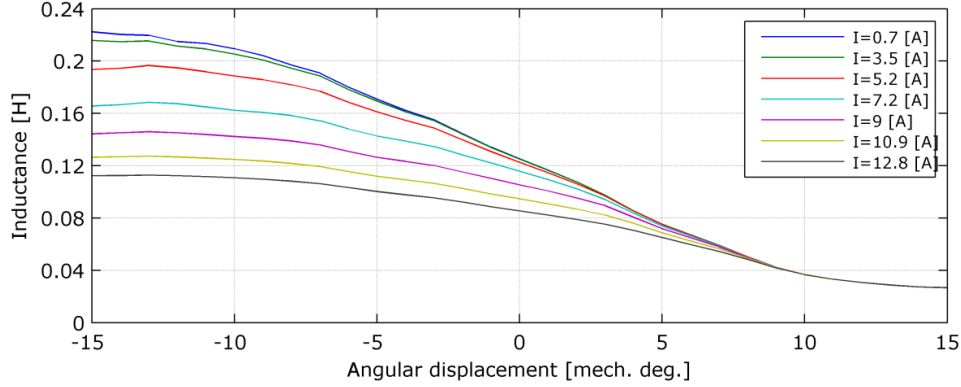
Fig.4.10. 2D-FEA inductance for a series connection of all phases

By connecting all phases in series, we get and equivalent series DC machine. This configuration was tested in [4.3]. For all phases in series current decay test **R** and **L** parameters from Fig. 4.1 represent the resistance and inductance of all phases connected in series. This simulates the series connection of a DC current machine. Experimental and finite element results can be studied in Fig. 4.9-4.10.

4.3 Run-out test

According to Newton second law of motion (eq. 4.5) total force exerted on a body is connected to object acceleration through its mass. For rotational bodies, mass, velocity and force from eq. 4.5 are replaced by moment of inertia J_m, angular speed Ω_r and torque (eq. 4.6). Drive transient behavior is strongly connected with the moment of inertia J_m through this law.

$$\frac{d\bar{p}}{dt} = \bar{F}; \ \bar{p} = m\bar{v}; \ \text{for velocities smaller than the speed of light}\left(\rightarrow \ \text{m=cst.}\right)$$

$$\Rightarrow \ m\frac{d\bar{v}}{dt} = \bar{F}$$

(4.5)

$$J_m\frac{d\Omega_r}{dt} = T_e - T_L - B \cdot \Omega_r - C \cdot \Omega_r^2$$

(4.6)

were:

$B \cdot \Omega -$ viscous friction torque; $\quad C \cdot \Omega_r^2 -$ windage torque

$T_e -$ electromagnetic torque; $\quad T_L -$ load torque

Although J_m can be found by an analytical approximation or by a CAD software, it is generally preferred to be determined by a simple experimental test. The most advantageous is the one that use existent experimental set-up, such as run-out test (also known as coasting test), which accounts for the complex rotor geometries and material properties. According to [4.6] an error of 10 % of inertia determination is usually acceptable when designing a drive control system for most applications.

We refer to J_m as the total drive inertia, since the BLDC-MRM is mechanically coupled to a 2.7 kW, 1500 rpm separately excited DC Machine with the following data: V_{field} = 110 V, I_a = 30 A, V_a = 110 V, R_a= 0.33 Ω, poles = 4 (Chapter 6.2).

Prior to run-out test the DC machine was evaluated with a few selected experiments. The machine output voltage for constant rated field current at different speeds is plotted in Fig. 4.11. No load test for base speed (250 rpm) and twice of it (500 rpm) is shown in Fig. 4.12, while short-circuit test is presented in Fig. 4.13.

The run-out test implies acceleration of the drive at rated speed and switching-off the power source when the steady state is reached, thus making the developed electromagnetic torque T_e = 0. The only existent losses will be the ones from mechanical friction upon the transient behavior depend together with J_m. The drive inertia can be determined from the slope of coasting curve, if all the losses during the decelerating time period are known.

The most convenient way is to use the well-known DC machine loss segregation. BLDC-MRM participates only through mechanical losses, which are part of drive mechanical losses.
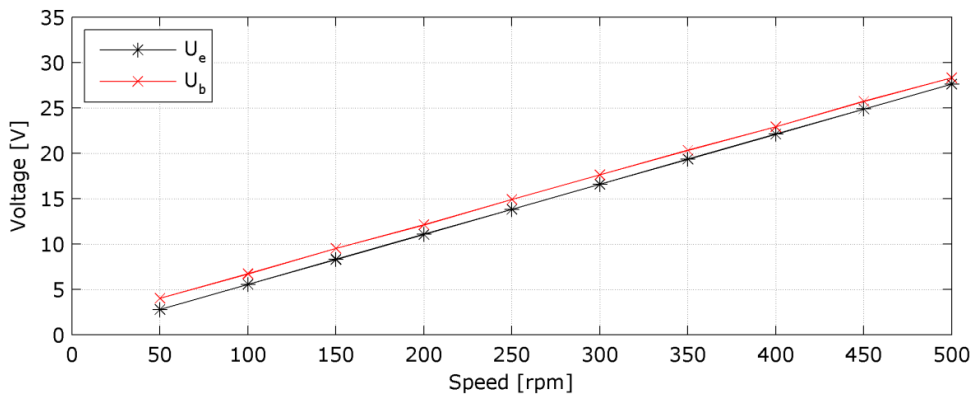
Fig.4.11. Voltage vs. speed for constant rated field current If = 1.1 A
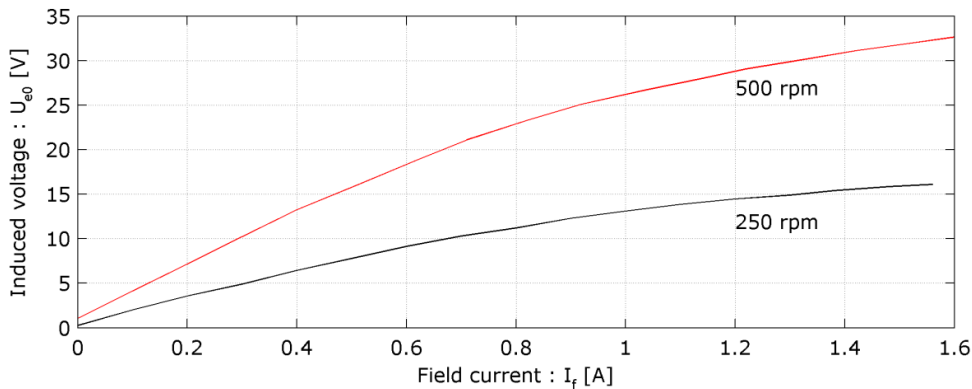
Fig.4.12. No load test at two speeds (250 rpm and 500 rpm)

        The sum of DC machine iron and total (drive) mechanical losses (Fig. 4.14) were computed by extracting the copper losses from input power. The speed is held constant by decreasing the field flux together with armature voltage. The lower limit of field winding voltage is imposed by the armature current that increases in this process. Two linear algebraic equations ($y_1(x)$ and $y_2(x)$) are obtained (by curve fitting) function of DC machine field winding voltage, for 250 rpm and 500 rpm. Obviously the mechanical losses don't depend on excitation flux, so by intersecting each line with y-axis ($U_f = 0$ V) mechanical losses are found. At 500 rpm they are **17.64** W, while at 250 rpm they are **8.05** W.

        Studying Fig. 4.15 one can observe 4 different situations, corresponding to base speed and double of that run-out test, with and without rotor iron losses. With DC machine field winding connected the additional loss toque makes the drive speed decrease almost twice as fast. Because the speed derivative value doesn't change during deceleration we can conclude that at the two tested speeds the *B* term from motion equation is negligible since. J_m was computed at 250 and 500 rpm, the average value being used. The tests were conducted after bringing the temperature of the bearings at rated temperature by 15 minutes of running at 1500 rpm. The average value of J_m from the two tests is found to be **0.049** kg·m^2.
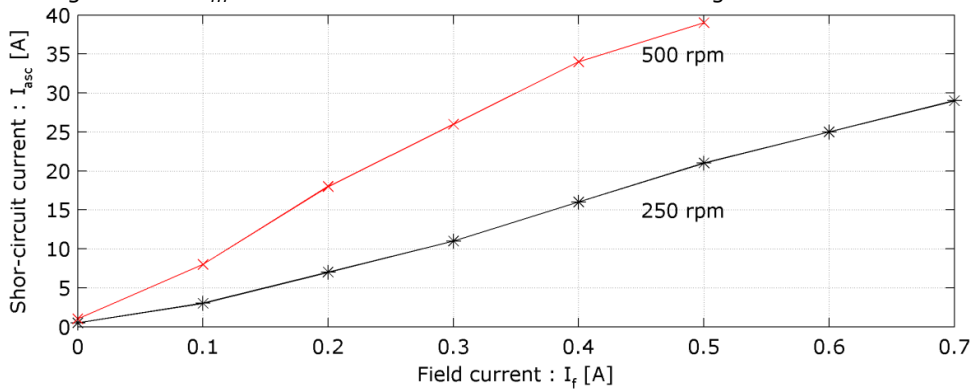
Fig.4.13. Short-circuit test at two speeds (250 rpm and 500 rpm)
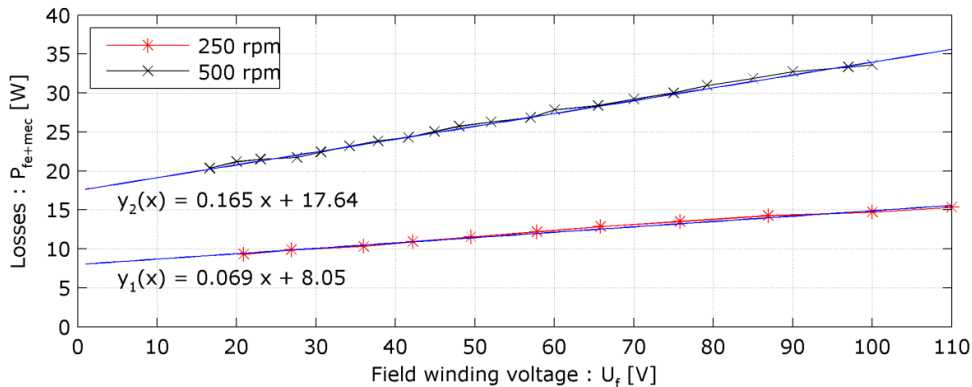
Fig.4.14. Mechanical loss separation at two speeds
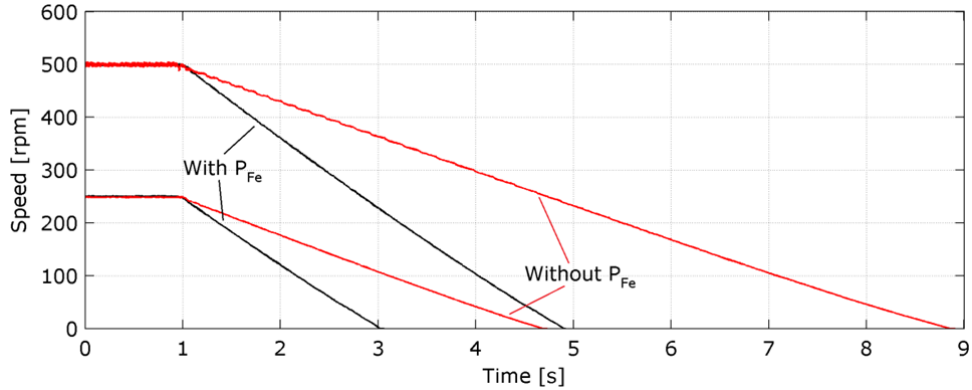
Fig.4.15. Run-out test with, and without DC machine iron loss (P_Fe) at two speeds

4.4 BLDC-MRM controlled dynamics

A good modeling should follow two rules: 1- clearly define the question to be answer by the model and 2- make the model no more complex than necessary to answer the question.

The dynamics of the machine were simulated using the graphical programming tool provided by Matworks, MatLab/Simulink. The general closed loop speed control is shown in Fig. 4.16. The "DNA" of this scheme is made of the inductance matrix and the drive moment of inertia. These unique characteristics bring the simulation closer to reality and must be changed if another machine is tested.
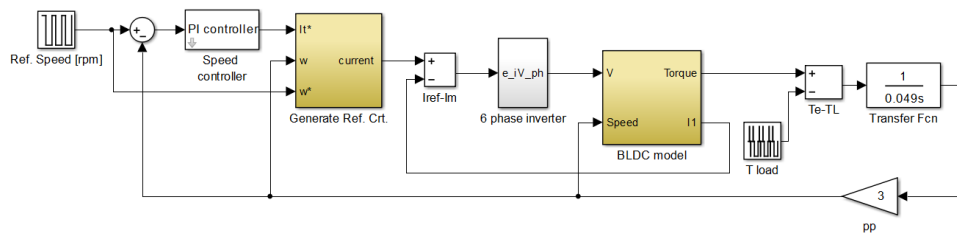
Fig.4.16. Six-phase BLDC-MRM speed control scheme in the Simulink environment

A speed PI controller (Fig. 4.17) regulates the speed error by providing the requested electromagnetic torque value (T_e). Knowing that BLDC-MRM T_e depends on the values of torque current, field current and the machine constant k_m (eq. 4.7) and considering the field weakening operation (eq. 4.8), torque current reference current can be computed by eq. 4.9. The constant k_m is computed a-priori through FEA torque computation at given currents. Anti-windup is avoided by limiting the output value of the integrator (± 70 Nm) and of the reference torque value (± 24 A). PI controller has the following constants: Kp = 10 , Ti = 0.01.

$$T_e = k_m \cdot I_t \cdot I_f; \quad (k_m = 0.243; \quad 6\text{-phase BLDC-MRM}) \tag{4.7}$$

$$I_f = \begin{cases} I_t & \omega_r < \omega_b \quad (\omega_r - \text{reference speed}) \\ I_t \cdot \dfrac{\omega_b}{\omega_r} & \omega_r > \omega_b \quad (\omega_b - \text{base speed}) \end{cases} \tag{4.8}$$

$$I_t = \begin{cases} \sqrt{\dfrac{T_e}{k_m}} & \omega_r < \omega_b \\ \sqrt{\dfrac{T_e \cdot \omega_r}{k_m \cdot \omega_b}} & \omega_r < \omega_b \end{cases} \tag{4.9}$$
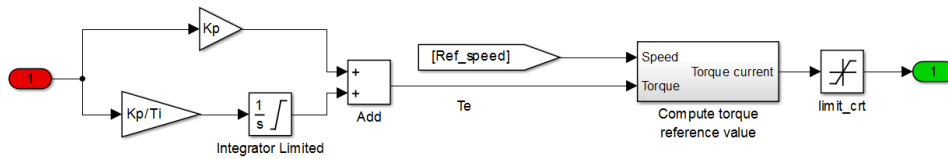
Fig.4.17. Speed controller
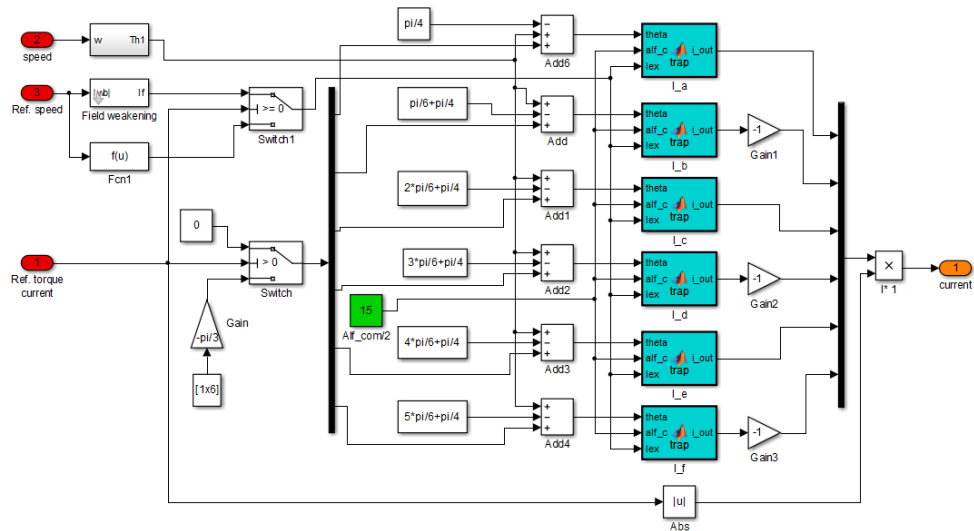
Fig.4.18. Reference current block generation

The next step is the generation of reference currents based on rotor position, reference torque current and prescribed speed (for field weakening operation) as can be observed in Fig. 4.18. The machine starts from a maximum torque position. The heart of this scheme is represented by a written MatLab function (Appendix 8) that generates the bipolar current waveform (bounded between -1 and 1) based on: rotor position (theta), time period (in electrical degrees) for current increase from 0 to rated value (here, half a slot pitch = 15°)

and the value of field current (between 0 and 1). The output is multiplied by prescribed torque current value. Phase current I_b, I_d and I_f are multiplied by -1 because of the chosen control strategy for the 6 phase machine with reduced number of switches, otherwise, for a full bridge inverter, the machine model don't use this negative gain (as for our tested 5 phase machine).

The cost of the converter could be decrease if instead of using a full bridge inverter for each phase, thus using $4·m$ total switches, a custom inverter with $2·(m+1)$ switches is used, with a null point connection of phases. Just by connecting all phases together is not enough, since BLDC-MRM use an unsymmetrical system of currents (at $π/m$ radians apart), making the null current to vary between $±m·I_{phase}$. An extra inverter leg is needed to regulate the null current, but in these conditions it will be oversized. A pretty elegant solution was provided in [4.7]. The idea is to connect each even phase backwards between inverter leg and null point, and supply that phase with a negative current (Fig. 4.18-4.19). The machine "sees" the same air-gap mmf as in the case of a full bridge inverter, but now the null current vary just between $±2·I_{phase}$ for an even number of phases machine, or between $± I_{phase}$ for an odd number of phases machine.
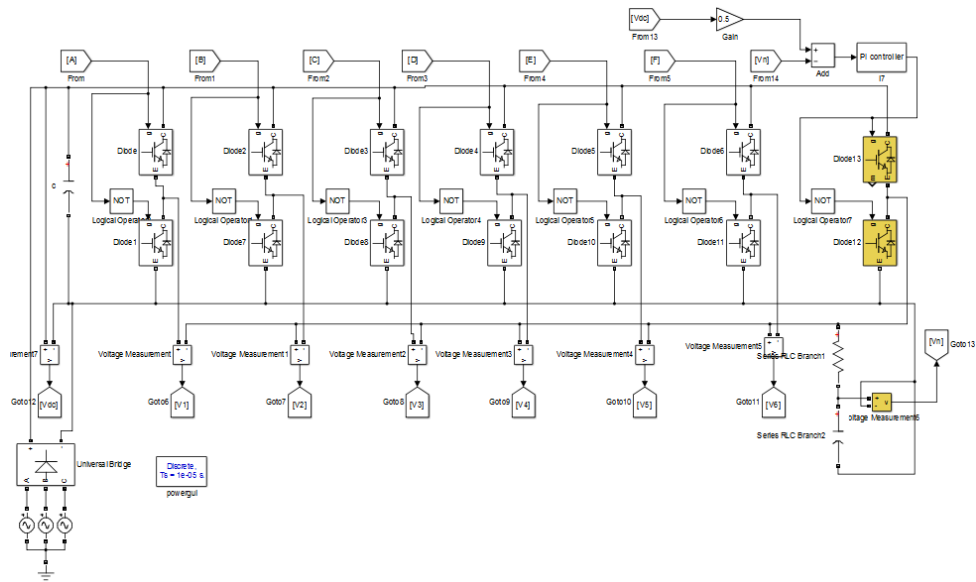
Fig.4.19. The 6 phase reduced number of switches inverter model

The 6 phase inverter model is shown in Fig. 4.19. The novelty of this scheme is that the seven inverter leg (null connected) is voltage controlled by a PI controller in such a way to keep the null point potential at half the DC voltage, with good results as we shall see in the next chapter.

The numerical dynamic model of the 6 phase BLDC-MRM is shown in Fig. 4.20.
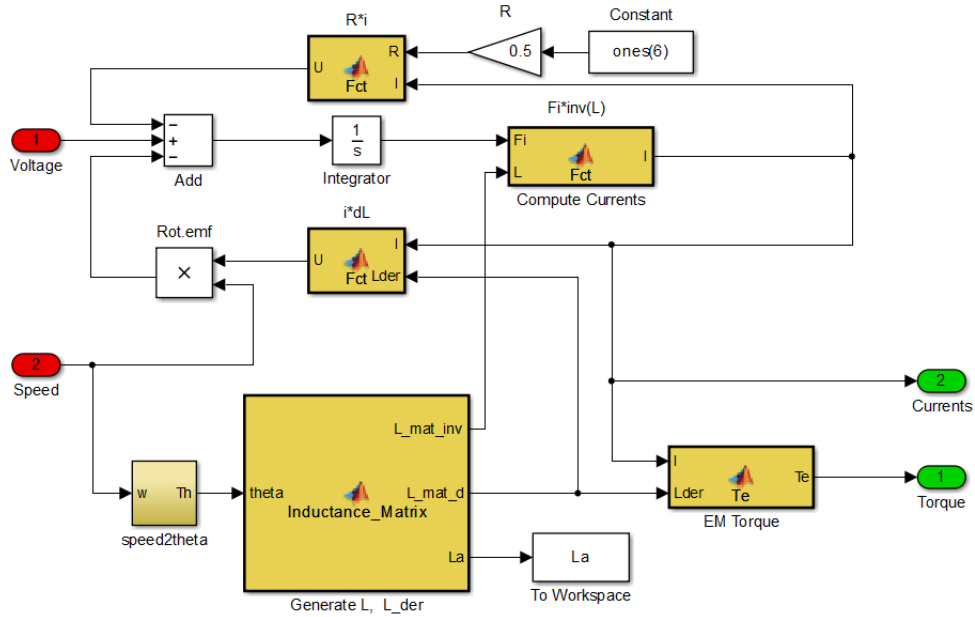
Fig.4.20. 6 phase BLDC-MRM dynamic model

The mathematical model of the BLDC-MRM is based on phase coordinates model, which makes use of global inductance matrix $\left[L\left(\theta_{er}\right)\right]$ with all terms dependent on rotor position. BLDC-MRM model is based on electrical equations (eq. 4.7-4.8) and mechanical equation (eq. 4.9). The model is shown for the 6 phase machine, but the same logic is used when the 5 phase machine model is built and simulated.

The electromagnetic torque T_e is computed based on the same principle (of total coenergy variation with rotor positon) as in the MEC model (eq. 4.10). The resulted system of nonlinear equations is not an issue for today's computing power.

$$\frac{d\left[\psi\right]}{dt} = \left[u\right] - \left[R\right]\cdot\left[i\right] - \left[i\right]\cdot\frac{\partial\left[L\left(\theta_{er}\right)\right]}{\partial\theta} \tag{4.7}$$

$$\left[\psi\right] = \left[L\left(\theta_{er}\right)\right]\cdot\left[i\right]; \tag{4.8}$$

Phase currents, voltages and fluxes are placed in vectors $[i]$, $[u]$ and $[\psi]$.

$$\left[i\right] = \left[i_a \ i_b \ i_c \ i_d \ i_e \ i_f\right]^t; \quad \left[u\right] = \left[u_a \ u_b \ u_c \ u_d \ u_e \ u_f\right]^t;$$

$$\left[\psi\right] = \left[\psi_a \ \psi_b \ \psi_c \ \psi_d \ \psi_e \ \psi_f\right]^t;$$

$$J\frac{d\Omega}{dt} = T_e - T_{load} - B\cdot\Omega \tag{4.9}$$

$$T_e = \frac{1}{2}\left[i\right]^t \cdot \frac{\partial\left[L\left(\theta_{er}\right)\right]}{\partial\theta}\cdot\left[i\right] \tag{4.10}$$

Conclusion

In this chapter the 6-phase, 6-poles BLDC-MRM is tested. Electrical and mechanical parameters identification is presented, for an accurate transient simulation. The decoupling of the two axes is also shown, besides the saturation.

The speed control scheme used for simulation is presented, and all the main parts: controller, converter and machine are explained. A mathematical model is developed based on determined parameters.

Simulation results are directly compared with experimental results in the next chapter for two BLDC-MRM machines, using two different control strategies and test-bed.

References

[4.1]   I. Boldea, "*Testing of Synchronous Generators*", in *Synchronous Generator*, CRC Press, Taylor & Francis, 2006, pp. 8-32 to 8-36

[4.2]   R. Babau, I. Boldea, T.J.E Miller, N. Muntean, "*Complete parameter identification of large induction machines from no load acceleration-deceleration tests*," IEEE Trans. On Industrial Electronics, Vol. IE-54, No. 4, pp. 1962-1972, 2007

[4.3]   S. Agarlita, D. Ursu, L.N. Tutelea, I. Boldea and B. Fahimi "*BLDC Multiphase Reluctance Machines: a Revival Attempt with 2D FEM Investigation and Standstill Tests*", Energy Conversion Congress and Exposition (ECCE), 2013 IEEE, pp. 1850 – 1857

[4.4]   P. Pillay and R. Krishnan, "*Modeling, simulation, and analysis of permanent-magnet motor drives, part II: the brushless DC motor drive*", IEEE Trans. On Industry Applications, Vol. IA-25, No. 2, 1989, pp. 274 -279

[4.5]   Jacek F. Gieras, "*Permanent Magnet Motor Technology – Design and applications*", book, 3rd edition, CRC Press, Taylor & Francis Group LLC, Boca Raton, Florida , 2010

[4.6]   W. Leonhard, "*Control of electric drives, 3rd ed.*", Springer, 2001, pp 14-15.

[4.7]   H. Weh and U. Schroder, "*Static Inverter concepts for multiphase machines with square-wave current-field distribution*", Proc. EPE Brussel, 1985, pp. 1147 -1152

5. BLDC-MRM control

Abstract

Control of the BDLC-MRM is presented in this chapter, for a 5 and a 6 phase BLDC-MRM configuration. Full load steady state operation (in a 4:1 speed range) of the 5 phase machine, connected to a full bridge inverter and controlled by a DSP, is presented in section 5.2. Since from an engineering point of view cost is a key issue to be solved, driving the machine with reduced number of switches is an important aspect from the economical perspective and drive efficiency. Based on these motivations, a rather new control strategy for the 6 phase BLDC-MRM with null phase connection, through the null phase voltage regulation is tested in section 5.3, with good transient behavior. Running experiments (motoring and generating) with speed reversal and field weakening using, a dSPACE platform (and ControlDesk interface) that drives three 3-phase inverters powering a star connected 6-phase BLDC-MRM are presented, hence showing operation with reduced number of switches. Experimental measurements are compared to simulation results, thus validating the developed circuit model from chapter 4.

5.1 Introduction

Previous studies [5.1] have shown that sinusoidal flux distribution in a multiphase machine with concentrated windings is often an undesirable feature of a multiphase machine since the stator iron is poorly used, i.e. just one stator tooth (the one under the maximum value of flux) being saturated. This phenomenon leads the designer to a trapezoidal current waveform (just like in a BLDC), where each current harmonic interact with correspondent flux harmonic and produce torque. By using a rectangular air-gap magnetic flux density waveform larger yoke is needed to manage the same flux, compared to the sinusoidal case, if the maximum value is kept.

The authors of [5.2] have found out that by using a rectangular current profile in a 6 phase multiphase induction machine, with a concentrated winding, at the same volume and copper losses, the torque density of the machine was 15% higher compared to sinusoidal current profile.

The birthplace of the BLDC-MRM (or FRM) concept was in München, in 1986, where authors from [5.3-5.5] proposed the application of inverted-fed multiphase synchronous machine, based on DC machine operation, with electronically commutated phases. The idea is to replace what it is done mechanically in a DC machine by a commutator (that ensures a fixed orientation of the armature current to the exciter field) with an electronically commutator through a voltage inverter and current regulators. This kind of current distribution involves implementation of a multiphase winding layout phases, the machine becoming a multiphase reluctance machine (MRM).

An excellent survey of the multiphase machines and drives is given in [5.6]. The advantages of multiphase machines are well known [5.7-5.9], among them being: fault tolerant operation and decreasing the torque ripple and inverter leg current.

A rectangular current profile was used for a 6 phase multiphase induction machine with a concentrated winding [5.10].

Authors from [5.11] show results for static torque vs. rotor position or maximum average static torque vs. current, without any steady state or transient behavior. Also full bridge converters were used without considering reducing the number of switches. The series connection of phases was studied in [5.12], but again failed to deliver conclusive experimental data.

Previous work related to BLDC-MRM principle [5.3-5.5, 5.11 and 5.12] show partial experimental results, without any transient behavior, torque (or speed) ripple, or comparison with a developed dynamic numerical model. The following sections attempt to cover some of these gaps.

5.2 Five-phase BLDC-MRM

5.2.1 Control strategy

The BLDC-MRM is connected through a torque meter to a doubly-fed induction machine (DFIM) working as an autonomous synchronous generator (SG) that supplies a resistive electronic load. Details of the 5-phase BLDC-MRM drive are given in section 6.1.

The presented speed control scheme (Fig. 5.1) is a version of the proposed closed loop speed control scheme from section 4.3. The speed is regulated by a PI controller with limitation (Kp = 0.005, Ki = 30, Up$_{\_limit}$ = 14, Down$_{\_limit}$ = -14), which provides the reference torque current level (I_T*). The machine constant k_m computed from measured rated average torque (33 Nm) at rated current ($I_T = I_F = 4$ A), is found to be equal to 2.062 (eq. 4.7).

The Current Generation Block (C.G.B.) generates the 5 phase flat-top bipolar reference currents (Ia*, Ib*, Ic*, Id* and Ie*) based on I_T*, rotor angular position and reference speed (for field weakening).

The field current level (I_F) is computed based on reference speed, providing a field weakening operation above rated speed (n_{base}), i.e. up to base speed $I_F = I_T$, while above n_{base} , $I_F = I_T \cdot (n_{base} / speed)$, (eq. 4.8). Compared to an IPMSM, in which flux weakening is obtained by a negative d-axis current (I_d), thus an increase of copper losses, here, flux weakening is obtained by a decrease of I_F (and copper losses).   The current error is regulated by a hysteresis current controller (band = 0.05 A) that applies ±Vdc (± 300 V) across each phase.

Machine dynamic model (based on curved fitted inductances from Fig. 2.11) and control was implemented in Simulink, as explained in sec. 4.3, but using a bang-bang current controller and full bridge inverter connected to a 300 V voltage source. Machine phase connection to the full bridge inverter is presented in Fig. 5.2.
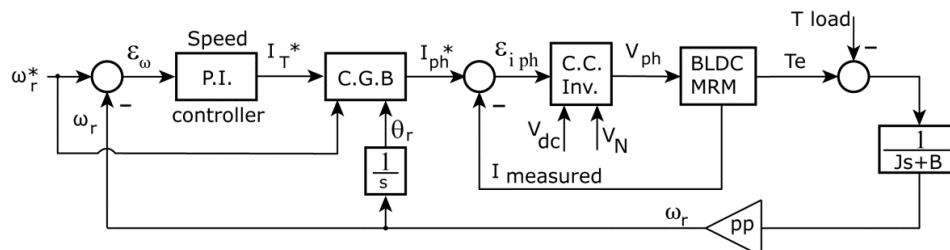
Fig.5.1. Five-phase BLDC-MRM control scheme
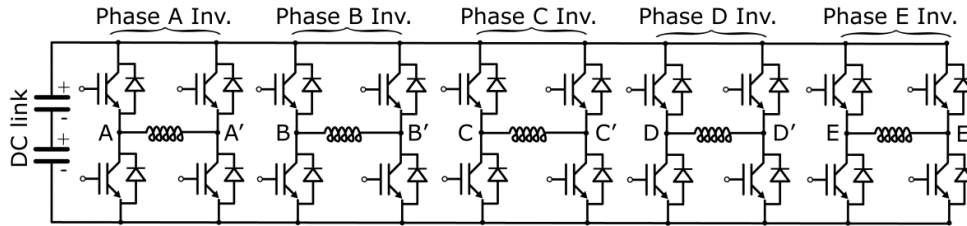
Fig.5.2. Five-phase BLDC-MRM full bridge connection

5.2.2 Steady state operation

Experiments were conducted for a steady state operation of the BLDC-MRM, from base speed up to 4 times base speed, thus proving a 4:1 speed ratio, with field weakening. For each speed (250 rpm , 500 rpm, 750 rpm and 1000 rpm) machine phase current waveform are presented (only 3 out of 5, due to limitation of digital oscilloscope - four acquisition channels : three for current and one for torque). After each measured current, a graph of simulated currents in the same conditions (based on the Simulink model) and a comparison between phase *a* measured and simulated current are provided. In order to save space, just Fig. 5.4 presents all 5 simulated phase currents on a graph, while for the other speeds one simulated current waveform is compared to one measured phase current (Fig.5.5, 5.7, 5.9, 5.11). The results are presented in Fig. 5.3-5.11, and prove a good agreement between experiments and simulations, thus the high harmonic rejection from inductance curve fitting procedure, do not affect the too much the accuracy, while making the machine model implementation easier in Matlab-Simulink environment.

The measured torque pulsations, at the above 4 mentioned speeds, are plotted in Fig. 5.12. The simulated torque pulsations (Fig. 5.13) seem to have a higher spectrum of harmonics, introduced by numerical solving algorithm ode4 – Runge-Kutta, though much lower torque pulsations (explained by a constant total load torque) appear. In both cases the torque pulsations are higher at low speed, than at high speeds.
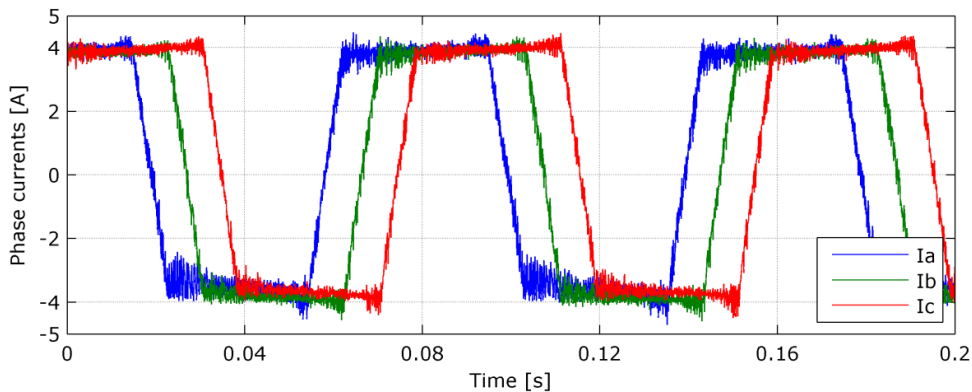
Fig.5.3. Measured phase currents at base speed (250 rpm)
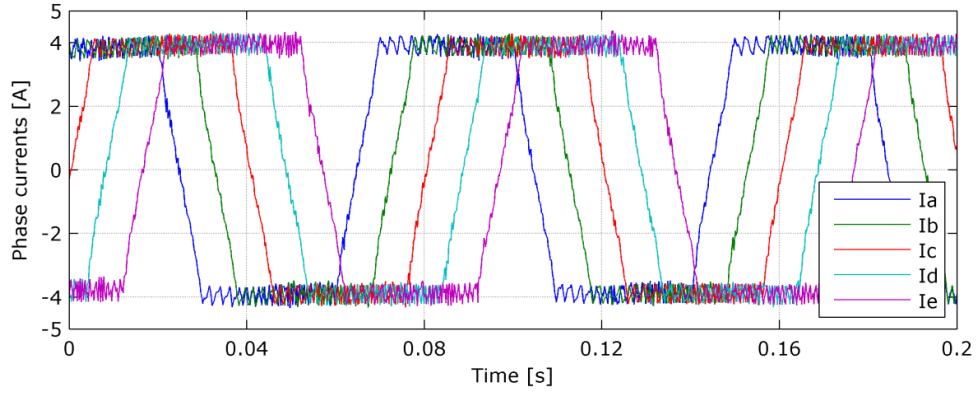
Fig.5.4. Simulated phase currents at base speed (250 rpm)
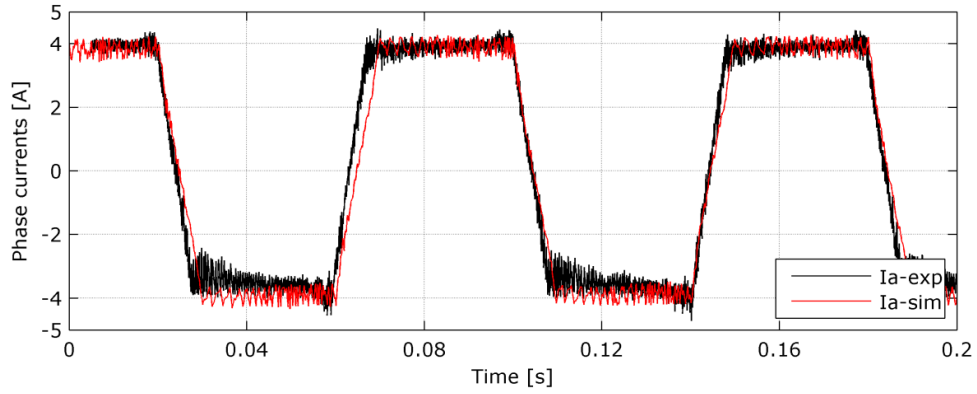
Fig.5.5. Phase *a* current comparison at base speed (250 rpm)
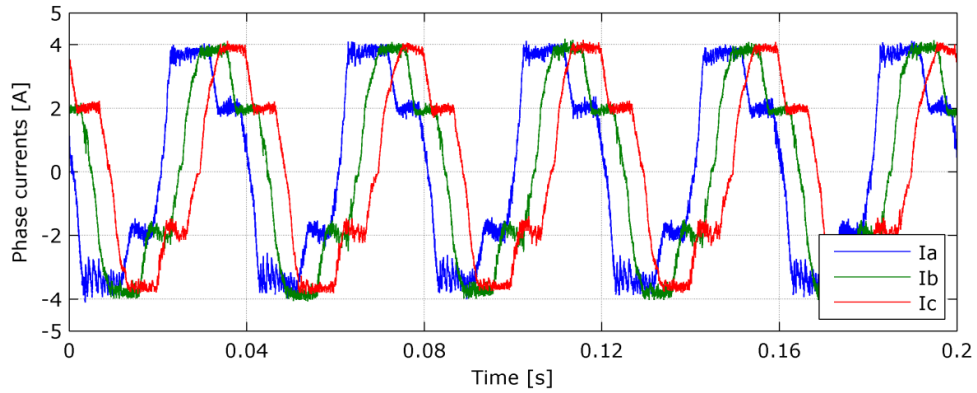
Fig.5.6. Measured phase currents at 500 rpm
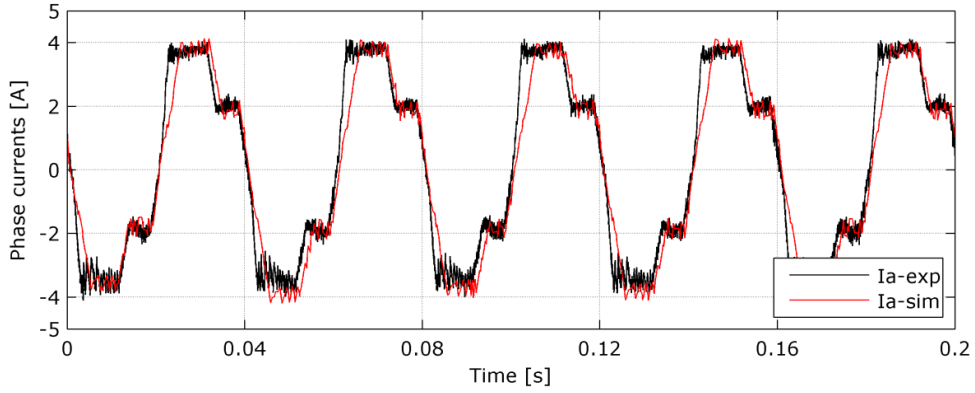
Fig.5.7. Phase *a* current comparison at 500 rpm
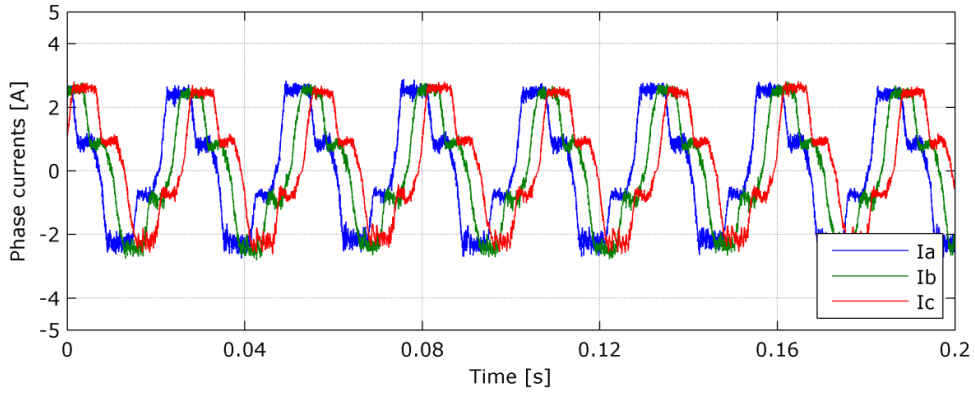
Fig.5.8. Measured phase currents at 750 rpm
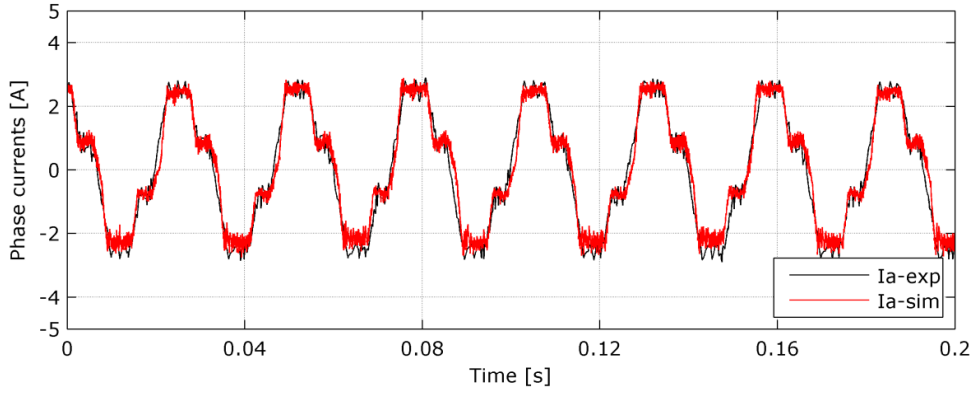
Fig.5.9. Phase *a* current comparison at 750 rpm
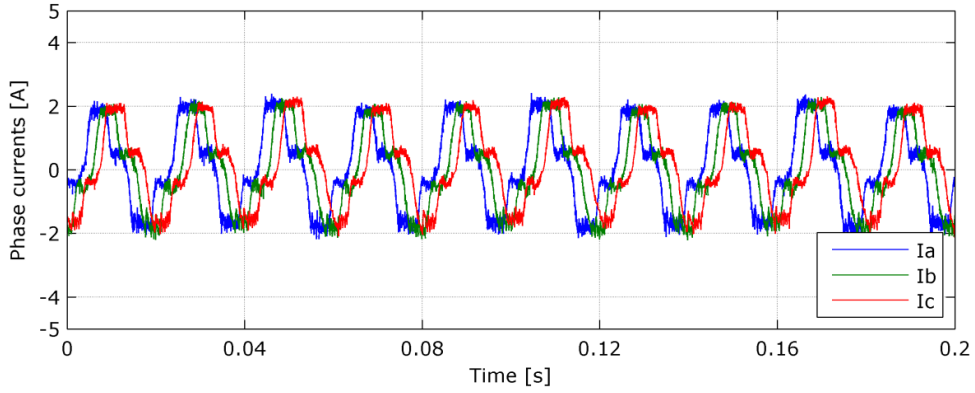
Fig.5.10. Measured currents at 1000 rpm
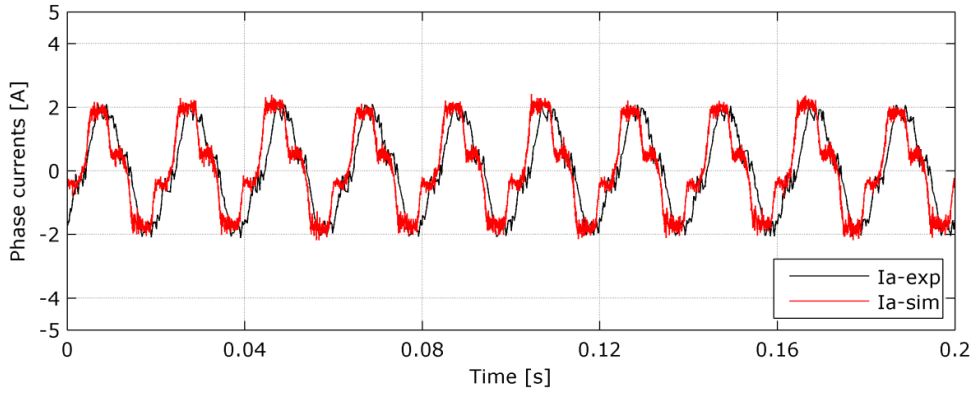
Fig.5.11. Phase *a* current comparison at 1000 rpm
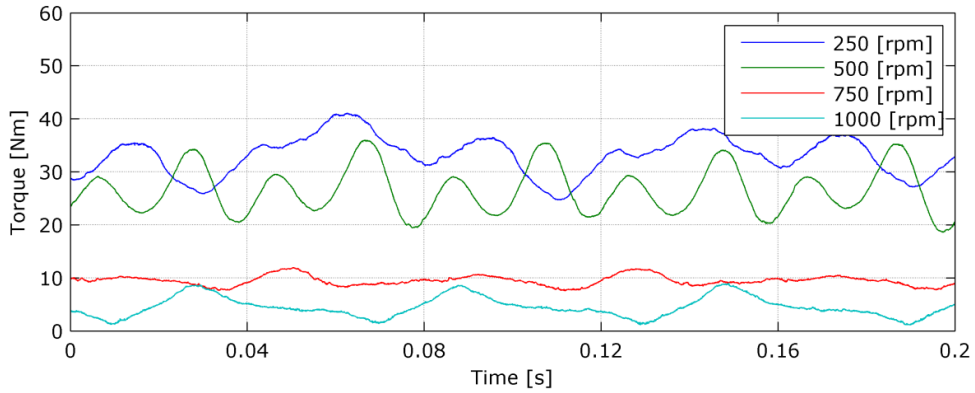
Fig.5.12. Experimental torque pulsations measured at four speeds
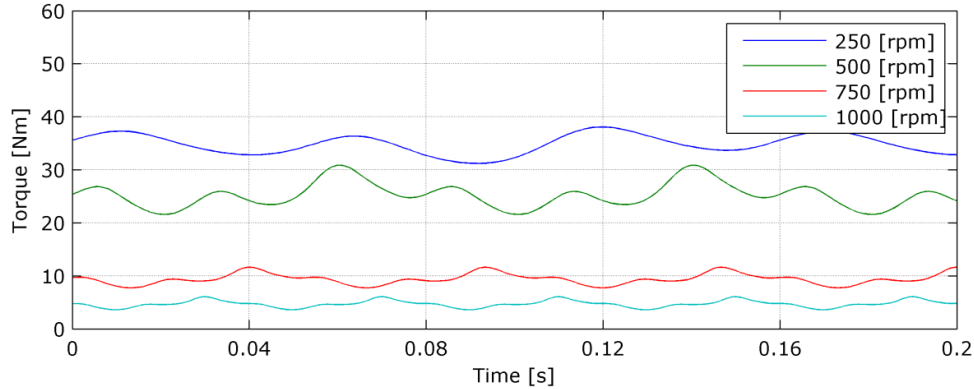
Fig.5.13. 2D-FEA torque pulsations computed at four speeds
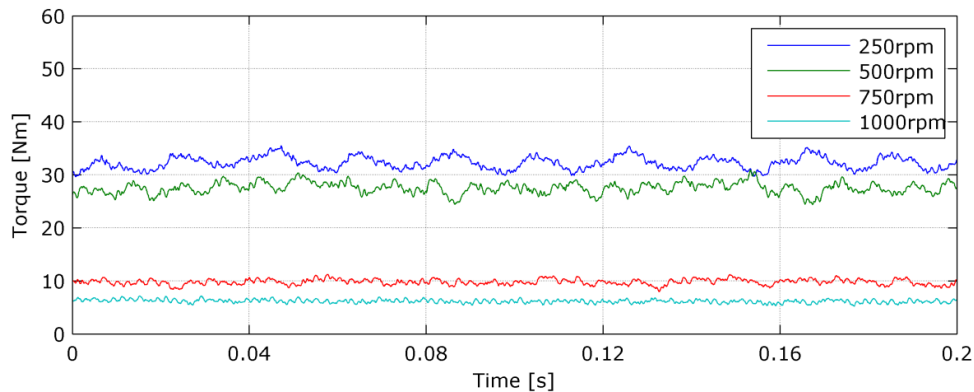
Fig.5.14. Simulated torque pulsations computed at four speeds

Supplying the machine FE model (presented in section 2.3.2.1) (at each speed) with the average values of the experimental obtained phase currents (Fig. 5.3, 5.6, 5.8, and 5.10), torque pulsations are computed and plotted in Fig. 5.13.

5.2.3 Review of machine performances

This section presents the machine performance. The graphs present two situation of the drive: with an electric load coupled to the generator (IM machine) and with electric no load of the same machine. Obviously mechanical, stray and iron losses need to be supported in the second regime by the power supply.

The non-linear relationship between 2D-FEA and experimental average torque (measured by torque meter) versus rotor speed became clear after a Spline interpolation (Fig. 5.15). Although the speed doubles the machine can still produce 80 % of base torque. Finite Element analysis tends to slightly overestimate the torque at base speed and underestimate it at 500 rpm, due to prediction of the local iron saturation at rated currents. The output power is presented Fig. 5.16. Since the input power represents the DC link electric power the measured efficiency (Fig. 5.17) includes the inverter efficiency also.
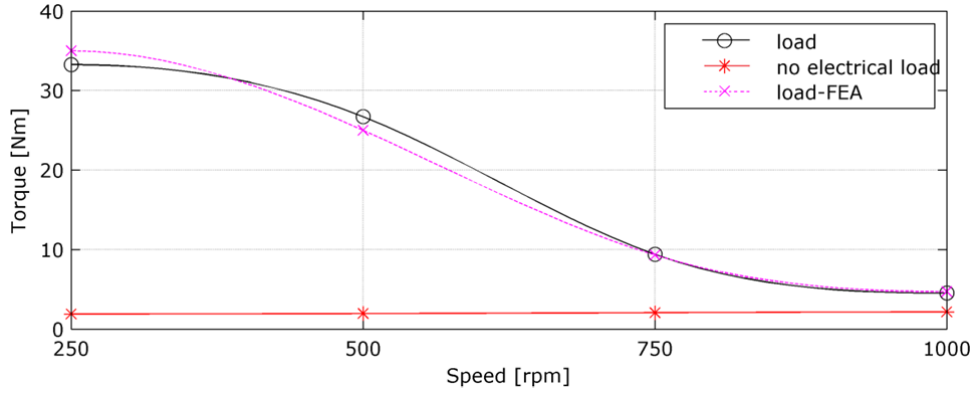
Fig.5.15. Measured and FEA average torque comparison for a 4:1 speed ratio
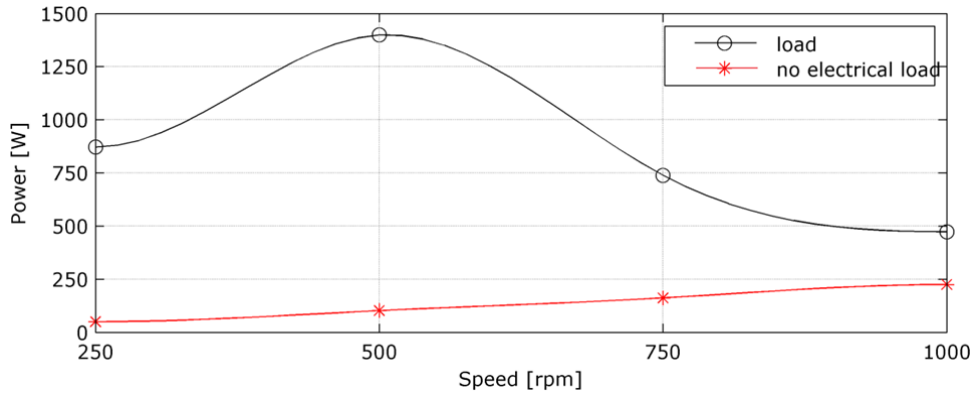
Fig.5.16. Measured output power for a 4:1 speed ratio
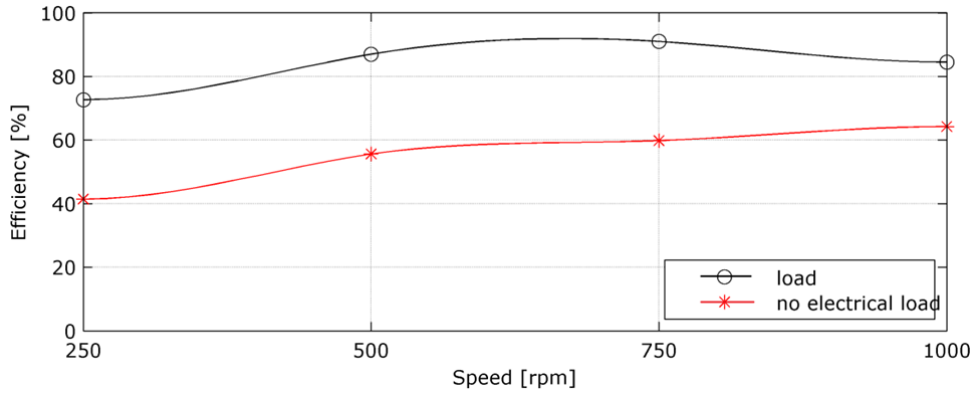
Fig.5.17. Measured efficiency for a 4:1 speed ratio

5.3 Six-phase BLDC-MRM

5.3.1 Control strategy

Controlling the BLDC-MRM with a reduced number of switches $2 \cdot (m+1)$ and normal connection of phases as in Fig. 5.18, could become an important issue, compared to $4 \cdot m$ switch utilization (employed in the full bridge inverter phase connection case). The problem is related to the symmetry aspect. An m-phase system is symmetrical if the electrical angle between adjacent phases is $2 \cdot \pi/m$, while the BLDC-MRM principle of operation imply using π/m phase shift. In this situation the null current (the sum of all phase current) will not be equal to zero, and for a 6-phase BLDC-MRM (connected as in Fig. 5.18) is has the variation presented in Fig. 5.19, presented for the worst case scenario, when $I_T = I_F$. The null current I_N (relative to phase current: in p.u. values) varies between $\pm m \cdot I_{phase}$, (in our case $\pm 6 \cdot 12$ A = ± 72 A) and the null inverter leg needs to be oversized.
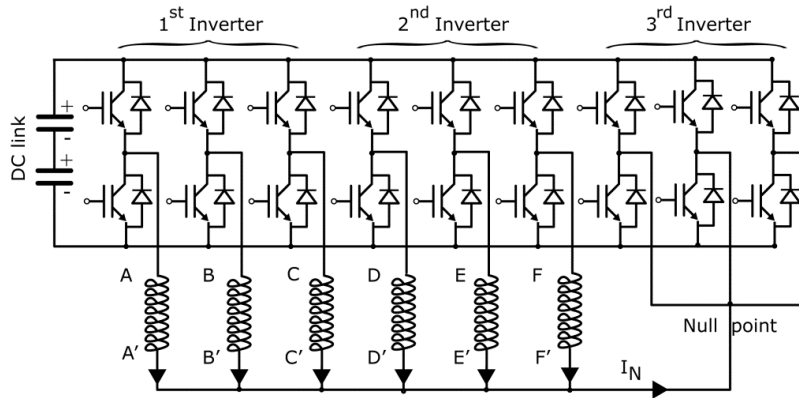
Fig.5.18. Usual phase connection for 6-phase BLDC-MRM control with reduced number of switches
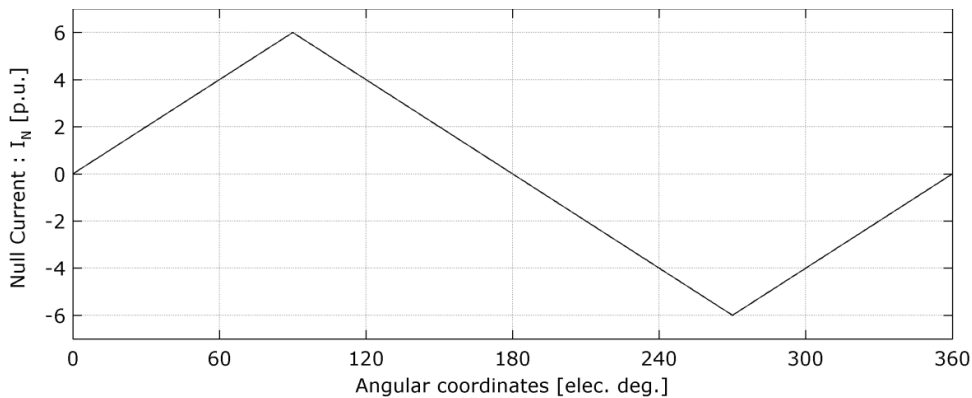
Fig.5.19. Six-phase BLDC-MRM simulated null current variation for usual phase connection in a reduced number of switches configuration
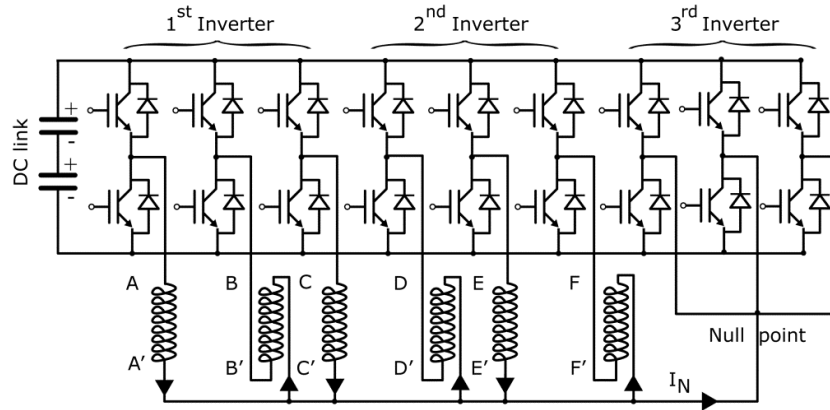
Fig.5.20. Improved phase connection for 6-phase BLDC-MRM control with reduced number of switches
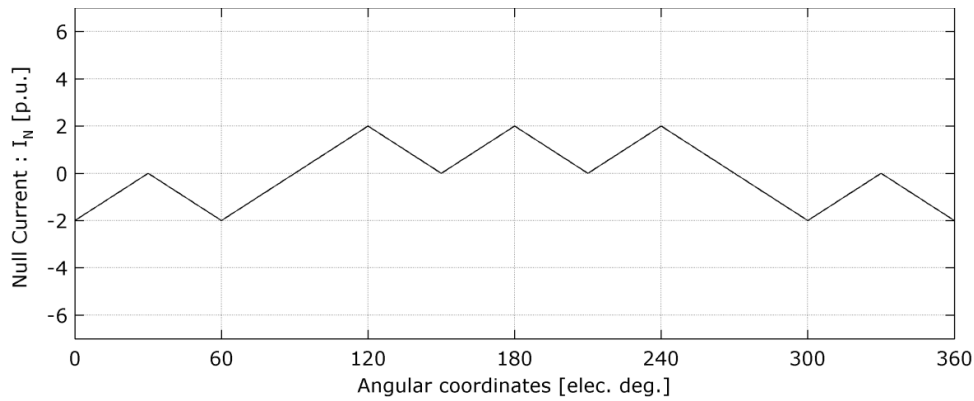
Fig.5.21. Six-phase BLDC-MRM simulated null current variation for improved phase connection in a reduced number of switches configuration

This situation can be drastically improved if each even phase is connected backwards to inverter while prescribing inverse current through (Fig. 5.20). From the machine point of view the same air-gap *mmf* is created [5.4]. The result is a null current variation in the range $\pm 2 \cdot I_{phase}$ (for an even number of phases) or $\pm I_{phase}$ (for an odd number of phases), as we can observe in Fig. 5.21. Although this idea is not new, no experimental work has been shown to "cement" this statement.

The inverter null leg should be designed with the above consideration. Since we use 3 industrial voltage source inverters (section 6.2) with I_{max} = 15 A, for protection reasoning the null point is divided in three and connected to the 3rd inverter while providing the same command signal to all three legs [5.15].

The control scheme for the 6-phase, 6 poles BLDC-MRM was presented in 4.3 and involves a speed PI controller (kp=3 and ki=300). The speed controller output is fed to the C.G.B. that will generate the reference currents based on rotor position and reference speed. This block assures a complete control of field/torque current levels and the commutation period. Current error is regulated by PI

controllers (kp=5, ki=5000) just like the null point voltage error (kp=0.001, ki=0.002), both of them being presented in Figs. 5.22- 5.23. The proposed control scheme is implemented as a discrete model in Matlab/Simulink simplifying the control algorithm implementation on DSpace 1103 platform.

Initial simulation results [5.13] used bang-bang current controllers and a full bridge inverter, but practical implementation has forced us to make use PI controllers for regulating current and null point voltage, since a hysteresis controller, though simpler, has the same problem as in DTC control applied on cage-less machines : high current (torque) ripple, high acoustical noise and vibrations [5.14]. Usually PI controllers are used for DC variables, but at tested current frequencies (12.5 Hz÷25 Hz) the introduced time delay is not disturbing.

Three particular cases have been studied and presented next: motoring mode at 250 rpm (base speed) and 500 rpm, generating mode at base speed and speed reversal with flux weakening operation.
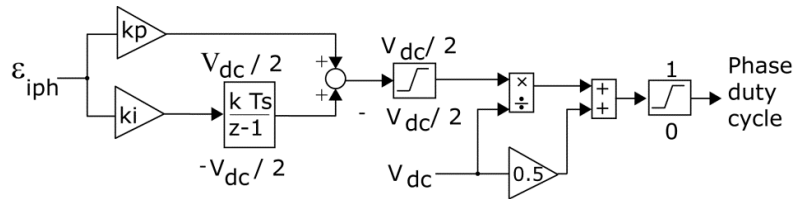
Fig.5.22. Phase current controller
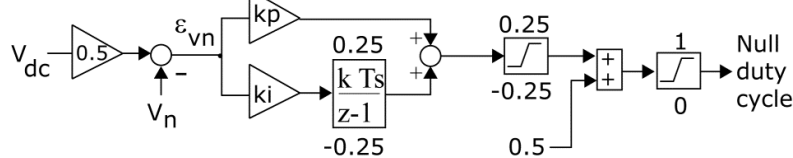
Fig.5.23. Null point voltage regulation

5.3.2 Motoring mode

The BLDC-MRM is power connected at t = 1.2 s (no load condition), then it is loaded through the DC machine (whose data were presented in 4.2), which at t = 4.7 s becomes a generator who supplies a resistive load. Since the induced voltage is small at 250 rpm (V_e=14 V) the armature circuit is short-circuited at base speed giving rise to an armature current of I_a = 37 A. Knowing all the losses of the DC machine (found in 4.2) the computed shaft torque is T_a = 20 Nm. This value agrees with static torque measurements (Fig. 2.20) at I_f =I_t =9 A => T_e=22 Nm, since in running conditions torque pulsations due to magnetic, mechanical and geometrical causes, makes the average torque smaller than the maximum value from Fig.2.20.

Measured speed is plotted in Fig. 5.24 and it shows a speed ripple of 0.8% at no load and 3.2% in load conditions. Experimental phase currents are plotted in Fig. 5.25 while in the next figure, for clarity in representation, one measured phase current is compared with a simulated phase current in identical loading conditions (Fig.5.26). The null current waveform (Fig. 5.27) is almost as predicted by theory, thus ensuring us that the PI null point voltage controller is the right solution to implement for this control system.
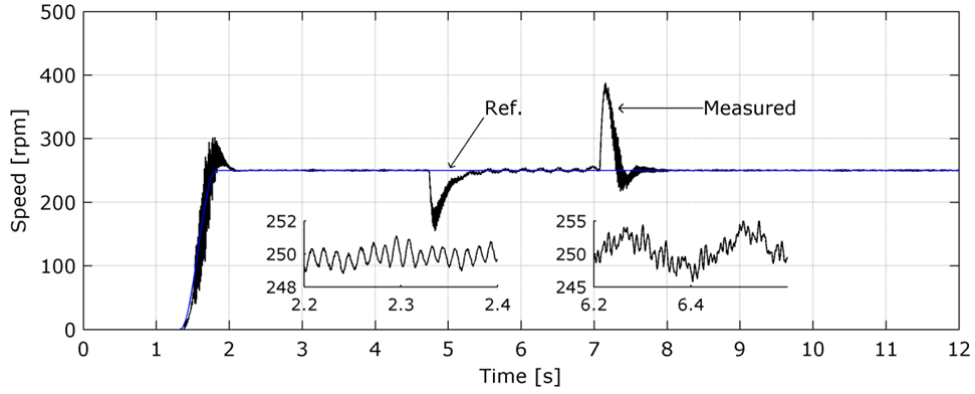
Fig.5.24. BLDC-MRM measured speed with no-load and load speed ripple zooming box
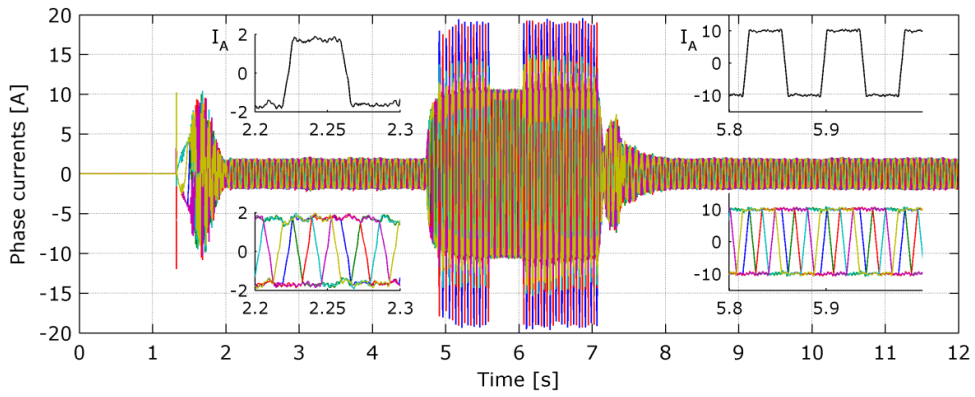
Fig.5.25. Measured phase currents at 250 rpm with zooming box at no-load and load operation
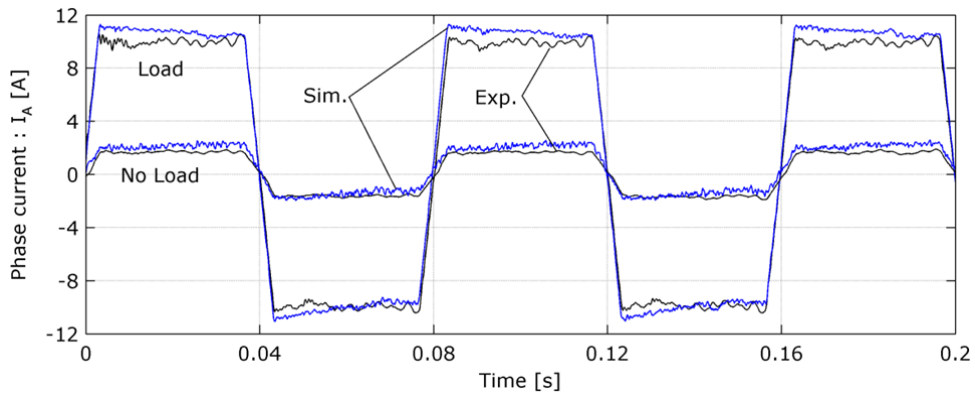
Fig.5.26. Simulated vs. Measured phase *a* current at base speed (no-load and load operation)
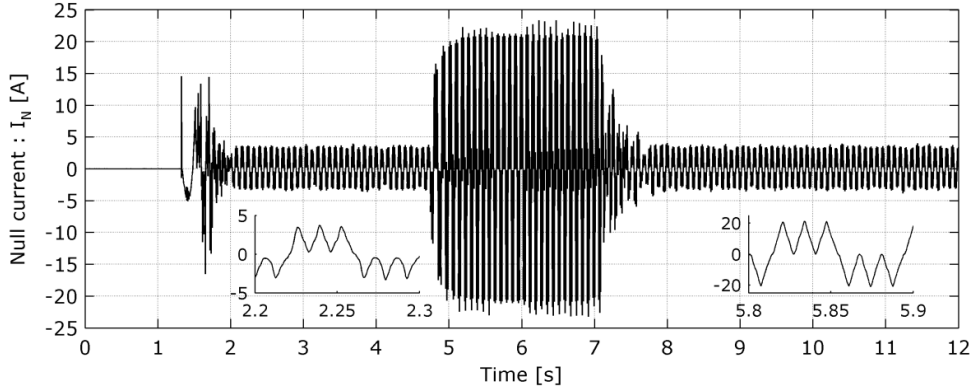
Fig.5.27. Measured null phase current I_N at base speed (no-load and load operation)

At 500 rpm the induced voltage in the DC machine becomes high enough (V_e =28V) for an external load resistance connection. The BLDC-MRM gets loaded through the DC generator at t=3.9 s, Fig. 5.28-5.31. Speed pulsations at no load are 0.3 % while at load they are 1.2 % (Fig. 5.28). In the absence of a torque-meter we can conclude by studying speed ripple that torque ripple are also small.

Now, the armature current is I_a = 39 A, which corresponds to a shaft torque of 21 N·m. This represents the upper limit at this speed, slightly higher than the expected 35 N·m / 2 = 17.5 Nm, needed for constant power speed range. Field weakening can be observed in the phase current waveforms (Fig. 5.29-5.30) by a decreased value of the field current over the span of the two slots corresponding to field phase position.
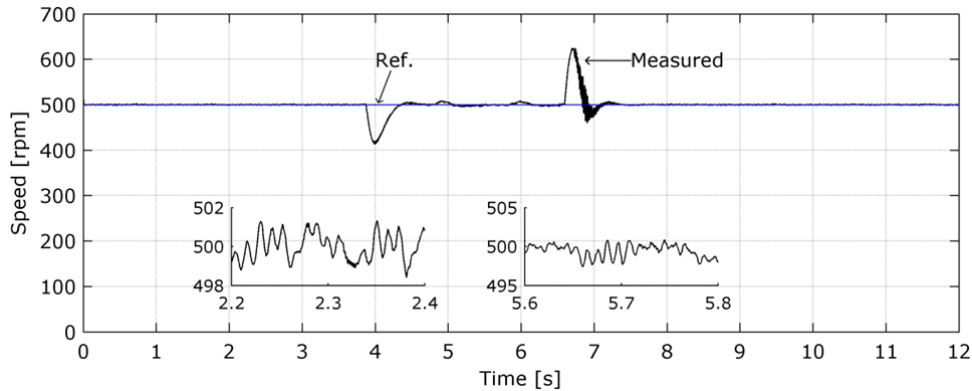
Fig.5.28. BLDC-MRM measured speed with no-load and load speed ripple zooming box
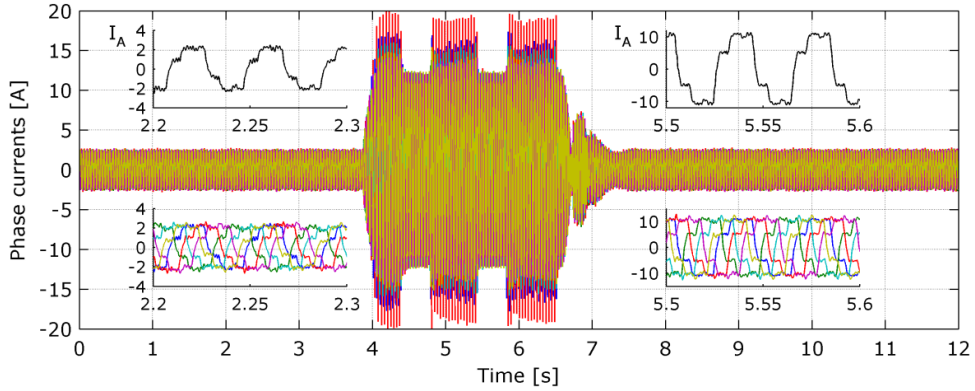
Fig.5.29. Measured phase currents at 500 rpm with zooming box at no-load and load operation
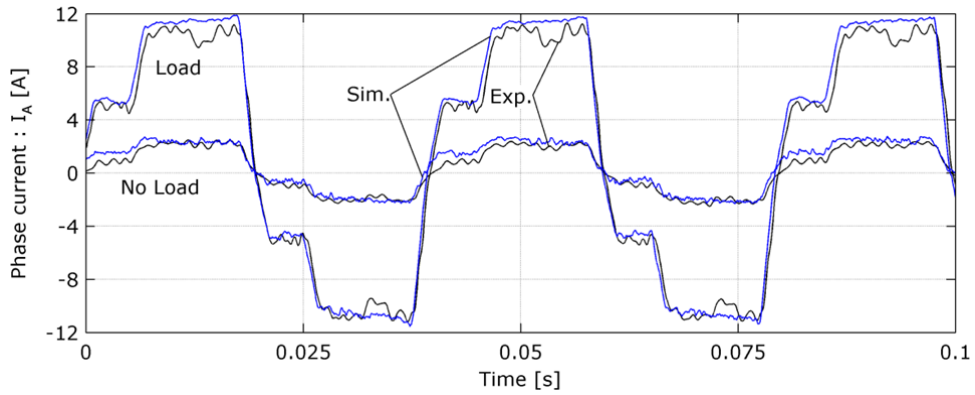
Fig.5.30. Simulated vs. Measured phase *a* current at 500 rpm (no-load and load operation)
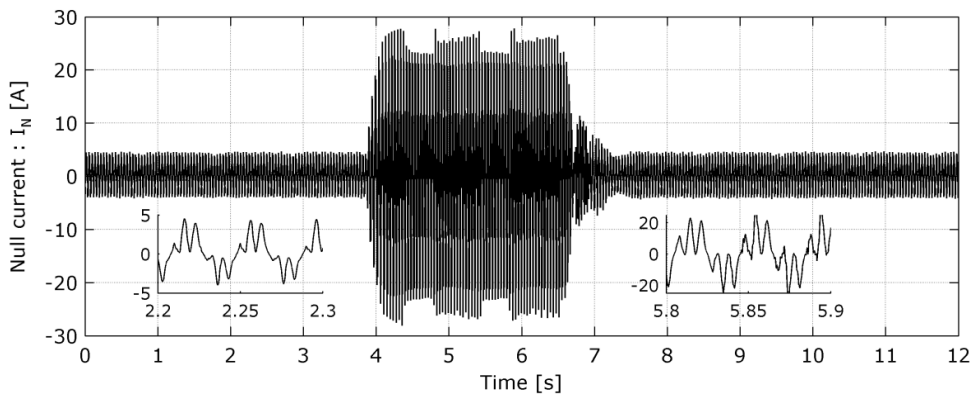
Fig.5.31. Measured null phase current I_N at 500 rpm (no-load and load operation)

5.3.3 Generating mode

As all electrical machines BLDC-MRM can also work as a generator. This section presents the generating mode which is tested by driving the DC machine as a motor at time period t = 1.9 s (Fig. 5.32), with an armature applied voltage V_a =32 V (which corresponds to a no-load speed of the DC motor equal to 600 rpm). Since the drive has a speed loop with a prescribed reference speed equal to base speed, the BLDC-MRM becomes a generator and receives mechanical power from the DC motor. The armature current in this case is equal to I_a =37 A. Figure 5.35 shows the prescribed torque current from the PI speed controller which clearly changes sign.
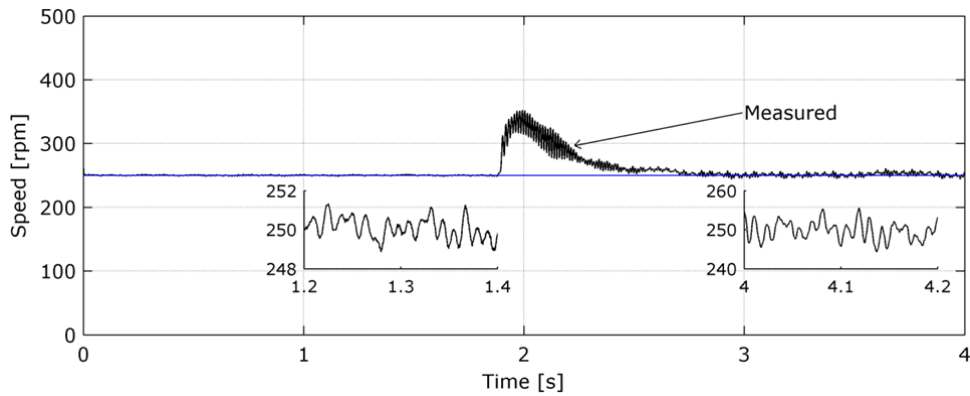
Fig.5.32. BLDC-MRM measured speed with no-load and load speed ripple zooming box
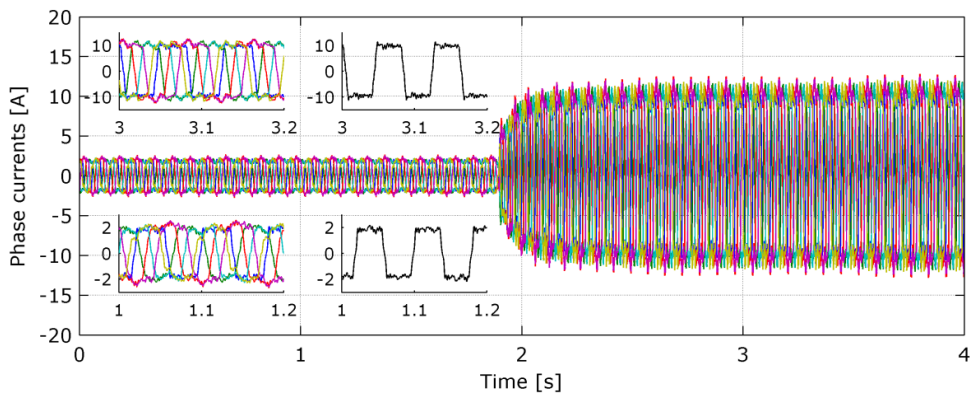
Fig.5.33. Measured phase currents with zooming box at no-load and load operation
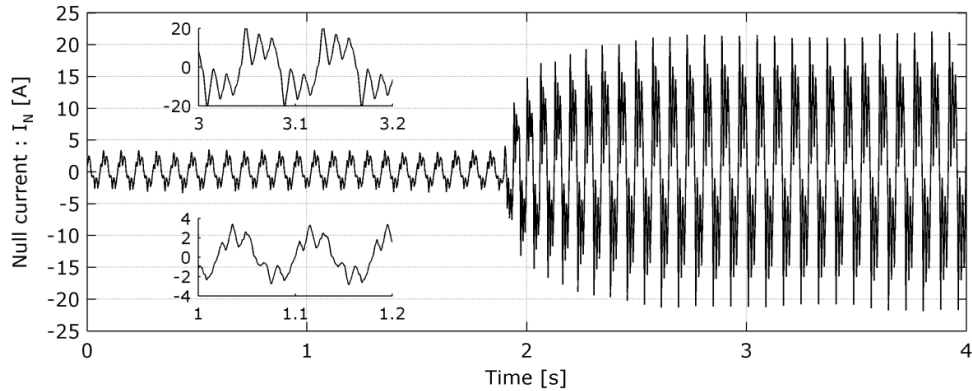
Fig.5.34. Measured null phase current I_N at 500 rpm (no-load and load operation)
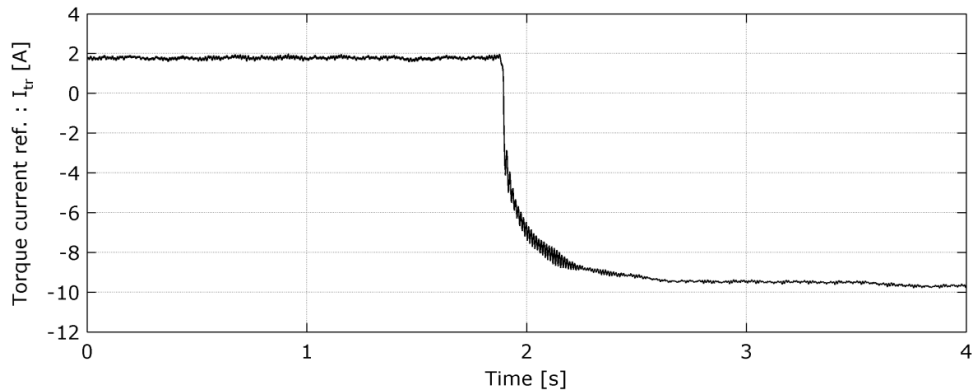
Fig.5.35. Prescribed torque current reference value

5.3.4 Field weakening mode

The rotor speed can be computed directly from the encoder incremental position (i.e. the number of pulses in the given time period - 100 µs), if a low pass filter (L.P.F.) is used. The downside of this method is that a delay of the measured speed arise, which affect the speed error that supply the speed PI controller. The filtering action without any delay is achieved by a phase loop lock (P.L.L) observer, a rather simple but elegant and powerful scheme (Fig. 5.36) [5.16]. A result comparison in the field weakening and speed reversal mode, between the use of a speed PLL (kp =300 , ki=100) and a LPF (tuned at 500 Hz) is shown for speed, phase currents and prescribed torque/field current levels, keeping all the other data unchanged.

The PLL speed observer has been implemented in the Simulink as an S-function (Appendix 9) because it is much easier to deal with integrator saturation compared to block-based design. All the previous experiments for motoring and generating modes have been done using the PLL instead of LPF.

Flux weakening and speed reversal operation is presented in Fig. 5.37-5.42. A lower speed ripple and much stable response can be observed for PLL speed observer case compared to LPF of speed (Figs. 5.37-5.38). Measured phase currents for the two situations with zooming boxes on I_A and I_B at 250 rpm and 500 rpm are shown in Figs. 5.39-5.40.

The ±500 rpm bound (2:1 speed range) is related to limits of the machine (not an optimal design) and not to control system or physical principles, since [5.13] show a 4:1 speed range is achievable by the BLDC-MRM.
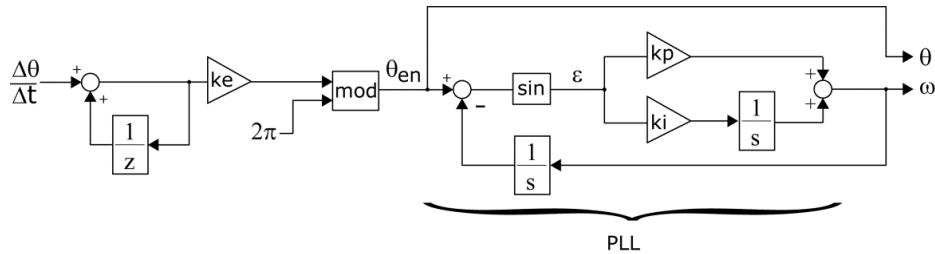
Fig.5.36. Angle and speed computation from delta encoder position from PLL speed observer
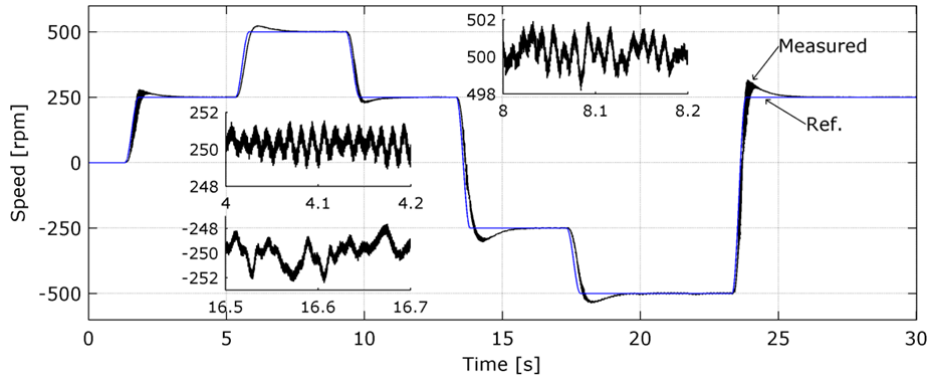
Fig.5.37. BLDC-MRM measured speed at field weakening and speed reversal, with PLL
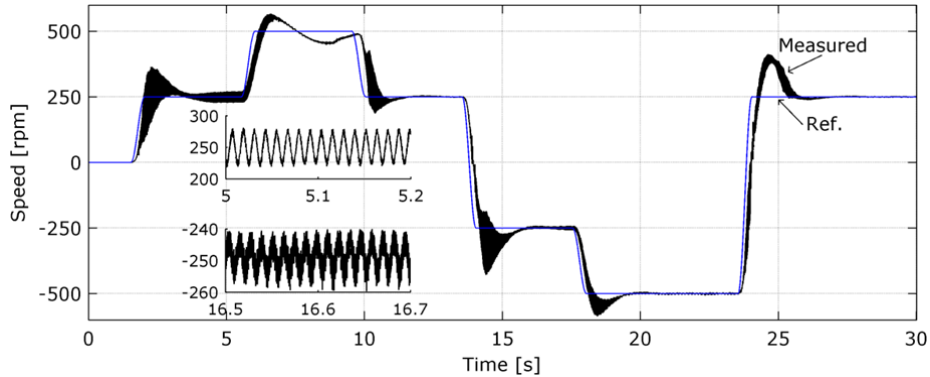
Fig.5.38. BLDC-MRM measured speed at field weakening and speed reversal, with LPF
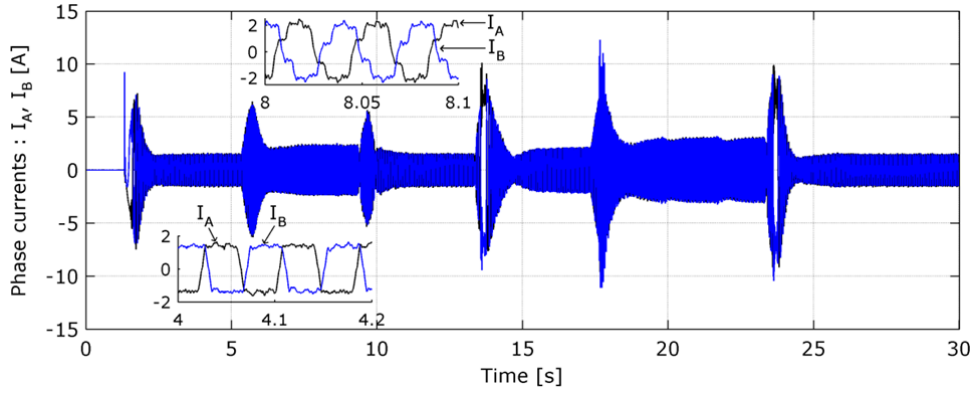
Fig.5.39. Measured phase currents (only two shown: I_A and I_B) , with PLL
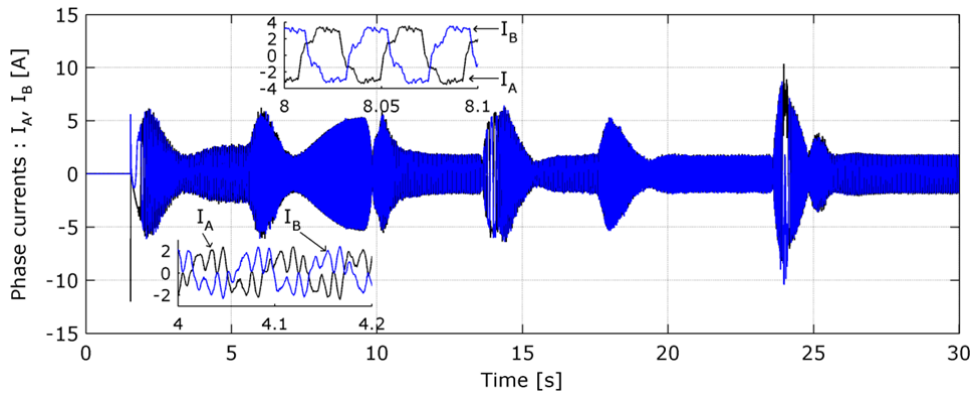
Fig.5.40. Measured phase currents (only two shown: I_A and I_B) , with LPF
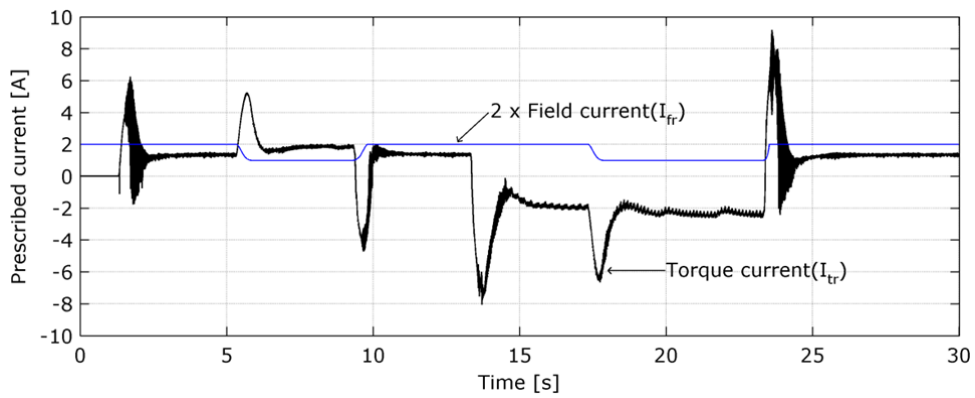
Fig.5.41. Prescribed torque and field current reference values, with PLL
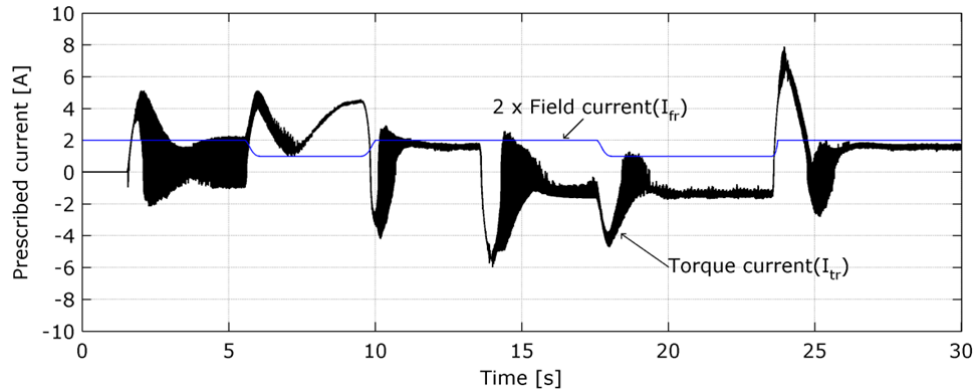
Fig.5.42. Prescribed torque and field current reference values, with LPF

Conclusion

This chapter presents a closed loop speed control for a 5-phase (FB rotor) and a 6-phase (ALA rotor) BLDC-MRM. Numerical simulation results agree with experimental work and validate the machine model and control in both cases.

Steady-state analyses up to a 4:1 speed range was tested on the 5 phase BLDC-MRM using a laboratory custom-made full bridge inverter (controlled by a floating-point 150 MHz DSP), bang-bang current controllers and a PI speed controller. The torque ripple seem a little high at rated conditions, but an optimal FEA-embedded machine design and a thorough study on control (current ramp and phase advance strategies) could improve the situation. The obtained efficiency is considered acceptable at this power-speed since the primary target was the testing of the configuration with minimum cost.

A new control strategy was introduced for the 6-phase BLDC-MRM in order to reduce the drive cost by using a reduced number of switches. The best situation will arise in an odd number of phases BLDC-MRM, since the needed extra inverter leg, for the null current, does not need to be oversized at all by using the phase the presented control. Both transients and steady-steady state operation in the motoring and generating mode were shown; some results never being presented in the past for the BLDC-MRM configuration, including the machine operation as a generator.

The dSPACE platform flexibility allowed more complex experiments to be carried due to its AD-converters, Simulink graphical programming connection and a user friendly data acquisition through Control Desk software.

We should notice that both controls use position information from an encoder and current sensor on each phase. Future work should focus on less current sensors and position sensor-less control for less sensitive applications. Nevertheless this chapter is considered a strong contribution to the subject and a pertinent starting point for future (less sensors/sensor-less) studies.

References

[5.1]   H.A. Toliyat, M.M. Rhimiam and T.A. Lipo, *"A five phase reluctance motor with high specific torque"*, IEEE Trans. On Industry Application, Vol. IA-28, 1992, pp. 659-667

[5.2]   T.A. Lipo, Feng X. Wang, *"Design and Performance of a Converter Optimized AC machine"*, IEEE Trans. On Industry Application, Vol. IA-20, No.4, 1984, pp. 834-844

[5.3]   R. Mayer, H. Mosebach, U. Schroder, H. Weh, *"Inverter-fed multiphase reluctance machine with reduced armature reaction and improved power density"*, in Proc. Of ICEM-1986, Munchen, Part.3, pp. 1138-1141

[5.4]   H. Weh and U. Schroder, *"Static Inverter concepts for multiphase machines with square-wave current-field distribution"*, Proc. EPE Brussel, 1985, pp. 1147 -1152

[5.5]   R. Mayer, H. Mosebach, U. Schroder and H. Weh, *"Inverter-fed multiphase reluctance machine with reduced armature reaction and improved power density"*, in Proc. Of ICEM-1986, München, Part.3, p.1138-1141

[5.6]   E. Levi, *"Multiphase Electric Machines for variable-speed applications",* IEEE Trans. On Industrial Electronics, Vol. IE-55, No.5, 2008, pp. 1893-1909

[5.7]   E. Levi, M. Jones, A. Iqbal, S.N. Vukosavic and H.A. Toliyat, *"Induction Machine/Syn-Rel Two Motor Five-Phase Series Connected Drive"*, IEEE, Trans. On Energy Conversion, Vol. EC-22, No.2, 2007, pp. 281 - 289

[5.8]   M.G. Simoes and P. Vieira, *"A high-torque low-speed multiphase brushless machine-a perspective application for electric vehicles"*, IEEE Trans. On Industrial Electronics, Vol. IE-49, No. 5, 2002, pp. 1154-1164

[5.9]   S. Williamson and S. Smith, *"Pulsating torque and losses in a Multiphase induction machine",* IEEE Trans. On Industry Applications, Vol. IA-39, No.4, 2003, pp. 986-994

[5.10] N. Gule, M.J. Kamper, *"Multiphase Cage-Rotor Induction-Machine Drive With Direct Implementation of Brush DC Operation"*, IEEE Trans. On Industry Applications, Vol. IA-48, No.6, 2012, pp. 2014-2021

[5.11] J. D. Law, A. Chertok and T.A. Lipo,*"Design and performance of field regulated reluctance machine"*, IEEE Trans. On Industry Applications, Vol. IA-30, No.5, 1994, pp. 1185-1192

[5.12] I. Boldea, G. Papusoiu, S.A. Nasar and Z. Fu, *"A novel series connected switched reluctance motor"*,in Proc. of ICEM-1990, Part 3, pp 1212-1217.

[5.13] D. Ursu, P. Shamsi, B. Fahimi and I. Boldea, *"5 phase BLDC-MRM: Design, Control, FEA and Steady-State Operation Experiments,"* International Conference on Optimization of Electrical and Electronic Equipment, OPTIM 2014

[5.14] C. Lascu, I. Boldea and F. Blaabjerg*, "Super-twisting sliding mode control of torque and flux in permanent magnet synchronous machine drives,"* Industrial Electronics Society, IECON 2013, pp. 3171 – 3176.

[5.15] S. Agarlita, D. Ursu, L. Tutelea, I. Boldea and B. Fahimi, *"BLDC multiphase reluctance machines: A revival attempt with 2D FEM investigation and standstill tests"*, Energy Conversion Congress and Exposition (ECCE), 2013 IEEE, pp. 1850 – 1857

[5.16] C. Lascu,*"Direct torque control of sensoreless induction machine drives"* PhD thesis, University "Politehnica" of Timisoara, 2002

6. Experimental test platforms

Abstract

This chapter presents the laboratory setup used for the experiments presented in chapter 5. Both hardware and software components are explained.

Two different platforms were employed for the BLDC-MRM testing. The test-rig for the 5-phase BLDC-MRM is based on a custom (laboratory made) full-bridge inverter, controlled by a TMS320F28335 floating point microcontroller and C-programming (under Code-Composer environment), while the test-rig for the 6 phase BLDC-MRM takes advantage of a graphical programming language (Simulink) connected to an on-line software (Control Desk) that handles a DS1103 dSPACE platform, which in the end drives three commercial (identical) Danfoss inverters.

The chapter ends with description of the 6 phase, 6 poles FB rotor BLDC-MRM designed for wind application, though no experiments were made on this machine yet.

6.1 Five phase BLDC-MRM drive

6.1.1 The machine

In order to reduce the cost of the overall project, the design of the 5 phase BLDC-MRM started from an existent (low speed) 5 phase /6 poles (q=1) PM machine from which we took out the PM rotor and we inserted a new designed rotor.

The stator and rotor lamination sheet main dimensions are presented in Fig. 6.1. The stator core is made up of 0.5 mm thick cold oriented M350-65 A (according to EN 10106-2007) laminations with a total length of 152 mm. The machine exhibits a 5 phase diametrical one layer winding, with a measured phase resistance of 4.7 Ω, and 132 turns/ coil. Obviously this will result in a high torque, low speed machine, due to large phase inductance (measured in Chapter 2).

Rotor design is based on the following requirements: necessity of having two phases out of five acting as field phases (in order to reduce torque pulsations); necessity of a high saliency (for a low armature reaction), resulting in high number of flux barriers; and a thin lamination sheet to reduce iron losses (due to air-gap magnetic flux harmonics). The chosen number of rotor teeth in our case is 9 per pole. A lower number will increase the torque pulsations, while a higher number will reduce mechanical rigidity and raise the rotor lamination cost (since the cutting length increases) [6.1].

The rotor lamination is made of a 0.5 mm thick M350-50A (according to EN 10106-2007) grade steel, which is a good trade-off between price and core loss (3.33 W/kg, at 50 Hz and 1.5 T). Another aspect that should be considered is the saturation of rotor teeth if the ratio bs / bt (see Fig. 6.1) is too large. Considering this ratio equal to 0.5 we can see that the nine rotor teeth (9 x 2.37 mm = 21.33 mm) will manage the flux received from the 3 stator teeth which provide the excitation field (3 x 7 mm = 21 mm). The machine stator and rotor core are shown in Fig. 6.2-6.3.
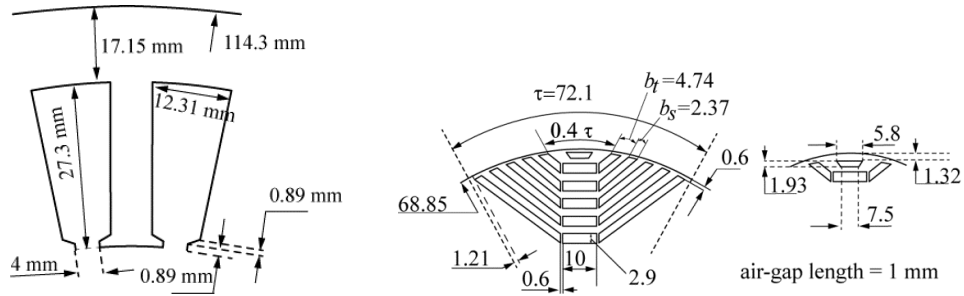
Fig.6.1. Stator lamination sheet (left) and rotor lamination sheet (right) main dimensions
(all in mm)
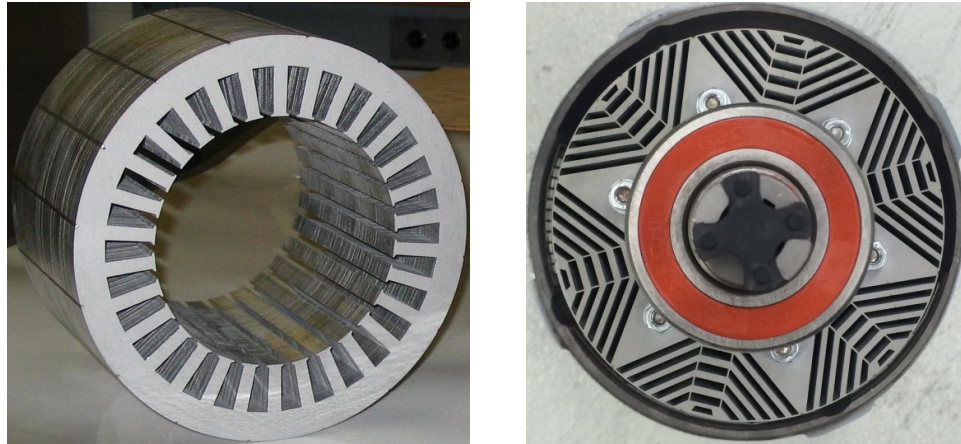
Fig.6.2. Stator core (left) and rotor core (right)
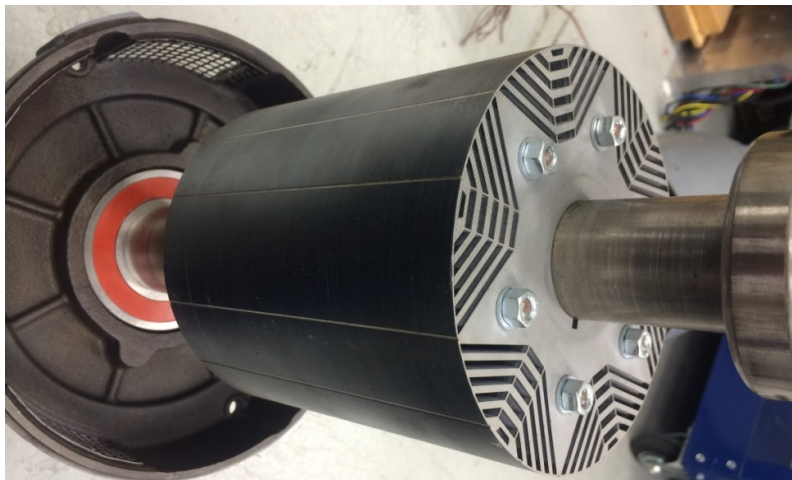
Fig.6.3. Six-poles BLDC-MRM FB rotor

6.1.2 The drive

The operation of a BLDC-MRM requires rotor position information (just as in the case of classical BLDC), which is used to control the frequency of phase currents. The tested drive (Fig. 6.4) consists of the 5 phase BLDC-MRM, that has a 4096 point encoder (CH25-4096 [6.2], Fig. 6.6) at one end, used to provide rotor position and a 3 phase, 4 poles, 15 kW, Doubly Fed Induction Machine (DFIM) coupled through a torque meter (at the other end), acting as a load. The 3 phase DFIM is driven as a 3 phase synchronous generator which supplies a 10 kW, 3 phase electronic load (Fig. 6.6). The power electronic board is custom laboratory made, consisting of a 5 phase forced air-cooled full bridge inverter, controlled by a 150 MHz, floating point microcontroller (TMS 320F28335 [6.3]). The control program was written in Code Composer 5 using C programming language (Appendix 11).

Sample results at two speeds are given in Fig. 6.7. One can notice that three channels were used for current acquisition while the 4th one was used for torque meter information regarding drive torque ripple.
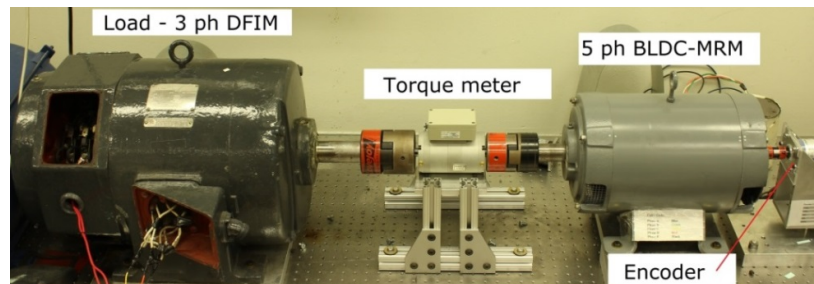
Fig.6.4. Five phase BLDC-MRM test rig
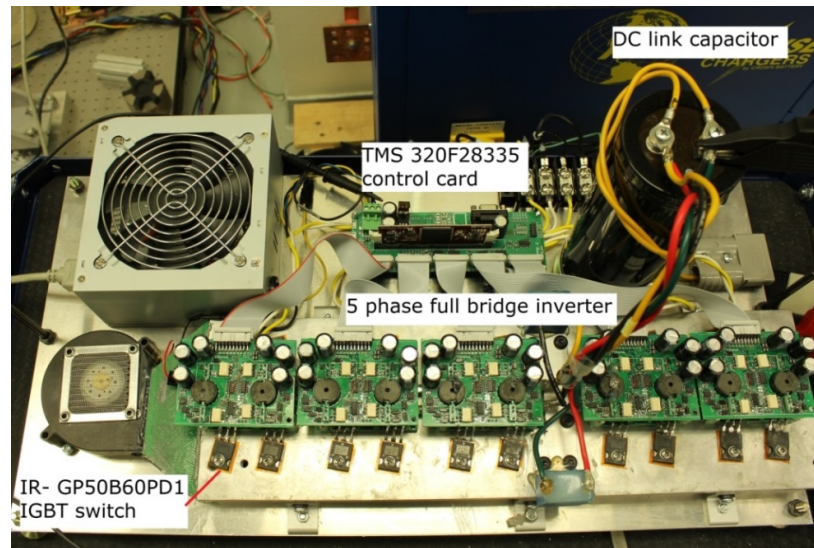
Fig.6.5. Power electronics board – five phase full bridge inverter and control card
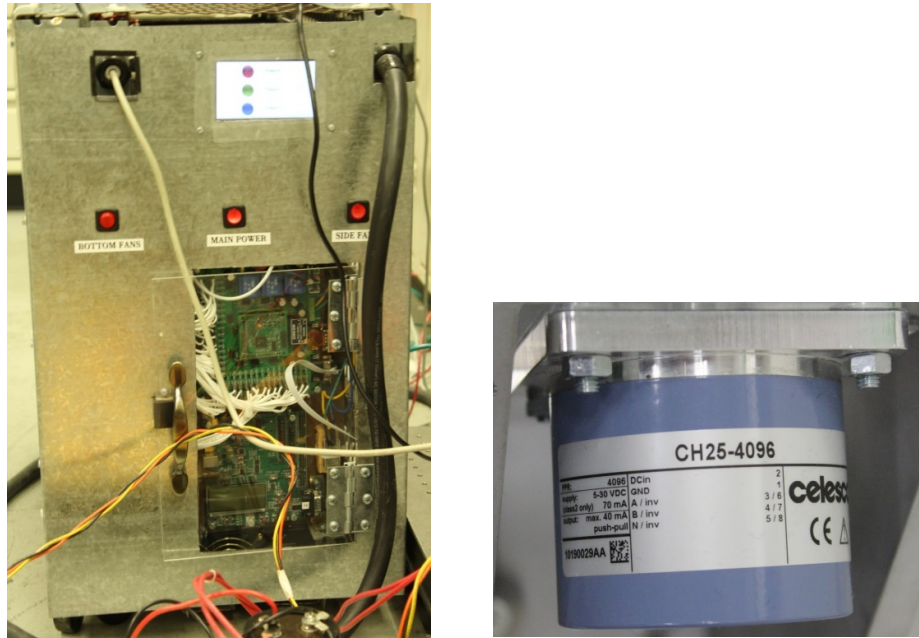
Fig.6.6. Three phase electronic load (left) and encoder (right)
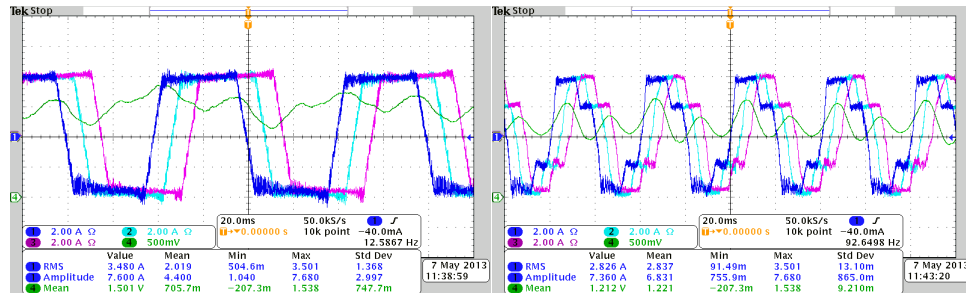
Fig.6.7. Sample results from the 4-chanell (3 for currents and 1 for torque pulsations) oscilloscope at 250 rpm (left) and 500 rpm (right)

6.2 Six phase BLDC-MRM drive

6.2.1 The machine

A 6-phase, 6 pole, 35 Nm, 250 rpm, 1 slot per pole per phase (q = 1) ALA rotor machine was investigated and built (Figs. 6.8) for experimental purpose as explained in [6.4-6.5]. The main dimensions are as follows: tooth width – 6.5 mm, slot width – 2.5 mm, air-gap length – 0.3 mm, slot area – 130 mm^2, stator inner diameter-104 mm, stator outer diameter – 170 mm, core length –145 mm, weight – 18 kg.
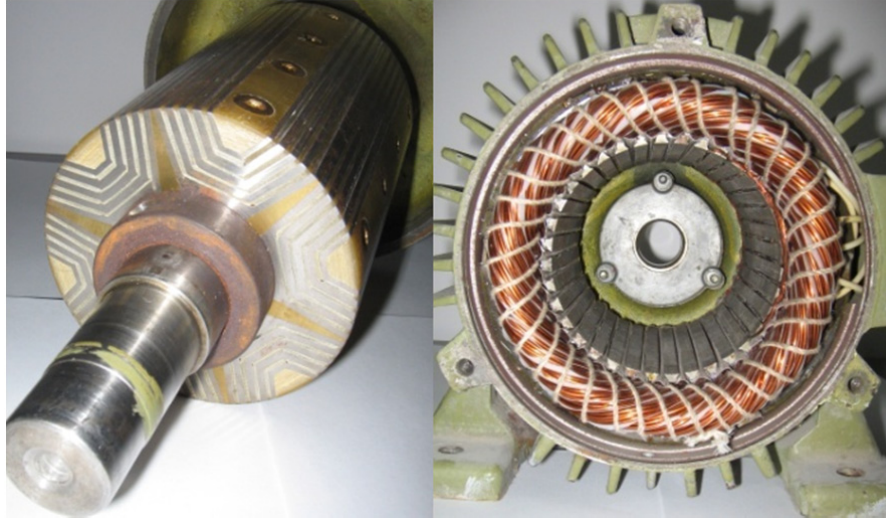
Fig.6.8. Experimental lab model of the 6-phase, 6 poles BLDC-MRM

6.2.2 The drive

A short description of the laboratory equipment used for the carried standstill and running experiments of the 6-phase, ALA rotor, BLDC-MRM is given here from the hardware and software point of view.

6.2.2.1 Hardware

Validation of the FEA standstill torque measurements and phase inductance function of rotor angular displacement (presented in Chapter 2) were done by a comparison with the experimental data provided by the setup from Fig. 6.9. At the maximum torque position the standstill developed torque of the 6 phase BLDC-MRM was computed by multiplying the force measured by the load cell (AEP transducer, type TCS-C2 [6.6]) with the steel bar length connected to the rotor.
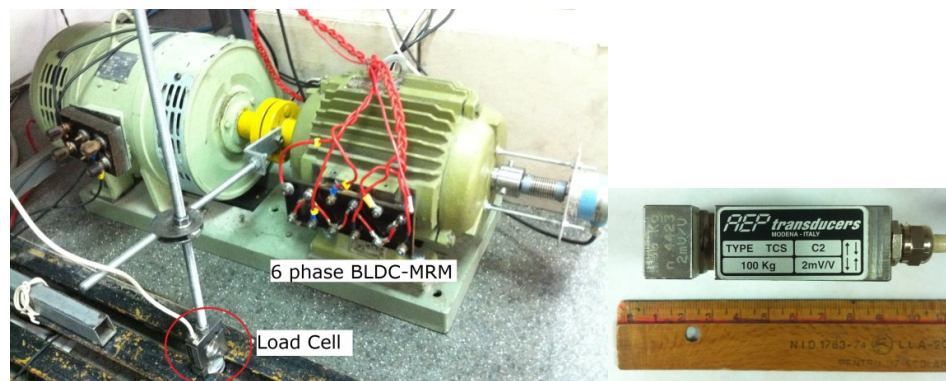
Fig.6.9. Test equipment for standstill torque measurements (left) and the load-cell (right)

The running experiments were done using the experimental test-rig presented in Fig. 6.10. The DC brush machine (plate data presented in section 4.2) was used in a separately excited mode, through two diode rectifiers.

The MRM rotor is coupled to a 5000 points encoder (Telemechanique XCC 151PR50R) connected to dSPACE [6.7,6.8] expansion board (Fig. 6.11).

An adaptation board connected to a 37 pins connector sends the gate and enable signals from the dSPACE to the three inverters through fiber optics (Fig. 6.11- 6.12).

The inverters command board was replaced with an interface and protection card design by dr. C. Lascu, providing full control over the IGBT gate drivers. The 3rd inverter interface board was modified, so that with one signal commands all three legs in a similar way, offering a better inverter protection by dividing the current that need to be handled by switches. The dead-time was set to 2us, while over-voltage (600 V limit), over-current (20 A limit) and over-temperature (100°C) protections watch over possible faults. Seven PWM signals (6 for each phase and one gate signal for null leg voltage regulation), and one enable signal for each converter are used.
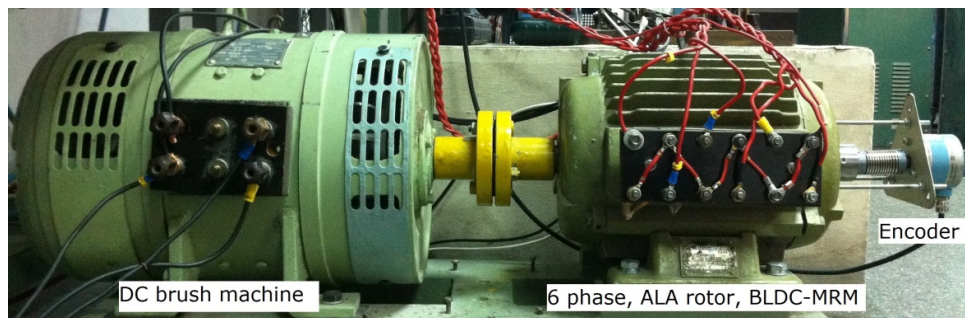
Fig.6.10. Experimental test-rig for the 6 phase BLDC-MRM
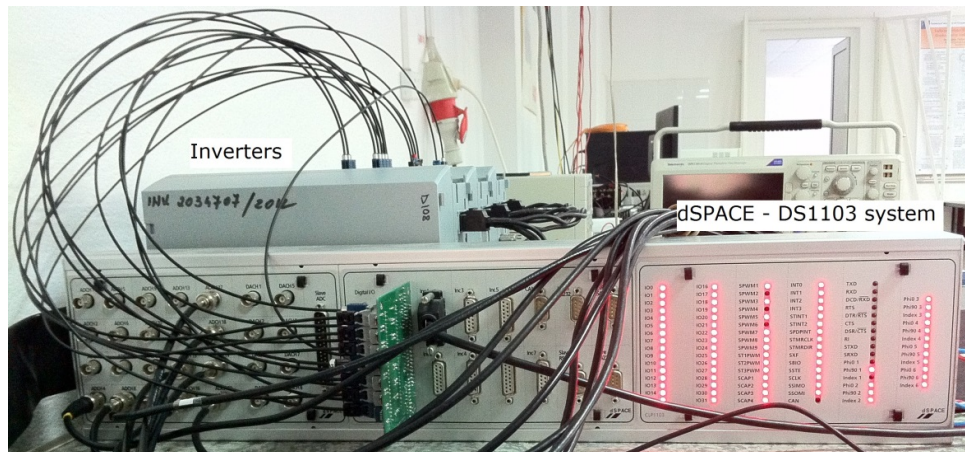
Fig.6.11. dSPACE platform (front) and the three (common DC-link) inverters (back)
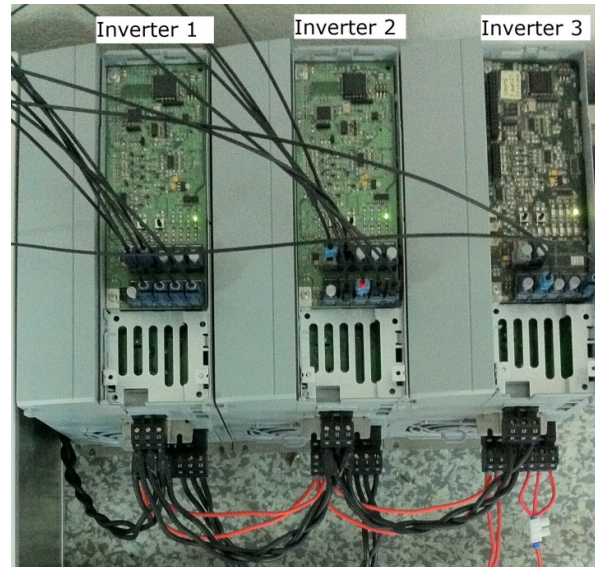
Fig.6.12. Danfoss FC-302P7K5 inverters
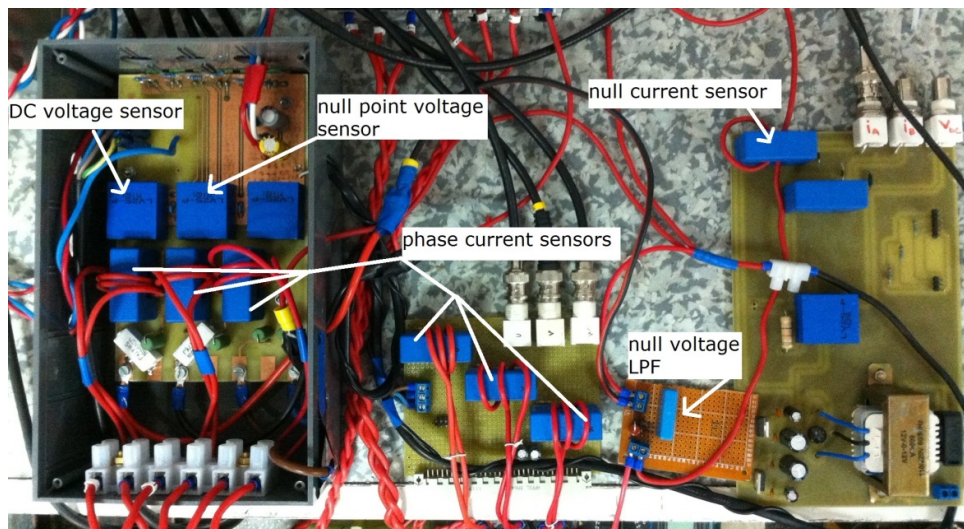
Fig.6.13. Current and voltage measurement setup

A voltage transducer LV25-P [6.9] is used for DC and null phase voltage measurements. Seven current transducers, type LA55-P [6.10] capable of measuring up to 50 A are used to acquire the 6 phase currents for control and the phase null current for monitoring purpose.

6.2.2.2 Software

The dSPACE platform allows rapid control algorithm prototyping by using Matlab/Simulink graphical programming environment and C-code "building" on the dSPACE DSP (TMS320F240). This makes both the algorithm implementation and debugging faster compared to line to line C-coding. dSPACE uses fast I/O ports for acquiring all the information from the external sensors while Real-time interface (RTI) allows a graphical configuration of I/O through Simulink block diagram environment.

The general control scheme is shown in Fig. 6.14 and it basically consists of four main parts: the encoder, the acquisition and scaling, the protections and the control. They will be discussed next.

The encoder delta position is used for angle calculation, after which the speed is estimated by the PLL speed observer (Fig. 6.15).

Current and voltage measurements were done using the ADC available converters that have a sampling time of 16 bit / 4us and 12 bit/800 ns. Current and voltage signal are received (from ADCH ports), scaled and then corrected accounting for the offset (though an S-function, Appendix 10) as can be seen in Fig. 6.16.
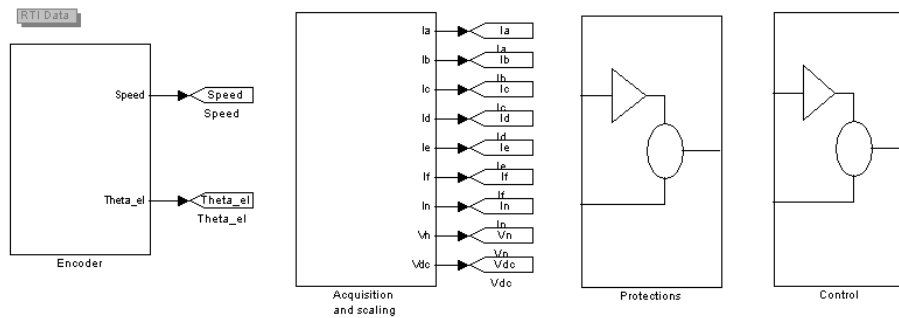
Fig.6.14. BLDC-MRM control scheme
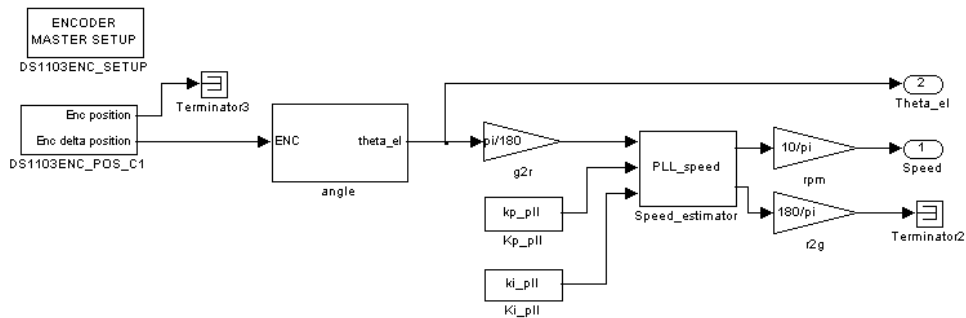
Fig.6.15. Encoder block
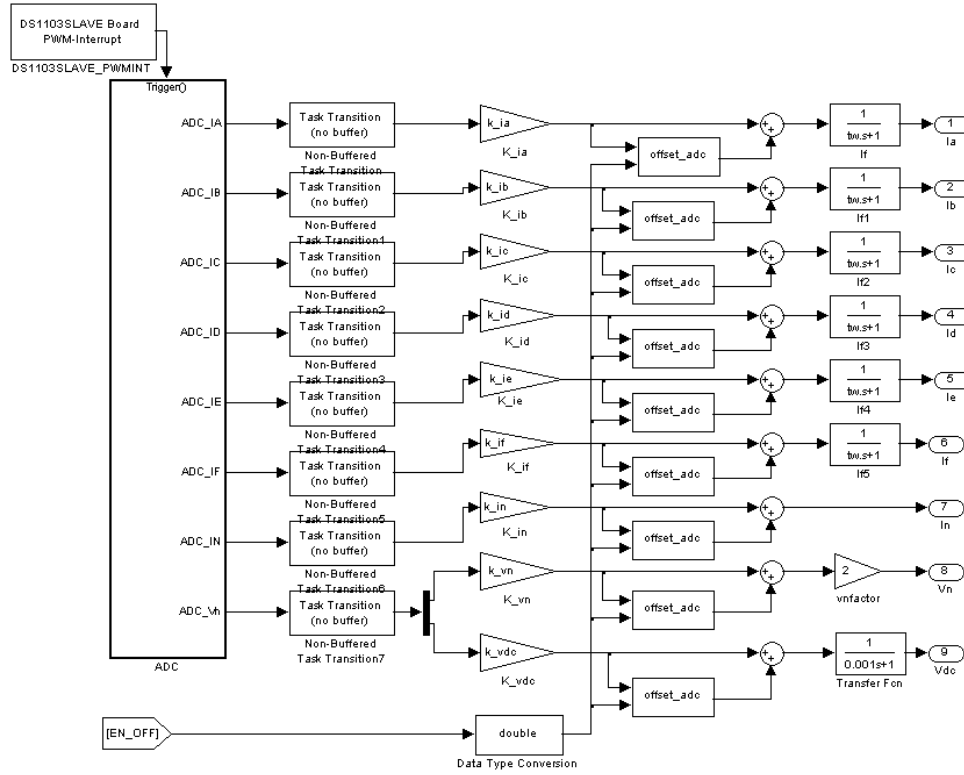
Fig.6.16. Current and voltage acquisition and filtering

The first line of defense against over-current is software implemented (Fig. 6.17), and it should kick in well before hardware protection notice the problem. Any detect fault will cut-off the provided enable signal to inverters.

The closed loop speed control scheme is shown in Fig. 6.18. In the top part the reference torque current value generation from the speed PI controller is presented, while in the bottom part the phase reference currents are created based on rotor position. The duty cycle (Fig. 6.19) is generated for each of the seven PWN signals. The DSP provides 6 complementary PWM channels and 4 independently PWM channels of which we make full use.

Control Desk (Fig. 6.20) is visual interface software that allows us to change or acquire certain variables from our program. The variables can be changed on-line to check the dynamic response of the system.
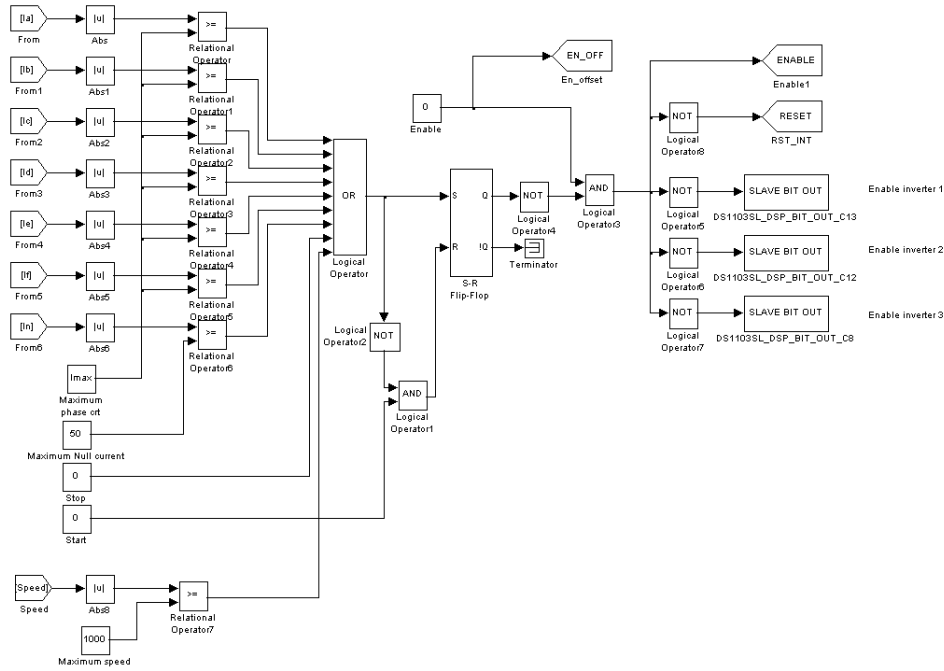
Fig.6.17. Software over-current protection logic
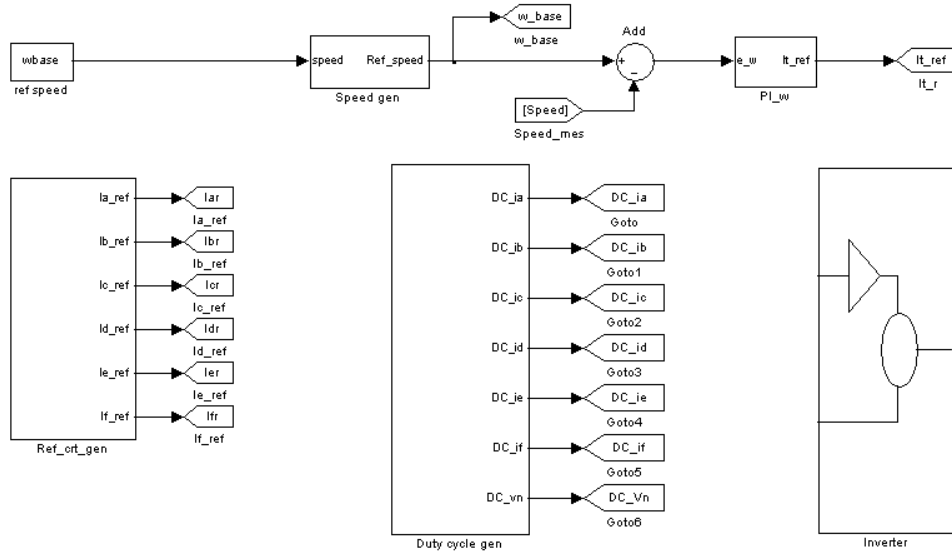
Fig.6.18. Closed loop control block
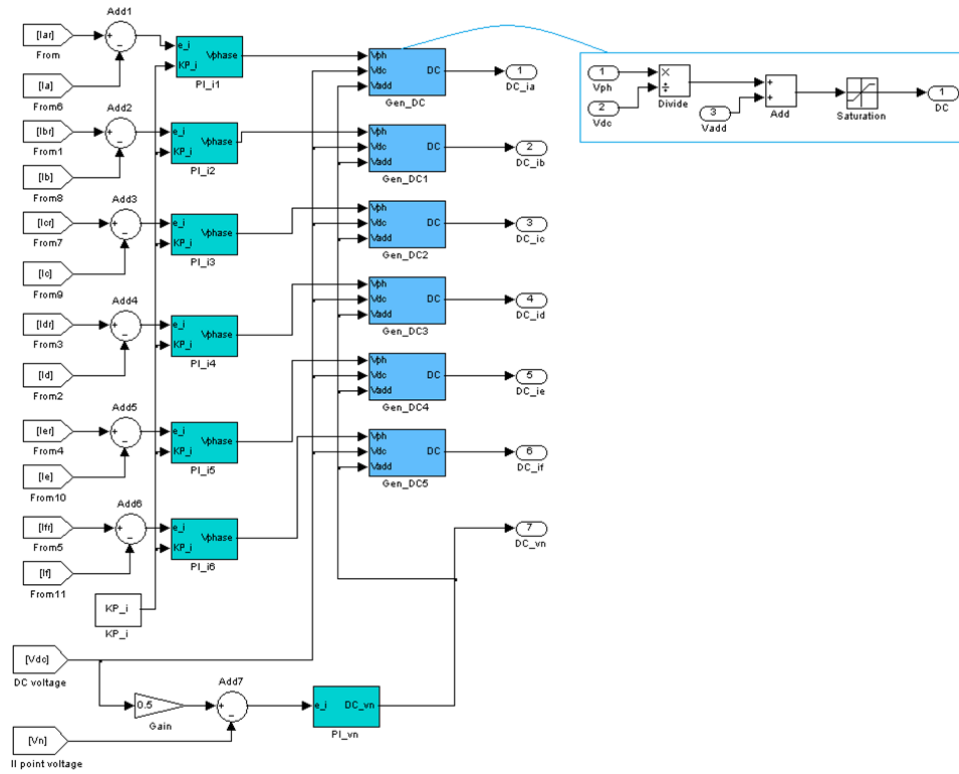
Fig.6.19. Duty-cycle generation
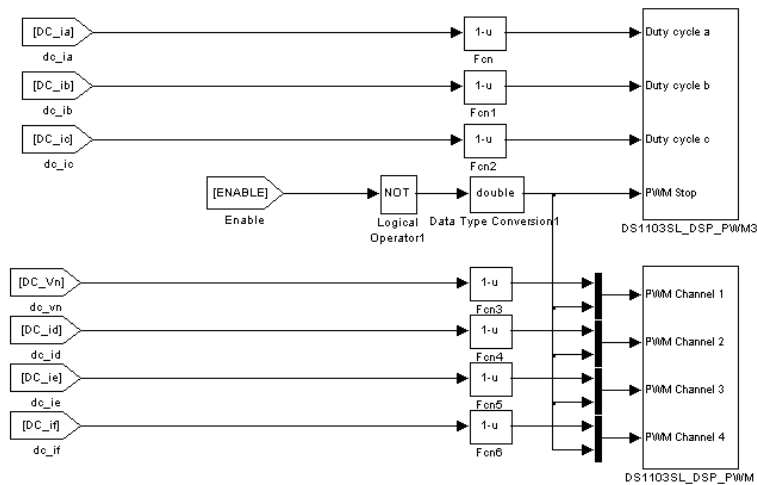
Fig.6.20. PWM interface block
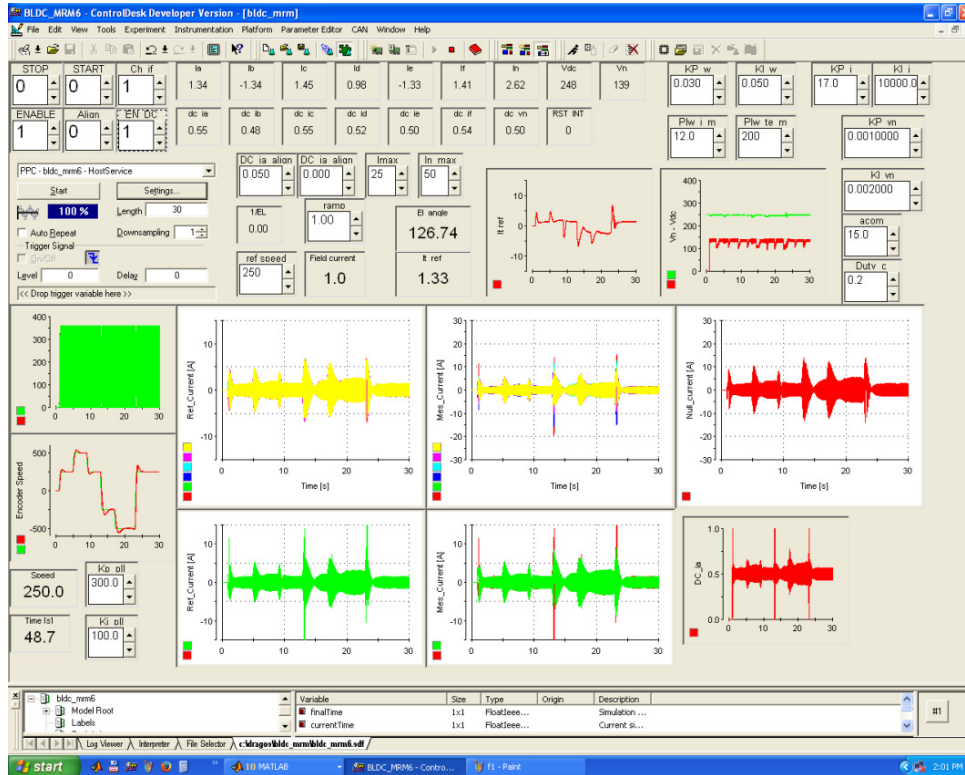
Fig.6.21. Control desk real-time interface – capture of flux weakening mode & speed reversal

6.3 Six phase, 12 poles, 200 Nm, FB – rotor BLDC-MRM

Stator lamination sheet and rotor lamination sheet dimensions (Fig. 6.22-6.23) are presented in the technical drawings from Appendix 12. Rotor dimensions resulted from the design from Chapter 2, starting from an existent stator (Fig. 6.24) for total cost reduction.
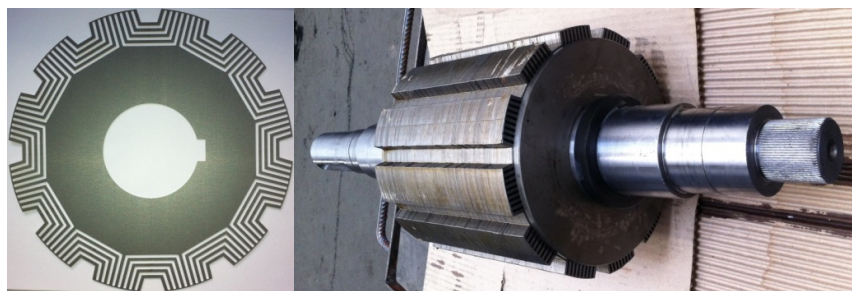
Fig.6.22. Rotor lamination sheet (left) and assembled rotor (right)
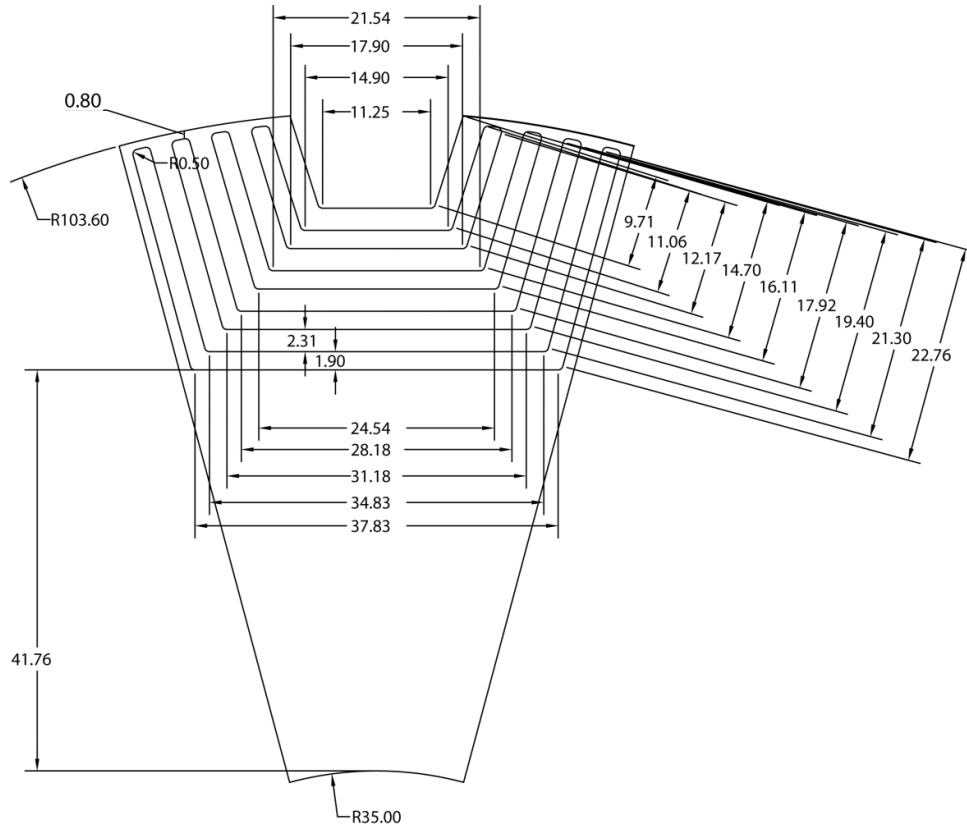
Fig.6.23. Rotor pole main dimensions
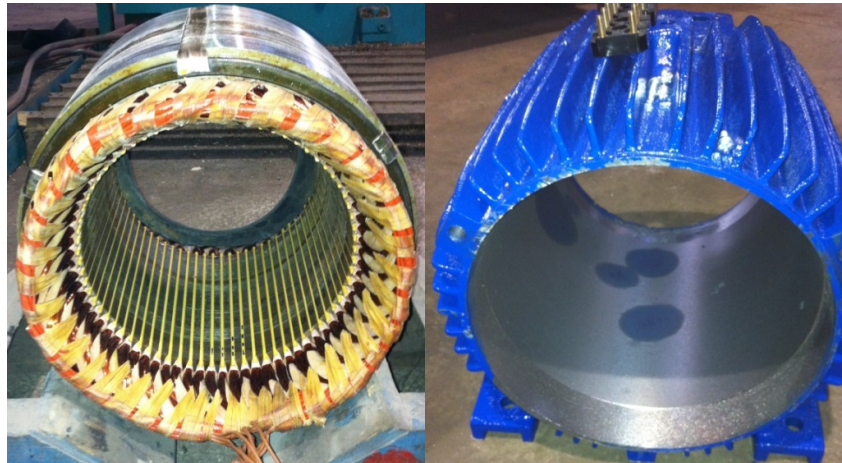
Fig.6.24. Wounded stator core (left) and stator housing

Conclusion

This chapter was dedicated entirely to experimental test benches for the results presented in Chapter 5. Electrical machines and additional hardware components were presented and analyzed mainly for the 5 and 6 phase BLDC-MRM configurations, while software provides a clearer view on the drive control.

The advantages regarding algorithm implementation time and the easiness to pass the control "know-how" from one user to another makes the dSPACE platform an invaluable item in a motion intelligent control research laboratory. If an industrial drive implementation is needed, a deeper knowledge of microcontroller programming and converter design are mandatory for a reliable, cost effective and energy efficient drive development.

The test platform for the 5 phase BLDC-MRM was built at University Texas at Dallas, while for the 6 phase BLDC-MRM was developed at University "Politehnica" of Timisoara.

References

[6.1]   D. Ursu, P. Shamsi, B. Fahimi and I. Boldea, *"5 phase BLDC-MRM: Design, Control, FEA and Steady-State Operation Experiments,"* International Conference on Optimization of Electrical and Electronic Equipment, OPTIM 2014.

[6.2]   www.sentech.nl , Celesto Rotary incremental encoder, CH25-4096

[6.3]   www.ti.com , Texas instruments, TMS320F28335.

[6.4]   L.N. Tutelea, *"Static commutation of the reluctance series motor"*, Diploma project, UPT, Romania, 1989, (in romanian).

[6.5]   I. Boldea, G. Papusoiu, S.A. Nasar and Z. Fu, "*A novel series connected switched reluctance motor*",in Proc. of ICEM-1990, Part 3, pp 1212-1217.

[6.6]   www.aeptransducers.com , AEP Load cell.

[6.7]   www.dspace.com

[6.8]   V.N. Gradinaru, " *dSPACE Working Guide – Work Steps and Applications for Embraco, version 1.0*", august 2008

[6.9]   www.lem.com , Voltage Transducer LV-25P.

[6.10] www.lem.com , Current Transducer LA-55P.

7. Original contributions and future work

7.1 Conclusions

This work was dedicated to design, analysis and control of Brushless DC Multiphase Reluctance Machine drives.

The thesis focused on the following topics:
- BLDC-MRM principle of operation analysis;
- analytical electromagnetic design;
- 2D finite element analysis;
- survey of state of the art stochastic algorithms;
- magnetic equivalent circuit modeling of BLDC-MRM;
- optimal design of the BLDC-MRM;
- electrical and mechanical parameter identification;
- full bridge control using a floating point DSP;
- reduced number of switches control using a dSPACE platform.

Based on the presented results, the main conclusions that can be drawn from this work are:
- Rather high price of high energy density PMs makes the PM-less and less PMs electrical machines essential in various industry applications.
- The BLDC-MRM operation may be explained in relation to the DC commutator machine.
- An electromagnetic design code is needed as a first stage of the machine design, for main geometrical parameters and winding computation. The code is a part of the optimization process later on.
- The machine axial symmetry makes the use of 2D-FEA accurate enough for our purpose as proved by a good agreement between various experiments and simulation results both in magneto-static and steady state (rotating) analysis.
- While 2D-FEA give realistic machine emulation in all tested regimes, the long computation time forces the designer to use other numerical methods for machine performance evaluation in the optimal design code, such as non-linear MEC. Attention should be paid when magnetic circuits are used due to low number of elements and related errors than could appear in torque computation in various positions.
- Meta-heuristic optimization algorithms have overpassed the gradient based ones, due to simpler structure and faster convergence with a greater accuracy to the best solution. PSO is a stochastic algorithm that proved to be a powerful enough to solve problems in various field.
- Optimization process in Electrical machine design is a tricky one because of the existent constraints and discrete space movement of each solution, due to various rounding and technological factors. Strong discontinuities are present which make finding the solution harder. The developed optimal design routine use MEC embedded for machine performance evaluation. MEC

model is much faster than 2D-FEA model and by an intelligent use of data results can be used in initial optimization process.

❖ A simulation model for transient analysis was created and (by using the experimental electrical and mechanical parameters) emulates the machine, drive and the inverter for two different cases.

❖ A 5-phase BLDC-MRM was designed, built and tested in steady-state operation with a 4:1 speed ratio, using a full bridge inverter and a close loop speed control with bang-bang current controllers. The drive measured efficiency was 90 % at 500 rpm.

❖ The 6-phase, 6 poles, ALA rotor BLDC-MRM was driven by commercial (Danfoss) inverters and dSPACE testing platform in all four quadrants of operation, using a reduced number of switches.

❖ A new control strategy was introduced, simulated and tested for the control of the 6 phase machine with null phase connection, based on voltage regulation of the null point, with acceptable dynamics in motoring and generating with field weakening operation.

❖ Using a dSPACE platform for BLDC-MRM control has many advantages over the DSP direct implementation in the initial testing stage of various prototypes, thus dynamic results for motoring and generating were presented for the 6 phase BLDC-MRM.

7.2 Original contributions

From the author point of view, the thesis presents the following original contributions:

✓ Analytical electromagnetic design of a 6 phase, FB rotor, BLDC-MRM as a starting point for optimal design.

✓ Thorough finite element analysis of 5/ 6 phase, ALA/FB rotor BLDC-MRM: field distribution, flux and inductance computation and torque pulsations computation.

✓ Advanced iron loss computation based on Fourier analysis of magnetic flux density variation in each element of the machine model 2D-FEA mesh.

✓ 2D-FEA model validation by static torque, flux and inductance measurements.

✓ Development of a non-linear MEC model of the 6 phase, FB rotor, for steady state analysis of iron loss and electromagnetic torque at base speed operation.

✓ Meta-heuristic optimization algorithms analysis.

✓ BLDC-MRM optimal design using the PSO algorithm and MEC routine for performance evaluation.

✓ Experimental identification of machine inductances through flux decay tests and moment of inertia through run-out tests.

✓ Development of a circuit numerical model for dynamics analysis, based on curve fitting of machine inductances.

✓ Design of a 5 phase, 6 poles, 250 rpm BLDC-MRM. Steady state analysis of this machine was done through a full bridge custom laboratory made inverter. A closed loop speed control was implemented on a floating point DSP. Experimental results (torque, currents and efficiency) are presented and validate the dynamic developed model.

- ✓ Development of a 4 quadrant control method (with flux weakening), for which the null-current is controlled indirectly through the null-point voltage pulsation control to provide symmetric phase current.
- ✓ Experimental validation of the developed control strategy on the 6 phase, ALA rotor BLDC-MRM with acceptable dynamic results.
- ✓ Driving the BLDC-MRM as a generator.
- ✓ Field weakening operation and speed reversal was studied.
- ✓ Two different philosophies were employed in developing two test benches in two laboratories with the existent equipment.

7.3 Future work

Although the thesis analyze the machine from different perspectives, since is only the second major work on this topology after 20 years of dormancy, a few subjects are susceptible to improvement while more have to raised and analyzed. They are briefly described below.

- Improving the accuracy of the dynamic model by replacing the BLDC-MRM (inductance based) model with an embedded Simulink 2D-FEA model or MEC model through an S-function. This could be necessary at high levels of powers (MW) or highly saturated designs.
- Reducing the number of current sensors from m current sensors to 2, one for field and one for torque by using current reconstruction methods. While this could be a solution at small loads and full bridge phase connection, it could represent a problem in a reduced number of switches operation.
- No motion sensor operation.
- A direct comparison of the 6 phase BLDC-MRM with the same machine working as 3 phase RSM (with q=2) in a FOC mode, at the same DC voltage is considered invaluable for inverter voltage utilization analysis.
- Grid connection of the existent 6 phase, 12 poles, FB rotor design BLDC-MRM generator.
- Design of a high speed BLDC-MRM drive for the HEV would prove that this PM-less, low-cost concept could also be a solution for automotive industry. This should also be compared with the reluctance machine with a passive rotor structure, to fully validate the concept.
- Improvement of the BLDC-MRM MEC model for better accounting of the torque pulsations.

Appendices

Appendix 1: Iron loss computation script

```
/ Dragos Ursu  01.05.2013
/ Vector Field Opera 2D v13.0
/ ----------------------------
/ Comand file that computes the iron loss based of the fourier series expansion
/ for the components of flux density at all element centroids.
$string filename '5ph_FB_RM_1000loss'
/
read &filename&.rm case=1 geometry=no
/
mesh DISPLAY=NO ERRORCHECK=NO
SECTION FIXEDASPECT=YES
RECONSTRUCT XMIN=1 XMAX=-1
$constant #doStator
$constant #doRotor  1
$constant #Nharm_start 0
$constant #Nharm 30
$constant #end 360
$constant #Ncases 360
$constant #start 1
$ constant #freq (1000/60)*3
$ constant #tcomp1 0.08/4
$ constant #length #lc*1e-3
$ constant #steel_dens 7650 'kg/m**3'
$ constant #kh 0.0183*#steel_dens
$ constant #ke 2*5.7*1e-5*#steel_dens |/2*alt losses=2*0.4373, for rot losses also

$ dialog START 'Input Data for Iron losses study of BLDC - MRM'
  $ ask #Nharm 'Maximum number of harmonics to be studied'
  $ ask #kh 'Hyst. coeff. kh'
  $ ask #ke 'Eddy current coeff. ke'
$ dialog STOP

$if (#doStator&&#doRotor) eq 1
  $string region A |/ all
$else
  $if #doStator eq 1
    $string region S |/stator
  $elif #doRotor eq 1
    $string region R |/rotor
  $end if
$end if

$do #n #Nharm_start #Nharm 1
 $EXIST '&filename&_BxA%int(#n)_&region&.table' |/ fisierul general
 $if FILEEXISTS eq 1
  $OS DEL '&filename&_BxA%int(#n)_&region&.table'  |/ pt coeficientul A-cos a lui Bx
  $OS DEL '&filename&_BxB%int(#n)_&region&.table'  |/ pt coeficientul B-sin a lui Bx
  $OS DEL '&filename&_ByA%int(#n)_&region&.table'  |/ pt coeficientul A-cos a lui By
  $OS DEL '&filename&_ByB%int(#n)_&region&.table'  |/ pt coeficientul B-sin a lui By
 $end if
$END DO

$do #n #Nharm_start #Nharm 1
/
  EXTRA
```

```
  TABLE  REG1=1  Reg2=*  TYPE=ELEM  MATE=ALL  NOT=ANY  COMP=0.0  NAME=BxA%int(#n)  UNIT=FLUXU
OPTI=NEW NUMB=1 |  Y
  TABLE  REG1=1  Reg2=*  TYPE=ELEM  MATE=ALL  NOT=ANY  COMP=0.0  NAME=BxB%int(#n)  UNIT=FLUXU
OPTI=NEW NUMB=2 |  Y
  TABLE  REG1=1  Reg2=*  TYPE=ELEM  MATE=ALL  NOT=ANY  COMP=0.0  NAME=ByA%int(#n)  UNIT=FLUXU
OPTI=NEW NUMB=3 |  Y
  TABLE  REG1=1  Reg2=*  TYPE=ELEM  MATE=ALL  NOT=ANY  COMP=0.0  NAME=ByB%int(#n)  UNIT=FLUXU
OPTI=NEW NUMB=4 |  Y
/
  SAVETABLE FILE=&filename&_BxA%int(#n)_&region&.table TABLE=BxA%int(#n)
  SAVETABLE FILE=&filename&_BxB%int(#n)_&region&.table TABLE=BxB%int(#n)
  SAVETABLE FILE=&filename&_ByA%int(#n)_&region&.table TABLE=ByA%int(#n)
  SAVETABLE FILE=&filename&_ByB%int(#n)_&region&.table TABLE=ByB%int(#n)
  QUITEXTRA
$END DO

$do #case #start #end 1
   Read case=#case geom=no
$constant #ang (2*pi/(#Ncases))*(#case)
  $do #n #Nharm_start #Nharm 1
       $if #n EQ 0
         $constant #scale 1/(2*PI)
       $else
         $constant #scale 1/(PI)
       $end IF

$constant #sinA (sin(#ang*#n))*((2*PI)/#Ncases)*#scale
$constant #cosA (cos(#ang*#n))*((2*PI)/#Ncases)*#scale
    EXTRA
/
    DELETEEXTRA TABLE 1 *
    LOADTABLE FILE=&filename&_BxA%int(#n)_&region&.table |/ opening file for reading
    LOADTABLE FILE=&filename&_BxB%int(#n)_&region&.table
    LOADTABLE FILE=&filename&_ByA%int(#n)_&region&.table
    LOADTABLE FILE=&filename&_ByB%int(#n)_&region&.table

    $if #doStator EQ 1
      $parameter #Bx (BX*x+BY*y)/sqrt(x**2+y**2)
      $parameter #By (BX*y-BY*x)/sqrt(x**2+y**2)
/     opening files for writing
      TABLE  REG1=1  REG2=35  TYPE=ELEM  MATE=5  NOT=any  COMP=#Bx*#cosA  NAME=BxA%int(#n)
UNIT=FLUXU OPTI=ADD NUMB=1 |/mate=all not=any
      TABLE  REG1=1  REG2=35  TYPE=ELEM  MATE=5  NOT=any  COMP=#Bx*#sinA  NAME=BxB%int(#n)
UNIT=FLUXU OPTI=ADD NUMB=2
      TABLE  REG1=1  REG2=35  TYPE=ELEM  MATE=5  NOT=any  COMP=#By*#cosA  NAME=ByA%int(#n)
UNIT=FLUXU OPTI=ADD NUMB=3
      TABLE  REG1=1  REG2=35  TYPE=ELEM  MATE=5  NOT=any  COMP=#By*#sinA  NAME=ByB%int(#n)
UNIT=FLUXU OPTI=ADD NUMB=4
    $end if

    $if #doRotor EQ 1
      $constant #rmangle (ttime*(2*pi/#tcomp1))/3 |/theta mec
      $parameter         #Bx        ((BX*x+BY*y)/sqrt(x**2+y**2))*cos(#rmangle)+((BX*y-
BY*x)/sqrt(x**2+y**2))*sin(#rmangle)
      $parameter         #By       -((BX*x+BY*y)/sqrt(x**2+y**2))*sin(#rmangle)+((BX*y-
BY*x)/sqrt(x**2+y**2))*cos(#rmangle)

      TABLE  REG1=36  REG2=*  TYPE=ELEM  MATE=3  NOT=any  COMP=#Bx*#cosA  NAME=BxA%int(#n)
UNIT=FLUXU OPTI=ADD NUMB=1
      TABLE  REG1=36  REG2=*  TYPE=ELEM  MATE=3  NOT=any  COMP=#Bx*#sinA  NAME=BxB%int(#n)
UNIT=FLUXU OPTI=ADD NUMB=2
      TABLE  REG1=36  REG2=*  TYPE=ELEM  MATE=3  NOT=any  COMP=#By*#cosA  NAME=ByA%int(#n)
UNIT=FLUXU OPTI=ADD NUMB=3
      TABLE  REG1=36  REG2=*  TYPE=ELEM  MATE=3  NOT=any  COMP=#By*#sinA  NAME=ByB%int(#n)
UNIT=FLUXU OPTI=ADD NUMB=4
    $end if
```

```
/   Save the tables in files
    SAVETABLE FILE=&filename&_BxA%int(#n)_&region&.table TABLE=BxA%int(#n) |     Y
    SAVETABLE FILE=&filename&_BxB%int(#n)_&region&.table TABLE=BxB%int(#n) |     Y
    SAVETABLE FILE=&filename&_ByA%int(#n)_&region&.table TABLE=ByA%int(#n) |     Y
    SAVETABLE FILE=&filename&_ByB%int(#n)_&region&.table TABLE=ByB%int(#n) |     Y
    QUITEXTRA
  $ end do  |/for harmonics
$ end do  |/for cases

  $if (#doStator&&#doRotor) eq 1
   $ constant #Ironloss_total 0
  $else
   $if #doStator eq 1    |/Stator
    $ constant #Ironloss_stator 0
   $elif #doRotor eq 1   |/
    $ constant #Ironloss_rotor 0
   $end if
  $end if
$EXIST '&filename&_Ptotal_&region&.table'
$if FILEEXISTS eq 1
 $OS DEL '&filename&_Ptotal_&region&.table'
$end if
/
EXTRA
  TABLE REG1=1 Reg2=* TYPE=ELEM MATE=ALL NOT=ANY COMP=0.0 NAME=Ptotal UNIT=FLUXU OPTI=NEW
NUMB=5 | Y
QUITEXTRA

$do #n 0 #Nharm  1

  EXTRA
  DELETEEXTRA TABLE 1 4
  LOADTABLE FILE=&filename&_BXA%int(#n)_&region&.table
  LOADTABLE FILE=&filename&_BXB%int(#n)_&region&.table
  LOADTABLE FILE=&filename&_BYA%int(#n)_&region&.table
  LOADTABLE FILE=&filename&_BYB%int(#n)_&region&.table
  QUITEXTRA

  $ parameter #Bh sqrt(BXA%int(#n)**2+BYA%int(#n)**2+BXB%int(#n)**2+BYB%int(#n)**2)
  $ parameter #nfac  1.86
  $ parameter #PHyst #kh*(#n*#freq)*#Bh**#nfac
  $ parameter #Peddy #ke*(#n*#freq)**2*#Bh**2
  $ parameter #ptotal #Physt+#Peddy
$if (#doStator&&#doRotor) eq 1
   intarea reg1=1 reg2=* comp=#ptotal*1e-6
  $ constant #Ironloss_total #Ironloss_total+INTEGRAL
  $ constant #Ironloss_tot_%int(#n) INTEGRAL*#poles*#length
$else
 $if #doStator eq 1    |/ Stator
    intarea reg1=1 reg2=35 comp=#ptotal*1e-6
    $ constant #Ironloss_stator #Ironloss_stator+INTEGRAL
    $ constant #Ironloss_stat_%int(#n) INTEGRAL*#poles*#length
 $elif #doRotor eq 1   |/ Rotor
    intarea reg1=36 reg2=* comp=#ptotal*1e-6
    $ constant #Ironloss_rotor #Ironloss_rotor+INTEGRAL
    $ constant #Ironloss_rot_%int(#n) INTEGRAL*#poles*#length
 $end if
$end if

/-----------------------------------------------------------
EXTRA
 $IF #doStator EQ 1
   TABLE  REG1=1  reg2=35  TYPE=ELEM  MATE=5  NOT=ANY  COMP=#ptotal  NAME=Ptotal  UNIT=FLUXU
OPTI=ADD NUMB=5
 $END IF
```

```
 $IF #doRotor EQ 1
    TABLE  REG1=36  reg2=*  TYPE=ELEM  MATE=3  NOT=ANY  COMP=#ptotal  NAME=Ptotal  UNIT=FLUXU
OPTI=ADD NUMB=5
 $END IF
QUITEXTRA

$end do  |/$do #i O #nh
EXTRA
 SAVETABLE FILE=&filename&_Ptotal_&region&.table TABLE=Ptotal
QUITEXTRA
$open 1 Iron_losses_nt1000.txt overwrite
$format 3 string string='% Harmonic number   Iron loss [W]'
$assign 3
$write 1 +OUTPUT
$assign O
$format 1 type=exp width=O
$format 2 type=string string='      '
$assign 1 2 1 2

$ dialog action=start title='Iron losses'

$if (#doStator&&#doRotor) eq 1
    $displayline 'Total iron losses (stator+rotor)'
$ constant #Ironloss_total #Ironloss_total*#poles*#length
          $displayline 'Total iron losses are : %real(#Ironloss_total) [W]'
    $do #n O #Nharm 1
       $ constant #Pfe_arm_%int(#n) #Ironloss_tot_%int(#n)
       $ write 1 #n #Pfe_arm_%int(#n) +OUTPUT
     $displayline 'Iron losses due to %int(#n) harmonic are : %real(#Pfe_arm_%int(#n))
[W]'
/
    $end do
 $ write 1 #n-#n #Ironloss_total +OUTPUT
$else
/-----------------------------
 $if #doStator eq 1   |/Stator
    $displayline 'Stator Iron losses'
  $ constant #Ironloss_stator #Ironloss_stator*#poles*#length
        $displayline 'Stator iron losses are : %real(#Ironloss_stator) [W]'
    $do #n O #Nharm 1
       $ constant #Pfe_arm_%int(#n) #Ironloss_stat_%int(#n)
       $ write 1 #n #Pfe_arm_%int(#n) +OUTPUT
     $displayline 'Iron losses due to %int(#n) harmonic are : %real(#Pfe_arm_%int(#n))
[W]'
/--
    $end do
 $ write 1 #n-#n #Ironloss_stator +OUTPUT
$elif #doRotor eq 1   |/ Rotor
    $displayline 'Rotor Iron losses'
  $ constant #Ironloss_rotor #Ironloss_rotor*#poles*#length
          $displayline 'Rotor iron losses are : %real(#Ironloss_rotor) [W]'
    $do #n O #Nharm 1
       $ constant #Pfe_arm_%int(#n) #Ironloss_rot_%int(#n)
       $ write 1 #n #Pfe_arm_%int(#n) +OUTPUT
     $displayline 'Iron losses due to %int(#n) harmonic are : %real(#Pfe_arm_%int(#n))
[W]'
/
    $end do
 $ write 1 #n-#n #Ironloss_rotor +OUTPUT
 $end if
$end if
$close 1
$ dialog action=stop
/ end of comi file
```

Appendix 2: MEC code

```
% MEC model of BLDC-MRM
% Dragos Ursu  20.06.2014
% ======================
function [Pfe, lamM, Te] = MEC_opt(variable)
    Ns = variable.Ns;
    poles = variable.poles ;
    fb = variable.fb;
    npack = variable.npack  ;
    hag = variable.hag  ;
    sByokesp = variable.sByokesp  ;
    sBtoothsp = variable.sBtoothsp  ;
    rByokesp = variable.rByokesp  ;
    rBtoothsp = variable.rBtoothsp  ;
    sDi = variable.sDi  ;
    sDo = variable.sDo  ;
    rDi = variable.rDi  ;
    rDo = variable.rDo  ;
    taus = variable.taus  ;
    taur = variable.taur;
    sMs = variable.sMs  ;
    bzr = variable.bzr  ;
    biz = variable.biz  ;
    sh4 = variable.sh4  ;
    sh3 = variable.sh3  ;
    sh1 = variable.sh1  ;
    sW3 = variable.sW3  ;
    stype = variable.stype ;
    if stype == 'a'
        sR = variable.sR ;
    elseif stype == 'b'
        sW1 = variable.sW1 ;
    end
    bz = variable.bz ;
    lc = variable.lc ;
    shy = variable.shy ;
    shOA = variable.shOA ;
    br_t = variable.br_t ;
    hr = variable.hr ;
    taur = variable.taur ;
    It = variable.It;
    CpS = variable.CpS ;
    yrt = variable.yrt ;
    xrt = variable.xrt;
    xlength = variable.xl;
    ylength = variable.yl;
% -------------------------------------------
Int_mat1 = diag(ones(1,11));
Int_mat2 = diag(-ones(1,10),-1);
Mtmmf = [Int_mat1+Int_mat2,zeros(11,1);ones(1,12)]; Mtmmf(1,12)=-1;
Ns = 2 * Ns / poles;
Nr = 4 * npack + 2;
% ---------------
constants;
nitermax = 50;
BerrorM  = 1e-3;
Bn = [sByokesp*ones(12,1);  sBtoothsp*ones(12,1);  1.5*ones(16,1);  rBtoothsp*ones(18,1);
rByokesp*ones(4,1)]; %T initial value
BerVect = zeros(size(Bn));
Dag = (sDi+rDo)/2;
wst = taus-sMs;
wrt = taur;
c1 = poles * 0.5;
gamat = c1  * (wst + wrt + sMs + biz) / Dag; %
```

```
gamatp= c1  * abs(wst-wrt) / Dag;       %
sh = [sh4 sh3 sh1];
if  strcmp(stype,'a')
    sw = [sMs 0.5*(sW3+sMs) 0.5*(sW3+2*sR)]*1e-3;
elseif strcmp(stype,'b');
    sw = [sMs 0.5*(sW3+sMs) 0.5*(sW3+2*sW1)]*1e-3;
end
As_leak = sh * lc *1e-6;
Aag_t = lc*min(wrt,wst)*1e-6; % maximum tooth area
% stator tooth permeance
if  strcmp(stype,'a')
    As_teeth = [bz*lc, (bz+sR)*lc]*1e-6; % teeth areas
    ls_teeth = [(shOA-sR), sR]*1e-3;
elseif strcmp(stype,'b')
    As_teeth = [bz*lc, bz*lc] *1e-6; % teeth areas
    ls_teeth = [shOA, shOA] *1e-3;
end
As_yoke = lc * shy * 1e-6; % stator yoke area
Ar_teeth = lc * bzr * 1e-6;
Ar_bridge = lc * br_t * 1e-6;
Ar_yoke = lc * ( hr-rDi) * 0.5 *1e-6;
lr_yoke  = (pi*(hr+rDi) * 0.5 * 1e-3) / (2 * poles);

c = (sMs/wst) / log(1+(sMs/wst)); % fringing coefficient

Gagmax = mu_0 * Aag_t * cf / (hag * 1e-3);
G_sy = mu_0 * Ns * As_yoke/(pi*(sDo-shy)*1e-3);
G_st = mu_0 / sum(ls_teeth./As_teeth);
%compute G stator leakage
G_sle = mu_0 / sum(sw./As_leak);
Gsl  = G_sle * ones(12,1);
%compute G rotor bridge
G_rb = mu_0 * Ar_bridge/(taur*1e-3);
%compute G rotor tooth
G_rt   =   mu_0   *   1e3   *   Ar_teeth./[yrt(1),yrt(2:5)+xrt(2:5),yrt(5:-1:2)+xrt(5:-
1:2),yrt(1),yrt(2:5)+xrt(2:5),yrt(5:-1:2)+xrt(5:-1:2)]';
%compute G rotor yoke
G_ry = mu_0 * Ar_yoke/lr_yoke;
%compute G rotor leakage
xcomp =  fliplr(xlength) * 1e-3; %need draw
ycomp =  fliplr(ylength) * 1e-3; %need draw
length = xcomp + ycomp;
As_leak = lc * 1e-3 * [length,length]' ;
Grl = mu_0 * As_leak / (biz * 1e-3);
%
iArea     =    1./[As_yoke*ones(12,1);    As_teeth(1)*ones(12,1);    Ar_bridge*ones(16,1);
Ar_teeth*ones(18,1); Ar_yoke*ones(4,1)];
mu_r = mure(Bn);
%------------------
G_ag  = zeros(Ns,Nr);
Nr1  = ceil(Nr * 3/2) +1 ;
% ------ init -------------------------------------------------------
Bsy = zeros(1,121);
Bst = zeros(1,121);
Brb = zeros(1,121);
Brt = zeros(1,121);
Bry = zeros(1,121);
Te_c = zeros(1,121);
Bpfe = zeros(62,1);
%---------------------------------------------------------
kacci = 0.44;
L = 0;
ip = 0;
del = 3;
T   = 360 ;
%-----------------------------
```

```
for th = ip : del : T+ip
    gama0 = mod(th * rad , 2*pi);
    Loop  = 0;
        L = L + 1;
%------ write air-gap permeance matrix ---------------
    G_ag_o = G_ag;
for ii = 1 : Ns
    for jj = 1 : Nr
            gamas = 2*pi*(ii-1)/Ns;
        if jj<=5
            gamar = 2*pi*(jj-1)/Nr1;
        elseif jj>5 && jj<=14
            gamar = 2*pi*(jj-1)/Nr1 + pi/3;
        else
            gamar = 2*pi*(jj-1)/Nr1 + 2*pi/3;
        end
        gama = gama0 + gamas - gamar;
        if gama > 2*pi
            gama = gama - 2 * pi;
        elseif gama < 0
            gama = gama + 2 * pi;
        end
        if gama < gamat
            if gama <= gamatp
                Gag = Gagmax;
            else
                Gag = Gagmax/2*(1+cos(pi*(gama-gamatp)/(gamat-gamatp)));
            end
        elseif gama > 2*pi-gamat
            if gama > 2*pi-gamatp
                Gag = Gagmax;
            else
                Gag = Gagmax / 2 * (1+cos(pi*(gama-2*pi+gamatp)/(gamat-gamatp)));
            end
        else
            Gag = 0;
        end
        G_ag(ii,jj) = Gag;
    end % for Nr
end % for Ns
   k = 165+60; %th = -th;
   ph1 = trap(th+k);      ph2 = trap(th+k+330); ph3 = trap(th+k+300);
   ph4 = trap(th+k+270);  ph5 = trap(th+k+240); ph6 = trap(th+k+210);
   Fc = [ph4 ph3 ph2  ph1 -ph6 -ph5 -ph4 -ph3 -ph2 -ph1 ph6 0]' * It * CpS ;
Berror = 1; kacc = kacci;
close all;
% compute the potentials accounting for BH curve
while ((Berror > BerrorM) && (Loop < nitermax))
      mur_calc = mure(Bn);
      mu_r = mu_r + kacc * (mur_calc - mu_r);
% compute only nonlinear permeances
    Gsy = mu_r(1:12)  * G_sy;
    Gst = mu_r(13:24) * G_st;
    Grb = mu_r(25:40) * G_rb;
    Grt = mu_r(41:58).* G_rt;
    Gry = mu_r(59:62) * G_ry;
% Permeance matrix asembly
    Gy1 = circshift(Gsy,1);
    Ss  = Gsy + Gy1 + Gst;
    Gy2 = diag(Gsy(1 : end -1), 1);
    Gy3 = diag(Gsy(1 : end -1),-1);
M1  = diag(Ss) - Gy2 - Gy3;
M1(12,1) = -Gsy(12); M1(1,12) = -Gsy(12);
M2  = -diag(Gst);
%
```

```
Sat=[sum(G_ag(1,:));    sum(G_ag(2,:));    sum(G_ag(3,:));    sum(G_ag(4,:));    sum(G_ag(5,:));
sum(G_ag(6,:)); ...
    sum(G_ag(7,:));    sum(G_ag(8,:));    sum(G_ag(9,:));    sum(G_ag(10,:));    sum(G_ag(11,:));
sum(G_ag(12,:)) ];
Sag = 2*Gsl+Gst+Sat;
Gsle1 = diag(Gsl(1:end-1),1);
Gsle2 = diag(Gsl(1:end-1),-1);
M3   = diag(Sag)-Gsle1-Gsle2;
M3(12,1)=-Gsl(12); M3(1,12)=-Gsl(12);
Mf1 = [M1 M2 zeros(12,30);M2 M3 -G_ag zeros(12,12)]; % 24 x 54
%prepare Sr
Sat  =[sum(G_ag(:,1));    sum(G_ag(:,2));    sum(G_ag(:,3));    sum(G_ag(:,4));    sum(G_ag(:,5));
sum(G_ag(:,6)); sum(G_ag(:,7)); sum(G_ag(:,8)); sum(G_ag(:,9)); ...
    sum(G_ag(:,10));  sum(G_ag(:,11));  sum(G_ag(:,12));  sum(G_ag(:,13));  sum(G_ag(:,14));
sum(G_ag(:,15)); sum(G_ag(:,16)); sum(G_ag(:,17)); sum(G_ag(:,18))];
Sr1 = [Grb(16); Grb(1:12); Grb(12:16)];
Sr2 = [Grb(1:4);0;0;Grb(5:11);0;0;Grb(13:15)];
Mgrb= [Grb(1:4);0;Grb(5:12);0;Grb(13:15)];
Mgrb1=diag((Mgrb),1); Mgrb2=diag((Mgrb),-1);
%write Sr
Sr = Sat+Sr1+Sr2+Grt;
%write M4
M4 = diag(Sr)-Mgrb1-Mgrb2;
M4(1,18) = -Grb(16);
%prepare M5,6
Mrt1=[Grt(1),     zeros(1,4);    zeros(1,4),    Grt(2);    zeros(1,3),     Grt(3),0;
zeros(1,2),Grt(4),zeros(1,2);0,Grt(5),zeros(1,3);...
    0,Grt(6),zeros(1,3);  zeros(1,2),Grt(7),zeros(1,2);zeros(1,3),  Grt(8),0  ;zeros(1,4),
Grt(9)];
Mrt2=[Grt(10),    zeros(1,5);    zeros(1,4),    Grt(11),0;    zeros(1,3),    Grt(12),zeros(1,2);
zeros(1,2),Grt(13),zeros(1,3);0,Grt(14),zeros(1,4);...
    0,Grt(15),    zeros(1,4);    zeros(1,2),Grt(16),zeros(1,3);zeros(1,3),    Grt(17),zeros(1,2)
;zeros(1,4), Grt(18),0];
M5=-[Mrt1,zeros(9,7);zeros(9,6), Mrt2];
M6=-[Mrt1',zeros(5,9);zeros(1,18);zeros(6,9),Mrt2'];
%prepare M7
Mgrl=[0; Grl(1:4); Gry(2);0;Grl(5:8)];
Mgrl1 = diag(Mgrl,1);
Mgrl2 = diag(Mgrl,-1);
Sr1=[Grt(1);Grt(5:-1:2);Gry(1:2);Grt(14:-1:11);0];
Sr2=[Gry(1);Grt(6:9);Gry(2:3);Grt(15:18);0];
Sr3=[Gry(4); Grl(1);Grl(1:4);0; Grl(5); Grl(5:7);0];
Sr4=[0;0;Grl(2:4);0;0;0;Grl(6:8);0];
Sr=Sr1+Sr2+Sr3+Sr4;
M7=diag(Sr)-Mgrl1-Mgrl2; M7(1,6)=-Gry(1);  M7(6,1)=-Gry(1);  M7(12,1)=-Gry(4); M7(12,7)=-
Gry(3);
M7(1,12)=0; M7(7,12)=0; M7(11,12)=0;
Gmain = [Mf1;zeros(18,12),G_ag',M4,M5;zeros(12,24),M6,M7];
Gmain = Gmain(1:end-1,1:end-1);
Ft = Mtmmf \ Fc;
Xt(:,L) = Ft; % tooth mmf
% generate the flux vector
Flux = [Ft.*Gst; -Ft.*Gst; zeros(29,1)];
%compute the node potentials
Vn = Gmain \ Flux;
% Nonlinear permeances
Gnonlin = [Gsy; Gst; Grb; Grt; Gry];
Vn1 = [Vn(1:12);Vn(1:12);Vn(25:28);Vn(30:37);Vn(39:42);Vn(25:42);Vn(43);Vn(48);Vn(49);0];
Vn2   =   [Vn(2:12);Vn(1);Vn(13:24)+Ft;Vn(26:29);Vn(31:38);Vn(40:42);Vn(25);Vn(43);Vn(47:-
1:44);...
    Vn(44:47);Vn(49);Vn(53:-1:50);Vn(50:53);Vn(48);Vn(49);0;Vn(43)];
% Compute the flux and iron Magnetic Flux Density
Flux_i = (Vn2-Vn1) .* Gnonlin;
Bnew   = Flux_i .* iArea;
% prof Tutelea code
%-----------------------------------------------
```

```
Berror_o  = Berror;
BerVect_o = BerVect;
BerVect   = Bnew - Bn;
error_prod= BerVect_o .* BerVect;
Berror    = norm(BerVect) / norm(Bnew);
if((Loop>1)&&((Berror>=Berror_o)&&(mean(error_prod)<0)))
    kacc = max(0.8*kacc,0.01); end
if(min(error_prod)>=0)
    kacc = min(1.1*kacc,1);     end
Bn = Bn + min(kacc*abs(BerVect),kacc).*sign(BerVect);
Loop = Loop+1;
end % while
%-------------------------------
 s = 0;
 for ii = 1 : Ns
    for jj = 1 : Nr
      s = s +  (Vn(12+ii) - Vn(24+jj))^2* (G_ag_o(ii,jj) - G_ag(ii,jj));
    end
end
 Te_c(L) = s * poles / (2 * del * rad) ;
 Te = max (Te_c);
   %-------------------------------------------------------------
% Save B at each time step for Iron loss comp
Bsy(L) = Bnew(1);
Bst(L) = Bnew(13);
Brb(L) = Bnew(25);
Brt(L) = Bnew(41);
Bry(L) = Bnew(59);
% -------------------------------------------------------------
end
% ============================================================================
msy = As_yoke * pi * (sDo - shy) * 1e-3 * iron_density;
mst = As_teeth(1) * ls_teeth(1) * iron_density * Ns;
mrb = Ar_bridge * taur *1e-3 * iron_density * 16 * poles / 2;
mrt    =     sum(Ar_teeth.*    1e-3   *    [yrt(1),yrt(2:5)+xrt(2:5),yrt(5:-1:2)+xrt(5:-
1:2),yrt(1),yrt(2:5)+xrt(2:5),yrt(5:-1:2)+xrt(5:-1:2)]') * iron_density * poles / 2;
mry = Ar_yoke * lr_yoke * iron_density * 2 * poles ;
lamM = msy + mst + mrb + mrt + mry;
% ============================================================================
Bsy = max(abs(Bsy)); %sqrt(mean(Bsy.^2));
Bst = max(abs(Bst)); % sqrt(mean(Bst.^2));
Brb = max(abs(Brb)); % sqrt(mean(Brb.^2));
Brt = max(abs(Brt)); % sqrt(mean(Brt.^2));
Bry = max(abs(Bry)); % sqrt(mean(Bry.^2));

lam_thick = 0.5e-3;                                        %lamination thickness
pfe10 = 3;                                                 % W/kg la 1 T si 50 Hz
ke  = pi^2 * lam_thick^2 * iron_cond / (6 *iron_density) ;     % W/kg, ke = pi^2 * d^2 *
kh  = 140 / iron_density;                                  % W/kg, kh = 140 W/m3
kf1 = pfe10 * ke  * (fb/50)^2;
kf2 = pfe10 * kh  * (6*fb/50)^2;
% kf2 = pfe10 * kh  * (fb/50)^1.1;
af = 2;%1.92;
Psy = (Bsy^2 * kf1 + Bsy^af * kf2 ) * msy;
Pst = (Bst^2 * kf1 + Bst^af * kf2 ) * mst;
Prb = (Brb^2 * kf1 + Brb^af * kf2 ) * mrb;
Prt = (Brt^2 * kf1 + Brt^af * kf2 ) * mrt;
Pry = (Bry^2 * kf1 + Bry^af * kf2 ) * mry;
Pfe = Psy + Pst + Prb + Prt +Pry;
% -------------- end of script -----------------------------------
```

Appendix 3: BHBO algorithm

```
% BHBO algorithm main file
% Dragos Ursu  13.01.2013
% ----------------------------
% BLACK HOLE BASED OPTIMIZATION
%=======================================================================
% based on paper
% "      Houssem R.E H. Bouchekara,
% "Optimal design of Electromagnetic Devices Using a BHBO Technique",
% IEEE Trans. on Mag. vol. 49, no. 12, Dec. 2013
%=======================================================================
% x_best = Black Hole position, i_gbest = Black hole number,
%-----------------------------------------------------------------------
function [x_gbest, fbest, fbest_i] = BHBO(variables)

    N = variables.N;
    P = variables.Planets;
    P_i = variables.Planets_i;
    x0 = variables.x0;
    IterM = variables.IterM;
    lb = variables.lb;
    ub = variables.ub;
    ObjFct = variables.ObjFct;
    str = func2str(ObjFct);
    time = variables.time;
    %------------------------------------------------------------
    [x, x_gbest, i_gbest, P_gbest] = Initialization(ObjFct,P, P_i, N, lb,ub,x0);
    %------------------------------------------------------------
    for iter = 1 : IterM
        P_gbesto = P_gbest;
        x = change_pos (P, i_gbest, x_gbest, N ,x);
        ObFcVal=ObjFct(x);
        [x_gbest,P_gbest] = best(x,ObFcVal);
        R=P_gbest/sum(ObFcVal);
    for i = 1 : P;
        D(i)=norm(x_gbest-x(i,:));
    end
        [x,ObFcVal] = StarGeneration(x, D , R, i_gbest, ObFcVal, lb, ub, N, ObjFct);
        [x_gbest, P_gbest] = best(x,ObFcVal);
        fbest_i(iter) = P_gbest;
        P_gbest = fbest_i(iter);
    end
    %-----------------------
    fbest = fbest_i(end);
    %-----------------------
end

function [x, x_gbest, i_gbest, P_gbest] = Initialization(ObjFct,P,P_i, N, lb,ub,x0)
    for i = 1 : P_i
        for k = 1 : N
            x(i,k) = lb(k) + rand*(ub(k) - lb(k));
        end
    end

    if ~ isempty (x0)
        x(end+1,:) = x0;
    end

    ObFcVal = ObjFct(x);
    [index1, index2] = sort(ObFcVal);
    x = x(index2(1:P),:);
    x_gbest = x(1,:);
    i_gbest = index2(1);
```

```
    P_gbest = ObFcVal(index2(1));
end

function x = change_pos (P, i_gbest, x_gbest, N, x)
        for i = 1 : P
          if i ~= i_gbest
            for k = 1 : N
            x(i,k) = x(i,k) + rand*(x_gbest(k) - x(i,k));
            end
          end
        end
end

function [x_gbest, P_gbest] = best(x, ObFcVal)
    [minx, i_gbest] = min(ObFcVal);
    x_gbest = x(i_gbest,:);
    P_gbest = minx;
end

function [x,ObFcVal] = StarGeneration(x,D,R,i_gbest,ObFcVal,lb,ub,N,ObjFct)
index = find(D<R);
  for i = 1 : length(index)
    if index(i) ~= i_gbest
        for k = 1 : N
            x(index(i),k) = lb(k) + rand*(ub(k) - lb(k));
        end
        ObFcVal(index(i)) = ObjFct(x(index(i),:));
    end
  end
end
```

Appendix 4: PSO algorithm

```
% PSO algorithm main file
% Dragos Ursu  17.01.2013
% ---------------------------
% PARTICLE SWARM OPTIMIZATION
%=======================================================================
% based on paper
% "     R.C. Eberhart , Y. Shi
% "Comparing Inertia weights and constriction factors in PSO"
% Evolutionary Computation, 2000. Proceedings of the 2000, pp,84- 88, vol.1
%=======================================================================
% c1 - cognitive constant (individual learning rate) = 2
% c2 - social constant (social parameter) = 2
% c1 + c2 < 4
% w - inertia weight
% wmin - minimum of inertia weight (0.4)
% wmax - maximum of inertia weight (0.9)
% IterM - how many time the birds change position in search for food
% x_gbest - global best position ;   P_gbest - global best objective function
% x_pbest - personal best position ; P_pbest - personal best objective function
%-----------------------------------------------------------------------
function [xbest, fbest, fbest_i] = PSO (variables)

    N = variables.N;
    P = variables.Planets;      % particles
    P_i = variables.Planets_i;
    x0 = variables.x0;
    IterM = variables.IterM;
    lb = variables.lb;
    ub = variables.ub;
    ObjFct = variables.ObjFct;
    str = func2str(ObjFct);
    time = variables.time;
    %-------------------------------------------------------------------
%     c1 = 2;
%     c2 = 2;
    %-------------------------------------------------------------------
    c1 = 2.05;
    c2 = 2.05;
    fi = c1 + c2;
    kc = 2 / abs ( 2- fi - sqrt(fi^2 - 4*fi));
    %-------------------------------------------------------------------
    wmin = 0.2; wmax = 0.9;
    m = (wmin - wmax) / IterM;
    v = zeros(P,N);
    vm = ub(1);
    fbest_i = ones(1,IterM);
    %-------------------------------------------------------------------
    [x, v, x_pbest, P_pbest, x_gbest, P_gbest] = initialization (P, P_i, N, lb, ub,
ObjFct,x0, v);
    %-------------------------------------------------------------------
    %Particle movement
    for iter = 1 : IterM
        w = m*iter + wmax;
        P_gbesto = P_gbest;
        [x, v] = change_pos(P, N, x, v, w, c1, c2, x_pbest, x_gbest, vm, kc);
        ObFcVal = ObjFct(x);
        [x_pbest, P_pbest, x_gbest, P_gbest] = compare(P, x, ObFcVal, x_pbest, P_pbest,
x_gbest, P_gbest);
        fbest_i(iter) = P_gbest;
        %-----------------------------------------------------------
    end
  %----------------------
```

```
    fbest = fbest_i(end);
    %----------------------
    xbest = x_gbest;
end

function [x, v, x_pbest, P_pbest, x_gbest, P_gbest] = initialization (P, P_i, N, lb, ub,
ObjFct,x0, v)
    for i = 1 : P_i
        for k = 1 : N
            x(i,k) = lb(k) + rand*(ub(k)-lb(k));
        end
    end
    for i = 1 : P
        for k = 1 : N
            v(i,k) = rand*2-1;
        end
    end
    if ~ isempty (x0)
        x(end+1,:) = x0;
    end

    ObFcVal = ObjFct(x);
    [index1, index2] = sort(ObFcVal);
    x = x(index2(1:P),:);
    x_gbest = x(1,:);
    P_gbest = ObFcVal(index2(1));
    x_pbest = x;
    P_pbest = ObFcVal(index2(1:P));
end

function [x, v] = change_pos(P, N, x, v, w, c1, c2, x_pbest, x_gbest, vm, kc)
    for i = 1 : P
        for k = 1 : N
%             v(i,k) = w * v(i,k) + c1 * rand * (x_pbest(i,k) - x(i,k)) + c2 * rand *
(x_gbest(1,k) - x(i,k)) ;
            v(i,k) = kc * ( v(i,k) + c1 * rand * (x_pbest(i,k) - x(i,k)) + c2 * rand *
(x_gbest(1,k) - x(i,k))) ;
            v(i,k) = sign(v(i,k)) * min(abs(v(i,k)),vm);
            x(i,k) = x(i,k) + v(i,k);
        end
    end
end

function [x_pbest, P_pbest, x_gbest, P_gbest] = compare(P, x, ObFcVal, x_pbest, P_pbest,
x_gbest, P_gbest)
    [P_best, BestPart] = min (ObFcVal);
    x_best = x(BestPart,:);
    for i = 1 : P
        if ObFcVal(i) < P_pbest(i)
            P_pbest(i) = ObFcVal(i);
            x_pbest(i,:) = x (i,:);
        end
    end
    if P_best < P_gbest
            P_gbest = P_best;
            x_gbest = x_best;
    end
end
```

Appendix 5: GSA algorithm

```
% GSA algorithm main file
% Dragos Ursu  15.01.2013
% ----------------------------
% GRAVITATION SEARCH ALGORITHM
%=========================================================================
% based on paper
% "     E. Rashedi, H. Nezamabadi-pour and S. Saryazdi,
% "GSA: A Gravitational Search Algorithm", Information sciences, vol. 179,
% no. 13, pp. 2232-2248, 2009."
%=========================================================================
% V - velocity;     a - acceleration;   M - mass;   N - dimension
% P - planets;      x - position of P;  R - distance between planets
% Rnorm - Norm of eq. 9;    Rpower - Power of R in eq. 7
%-------------------------------------------------------------------------
function [xbest, fbest, fbest_i] = GSA(variables)

    N  = variables.N;
    P  = variables.Planets;
    P_i= variables.Planets_i;
    xO = variables.xO;
    IterM = variables.IterM;
    lb = variables.lb;
    ub = variables.ub;
    ObjFct = variables.ObjFct;
    str = func2str(ObjFct);
    time = variables.time;
    %----------
    Rnorm=2;
    Rpower = 1;
    v = zeros(P,N);
    %-----------------------------------------------------------------
     [x, xbest, ObFcVal, P_gbest] = initialization(N, P, P_i, lb, ub, ObjFct, xO);
    %-----------------------------------------------------------------
    for iter = 1 : IterM
       P_gbesto = P_gbest;
       M = M_calc(ObFcVal);
       G = G_cst(iter, IterM);
       a = Acceleration(M, N, P, x, G, Rnorm, Rpower, iter, IterM);
       [x, v] = move(x, a, v, P, N);
       x = check_P_pos(P, N, x, lb, ub);
       ObFcVal = ObjFct(x);
       [xbest, P_gbest] = best(x, ObFcVal);
       fbest_i(iter) = P_gbest;
    end
    fbest = fbest_i(end);
end

function [x, xbest, ObFcVal, P_gbest] = initialization(N, P, P_i, lb, ub, ObjFct, xO)
    for i = 1 : P_i
        for k = 1 : N
            x(i,k) = lb(k) + rand*(ub(k) - lb(k));
        end
    end

    if ~ isempty (xO)
        x(end+1,:) = xO;
    end

    ObFcVal = ObjFct(x);
    [index1, index2] = sort(ObFcVal);
    x = x(index2(1:P),:);
    xbest = x(1,:);
```

```
        ObFcVal = ObFcVal(index2(1:P));
        P_gbest = min(ObFcVal);
end

function M = M_calc(ObFcVal)
    bst = min(ObFcVal);
    wst = max(ObFcVal);
    M = (ObFcVal-wst)./(bst-wst);
    M = M./sum(M);
end

function G = G_cst(iter, IterM)
    alf = 20; GO = 100;
    G = GO*exp(-alf*iter/IterM);
end

function a = Acceleration(M,N,P,x,G,Rnorm,Rpower,iter,IterM)
    kchoice = ceil(P*(1-iter/(IterM+1)));
    [Mp dp] = sort(M,'descend');
    for i = 1 : P
        F(i,:) = zeros (1, N);
        for ii = 1 : kchoice
            j  = dp(ii);
            if j ~= i
                R = norm(x(i,:)-x(j,:),Rnorm);
                for k = 1 : N
                    F(i,k) = F(i,k) + rand * M(j) * ((x(j,k)-x(i,k))/(R^Rpower+eps));
                end
            end
        end
    end
    a = F.*G;
end

function [x, v] = move(x,a,v,P,N)
    for i = 1 : P
        for k = 1 : N
            v(i,k) = rand*v(i,k) + a(i,k);
            x(i,k) = v(i,k) + x(i,k);
        end
    end
end

function x = check_P_pos(P,N,x,lb,ub)
    for i = 1 : P
        for k = 1 : N
            if (x(i,k) > ub(k)) || (x(i,k) < lb(k))
                x(i,k)=lb(k)+rand*(ub(k)-lb(k));
            end
        end
    end
end

function [xbest, P_gbest] = best(x, ObFcVal)
  [minFob, Pbest] = min(ObFcVal);
  xbest = x(Pbest,:);
  P_gbest = ObFcVal(Pbest);
End
```

Appendix 6: PSOGSA algorithm

```
% PSOGSA algorithm main file
% Dragos Ursu  19.01.2013
% ---------------------------------------------------------------
% HYBRID PARTICLE SWARM OPTIMIZATION GRAVITATION SEARCH ALGORITHM
% =======================================================================
% based on paper
% "Seyed Mirjalili, Siti Zaiton Mohd Hashim
% "A new hybrid PSOGSA Algorithm for function optimization"
% Computer and Information Application (ICCIA), 2010, pp,374-377
% =======================================================================
% c1 - cognitive constant (individual learning rate) = 2
% c2 - social constant (social parameter) = 2
% c1 + c2 < 4
% w - inertia weight
% wmin - minimum of inertia weight (0.4)
% wmax - maximum of inertia weight (0.9)
% IterM - how many time the birds change position in search for food
% x_gbest - global best position ;   P_gbest - global best objective function
% x_pbest - personal best position ; P_pbest - personal best objective function
% ----    ----    ----    ----    ----    ----    ----    ----    ----
% V - velocity;     a - acceleration;   M - mass;   N - dimension
% P - planets;      x - position of P;  R - distance between planets
% Rnorm - Norm of eq. 9;   Rpower - Power of R in eq. 7
% -------------------------------------------------------------------------
function [xbest, fbest, fbest_i] = PSOGSA (variables)

    N = variables.N;
    P = variables.Planets;
    P_i = variables.Planets_i;
    x0 = variables.x0;
    IterM = variables.IterM;
    lb = variables.lb;
    ub = variables.ub;
    ObjFct = variables.ObjFct;
    str = func2str(ObjFct);
    time = variables.time;
    %-------------------------------------------------------------------
    Rnorm=2;
    Rpower = 1;
    %-------------------------------------------------------------------
    v = zeros(P,N);
    c1 = 0.5;
    c2 = 1.5;
    wmin = 0.2; wmax = 0.9;
    m = (wmin - wmax) / IterM;
    %-------------------------------------------------------------------
    v = zeros(P,N);
    vm = ub(1);
    fbest_i = ones(1,IterM);
    %-------------------------------------------------------------------
    [x, v, x_pbest, P_pbest, x_gbest, P_gbest] = initialization (P, P_i, N, lb, ub,
ObjFct,x0, v);
    %-------------------------------------------------------------------
    ObFcVal = P_pbest;
    %Particle movement
    for iter = 1 : IterM
        w = m*iter + wmax;
        P_gbesto = P_gbest;
        %GSA
        M = M_calc(ObFcVal);
        G = G_cst(iter, IterM);
        acc = Acceleration(M, N, P, x, G, Rnorm, Rpower, iter, IterM);
```

```matlab
        %PSO
        [x, v] = change_pos(P, N, x, v, c1, c2, w, acc, x_gbest, vm);
        ObFcVal = ObjFct(x);
        [x_pbest, P_pbest, x_gbest, P_gbest] = compare(P, x, ObFcVal, x_pbest, P_pbest,
x_gbest, P_gbest);
        fbest_i(iter) = P_gbest;
    end
    fbest = fbest_i(end);
    xbest = x_gbest;
end

function [x, v, x_pbest, P_pbest, x_gbest, P_gbest] = initialization (P, P_i, N, lb, ub,
ObjFct,x0, v)
    for i = 1 : P_i
        for k = 1 : N
            x(i,k) = lb(k) + rand*(ub(k)-lb(k));
            v(i,k) = rand*2-1;
        end
    end

    if ~ isempty (x0)
        x(end+1,:) = x0;
    end

    ObFcVal = ObjFct(x);
    [index1, index2] = sort(ObFcVal);
    x = x(index2(1:P),:);
    x_gbest = x(1,:);
    P_gbest = ObFcVal(index2(1));
    x_pbest = x;
    P_pbest = ObFcVal(index2(1:P));
end

function M = M_calc(ObFcVal)
    bst = min(ObFcVal);
    wst = max(ObFcVal);
    M = (ObFcVal-wst)./(bst-wst);
    M = M./sum(M);
end

function G = G_cst(iter, IterM)
    alf = 20; G0 = 1;
    G = G0*exp(-alf*iter/IterM);
end

function acc = Acceleration(M,N,P,x,G,Rnorm,Rpower,iter,IterM)
    kchoice = ceil(P*(1-iter/(IterM+1)));
    [Mp dp] = sort(M,'descend');
    for i = 1 : P
        F(i,:) = zeros (1, N);
        for ii = 1 : kchoice
            j  = dp(ii);
            if j ~= i
                R = norm(x(i,:)-x(j,:),Rnorm);
                for k = 1 : N
                    F(i,k) = F(i,k) + rand * M(j) * ((x(j,k)-x(i,k))/(R^Rpower+eps));
                end
            end
        end
    end
    acc = F.*G;
end

function [x, v] = change_pos(P, N, x, v, c1, c2, w, acc, x_gbest, vm)
    for i = 1 : P
        for k = 1 : N
```

```
            v(i,k) = w * v(i,k) + c1 * rand * acc(i,k) + c2 * rand * (x_gbest(1,k) -
x(i,k)) ;
            v(i,k) = sign(v(i,k)) * min(abs(v(i,k)),vm);
            x(i,k) = x(i,k) + v(i,k);
        end
    end
end

function [x_pbest, P_pbest, x_gbest, P_gbest] = compare(P, x, ObFcVal, x_pbest, P_pbest,
x_gbest, P_gbest)
    [P_best, BestPart] = min (ObFcVal);
    x_best = x(BestPart,:);

    for i = 1 : P
        if ObFcVal(i) < P_pbest(i)
            P_pbest(i) = ObFcVal(i);
            x_pbest(i,:) = x (i,:);
        end
    end

    if P_best < P_gbest
            P_gbest = P_best;
            x_gbest = x_best;
    end
end
```

Appendix 7: Test functions

```
function [F] = Ackley(x)
F=zeros(1,size(x,1));
n = size(x,2);
a = 20; b = 0.2; c = 2*pi;
for index=1:size(x,1)
    x0=x(index,:);
    s1 = 0; s2 = 0;
    for i=1:n;
        s1 = s1+x0(i)^2;
        s2 = s2+cos(c*x0(i));
    end
    F(index) = -a*exp(-b*sqrt(1/n*s1))-exp(1/n*s2)+a+exp(1);
end

%-------------------------------------------------------------------------

function [F] = DeJong(x)
F=zeros(1,size(x,1));
n = size(x,2);
for index = 1 : size(x,1)
    x0 = x(index,:);
    sum = 0;
        for i = 1 : n;
            sum = sum + x0(i)^2;
        end
    F(index) = sum;
End

%-------------------------------------------------------------------------

function [F] = Rastring(x)
F=zeros(1,size(x,1));
n = size(x,2);
a = 10; b = 2*pi;
for index=1:size(x,1)
    x0=x(index,:);
    sum1 = 0; sum2 = 0;
    for i=1:n;
        sum1 = sum1 + x0(i)^2;
        sum2 = sum2 + cos(b*x0(i));
    end
    F(index) = a*n + sum1 - a*sum2;
end

%-------------------------------------------------------------------------

function [F] = Rosenbrock(x)
F=zeros(1,size(x,1));
n = size(x,2);
a = 100;
for index=1:size(x,1)
    x0=x(index,:);
    sum1 = 0; sum2 = 0; sum3 = 0;  sum4 = 0;
    for i=1:n-1;
        sum1 = sum1 + x0(i+1)^2;
        sum2 = sum2 + x0(i+1)*x0(i)^2;
        sum3 = sum3 + x0(i)^4;
        sum4 = sum4 + (1-x0(i))^2;
    end
    F(index) = a*sum1 - 2*a*sum2 + a*sum3 + sum4;
End
```

Appendix 8: Current generation function

```
% Ursu Dragos 2011
% --------------------------
% 2-level trapezoidal function
% --------------------------
function i_out=trap(theta)
a = mod(theta,360);
alf_c=15;
a1=alf_c;
a2=60;
a2_1=a2-a1/2;
a2_2=a2+a1/2;
a3=180-alf_c;
a4=180;
a5=a4+a1;
a6_1=a4+a2_1;
a6_2=a4+a2_2;
a7=a4+a3;
Itq=1;
Iex=1;
if (0<=a)&&(a<a1)
    i_out=(Iex/a1)*a;
elseif (a1<=a)&&(a<=a2_1)
    i_out=Iex;
elseif ((a2_1)<a)&&(a<(a2_2))
    i_out=Iex+((Itq-Iex)/a1)*(a-a2_1);
elseif ((a2_2)<=a)&&(a<=a3)
    i_out=Itq;
elseif (a3<a)&&(a<=a4)
    i_out=Itq-((Itq/(a4-a3))*(a-a3));
elseif (a4<a)&&(a<a5)
    i_out=-((Iex/a1)*(a-a4));
elseif (a5<=a)&&(a<=a6_1)
    i_out=-Iex;
elseif ((a6_1)<a)&&(a<(a6_2))
    i_out=Iex-((Itq-Iex)/a1)*(a-a6_1));
elseif ((a6_2)<=a)&&(a<=a7)
    i_out=-Itq;
elseif (a7<a)&&(a<=360)
    i_out=Itq+((Itq/(a4-a3))*(a-a7)));
end
```

Appendix 9: PLL speed observer

```c
/**********************************************************************\
*                         BLDC-MRM 6phase                            *
*                                                                    *
*                                                                    *
* Author:  Dragos Ursu, 2014                                         *
*                                                                    *
* Content :  Speed PLL - estimates speed from theta                  *
* Input  1:  Theta | el. radians                                     *
* Input  2:  Kp                                                      *
* Input  3:  Ki                                                      *
* Output 1:  speed | el. rad/s                                       *
* Output 2:  angle                                                   *
\**********************************************************************/
#define S_FUNCTION_NAME  PLL_speed
#define S_FUNCTION_LEVEL 2
#define PI 3.1415926535898
#define step 0.0001

#include "simstruc.h"
#include "math.h"

static void mdlInitializeSizes(SimStruct *S)
{
    ssSetNumSFcnParams(S, 0);
    if (ssGetNumSFcnParams(S) != ssGetSFcnParamsCount(S)) {
        return;
    }
    ssSetNumContStates(S, 0);
    ssSetNumDiscStates(S, 3);
    if (!ssSetNumInputPorts(S, 3)) return;
    ssSetInputPortWidth(S, 0, 1);
    ssSetInputPortDirectFeedThrough(S, 0, 1);
    ssSetInputPortWidth(S, 1, 1);
    ssSetInputPortDirectFeedThrough(S, 1, 1);
    ssSetInputPortWidth(S, 2, 1);
    ssSetInputPortDirectFeedThrough(S, 2, 1);
    if (!ssSetNumOutputPorts(S, 2)) return;
    ssSetOutputPortWidth(S, 0, 1);
    ssSetOutputPortWidth(S, 1, 1);
    ssSetNumSampleTimes(S, 1);
    ssSetOptions(S, SS_OPTION_EXCEPTION_FREE_CODE);
}
static void mdlInitializeSampleTimes(SimStruct *S)
{
    ssSetSampleTime(S, 0, INHERITED_SAMPLE_TIME);
    ssSetOffsetTime(S, 0, 0);
}
#define MDL_INITIALIZE_CONDITIONS
#if defined(MDL_INITIALIZE_CONDITIONS)
static void mdlInitializeConditions(SimStruct *S)
{
    real_T *w = ssGetOutputPortRealSignal(S,0);
    real_T *a = ssGetOutputPortRealSignal(S,1);
    real_T *t = ssGetRealDiscStates(S);
    w[0] = 0.0;
    a[0] = 0.0;
    t[0] = 0.0;
    t[1] = 0.0;
    t[2] = 0.0;
}
#endif
```

```
static void mdlOutputs(SimStruct *S, int_T tid)
{
    InputRealPtrsType theta = ssGetInputPortRealSignalPtrs(S,0);
    InputRealPtrsType   kp = ssGetInputPortRealSignalPtrs(S,1);
    InputRealPtrsType   ki = ssGetInputPortRealSignalPtrs(S,2);
    real_T             *w = ssGetOutputPortRealSignal(S,0);
    real_T             *a = ssGetOutputPortRealSignal(S,1);
    real_T             *t = ssGetRealDiscStates(S);
    float err = sin (*theta[0]-t[1]);
    w[0] = t[0] + (*kp[0] + *ki[0] * step) * err ;
    t[0] = w[0] * step ;
    t[1] = t[2] + w[0] * step ;
    t[2] = t[1] ;
    t[1] = fmod(t[1], 2*PI);
    a[0] = t[1];
}
static void mdlTerminate(SimStruct *S)
{
}
#ifdef  MATLAB_MEX_FILE
#include "simulink.c"
#else
#include "cg_sfun.h"
#endif
```

Appendix 10: Signal offset S-function

```
/*********************************************************************\
*                         BLDC-MRM 6phase                           *
*                                                                   *
*                                                                   *
* Author:  Dragos Ursu, 2013                                        *
*                                                                   *
* Content :  Auto offset ADC signals if enable == 0                 *
* Input  1:  ADC signal                                             *
* Input  2:  Enable                                                 *
* Output 1:  Offset                                                 *
\*********************************************************************/

#define S_FUNCTION_NAME  offset_adc
#define S_FUNCTION_LEVEL 2
#include "simstruc.h"

static void mdlInitializeSizes(SimStruct *S)
{
    ssSetNumSFcnParams(S, 0);
    if (ssGetNumSFcnParams(S) != ssGetSFcnParamsCount(S)) {
            return;
    }

    ssSetNumContStates(S, 0);
    ssSetNumDiscStates(S, 0);
    if (!ssSetNumInputPorts(S, 2)) return;
    ssSetInputPortWidth(S, 0, 1);
    ssSetInputPortDirectFeedThrough(S, 0, 1);
    ssSetInputPortWidth(S, 1, 1);
    ssSetInputPortDirectFeedThrough(S, 1, 1);
    if (!ssSetNumOutputPorts(S, 1)) return;
    ssSetOutputPortWidth(S, 0, 1);

    ssSetNumSampleTimes(S, 1);
    ssSetOptions(S, SS_OPTION_EXCEPTION_FREE_CODE);
}

static void mdlInitializeSampleTimes(SimStruct *S)
{
    ssSetSampleTime(S, 0, INHERITED_SAMPLE_TIME);
    ssSetOffsetTime(S, 0, 0.0);
}
static void mdlOutputs(SimStruct *S, int_T tid)
{
    InputRealPtrsType offPtr = ssGetInputPortRealSignalPtrs(S,0);
    InputRealPtrsType enablePtr = ssGetInputPortRealSignalPtrs(S,1);
    real_T             *x_offset = ssGetOutputPortRealSignal(S,0);

        if (*enablePtr[0]==0)
                {
                        *x_offset = - *offPtr[0];
                }
 }
static void mdlTerminate(SimStruct *S)
{
}
#ifdef  MATLAB_MEX_FILE
#include "simulink.c"
#else
#include "cg_sfun.h"
#endif
```

Appendix 11: C-code sample for the 5-phase BLDC-MRM control

```
// Pourya Shamsi @ 2013
#include "DSP28x_Project.h"
#include "defines5.h"
#include "cmds5.h"

#define _Jump 10
///////////////////////////
unsigned int timer,timer_srm;
int Jump,mode_count,ctrlmode,speed_count1,speed_count2;
float
teta_srm,Irefa,Irefb,Irefc,Irefd,Irefe,srm_mode,srm_phase,hys,hys1,hysg,loccur,teta_zero;
float start[5],end[5],pre_m[5],pre_g[5],preband,startg[5],endg[5],enda[5];
float
speed,spe[10],phase,phase_old,speedref,speedold,intspeed,kp_speed,ki_speed,limup_speed,liml
ow_speed;
unsigned long int speed_count;
float Ireff,Irefq;

int statea,stateb,statec,stated,statee;
///////////////////////////

#pragma CODE_SECTION(CONTROL, "ramfuncs");
interrupt void CONTROL(void){
                modes();
                phase=((float)EQep2Regs.QPOSCNT)*((float)-0.021972656);

                zig_t_en=zig_t_en+1;
                if (zig_t_en==1){
                                SciaRegs.SCITXBUF=zig_r1_;
                }else if (zig_t_en==5){
                                SciaRegs.SCITXBUF=zig_r2_;
                }else if (zig_t_en==9){
                                SciaRegs.SCITXBUF=zig_r3_;
                }else if (zig_t_en==13){
                                SciaRegs.SCITXBUF=zig_r4_;
                }else if (zig_t_en==17){
                                SciaRegs.SCITXBUF=zig_r5_;
                }else if (zig_t_en==21){
                                SciaRegs.SCITXBUF=zig_r6_;
                }else if (zig_t_en==25){
                                SciaRegs.SCITXBUF=ZIG_SERV;
                }else if (zig_t_en>=30){
                        zig_t_en=300;
                        zig_check=1;
                }

        Jump=Jump-1;
        if (Jump<=0)
        {
                Jump=0;
        }
                timer=timer+1;
                if (timer>20000){
                        timer=0;
                }
        EPwm1Regs.ETCLR.bit.INT=1;
        PieCtrlRegs.PIEACK.all |= PIEACK_GROUP3;
        return;
}

#pragma CODE_SECTION(modes, "ramfuncs");
```

```c
void modes(){
#ifdef _fluxb
        speed_count=speed_count+1;
        if (speed_count>=20){
                speed_count=0;

                spe[0]=(phase-phase_old)*(float)(333.333333333);
                        if ((phase<5) && (phase_old>355)){
                                spe[0]=spe[0]+120000.0;
                        }
                        if ((phase_old<5) && (phase>355)){
                                spe[0]=spe[0]-120000.0;
                        }
                        if ((spe[0]>8000) || (spe[0]<-8000)){
                                spe[0]=spe[1];
                        }
                        phase_old=phase;

                        speed=((float)2.0*(spe[1]))+spe[0]+spe[2];
                        speed=speed*0.0674552;
                        speed=(1.14298*(spe[3]))+speed;
                        speed=(-0.412801*(spe[4]))+speed;
                        spe[4]=spe[3];
                        spe[3]=speed;
                        spe[2]=spe[1];
                        spe[1]=spe[0];

                        tempf1=ki_speed*20;
                        if (ctrlmode>0){

        PI(&speedref,&speed,&speedold,&intspeed,&Irefq,&kp_speed,&tempf1,&limup_speed,&lim
low_speed,&limup_speed,&limlow_speed);
                                if (ctrlmode==1){
                                        ctrlmode=2;
                                }
                        }
                }
        Ia[lf]=((Ia[0]+Ia[1]+Ia[2]+Ia[3]-9051.28)*GAIN_Ia2);
        Ib[lf]=((Ib[0]+Ib[1]+Ib[2]+Ib[3]-6673.0)*GAIN_Ib2);
        Ic[lf]=((Ic[0]+Ic[1]+Ic[2]+Ic[3]-7310.3)*GAIN_Ic2);
        Id[lf]=((Id[0]+Id[1]+Id[2]+Id[3]-7924.7)*GAIN_Id2);
        Ie[lf]=((Ie[0]+Ie[1]+Ie[2]+Ie[3]-7525.5)*GAIN_Ie2);
/*

        if (Ia[lf]>Ifault){
                Fault=1;
        }
        if (Ib[lf]>Ifault){
                        Fault=1;
        }
        if (Ic[lf]>Ifault){
                        Fault=1;
        }
        if (Id[lf]>Ifault){
                        Fault=1;
        }
        if (Ie[lf]>Ifault){
                        Fault=1;
        }
*/
        if (Fault==1){Fault=0;}
        teta_srm=phase+teta_zero;

        if (teta_srm>=240){
                        teta_srm=teta_srm-240;
        }
```

```
if (teta_srm>=120){
              teta_srm=teta_srm-120;
}
if (teta_srm>=120){
              teta_srm=teta_srm-120;
}
if (teta_srm>=120){
              teta_srm=teta_srm-120;
}

if (teta_srm<=-240){
        teta_srm=teta_srm+240;
}
if (teta_srm<=-120){
        teta_srm=teta_srm+120;
}
if (teta_srm<=-120){
        teta_srm=teta_srm+120;
}
if (teta_srm<0){
              teta_srm=teta_srm+120;
}
if (teta_srm<0){
              teta_srm=teta_srm+120;
}

if (srm_mode>2){
        tempf2=3.0*(teta_srm-15.0);
        tempf1=tempf2;
        Boldea(&tempf1,&Irefa);

        tempf1=tempf2-36.0;
        Boldea(&tempf1,&Irefb);

        tempf1=tempf2-72.0;
        Boldea(&tempf1,&Irefc);

        tempf1=tempf2-108.0;
        Boldea(&tempf1,&Irefd);

        tempf1=tempf2-144.0;
        Boldea(&tempf1,&Irefe);
}

if (srm_mode==10 && Fault==0){
              if ((speed-speedref)>100){intspeed=intspeed-0.00002;}

              if (Ia[lf]>=Irefa){
                      statea=-1;
              }else{
                      statea=1;
              }

              if (Ib[lf]>=Irefb){
                      stateb=-1;
              }else{
                      stateb=1;
              }

              if (Ic[lf]>=Irefc){
                      statec=-1;
              }else{
                      statec=1;
              }
              if (Id[lf]>=Irefd){
                      stated=-1;
```

```
        }else{
                stated=1;
        }

        if (Ie[lf]>=Irefe){
                statee=-1;
        }else{
                statee=1;
        }


        if (statea==1){
                Ant_off;
                Anb_off;
        }else{
                Apt_off;
                Apb_off;
        }

        if (stateb==1){
                Bnt_off;
                Bnb_off;
        }else{
                Bpt_off;
                Bpb_off;
        }

        if (statec==1){
                Cnt_off;
                Cnb_off;
        }else{
                Cpt_off;
                Cpb_off;
        }


        if (stated==1){
                Dnt_off;
                Dnb_off;
        }else{
                Dpt_off;
                Dpb_off;
        }


        if (statee==1){
                Ent_off;
                Enb_off;
        }else{
                Ept_off;
                Epb_off;
        }

        d_100ns(12);

        if (statea==1){
                Apt_on;
                Apb_on;
        }else{
                Ant_on;
                Anb_on;
        }

        if (stateb==1){
                Bpt_on;
```

```
                                Bpb_on;
                }else{
                                Bnt_on;
                                Bnb_on;
                }

                if (statec==1){
                                Cpt_on;
                                Cpb_on;
                }else{
                                Cnt_on;
                                Cnb_on;
                }

                if (stated==1){
                                Dpt_on;
                                Dpb_on;
                }else{
                                Dnt_on;
                                Dnb_on;
                }

                if (statee==1){
                                Ept_on;
                                Epb_on;
                }else{
                                Ent_on;
                                Enb_on;
                }

        if (speed>5000 || speed<-5000){Fault=2;}
        if (Fault==1 || Fault==2){
                        Apt_off;
                        Apb_off;
                        Bpt_off;
                        Bpb_off;
                        Cpt_off;
                        Cpb_off;
                        Dpt_off;
                        Dpb_off;
                        Ept_off;
                        Epb_off;
                        Ant_off;
                        Anb_off;
                        Bnt_off;
                        Bnb_off;
                        Cnt_off;
                        Cnb_off;
                        Dnt_off;
                        Dnb_off;
                        Ent_off;
                        Enb_off;
                        srm_mode=200;
                        Fault_keep=Fault;
                }
        }


        if (srm_mode==200){
                Apt_off;
                Apb_off;
                Bpt_off;
                Bpb_off;
                Cpt_off;
                Cpb_off;
```
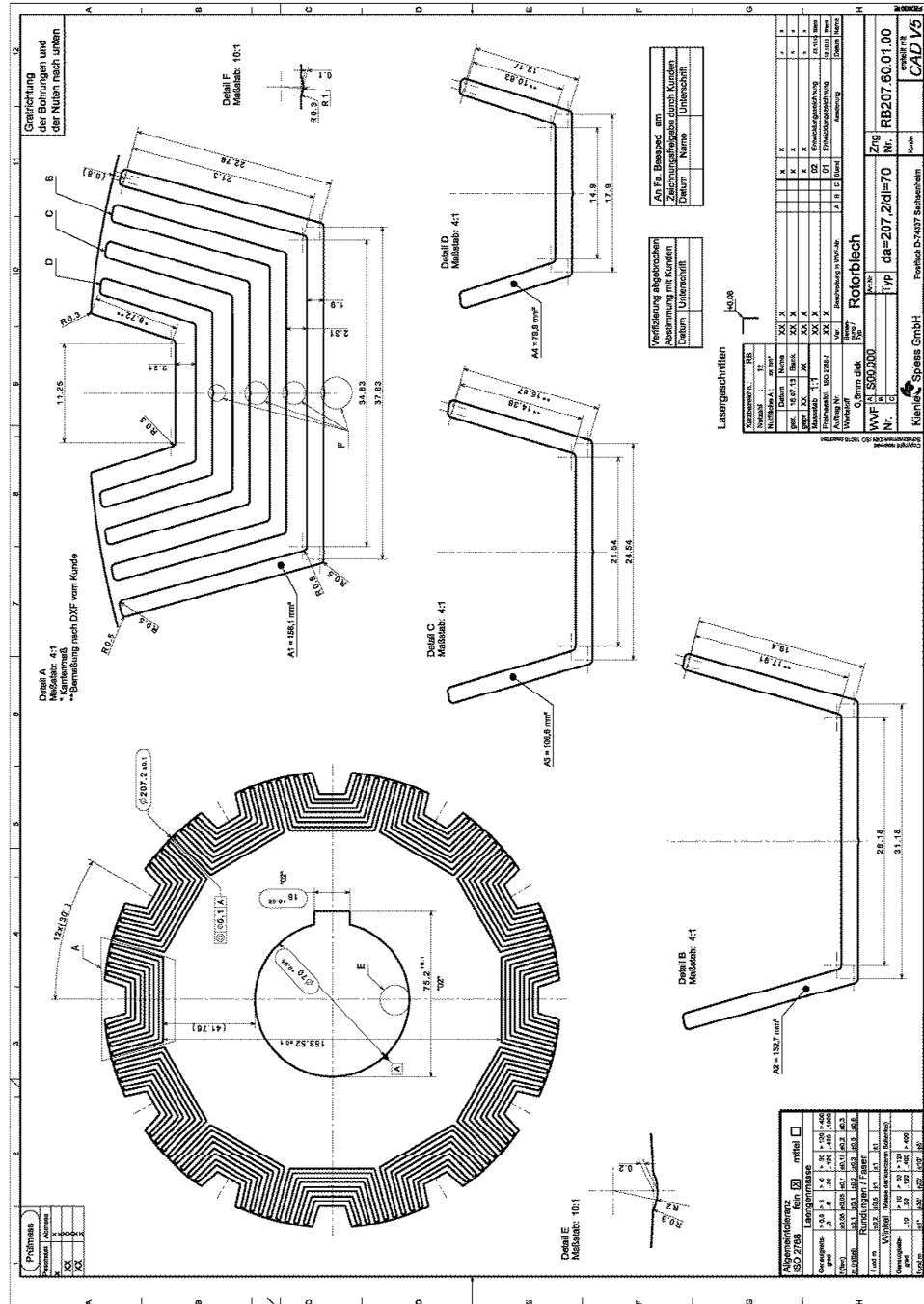
```
                Dpt_off;
                Dpb_off;
                Ept_off;
                Epb_off;
                Ant_off;
                Anb_off;
                Bnt_off;
                Bnb_off;
                Cnt_off;
                Cnb_off;
                Dnt_off;
                Dnb_off;
                Ent_off;
                Enb_off;
                srm_mode=0;
                mode_count=0;
        }

#endif


}
```

Appendix 12: Technical drawing for BLDC-MRM Gen.

Summary in Romanian

În condiţiile preţului ridicat a magneţilor permanenţi de energie înaltă, tema studiată este de acută actualitate şi face referite la studiul invertoarele şi maşinile multifazate fără perii, fără magneţi permanenţi şi controlate prin curenţi de fază trapezoidali, prezentând următoarele avantaje: cost redus, densitate ridicată de cuplu (şi putere), toleranţă la defecte, simplitatea controlului şi utilizarea eficientă a elementelor de comutaţie din invertor.

Teza se bazează pe revitalizarea unei soluţii propuse in 1986, dar care nu a putut fi analizată şi testată la adevăratul potenţial din cauza tehnologiei elementelor de comutaţie, sistemelor de calcul şi achiziţie de date existente în acel moment, cât şi concentrarea eforturilor pe noile soluţii cu magneţi permanenţi ce promiteau performanţe mărite la un cost acceptabil. Lucrarea urmăreşte atât testarea ideilor nevalidate în trecut, cât şi propunerea de soluţii noi de analiză şi experimentare, ce se încadrează în contextul actual al industriei de acţionări electrice speciale.

Obiectivele avute în vedere pe parcursul tezei sunt rezumate după cum urmează:

- dezvoltarea unei metode analitice de proiectare a maşinii de tip BLDC-MRM;
- analiza programelor de modelare numerică cu FEM, alegerea celui mai potrivit, şi folosirea acestuia pentru calculul performanţelor în cadrul a trei maşini diferite, cu validare experimentală a modelelor propuse. Calculul pierderilor in fier pe baza variaţiei inducţiei electromagnetice în fiecare element de discretizare corespunzător unui material feromagnetic, a fost de asemenea studiat in detaliu;
- dezvoltare unui model neliniar a BLDC-MRM bazat pe metoda circuitelor magnetice, pentru studiul cuplului şi al pierderilor in fier în regim permanent în programul de optimizare cu bune performanţe de timp comparativ cu folosirea FEM.
- propunerea unui model de circuit neliniar bazat pe parametrii calculaţi din FEM sau determinaţi experimental, pentru a simula comportarea in regimurile dinamice a maşinii conectate la invertor, cu control a erorii de viteză şi de curent (pe fiecare fază).
- controlul unei maşini cu 5 faze cu invertor dedicat de tip full-bridge, în regim de motor şi slăbire de câmp într-o plajă de turaţie de 4:1.
- testarea unei strategii de control în 4 cadrane (şi slăbire de câmp) pentru maşina cu 6 faze conectată la invertoare comerciale cu un conductor de nul şi număr redus de elemente de comutaţie.
- realizarea a 2 standuri experimentale complete pentru acţionările propuse cu BLDC-MRM, unul pentru maşina cu 5 faze (dezvoltat în cadrul Universităţii Texas din Dallas), iar celalalt pentru maşina cu 6 faze (realizat în cadrul UPT).

Toate aceste obiective au fost realizate, o mare parte dintre ele reprezentând contribuţii originale publicate în 4 conferinţe IEEE (3 în Europa şi una in SUA) sau propuse spre publicare la reviste din cadrul IEEE.

Author's papers related to PhD thesis

[1]   L.N. Tutelea, D. Ursu, I. Boldea and Sorin Agarlita: *„IPM Claw Pole Alternator System for more vehicle braking energy recuperation"*, Journal of electrical engineering, www.jee.ro, Vol. 12, No. 3, 2012 (IEE INSPEC)

[2]   I. Boldea, L.N. Tutelea and D. Ursu*,"BLDC Multiphase Reluctance Machines for Wide Range Applications: a revival attempt"*, Power Electronics and Motion control Conference, EPE/PEMC-2012, pp. LS1b.1-1 - LS1b.1-6   Novi-Sad, Serbia, Print ISBN 978-1-4673-1970-6, (IEEE Explore, SCOPUS, ISI Proceedings)

[3]   D. Ursu, L.N Tutelea, I. Boldea, *"Proposal with 2D FEM analysis of a six phase, 12 poles, 3kW, 200 rpm BLDC Multiphase Reluctance Machine wind generator"*, Power Electronics and Applications European Conference, EPE-2013, pp.1-9, Lille, France, (IEEE Explore, SCOPUS, INSPEC, pending for ISI indexing,)

[4]   S. Agarlita, D. Ursu, L. Tutelea, I. Boldea and B. Fahimi, *"BLDC multiphase reluctance machines: A revival attempt with 2D FEM investigation and standstill tests"*, Energy Conversion Congress and Exposition, ECCE-2013, pp. 1850 – 1857, Denver, Colorado, USA (IEEE Explore, INSPEC, pending for ISI indexing)

[5]   D. Ursu, P. Shamsi, B. Fahimi and I. Boldea, *"5 phase BLDC-MRM: Design, Control, FEA and Steady-State Operation Experiments,"* International Conference on Optimization of Electrical and Electronic Equipment, OPTIM-2014, pp. 354 - 361, Brasov, Romania (IEEE Explore, SCOPUS, INSPEC, pending for ISI indexing,)

[6]   D. Ursu, V. Gradinaru, B. Fahimi and I. Boldea, *"BLDC multiphase reluctance machines: a revival attempt with 2D FEA, standstill and running experiments"*, pending for IEEE Trans. On Industry Applications, (ISI journal)

IEEE *Xplore*®
DIGITAL LIBRARY

Institutional Sign In

◆IEEE

SEARCH RESULTS

You searched for: **Ursu**

4 Results returned

BLDC multiphase reluctance machines: A revival attempt with 2D FEM investigation and standstill tests
Agarlita, S. ; Ursu, D. ; Tutelea, L. ; Boldea, I. ; Fahimi, B.
Energy Conversion Congress and Exposition (ECCE), 2013 IEEE
DOI: 10.1109/ECCE.2013.6646933
Publication Year: 2013 , Page(s): 1850 - 1857
IEEE CONFERENCE PUBLICATIONS

---

5 phase BLDC-MRM: Design, control, FEA and steady-state operation experiments
Ursu, Dragos ; Shamsi, Pourya ; Fahimi, Babak ; Boldea, Ion
Optimization of Electrical and Electronic Equipment (OPTIM), 2014 International Conference on
DOI: 10.1109/OPTIM.2014.6850880
Publication Year: 2014 , Page(s): 354 - 361
IEEE CONFERENCE PUBLICATIONS

Proposal with 2D FEM analysis of a six phase, 12 poles, 3kW, 200 rpm BLDC multiphase reluctance machine wind generator
Ursu, D. ; Tutelea, L. ; Boldea, I.
Power Electronics and Applications (EPE), 2013 15th European Conference on
DOI: 10.1109/EPE.2013.6631885
Publication Year: 2013 , Page(s): 1 - 9
Cited by: Papers (1)
IEEE CONFERENCE PUBLICATIONS

BLDC multiphase reluctance machines for wide range applications: A revival attempt
Boldea, I. ; Tutelea, L. ; Ursu, D.
Power Electronics and Motion Control Conference (EPE/PEMC), 2012 15th International
DOI: 10.1109/EPEPEMC.2012.6397385
Publication Year: 2012 , Page(s): LS1b.1-1 - LS1b.1-6
Cited by: Papers (2)
IEEE CONFERENCE PUBLICATIONS

Sign In | Create Account

BUPT

WEB OF SCIENCE™

Back to Search   My Tools ▼   Search History   Marked List

Results: 1
(from All Databases)

You searched for: AUTHOR: (Ursu Dragos) **...More**

Refine Results

Search within results for...

| Databases | ◄ |

| Research Domains | ▼ |

None of the results contain data in this field.

| Research Areas | ▼ |

None of the results contain data in this field.

Document Types	◄
Authors	◄
Group/Corporate Authors	◄
Editors	◄
Funding Agencies	◄
Source Titles	◄
Conference/Meeting Titles	◄
Publication Years	◄
Languages	◄
Countries/Territories	◄

Sort by: Publication Date -- newest to oldest   Page 1 of 1

☐ Select Page   Save to EndNote online   Add to Marked List

Create Citation Report

☐ 1.   **BLDC Multiphase Reluctance Machines for Wide Range Applications: a revival attempt**

By: Boldea, Ion; Tutelea, Lucian-Nicolae; Ursu, Dragos
Book Group Author(s): IEEE
Conference: 15th International Power Electronics and Motion Control Conference and Exposition (EPE-PEMC ECCE Europe)
Location: Novi Sad, SERBIA Date: SEP 04-06, 2012
Sponsor(s): Univ Novi Sad, Fac Tech Sci; Provincial Secretariat Sci & Technol Dev & High Educ AP Vojvodina; Minist Educ Sci & Technol Dev Repub Serbia; IEEE PELS
2012 15TH INTERNATIONAL POWER ELECTRONICS AND MOTION CONTROL CONFERENCE (EPE/PEMC) Published: 2012

Times Cited: 0
(from All Databases)

View Abstract

☐ Select Page   Save to EndNote online   Add to Marked List

Sort by: Publication Date -- newest to oldest   Page 1 of 1
Show: 10 per page

Approximately 1 records matched your query of the 64,066,758 (contains duplicates) in the data limits you selected.

Scopus

Search Alerts My list Settings

Live Chat Help and Contact Tutorials

AUTHOR-NAME (**dragos ursu**) Edit | Save | Set alert | Set feed

3 document results View secondary documents | Analyze results

Sort on: **Date** Cited by Relevance ☐

Search within results...

☐ Export | Download | View citation overview | View Cited by | More... Show all abstracts

Refine

Limit to   Exclude

Year
☐ 2014	(1)
☐ 2013	(1)
☐ 2012	(1)

Author Name
☐ Boldea, I.	(3)
☐ Ursu, D.	(3)
☐ Fahimi, B.	(1)
☐ Shamsi, P.	(1)
☐ Tutelea, L.	(1)

Subject Area
☐ Engineering	(3)
☐ Energy	(1)

Document Type
☐ Conference Paper	(3)

Source Title
Keyword
Affiliation
Country
Source Type
Language

Limit to   Exclude

Export refine

☐ 1 5 phase BLDC-MRM: Design, control, FEA and steady-state operation experiments — Ursu, D., Shamsi, P., Fahimi, B., Boldea, I. — 2014 — 2014 International Conference on Optimization of Electrical and Electronic Equipment, OPTIM 2014 — 0

View at Publisher

☐ 2 Proposal with 2D FEM analysis of a six phase, 12 poles, 3kW, 200 rpm BLDC multiphase reluctance machine wind generator — Ursu, D., Tutelea, L., Boldea, I. — 2013 — 2013 15th European Conference on Power Electronics and Applications, EPE 2013 — 0

View at Publisher

☐ 3 BLDC multiphase reluctance machines for wide range applications: A revival attempt — Boldea, I., Tutelea, L.-N., Ursu, D. — 2012 — 15th International Power Electronics and Motion Control Conference and Exposition, EPE-PEMC 2012 ECCE Europe — 0

View at Publisher

Display 20 results per page   Page 1

Top of page ▲

BUPT

Author's CV

Office: University "POLITEHNICA" of Timisoara, Romania
Blvd. Vasile Parvan, no. 2, room D108
Tel: +40 256 403463
Email: dragos.ursu@upt.ro

Home Address: Joseph Gabriel Street, no. 20
Timisoara, Timis, Romania
Mobile: +40 757 330343

EDUCATION:

2011-2014	Ph.D. student at University "POLITEHNICA" of Timisoara Faculty of Electrical and Power Engineering, Department of Electrical Engineering Motion control laboratory
2011	M.Sc. degree in Electrical Engineering and Power Electronics
2009-2011	Master student at University "POLITEHNICA" of Timisoara Faculty of Electrical and Power Engineering, Department of Electrical Engineering
2009	B.Sc. degree in Electrical Engineering
2005-2009	Student at University "POLITEHNICA" of Timisoara Faculty of Electrical and Power Engineering, Department of Electrical Engineering
2005	Technician degree in Electronics
2001-2005	Electronics and Telecommunications High School, Timisoara

PROFESSIONAL EXPERIENCE:

April 2012 - present day	*Research Assistant*, U.P.T., Dept. of E.E. Grant name: „Small power grid integrated renewable energy conversion hybrid systems"
Jan. 2013 – May 2013	*Visiting Scientist* at University Texas at Dallas, Dept. of EE, R.E.V.T. laboratory, USA
Oct. 2011 – Oct. 2012	*Teaching Assistant*, U.P.T., Dept. of E.E.
April 2011 – Aug. 2012	*Research Assistant*, U.P.T., Dept. of E.E. Grant name: „Energy efficient vehicles for road transport" – EE-VERT, FP7

PERSONAL INFORMATION:

Born: May 15, 1986

Family: Unmarried